A FUNDAMENTAL FLOTATION MODEL AND FLOTATION COLUMN SCALE-UP

Glenn Stephen Dobby

A thesis submitted to the
Faculty of Graduate Studies and Research
in partial fulfillment of the requirements for
the degree of
Doctor of Philosophy

Department of Mining and Metallurgical Engineering
McGill University
Montreal, Canada

ABSTRACT

A comprehensive model of particle collection in flotation is developed from a rigorous analysis of the relative motion between a particle and a bubble prior to and during particle-bubble contact. Collection efficiency E_K is derived as a product of collision efficiency E_C and attachment efficiency E_A. From trajectory calculations E_C is correlated to the bubble Reynolds number and the Stokes number, a dimensionless inertia term. E_A is calculated as the fraction of particles which reside on the bubble for a time greater than the induction time. As a result of the velocity gradient at the bubble surface E_A decreases with increasing particle size. The model explains the peak in size-by-size recovery data that is often observed at intermediate particle sizes. The peak location is shown to shift to smaller sizes as induction time increases.

A scale-up model for flotation columns is also developed. The model uses measured values of collection rate constants and an experimental correlation of plant column mixing parameters to calculate collection zone recovery R_K. R_K is interfaced with a variable cleaning zone recovery to yield a grade-recovery relationship for the plant column. The onset of bubble loading is accounted for.

RESUMÉ

Un modèle, destiné à comprendre le phénomène de capture des particules dans les procédés de flottation, est développé à partir d'une analyse rigoureuse du mouvement relatif d'une bulle et d'une particule, avant et pendant le contact bulle-particule. L'efficacité de capture E_K est évaluée comme le produit de l'efficacité de collision E_C et de l'efficacité de fixation E_A. A partir de calcul de trajectoires, E_C est reliée au nombre de Reynolds de la bulle et au nombre de Stokes, une variable d'inertie sans dimension. E_A est définie comme la fraction des particules qui résident sur la bulle pendant un temps supérieur au temps d'induction. En raison du gradient de vitesse à la surface de la bulle, E_A décroît lorsque la taille de la particule croît. Le modèle explique le pic souvent observé dans les données de récupération taille par taille, pour des particules de taille moyenne. Il est montré que l'emplacement de ce pic se déplace vers les plus petites tailles lorsque le temps d'induction augmente.

Un modèle de dimensionnement pour les colonnes de flottation est aussi développé. Ce modèle utilise des données mesurées des taux de capture ainsi qu'une corrélation experimentale sur les paramètres de transport de colonnes industrielles. Le modèle peut alors calculer la récupération au sein de la zone de capture R_K. R_K est relié à une variable de récupération au sein de la zone d'ipuration pour finale-

ment conduire à une relation donnant la récupération totale pour la colonne industrielle. On tient compte du moment de départ de la charge d'une bulle.

ACKNOWLEDGEMENTS

I am indebted especially to two people:

my wife, Gail, for her understanding and encouragement throughout the past three years, and

Prof. J.A. Finch, for his enthusiasm, keen interest and constant support throughout the research program.

As well, I gratefully acknowledge Prof. M.E. Weber, for his help in initiating the theoretical treatment of particle-bubble interaction; my colleague René del Villar, for his computer help and comradeship; Michel Leroux, for his help in the laboratory and during the plant experiments; Don Wheeler, Column Flotation Company of Canada, for enthusiastically sharing his expertise in flotation columns; Roger Amelunxen, Gibraltar Mines, for sharing his knowledge on the operation of plant columns; and the concentrator staffs at Mines Gaspé and Brunswick Mining and Smelting.

I am sincerely grateful to the Centre de Recherche Noranda for three years of financial support from the Noranda Graduate Research Fellowship.

TABLE OF CONTENTS

NOMENCLATURE

A	cross sectional area of a column or flotation cell
a	dimensionless grouping, equation 2.10
C_p	concentration of particles
C_D	drag coefficient
C_{DSk}	drag coefficient for Stokes flow
C_o	slope (negative) of drift-flux plot
c	tracer concentration
$c(t)$	tracer concentration at time t
$c_m(t)$	measured tracer concentration at time t, normalized
$c_f(t)$	fitted tracer concentration at time t, normalized
D	axial dispersion coefficient, any phase
D_ℓ	axial dispersion coefficient of liquid
D_p	axial dispersion coefficient of particle
d_b	bubble diameter
$\bar{d}_b$	volumetric mean bubble diameter
$\bar{d}_{bA}$	area mean bubble diameter
d_c	column diameter (for a column with noncircular cross-section $d_c = (4A/\pi)^{\frac{1}{2}}$)
d_e	volume equivalent bubble diameter
d_p	particle diameter
E_A	attachment efficiency, fraction or percentage
E_C	collision efficiency, fraction or percentage
E_{Cg}	collision efficiency by gravitation
E_{Ci}	collision efficiency by interception
E_{Co}	E_C calculated assuming $Sk = 0$ when $Sk > 0.05$

$E_{C\phi}$	E_C at gas holdup ϕ_g
E_K	collection efficiency, fraction or percentage
F(s)	Laplace transform
G	velocity gradient
g	acceleration due to gravity
g_j	component of g in the j direction
h	height of liquid or slurry through which a gas bubble rises
h_L	height of bubble rise to attain Γ
h_i	initial thickness of thin film between particle and bubble
h_o	thickness of thin film between particle and bubble at which spontaneous attachment occurs
K_o	terminal velocity coefficient in drift-flux analysis
K_i	i^{th} weighted cumulant
k	rate constant
$k_1 \div k_4$	Runge-Kutta coefficients
L	length of column recovery zone, vessel length
M	μ/ρ_ℓ in equation 2.12
M_k	k^{th} weighted moment
N_d	vessel dispersion number for liquid or solid particles, D/u_tL
N_ℓ	vessel dispersion number for liquid, $D_\ell/u_\ell L$
N_p	vessel dispersion number for particles, $D_p/u_{pi}L$
N_r	total number of particles removed by a bubble during its ascent
N_t	total number of particles in a cell of volume V

n	exponent in relationship $t_i \propto d_p^n$
n_θ	fraction of colliding particles that collide between $\theta = 0$ and $\theta = \theta_n$
P	grouping in equation 2.12
Q_C	volumetric overflow, or concentrate, flow rate
Q_F	volumetric feed flow rate
Q_T	volumetric underflow, or tailings, flow rate
Q_W	volumetric wash water flow rate
Q_g	volumetric gas flow rate
Q_ℓ	volumetric liquid flow rate down the recovery zone of a column
R	recovery, fractional
R_C	capture radius
R_F	recovery in cleaning zone, fractional
R_K	recovery in collection zone, fractional
R_T	total recovery, fractional
r	radial coordinate (at r_b, $r=1$)
r_b	bubble radius
r_p	particle radius
Re	Reynolds number
Re_b	Reynolds number of bubble, $u_b \rho_\ell d_b/\mu$
Re_p	Reynolds number of particle, $u_p \rho_\ell d_p/\mu$
Sk	Stokes number, $\frac{1}{9} \frac{\rho_p}{\rho_\ell} \left[\frac{d_p}{d_b}\right]^2 Re_b$
s	Laplace operator, weighting factor

s_{Opt}	optimum value for s
T	maximum time of residence time distribution
T_R	ratio of solids mass rejected from the cleaning zone to feed mass
t	time
t_L	time of bubble rise to attain Γ
t_M	mode (time) of residence time distribution
t_i	induction time
t_s	sliding time (time of particle-bubble contact)
t^*	$u_b t/d_b$
U_T	terminal velocity in unbounded fluid (particle or bubble)
u	velocity, any phase
u_b	bubble rise velocity
u_g	interstitial gas velocity, v_g/ϕ_g
u_j	liquid velocity around a bubble in the j direction
u_ℓ	interstitial liquid velocity, $v_\ell/(1-\phi_g)$
u_p	velocity of particle relative to liquid
u_{pi}	interstitial particle velocity, $u_p + u_\ell$
u_{pr}	radial particle velocity, $u_r + u_p \cos\theta$
$u_{p\theta}$	tangential particle velocity, $u_\theta + u_p \sin\theta$
u_r	radial component of liquid velocity around a sphere
u_s	slip velocity, $u_\ell + u_g$

u_t	interstial velocity of either liquid or particle
u_x, u_y	components of liquid velocity around a sphere in the x and y directions
u_Θ	tangential component of liquid velocity around a sphere
u^*	u_p/u_b
u^*_P	u^*_r or u^*_Θ at potential flow
u^*_S	u^*_r or u^*_Θ at Stokes flow
u^*_{Re}	u^*_r or u^*_Θ for bubble with Re_b
u^*_r	u_r/u_b
u^*_x	u_x/u_b
u^*_y	u_y/u_b
u^*_Θ	u_Θ/u_b
V	volume of reactor, column or flotation cell
V_P	volume of plug-flow reactor
v_g	superficial gas velocity, Q_g/A
v_j	particle velocity around a bubble in the j direction
v_ℓ	superficial liquid velocity, Q_ℓ/A or Q_T/A
v^*	v^*_x or v^*_y
v^*_n	v^* at coordinate location n
v^*_x	v_x/u_b
v^*_y	v_y/u_b
$w_k(t)$	weighting term in weighted moments equation

x	column axial distance from tracer injection point (positive down)
x, y	Cartesian coordinates, zero at center of bubble
x_s, y_s	starting coordinates for trajectory calculations
z	ratio of particle return radial velocity to impact radial velocity when a particle hits a bubble (absolute value)
β	rate of particle collection by a single bubble (mass/time)
Γ	maximum monolayer coverage (mass) of particles on a single gas bubble
Γ_M	maximum mass of solids that can be carried by a unit volume of gas
Γ_C	the mass of solids carried by a unit volume of gas (at the top of the collection zone)
γ	fractional packing density of particles on a bubble surface
Δ	step size in Runge-Kutta approximation
θ	angular coordinate, measured from front stagnation point (top) of bubble
θ_C	angle of closest approach of liquid streamlines
θ_G	angle of collision for grazing trajectory
θ_M	maximum angle of contact between sliding particle and bubble
θ_n	collision angle
θ_n	θ_n that yields $t_s = t_i$
μ	liquid viscosity
μ_k	k^{th} ordinary moment of a distribution
μ_r	ratio of slurry viscosity to liquid viscosity
ξ_s	surface vorticity, dimensionless

$\xi_{s\phi}$	ξ_s at gas holdup ϕ_g
ρ_ℓ	density of liquid
ρ_p	density of particle
τ	mean residence time, any phase
τ_ℓ	mean residence time of liquid
τ_p	mean residence time of particle
τ_r	period of rotation of particle spinning in a velocity gradient
ϕ_g	gas holdup, fractional
ϕ_s	solids volumetric holdup, fractional
Ψ	stream function, dimensionless
Ω	angular velocity of particle spinning in a velocity gradient

LIST OF FIGURES

FIGURE PAGE

FIGURE PAGE

FIGURE PAGE

LIST OF TABLES

CHAPTER 1

INTRODUCTION

A radical departure from conventional flotation machine design was introduced in the 1960's with the flotation column(1,2,3). While the flotation column is not the only innovative machine to be developed during the past two decades, it is the first of the nonmechanical machines to show significant industrial success(4,5). As with any equipment or process novel to the mineral industry, these successes did not occur overnight. The operating principles of a column differ markedly from those of conventional machines. This factor, combined with mechanical growing pains, has led to very slow industrial acceptance of the flotation column. A major difficulty still lies in scale-up from laboratory obtained data to industrial operation. The uncertainty in translating laboratory data to plant performance is a significant problem that must be overcome before there is a more universal acceptance of the flotation column. As one of two principal thrusts of this thesis, the problem of column scale-up is addressed, at the same time developing a better understanding of the transport mechanisms of a flotation column.

In common with any flotation machine the heart of column flotation is the capture of mineral particles by bubbles. The counter-current flow of particles and bubbles in the column, without mechanically induced agitation, provides an ideal situation for the application of a fundamental particle collection model. Compared to flotation chemistry, little flotation research has been devoted to the physics of flotation, in particular, to particle motion prior to and during particle-bubble contact. The second thrust of this thesis is a detailed study of the particle collection event and formulation of a fundamental model.

In the remainder of this chapter the most successful of todays' nonmechanical flotation machines are described. Particular attention is paid to two 'column' designs - the Leeds Column and the unit designed by the Column Flotation Co. of Canada.

The operating fundamentals of column operation are described in chapter 2. Particle collection kinetics, bubble loading and the effect of axial mixing are examined. An important factor considered is the rejection of particles from the cleaning zone back to the recovery zone with the consequent effect upon recovery and grade.

In chapter 3 previous work related to the physics of flotation is reviewed, followed by a complete description of the proposed flotation model. Models of the collision and attachment events are developed separately and then combined to form a comprehensive collection model. The role of all parameters is considered, particularly that of particle size.

Tracer experiments have been performed on industrial flotation columns in order to quantify the mixing conditions of large columns. In the laboratory, particle collection kinetics have been measured using a flotation column designed to eliminate both entrainment and the froth cleaning stage. The apparatus and experimental techniques of the plant and laboratory tests are described in chapter 4. The test results are presented in chapter 5.

In chapter 6 the proposed flotation model is closely examined using the present experimental data as well as prior published data. It is demonstrated that the model provides a rational explanation for several particle and bubble size related phenomena.

A scale-up methodology for flotation columns is presented in chapter 7. The methodology involves laboratory measurement of the collection kinetics followed by computer simulation of the plant size column. The scale-up model accounts for mixing conditions and bubble load.

Finally, the flotation model and the scale-up methodology are critically discussed in chapter 8, and in chapter 9 thesis conclusions, with suggestions for future work, are presented.

The scale-up of flotation columns and the modelling of particle collection by bubbles are developed in parallel throughout this thesis. The knowledge derived from the collection model provides a clearer understanding of the selectivity of flotation separation, especially with respect to the role of particle size, and contributes toward a rational column scale-up approach.

1.1 Recent Innovations in Flotation Machine Design

A critical review of flotation machine design has been provided recently by Young(6). He classifies flotation machines into four types: mechanical, pneumatic, column and froth separator. Allowing for the industrial dominance of the mechanical machine it would be simpler perhaps to consider just two classes: mechanical, and all others. Young suggests that the dominance of the mechanical machine is more a question of commercial realities and conservatism in equipment selection rather than design excellence. However, the mechanical machine has been the mainstay of froth flotation equipment for more than 50 years. The basic design and operating principles of the mechanical machine are well known (see, for example, Harris(7)) and require no further discussion here. This section focuses on non-mechanical flotation machines that have shown sufficient potential to reach the stage of either pilot plant testing or full scale operation. Specifically, four devices are described and discussed: the Flotaire, the Davcra, the Leeds Column and the flotation column. (Another design, the Russian froth separator(6), is intended primarily for flotation of large particles.)

Flotaire. Deister Concentrator Co. Inc. manufactures the Flotaire machine, shown schematically in Figure 1(a)(8). The tank is 4.5 m high and 2 to 4 m in diameter. There is no mechanical agitation. Bubbles are generated by aspirating air with high pressure water (containing dissolved frother) and pumping the water-air mixture through constriction plates located at the cell bottom and in the feed tank. Feed slurry

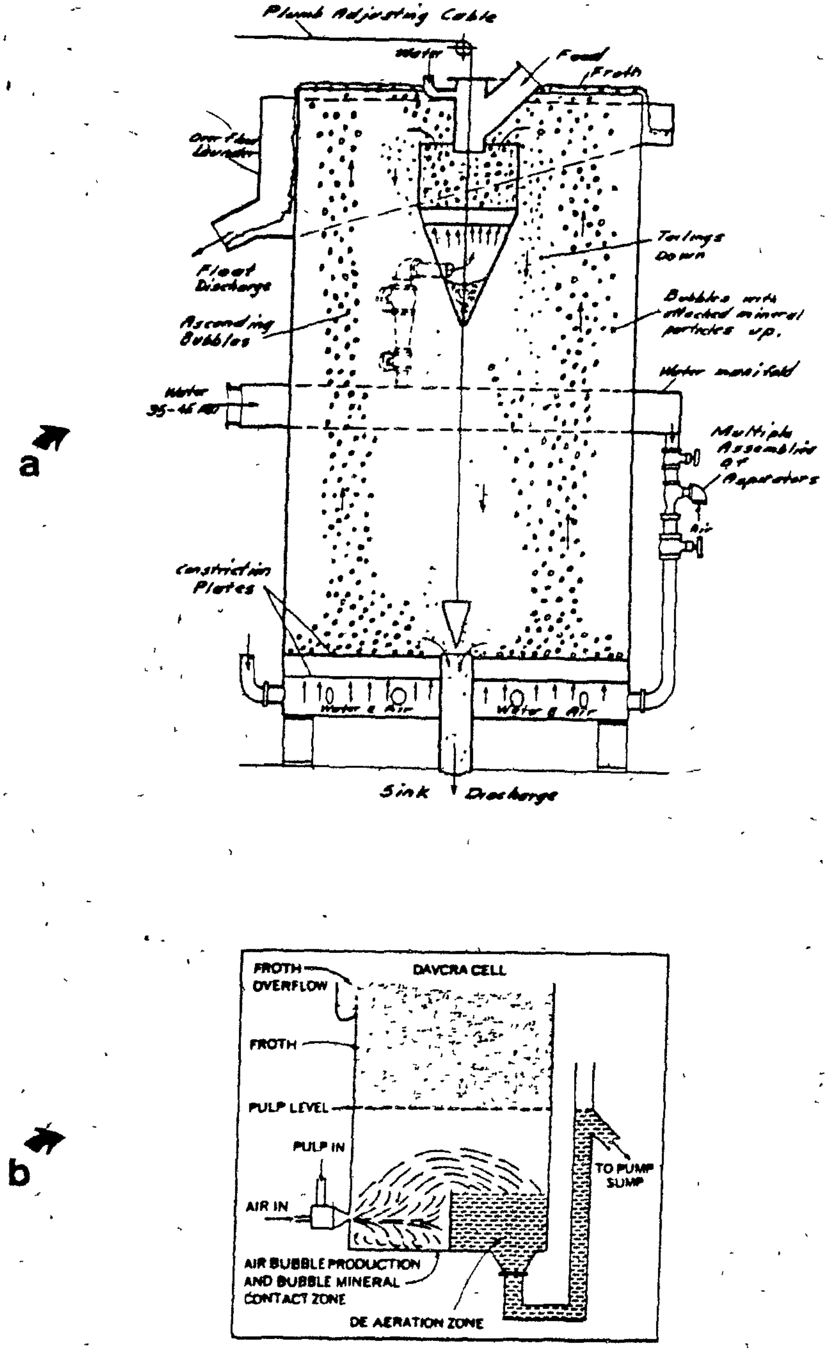

1 Schematic illustrations of
a) Flotaire machine(8), and
b) Davcra cell(9).

enters at the top and flows downward counter-current to the rising bubbles. A conventional froth bed is employed, with no wash water. The Flotaire has been used for phosphate flotation in Florida. No other applications have been reported, nor have any performance figures on phosphate been published.

Davcra. Developed at the Zinc Corporation Ltd., Australia, this machine consists of a single rectangular tank into which is fed, at the bottom, a mixture of feed slurry and air. See Figure 1(b). Bubbles are generated by injecting air into the central core of a cyclone-type orifice, into which slurry is tangentially fed. A conventional, but deep, froth is employed. Steady operation is maintained by automatic control of the feed rate and tailings rate. Abrasion of the feed nozzle is high, but is minimized with ceramic linings. Performance figures were published in 1971(9) for lead and copper roughing and zinc scavaging; however, there has been no major publication since then. Operation has been limited to Australian and South African plants.

Columns: Leeds Column / Flotation Column. An inherent limitation with flotation of fine particles in conventional cells is recovery of hydrophilic (gangue) particles by mechanical entrainment in the water reporting to the froth. The conventional method of minimizing entrainment is to create a 5-30 cm thick froth at the slurry surface. The froth permits the gangue to drain back to the pulp while retaining the hydrophobic particles, which are eventually discharged over the cell lip. Trahar(10) discussed the relationship between the recovery of hydrophilic particles and water recovery, reporting that recovery of minus 5 μm quartz was 72% of that of the water, compared to 59% for 9 μm quartz and 35% for 20 μm quartz. Water recovery to the concentrate in roughing and cleaning circuits typically will be between 20 and 40%. These numbers illustrate the significant impact of entrainment, and the inefficiency of conventional froth cleaning.

Alternative approaches to the cleaning of entrained particles have been introduced with the Leeds Column and the Canadian Flotation Column (referred to hereon simply as the flotation column). While these two devices are very different from each other, they share the common design principle of unconventional froth cleaning.

Leeds Column. This unique machine is designed to perform multiple cleaning steps in a single stage by placing several rows of horizontal barriers across the cell, between the cell top and the impeller. Each barrier consists of two parallel sets of cylindrical bars arranged such that the upper bars rest in spaces between the lower bars. The bars are so designed as to trap a thin layer of froth underneath and then allow bubbles and their attached particles to pass up through the barrier, at the same time discharging (entrained) gangue particles from the zone above. A certain quantity of wash water is added at the top. A diagram of the Leeds Column and detail of the barrier operation is given in Figure 2. The use of four to six barriers can produce an almost perfect separation. Figure 3 shows that the machine is arranged in series connection similar to

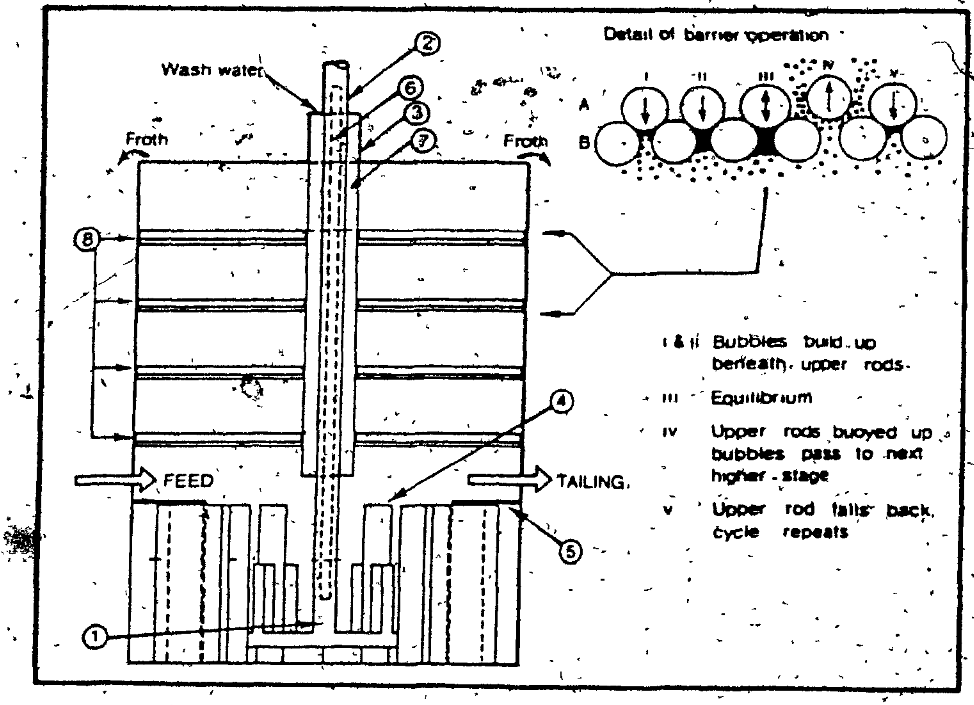

2 Schematic illustration of the Leeds column[6]. (1) Impellar; (2) Shaft; (3) Partition box; (4) Baffle vanes; (5) Corner baffle plates; (6) Dual gas line; (7) Wash water chamber; (8) Barrier Levels - 4 shown.

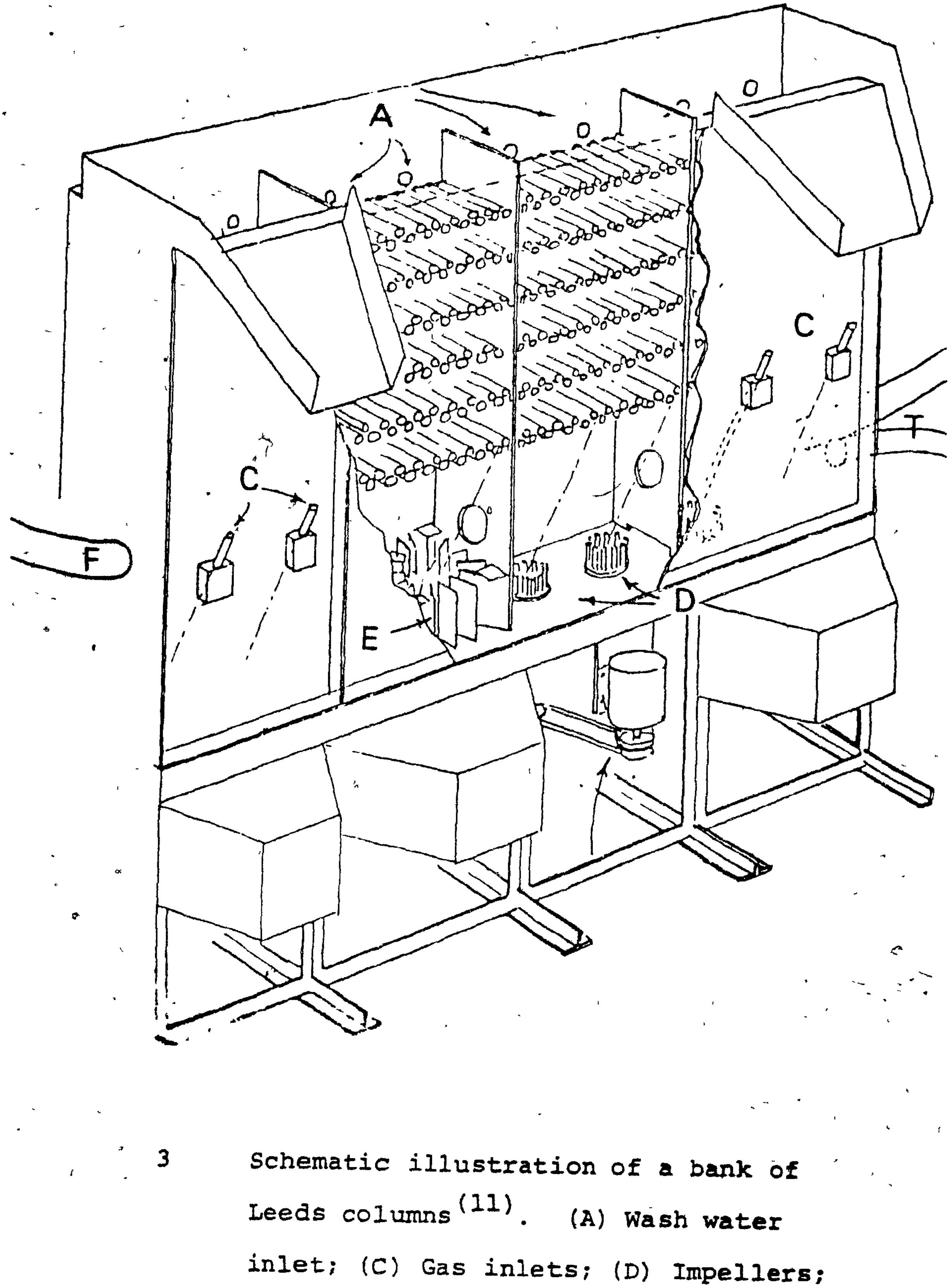

3 Schematic illustration of a bank of Leeds columns(11). (A) Wash water inlet; (C) Gas inlets; (D) Impellers; (E) Baffle vanes; (F) Feed inlet; (T) Tailings outlet.

conventional mechanical cells (unlike the diagram in Figure 3, the full scale machine now employs top driven agitators).

The cell was invented by C. Dell of Leeds University, England. (To date, this is the only significant flotation machine design produced from a university environment.) The machine has been described in detail by Dell and Jenkins(11) and is presently undergoing plant testing in coal preparation plants in England. Commercial development is through the U.K. National Research Development Corporation. A laboratory version of the Leeds Column can be used on top of the Leeds open-top laboratory flotation cell(12,13).

Flotation Column. A schematic of a flotation column is shown in Figure 4. Industrial columns are up to 13 m high and 0.3 to 1.8 m in cross section (either square or circular). Three zones can be identified: a collection zone, with feed entering 2 to 3 m below the top of the column and descending against rising bubbles generated at a gas sparger; a washing zone, where a packed bubble bed is generated by a downward flow of wash water; and a conventional froth (2 - 5 cm thick) for particle transport to the launder. The tailings withdrawal at the bottom of the column is controlled at a rate slightly greater than the feed flowrate, called a positive bias. An important element is the washwater, added just below the froth zone, which makes up the bias and suppresses gangue entrainment. The column is particularly attractive for cleaning applications and can upgrade in a single stage compared to several stages of mechanical cells, resulting in simpler more

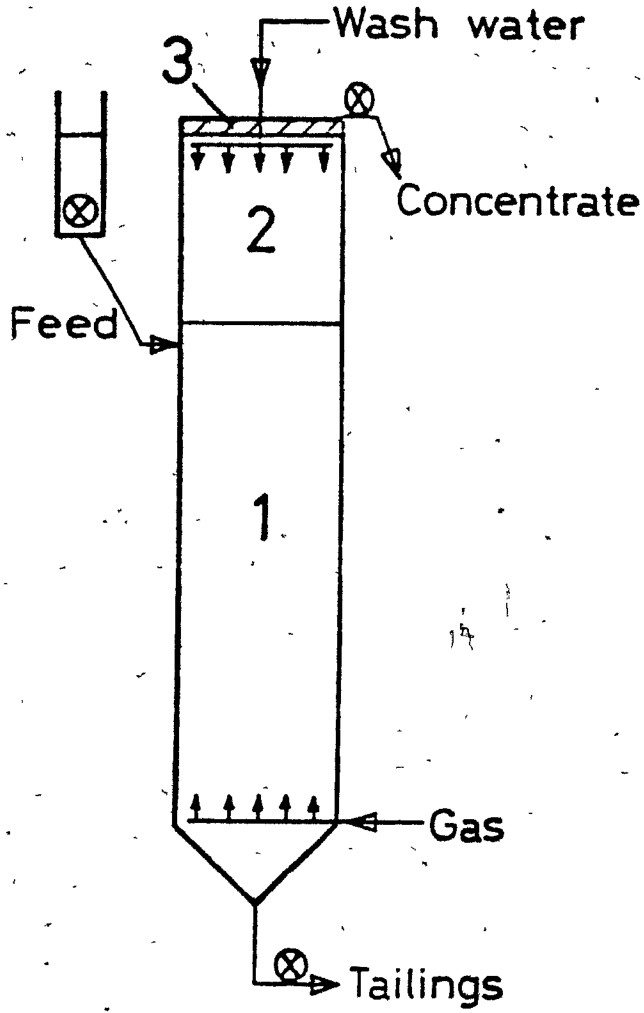

4 Schematic illustration of flotation column (1) collection zone; (2) washing zone; (3) thin froth layer.

controllable circuits. The column itself is well suited to computer control.

Making a distinction of a sharp boundary between zones 2 and 3 may be arbitrary; there could in fact be a gradual transition from a packed bubble bed to a conventional froth. The concept of two zones, however, recognizes that there exist two significantly different regimes, and the sole purpose of the conventional froth is for concentrate removal. Combined zones 2 and 3 will be referred to hereafter as the cleaning zone.

Development of the flotation column has been described in several publications(1,2,3,14). The first successful commercial application in the Western World was at Mines Gaspé, Québec, on molybdenum upgrading(4). Three columns in series replaced 13 conventional cleaners with superior results. A 0.9 m square column is operating as a zinc scavenger at Geco Mines, Ontario. Gibraltar Mines(5), British Columbia, is employing three cylindrical columns between 0.5 and 0.9 m in diameter for molybdenum cleaning and bulk copper-molybdenum flotation, with plans for further column expansion. Extensive plant tests have been conducted on iron ore(1), coal(14) (1.8 m square column), copper sulfide(2,3,14) and graphite(15).

In the early 1970's the concept of the flotation column was embraced by engineers in Poland and the U.S.S.R. who embarked on seemingly endless modifications to the basic concept. A recent translation of a text by Tyurnikova and Naumov(16) reviewed some of the Polish and Russian designs of 'pneumatic counter-flow flotation' machines. Some of the column designs are summarized in Figure 5; the variety of design is obvious. It is important to note that none of these machines uses wash water, but rather a secondary froth concentration stage. In this sense, they are quite different from the Canadian column.

Flotation Column Operation. Operating principles and instrumentation control loops of a flotation column are summarized in the diagrams of Figure 6(4). The diagrams are mostly self-explanatory. Bias is typically 10 - 20% of the feed volumetric flowrate. The interface between the recovery and cleaning zones is distinct, and is maintained at a pre-set level by static pressure measurement controlling the wash water rate. It is important to remember that when wash water is changed, the incremental change in flowrate is accounted for completely by a change in concentrate flowrate. The gas spargers are obviously an important component. Bubblers that are presently in use consist of cylindrical, steel mandrals, approximately 7 cm in diameter, covered with a sleeve of either filter cloth or rubber (the latter is pierced with 150 holes/cm^2). Typical gas superficial velocity (flowrate/cross sectional area of column) is between 1.0 and 2.5 cm/s, and typical superficial slurry velocity is between 0.5 and 2.0 cm/s (downward).

Flotation Column Simulation. The laboratory glass column manufactured by Column Flotation of Canada Ltd. (the only supplier of commercial columns) is 5 cm in diameter and 7.5 m in height. Presently, there exists no methodology for translating laboratory performance to expected plant performance. (As well, using an 8 m high device is not feasible for many laboratories.)

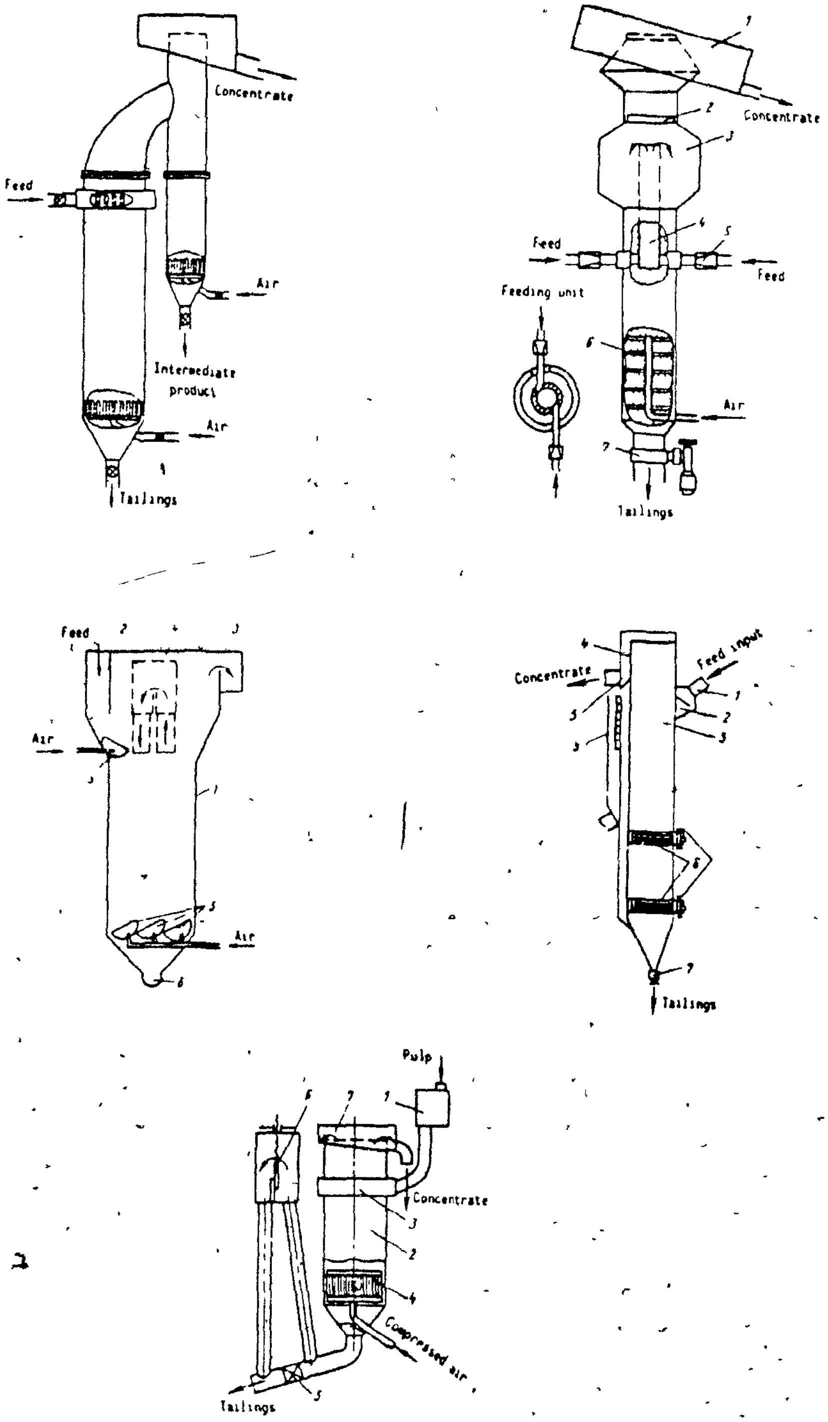

5 Examples of Russian and Polish designed columns(16). None employ wash water.

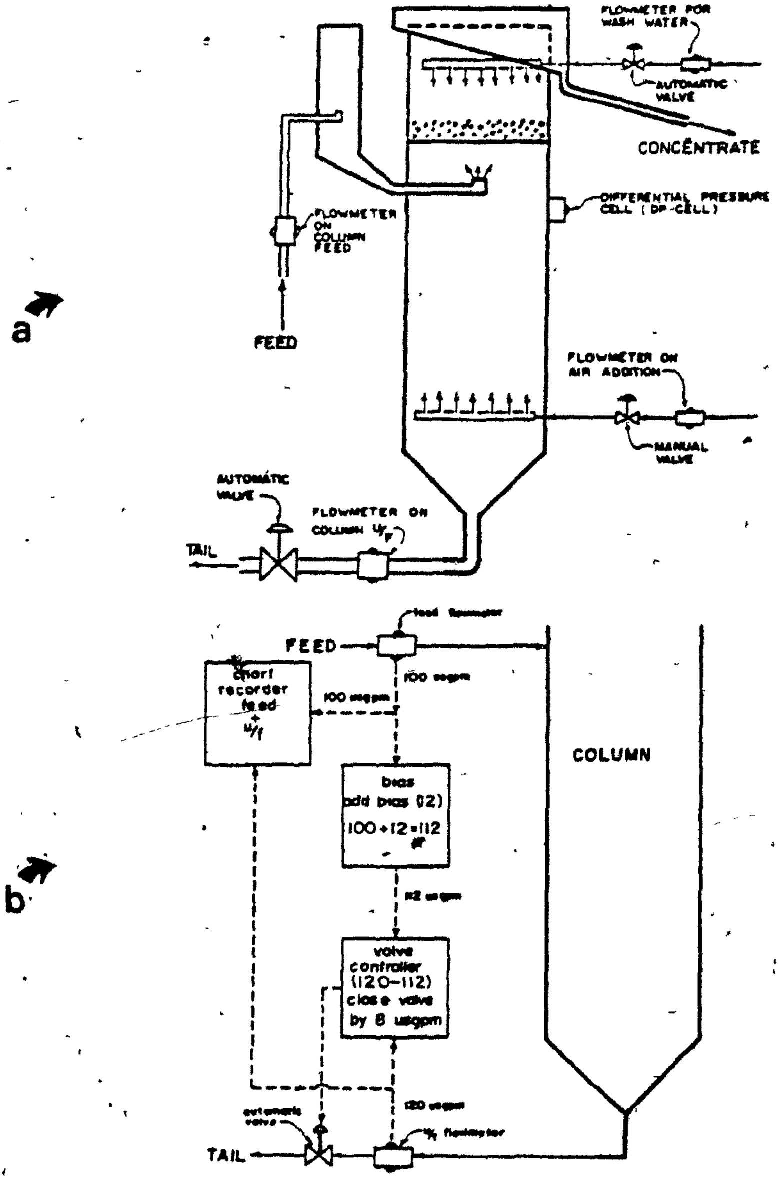

6 Flotation column controls$^{(4)}$;

(a) Instrument control loops,

(b) Feed bias underflow control loop,

cont'd

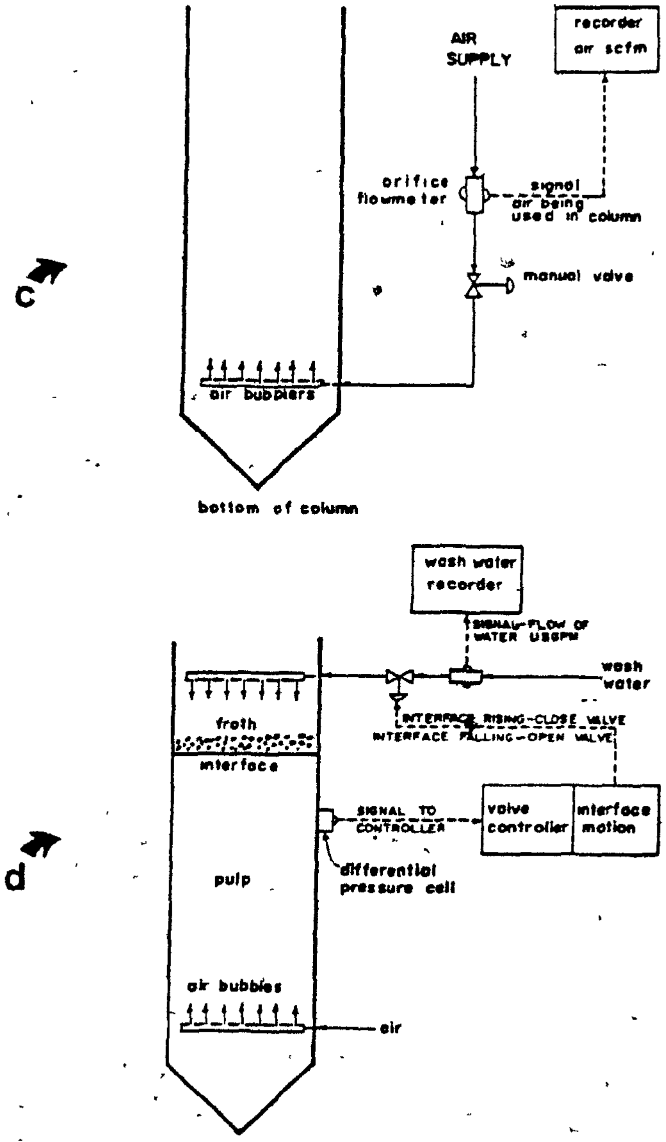

6 (cont'd) (c) Air addition control loop,
(d) Interface-wash water control loop.

However, the flotation column appears to be considerably more amenable to the application of process models based upon fundamental physico-chemical principles than is the conventional mechanical flotation machine, for the following reasons. First, the counter-current flow of particles and bubbles provides a well defined flow regime, unlike mechanical cells where the degree of suspension of particles (particularly the larger and denser particles) is difficult to estimate and simulate. Second, the column has no mechanical turbulence that must be matched in a laboratory machine. Third, particle recovery to the concentrate via entrainment should be minimal compared to that of mechanical cells employing conventional froths. And, fourth, the existence of a single three-dimensional froth in the column makes froth modelling less complicated than that for a bank of mechanical cells, where the froth characteristics change from cell to cell.

CHAPTER 2

THEORY - COLUMN OPERATING FUNDAMENTALS

For the purposes of either simulation or scale-up it is logical to consider the column as consisting of two regimes, the collection zone and the cleaning zone, and to develop an understanding of the kinetics of each regime separately. Then, the simulations or scale-up models of the two regimes can be combined to yield an overall column model. This is the approach taken here.

2.1 Collection Zone

A mineral particle is collected by a gas bubble by one of two methods: 1. particle-bubble collision followed by attachment due to the hydrophobic nature of the mineral surface, or 2. entrainment of the particle within the boundary layer and wake of the bubble. (In a column, precipitation of air bubbles on hydrophobic surfaces is not a significant factor). The importance of entrainment as a mechanism of particle collection has been discussed already. In the flotation column, the concept of the downward flow of wash water in the cleaning zone is to prevent feed water from reporting to the concentrate, and, therefore, to prevent recovery to the concentrate of entrained hydrophilic particles. The extent to which this objective is met in industrial columns requires testing. However, it will be assumed for now that, while particles may be collected via entrainment in a flotation column, they are completely rejected back to the recovery zone by the wash water. Fruitful particle recovery will be considered to occur by the collision-attachment mechanism alone.

The collection process can be studied by considering a gas bubble rising through a downward flowing slurry. Collection efficiency, E_K, is defined as the fraction of all particles swept out by the projected area of the bubble that collide with, attach to and remain attached to the bubble until reaching the cleaning zone. For a given system, the collection efficiency is a complex function of many parameters, the most obvious being particle diameter, bubble diameter and particle hydrophobicity. There presently exists no fundamental model relating collection efficiency to the pertinent process parameters. The development of such a model is the subject of chapter 3.

The importance of being able to predict E_K, or at least understanding the impact upon E_K of the various parameters, is that E_K is directly related to the collection rate constant k. The following rate expressions are similar in concept to those presented by Jameson et al$^{(17)}$ and are particularly suited to collection in a flotation column. Consider a cell of height h and cross sectional area A. At any instant the total number of particles of a specific size and hydrobicity is N_t, and the concentration of these particles at any instant is $C_p = N_t/(hA)$. The total number of the particles removed by a single gas bubble of diameter d_b during its ascent, N_r, is

$$N_r = (1/4\ \pi d_b^{\ 2}) h\ C_p\ E_K \qquad (2.1)$$

The rate of bubble generation is $Q_g/(1/6\ \pi d_b^{\ 3})$ for a gas volumetric flowrate Q_g. Then, the rate of removal of the particles is expressed by

$$\frac{dN_t}{dt} = -1.5\ \frac{Q_g\ h\ C_p\ E_K}{d_b} \qquad (2.2)$$

Substituting $N_t = C_p\ (hA)$ and using the superficial gas velocity $v_g = Q_g/A$ gives

$$\frac{dC_p}{dt} = -\left(\frac{1.5\ v_g\ E_K}{d_b}\right) C_p \qquad (2.3)$$

Thus, the rate constant for the particles in question is

$$k = 1.5\ v_g\ E_K/d_b \qquad (2.4)$$

Note that the value for E_K in equations 2.2 - 2.4 is for a bubble within a bubble swarm, and would likely be different from the value of E_K in equation 2.1, which is that for a single undisturbed bubble.

The preceding discussion shows that the collection rate mechanism is first-order with respect to particle concentration if E_K does not vary with solids content. It is intuitive that E_K is constant only for a narrow range of particle size and for a single value of hydrophobicity. In a real mineral system there will exist a distribution of rate constants, reflecting a range of particle sizes and a complete spectrum of hydrophobicity due to the interlocking of the different mineral species. A scale-up methodology must be able to utilize the collection rate constant distribution of the given mineral system. For now, it is assumed that, given a narrow range of particle size and a single value of hydrophobicity, E_K is constant and particle collection follows first-order kinetics.

It is of course the fractional recovery R of a mineral, rather than just the rate constant, that the engineer wishes to know. Recovery is determined by three factors: the rate constant, the mean residence time of the particles in the collection zone, and the mixing conditions of the collection zone. One extreme of mixing is plug flow, where the residence time of all elements of the fluid (and all mineral particles) is the same. Consequently a concentration gradient of floatable mineral along the axis of the column exists. The other extreme is a completely mixed reactor, where there is a distribution of retention time (beginning with time zero) and where the concentration is the same throughout the reactor. For a first-order rate reaction system exhibiting plug flow and a retention time τ

$$R = 1 - \exp(-k\tau) \tag{2.5}$$

and for a completely stirred first-order reaction system having a mean residence time τ

$$R = \frac{k\tau}{1 + k\tau} \tag{2.6}$$

The flow conditions in a laboratory flotation column would approximate plug flow, while the liquid and solids in plant columns are transported under conditions between plug flow and completely mixed. The difference in performance between plug flow and completely stirred reactors is significant. For example a recovery of 90% obtained in a plug flow reactor (i.e. $k\tau = 2.30$) equates to only 70% in a completely mixed reactor of the same mean residence time and rate constant as that of the plug flow reactor (from equations 2.5 and 2.6). It is important to know, therefore, the degree of mixing of industrial columns and to relate that mixing to recovery.

2.1.1 Axial Mixing in Bubble Columns

For bubble columns operating at relatively low air flow rates and with small bubbles, which corresponds to the recovery zone of flotation columns, the plug flow dispersion model has been shown to provide a good description of the axial mixing process(18,19). Consider the downward flow of either water or mineral particles in a flotation column. When a tracer (liquid or solid) is impulse injected at the top of a recovery zone of length L, the mass transport equation that describes its concentration c at an axial distance x downstream from the injection point at time t is

$$D \frac{\partial^2 c}{\partial x^2} - u_i \frac{\partial c}{\partial x} - \frac{\partial c}{\partial t} = 0 \qquad (2.7)$$

where D is the axial dispersion coefficient, due to turbulent eddies and diffusion (units of length^2 time^{-1}), and u_i is the interstial velocity of the liquid or particle. This is a one-dimensional model; radial dispersion and nonuniform velocity profiles are not considered. If concentration of the tracer at the tailings discharge is measured with time (time zero corresponding to the impulse injection) then a residence time distribution (RTD) of the liquid or solid is obtained. Such a distribution also can be obtained theoretically by using two parameters to describe the mixing conditions: the mean residence time τ and the dimensionless vessel dispersion number $N_d = D/u_iL$. For a system where end effects are absent the Laplace transform of equation 2.7 is(20)

$$F(s) = \exp\left[\frac{1}{2N_d}\left[1-(1+4N_d\tau s)^{1/2}\right]\right] \qquad (2.8)$$

where s is the Laplace operator. The corresponding time domain solution is a unique function of τ and N_d (19):

$$c(t) = \left(\frac{\tau}{4\pi t^3 N_d}\right)^{1/2} \exp\left[\frac{1}{4N_d}\left(2 - \frac{t}{\tau} - \frac{\tau}{t}\right)\right] \qquad (2.9)$$

Equation 2.9 satisfies the mass transport equation 2.7 for $x = L$ and provides a residence time distribution for an open-ended reactor (end effects ignored). The RTD's for reactors having values of N_d between zero and ∞ , and the same mean residence time, $\tau = 1$, are shown in Figure 7. $N_d = 0$ corresponds to plug flow and $N_d = \infty$ corresponds to completely mixed flow. N_d and τ can be estimated from the experimentally obtained RTD. This is discussed in section 4.1.2.

The objective of measuring the mixing parameters is to quantify the mixing effect upon recovery. Equation 2.7 has been solved analytically(21) for first-order reactions, and, for vessels with any kind of entrance and exit conditions, the solution is(22)

$$R = 1 - \frac{4a \exp\left(\frac{1}{2N_d}\right)}{(1+a)^2 \exp\left(\frac{a}{2N_d}\right) - (1-a)^2 \exp\left(-\frac{a}{2N_d}\right)} \qquad (2.10)$$

where

$$a = (1 + 4k\tau N_d)^{1/2}$$

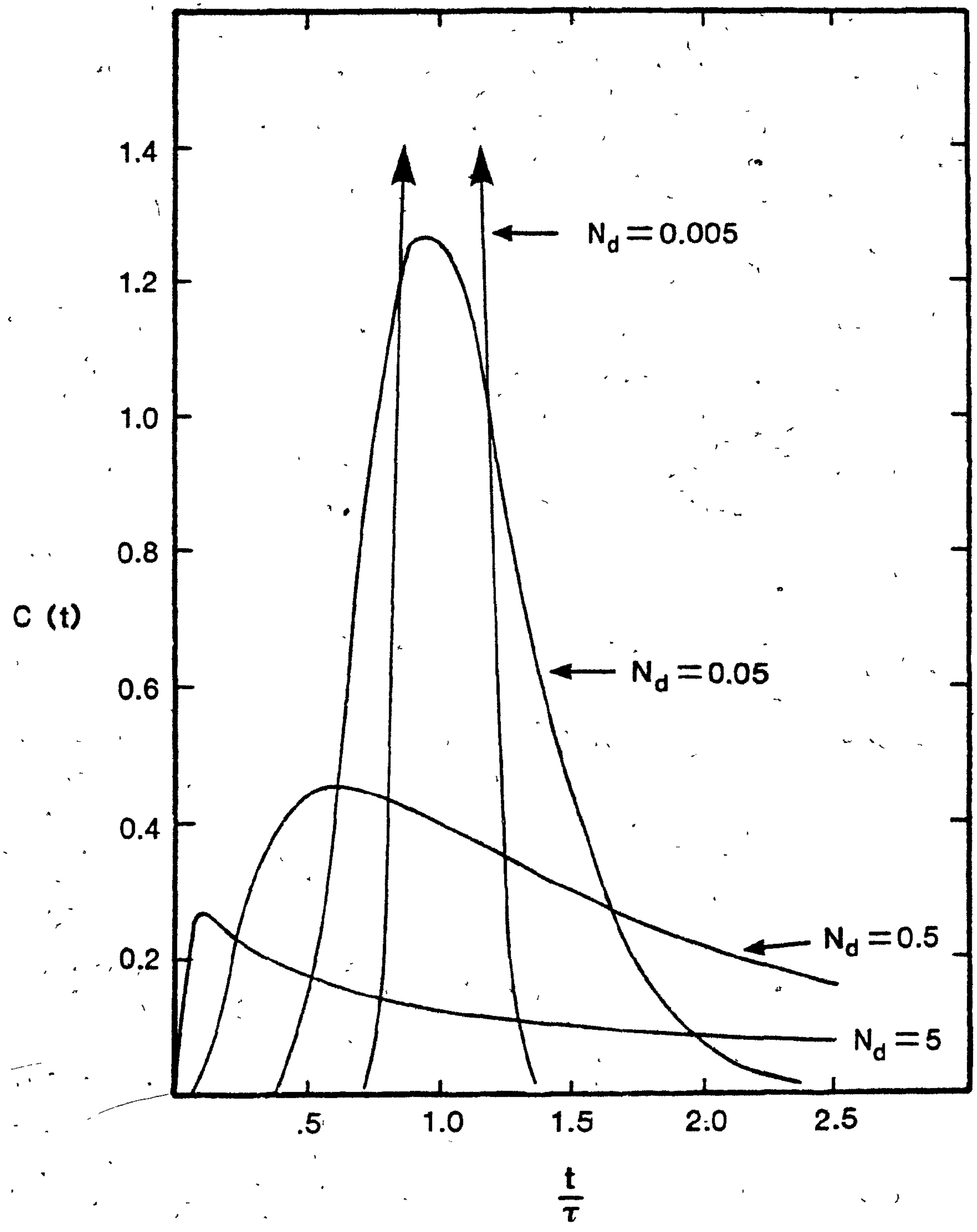

7 Residence time distributions satisfying equation 2.9 for different vessel dispersion numbers N_d.

Levenspeil$^{(22)}$ expresses equation 2.10 graphically at the same time as showing the ratio V/V_p, where V is the volume of a real reactor and V_p is the volume of a plug flow reactor that gives the same recovery as obtained with the real reactor. A diagram similar to Levenspeil's is shown in Figure 8. The $k\tau$ lines represent lines of equal volume, or holding time, for constant k. As an example of the application, ~~in~~ scale-up practice, of Figure 8 and equation 2.10 consider the following hypothetical data. Plug flow laboratory conditions (a reasonable approximation for a laboratory flotation column) yields a recovery (with first-order rate kinetics) of a certain mineral of 86.5%, in a reaction time of 5 minutes ($k = 0.4\ \text{min}^{-1}$, $k\tau = 2$). If the same reaction is to be performed in a plant reactor having a known vessel dispersion number $N_d = 0.5$, then employing a 5 minute mean retention time in that reactor will yield a recovery of only 75.1%. To attain the 86.5% recovery would require a mean residence time of 7.2 minutes ($V/V_p = 1.44$).

To complete this discussion of column mixing the present knowledge of mixing in large bubble columns is now reviewed.

Liquid Dispersion

The effect of various physical and operating parameters upon the liquid axial dispersion coefficient in bubble columns has been reviewed by Shah, Stiegel and Sharma$^{(23)}$. They conclude that for cylindrical columns D_ℓ is essentially independent of liquid velocity and liquid properties such as viscosity, surface tension, density, etc. In a subsequent review article,

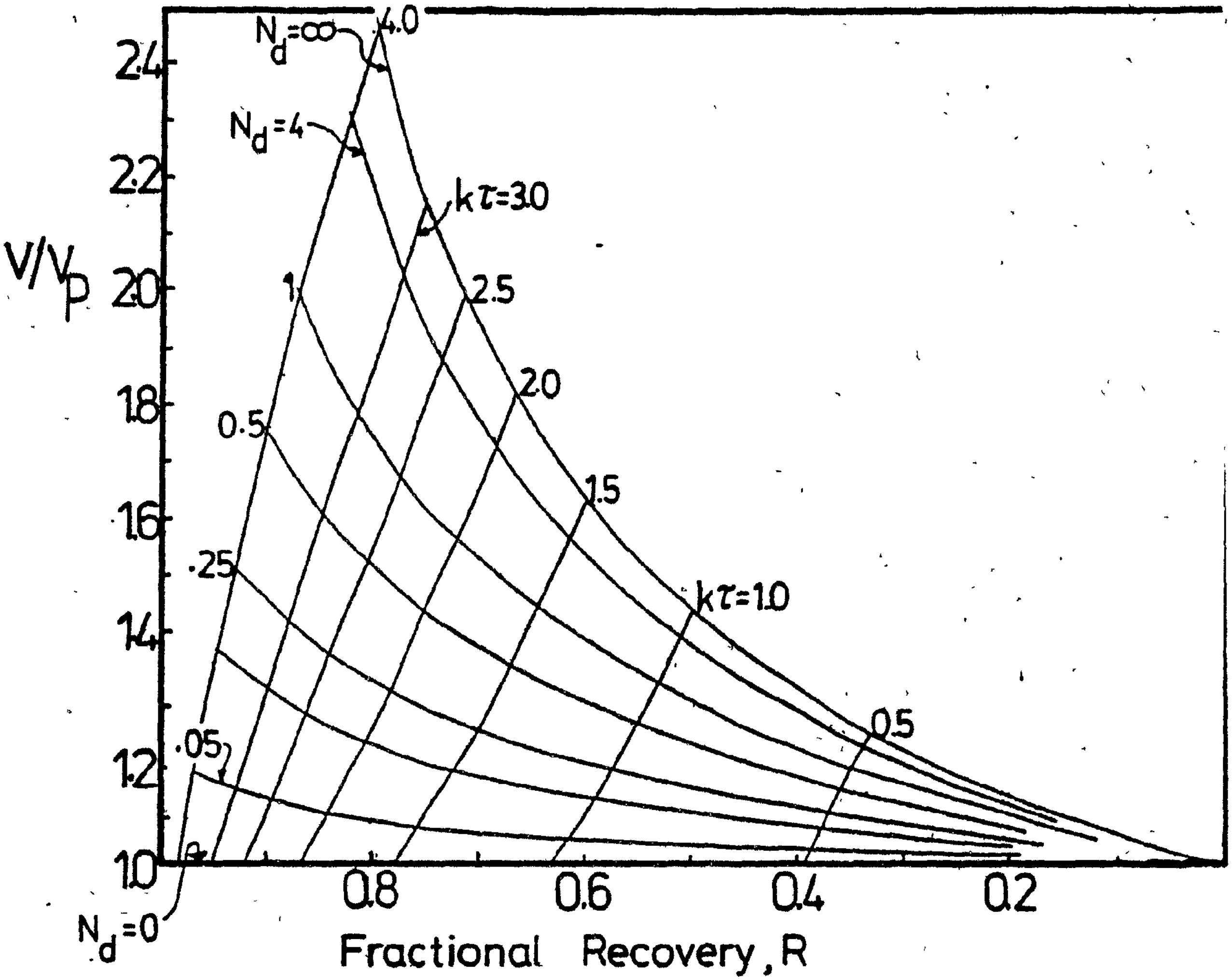

8 . Extent of reaction as a function of N_d and $k\tau$ for first-order rate reaction$^{(22)}$. V_p is the volume of a plug flow reactor and V is the volume of a real reactor.

Shah et al$^{(24)}$ generalize the effect of column diameter d_c and superficial gas velocity v_g with $D_\ell = d_c^k v_g^n$, where $1 \le k \le 1.5$ and $0.3 \le n \le 2$. Since the present concern is with flotation columns having a large radial dimension it is worthwhile to examine the scarce quantity of published data on large diameter columns.

Magnussen and Schumacher$^{(25)}$ experimented with cylindrical columns having $0.04 \le d_c \le 1m$ at $0.01 \le v_g \le 0.1$ m/s while operating in the counter-current mode. For columns with no internal baffling they found $k = 1$ and $n = 0.23$. No mention is made of the mode of bubble generation. Towell and Ackerman$^{(26)}$ operated in the concurrent mode, with both gas and liquid injected through a sparger having a small number of relatively large holes (0.64 cm), on columns of 0.4 and 1.07 m diameter and $0 \le v_g \le 0.15$ m/s. They found $k = 1.5$ and $n = 0.5$.

A noncircular shape of the column radial section is a complicating factor. Alexander and Shah$^{(27)}$ showed that a rectangular column 0.076 x 0.23 m in cross-section gave a considerably larger axial diffusion coefficient than a cylindrical column of equivalent diameter (diameter of a circle having the same area as the rectangle). Akita and Yoshida$^{(28)}$, working with a 0.15 m square section bubble column, determined that the liquid phase mass transfer coefficient was the same as that of a cylindrical column having a diameter equal to a side of the square. By extension, this would imply that the liquid axial dispersion coefficients were also similar.

Particle Dispersion

In column flotation it is the dispersion parameters of the solid particles, not the liquid, that is of prime importance. Several investigators(19,29,30) have suggested that the axial dispersion coefficient of fine solids in a bubble column is the same as that of the liquid, i.e., $D_p = D_\ell$, where D_p is the solids axial dispersion coefficient. No upper particle size, or mass, for which this is valid has been suggested. The other solids dispersion parameter, the particle mean residence time, τ_p, should be a function of the relative settling velocity of the particle, u_p. For the case of a descending slurry which is not contacted with gas bubbles, a measure of τ_p is:

$$\tau_p = \tau_\ell \left(\frac{u_\ell}{u_\ell + u_p}\right) \qquad (2.11)$$

The effect of a bubble swarm upon this relationship is unknown and, to the authors' knowledge, unmeasured. It is suggested here that this effect is minimal at the relatively low gas velocities employed in a flotation column, and that equation 2.11 is suitable for scale-up purposes. The relative settling velocity can be estimated using the method developed by Concha and Almendra for single spheres(31), subsequently corrected to account for hindered settling. The terminal velocity U_T of a spherical particle of diameter d_p is given by(31):

$$U_T = \frac{20.52M}{d_p} \left[\left[1 + 0.0921 \left(\frac{d_p}{P}\right)^{3/2}\right]^{1/2} - 1\right]^2 \qquad (2.12)$$

where

$$M = \mu/\rho_\ell$$

and

$$P = \left[\frac{3}{4}\,\frac{\mu^2}{(\rho_p - \rho_\ell)\rho_\ell\, g}\right]^{1/3}$$

where μ is the liquid viscosity, and ρ_p and ρ_ℓ are the particle and liquid densities, respectively. Then, U_T can be corrected to account for the effect of volume fraction solids ϕ_s using the empirical relationship developed by Richardson and Zaki(32):

$$\frac{u_p}{U_T} = (1 - \phi_s)^m \qquad (2.13)$$

where $m = 4.65$ for $Re_p < 0.2$, $m = 4.35\ Re_p^{-0.03}$ for $0.2 < Re_p < 1.0$, $m = 4.45\ Re^{-0.1}$ for $1.0 < Re_p < 500$ and $m = 2.39$ for $Re_p < 500$. Since the volume fraction solids will decrease with increasing x, due to capture onto bubbles of many of the floatable particles, u_p will increase during the particle descent. An average value of u_p is obtained by using the average of ϕ_s(feed), at $x = 0$, and ϕ_s(tailings), at $x = L$, in equation 2.13.

Gas Dispersion

If the bubble column has a sufficiently large length to diameter ratio, the gas phase is assumed to move in plug flow(23). This is a reasonable assumption for gas in the recovery zone of a flotation column, since the gas bubbles travel at 8-14 cm/s compared to 0.5 - 3.0 cm/s for the liquid and particles.

2.1.2 Bubble Load

The residence time of a bubble in the recovery zone of a flotation column is 5 - 10 times longer than that in a conventional machine. Thus, the possibility of a bubble becoming fully loaded (and ceasing to collect particles) is considerably greater in a column, particularly in roughing and cleaning applications. Bubble loading becomes a very important design and scale-up consideration.

The surface on the front of a rising bubble is the area where particle-bubble collision will occur. Upon adhesion to the bubble, particles will slide to the rear (bottom). Weber(33) has shown that for flotation sized bubbles (~0.06 to 0.15 cm) the fluid streamline around the bubble has a closest approach to the bubble at angle $\theta_C < 90^\circ$, measured from the front stagnation point of the bubble. There would be no collisions at an angle greater than θ_C. As an example, a bubble with $d_b = 0.10$ cm rising at 10 cm/s would have $\theta_C \approx 63^\circ$. The consequence of this, related to bubble loading, is that unimpeded collisions can occur until approximately 70% of the bubble surface is packed with particles. After that point the rate of collection will steadily decrease and the reaction rate will no longer be first-order.

The onset of full bubble load (or hindered flotation) can be estimated. Consider a single bubble. The rate β of particle collection by the bubble is given as:

$$\beta = \frac{1}{4} \pi d_b^2 u_b (\rho_p \phi_s') E_K \tag{2.14}$$

where ϕ_s' is the average volume fraction floatable solids in the slurry, and $\rho_p \phi_s'$ is the particle concentration in terms of mass of particles/unit volume slurry. The units of β are mass time^{-1}. If coverage of the bubble surface by a monolayer is considered to occur until 70% of the bubble surface is covered, then this load Γ is given by

$$\Gamma = 0.7 \pi d_p \rho_p d_b^2 \gamma \tag{2.15}$$

where γ is the fractional packing density of the monolayer coverage of particles. The units of Γ are mass. Then, the time t_L of bubble rise to attain Γ (the onset of hindered flotation) is

$$t_L = \frac{\Gamma}{\beta} = \frac{2.8 d_p \gamma}{u_b \phi_s' E_K} \tag{2.16}$$

and the height h_L of bubble rise in conditions of free flotation is

$$h_L = u_b t_L = \frac{2.8 d_p \gamma}{\phi_s' E_K} \tag{2.17}$$

There is some evidence that a bubble will carry more than a monolayer coverage of particles, explained probably by particle-particle adhesion. Tomlinson and Fleming(34) calculated a surface coverage of apatite as high as 120% on 0.08 cm diameter bubbles. King et al(35) studied the loading of fairly large bubbles; $d_b = 0.33$ to 0.62 cm. Over this range they observed that the smaller bubbles picked up a greater load per unit area than the larger bubbles, and postulated that the increased curvature of the smaller bubbles allowed for a greater packing density of the irregularly shaped solids. It seems that using $\gamma = 1$ for flotation sized bubbles is reasonable.

2.2 Cleaning Zone

Consider the dimensional comparison presented in Table 1 between a 1.83 m square column and three sizes of Denver flotation machine. The number of Denver cells was selected to give the same pulp volume as that of the column (9.5 m high x $1.83^2 m^2$). For similar residence times and approximately similar mixing conditions, the mechanical cells have available 5 to 8 times more froth area and 1.5 to 2.5 times more lip length. The gas requirement, in terms of volumetric flowrate per unit volume of pulp, is 10 times greater in the mechanical machines.

These three comparisons serve to illustrate significant differences between columns and mechanical machines. Upon arriving at the bottom of the cleaning zone the bubbles in a column will, in most cases, be close to or completely covered

Table 1

Area and Lip Length Comparisons

Column vs Denver D-R

		Volume of Pulp (m^3)	# of cells	Total Surface Area (m^2)	Typical Gas Requirement (m^3/min)/(m^3 pulp)	Lip Length (m)
Column 1.83m^2		31.8	1	3.35	0.1	7.3
Denver D-R(6)	100	30.8	11	27.1	1.4	16.8
	180	30.6	6	19.9	1.0	10.9
	300	34.0	4	19.9	0.9	17.8*

* removal on two sides

with particles, while this would likely occur only in the first few cells of a conventional cleaning or roughing bank (if at all). To prevent a major release of the collected particles, coalescence of the gas bubbles must be minimized (coalescence results in reduced interfacial area and, thus, reduced solids carrying capacity). This is attained by the downward flow of wash water that generates a packed bubble bed regime instead of a froth. Coalescence eventually does occur, as evidenced by the conventional froth that overflows the top of the column. What is unknown is whether this coalescence occurs gradually, from bottom to top of the cleaning zone, or rapidly, close to the wash water addition point.

The level in the cleaning zone at which coalescence occurs, and at which particles are forced off of the gas/liquid interface into the wash water, is an important consideration, for the following reason. A significant portion of the wash water reports to the concentrate. This water is added only 5 cm from the column top, but it is likely that it penetrates a certain depth into the cleaning zone due to fairly strong mixing conditions. Thus, for a particle rejected from the gas/liquid interface, the closer to the top of the column that the rejection occurs, the greater is the probability that the particle will reach the concentrate anyway - carried by the wash water rather than attached to a bubble. Cienski and Coffin (36) reported increased weight recovery with increased wash water rate for 0.45 and 0.9 m square columns operating as molybdenum cleaners. It is unclear what mechanism causes this; either a reduced rate of bubble coalescence, or greater penetration of the wash water with resulting increased capacity to recover particles that have been dropped from the gas bubbles.

The flow patterns in a water-drained froth are very complex and are dependent upon a large number of variables; gas rate, wash water rate, solids concentration, particle size (distribution), particle hydrophobicity, liquid viscosity, surface tension, mixing conditions, and more. There are presently no models to simulate water drained froths, and there will be no attempt to develop one here. What is recognized, though, is that a certain fraction of the collected particles reaching the cleaning zone is almost always rejected back to the recovery zone; that is, recovery in the cleaning zone is less than 100%. Plant testing is required to determine a typical range of cleaning zone recovery.

2.3 Interfacing the Collection and Cleaning Zones

Three mineral categories can be identified in a froth flotation separation, classified according to their hydrophobicity. The first category is the strongly floating mineral, intentionally promoted with a collector. The second category is the completely hydrophilic mineral that shows a contact angle of zero, or close to zero; i.e. the gangue. The third category is the weakly to moderately floating mineral, intentionally depressed in some manner but without complete success. (A fourth category could be the mixture of interlocked minerals from categories 1, 2 and 3.) The manner in which a flotation column prevents recovery of the gangue, category 2 mineral, is via wash water replacement of feed pulp. Maximization of the separation between strongly and weakly floating particles, categories 1 and 3, is attained, not through wash water replacement, but by multiple recleaning.

Consider the multiple recleaning process in a column. Accepting that a fraction of the particles is returned from the cleaning zone to the recovery zone, then these returned particles undergo a repeat of the process of collection (as when first fed into the column). Underlying the simplicity of this is an important concept; each time that a particle undergoes the collection process it has available to it 100% of the original retention time. Contrast this to a bank of mechanical cleaning cells, where each collection event subsequent to drop-back from the froth has a reduced retention time. This is particularly important for selective separation (between category 1 and category 3 minerals).

Defining the cleaning zone recovery R_F as the recovery to the concentrate of particles entering the cleaning zone from the collection zone then, for a collection recovery of R_K, the total column recovery R_T is

$$R_T = R_K R_F \left[1 + R_K(1 - R_F) + R_K^2 (1 - R_F)^2 \ldots + R_K^n (1 - R_F)^n\right] \qquad (2.18)$$

where recoveries are fractional quantities. Since $|R_K(1 - R_F)| < 1$, then as $n \longrightarrow \infty$ equation 2.18 converges to

$$R_T = \frac{R_K R_F}{1 - R_K (1 - R_F)} \qquad (2.19)$$

The ratio T_R of recycle mass to feed mass is given by

$$T_R = R_K (1 - R_F) + (R_K{}^2 (1 - R_F)^2 \ldots$$
$$+ R_K{}^n (1 - R_F)^n \qquad (2.20)$$

which also converges, to give

$$T_R = \frac{1}{1 - R_K (1 - R_F)} - 1 \qquad (2.21)$$

(It is assumed that complete bubble load does not occur.)

Equation 2.19 can be used to illustrate the cleaning action in a column. Consider an idealized column feed consisting of 50% mineral A and 50% mineral B, completely liberated. It is assumed that the recovery of both minerals follows first-order kinetics, and that R_K of mineral A is 0.95 and R_K of mineral B is 0.20; i.e. A is a category 1 mineral and B is a category 3 mineral. It is also assumed that R_F is the same for both minerals. The effect of varying R_F upon recovery and grade is summarized in Table 2. A decrease in R_F decreases the recovery of both minerals while increasing the grade of mineral

Table 2

Effect of Froth Removal Rate Upon Selective Separation

R_K Mineral A = 0.95

R_K Mineral B = 0.20

R_F (x100%)	R_T (x100%) A	B	Grade % A
100	95.0	20.0	82.6
80	93.8	16.7	84.9
60	91.9	13.0	87.6
40	88.3	9.1	90.7
20	79.0	4.8	94.3
10	65.2	2.4	96.4

A. This result is not unexpected; it demonstrates the principle of sequential cleaning of two minerals with different, but finite, collection rates. The importance here is that it is performed in a single machine.

CHAPTER 3

THEORY - THE COLLECTION OF MINERAL PARTICLES BY BUBBLES

3.1 Previous Work

The most comprehensive flotation model to date was published in 1948 by K.L. Sutherland(37). This model calculated, from fundamental principles, the probability of a particle colliding with a bubble as well as the probability of attachment subsequent to collision. The attachment probability compared the time of particle-bubble contact with the induction time, where induction time is the time which elapses between apparent contact and true contact, i.e. formation of a three-phase contact line(38). A distribution of contact time was determined by considering the distribution of contact angles and the tangential velocity of the particle over the bubble surface. The possibility of detachment subsequent to adhesion was not considered. Sutherland extended his analysis of a single particle-bubble system to a swarm of bubbles in a slurry, and developed a relationship between the rate of flotation and the pertinent operating parameters including particle size and induction time. Jowett(39) has applied Sutherland's model to laboratory data in order to estimate the relationship between particle size and induction time. His analysis is discussed further in section 3.1.3.

In the years since Sutherland proposed his model there have been significant developments in the knowledge of the fluid flow patterns around spheres having Reynolds numbers similar to that of flotation sized bubbles. These developments show that there are serious errors in the basic assumptions used by Sutherland to calculate collision and attachment probabilities. The more important errors are noted in the following sections and during the discussion describing the proposed model. However, the basic form of Sutherland's model is sound; his work is a landmark for flotation modelling. While there has been no attempt to improve upon the complete form of Sutherland's model there have been developments in the understanding of specific aspects of the collection process, notably the collision event, contact time, induction time, and detachment.

3.1.1 Collision

The particle-bubble collision process has been studied theoretically by several investigators since the late 1960's; the most relevant are by Flint and Howarth(40) (1971), Reay and Ratcliff(41,42) (1973, 1975), Anfruns and Kitchener(43) (1977), Weber(33) (1981) and Weber and Paddock(44) (1983). Experimental results have been reported by Flint and Howarth, Reay and Ratcliff, Anfruns and Kitchener and by Schulze and Gottschalk(45,46). Each of these authors based their analysis on the equation of motion of a spherical particle relative to a spherical bubble (that is large compared to the particle) rising in an infinite pool of liquid. Hydrodynamic drag will tend to sweep the particle around the bubble, following the fluid streamlines. Particle inertia and gravity act in a combined manner to move the particle out of the fluid streamline and toward the top of the bubble. The equation of motion is

$$\frac{1}{6} \pi d_p^3 \frac{\partial v_j}{\partial t} = \frac{1}{6} \pi d_p^3 (\rho_p - \rho_\ell) g_j + \frac{1}{8} \pi C_D \rho_\ell d_p^2 (u_j - v_j)^2 \tag{3.1}$$

where v_j is the particle velocity in the j direction, u_j is the velocity in the j direction that the liquid would have if the particle were not there, g_j is the component of gravitational acceleration in the j direction, and C_D is the particle drag coefficient. The second term on the right side of equation 3.1 is the steady state drag term; the first term on the right side is the particle body force due to relative gravitational acceleration, and the term on the left side is the body force accounting for particle inertia.

A diagram illustrating the approach of the particle toward the bubble is shown in Figure 9. The bubble is assumed to be held stationary by a flow of liquid in the negative y direction equal to the bubble rise velocity u_b. Allowing the particle drag coefficient to be that of a sphere in Stokes flow (i.e. $C_D = C_{DSk} = 24/Re_p$) then Equation 3.1 can be described in

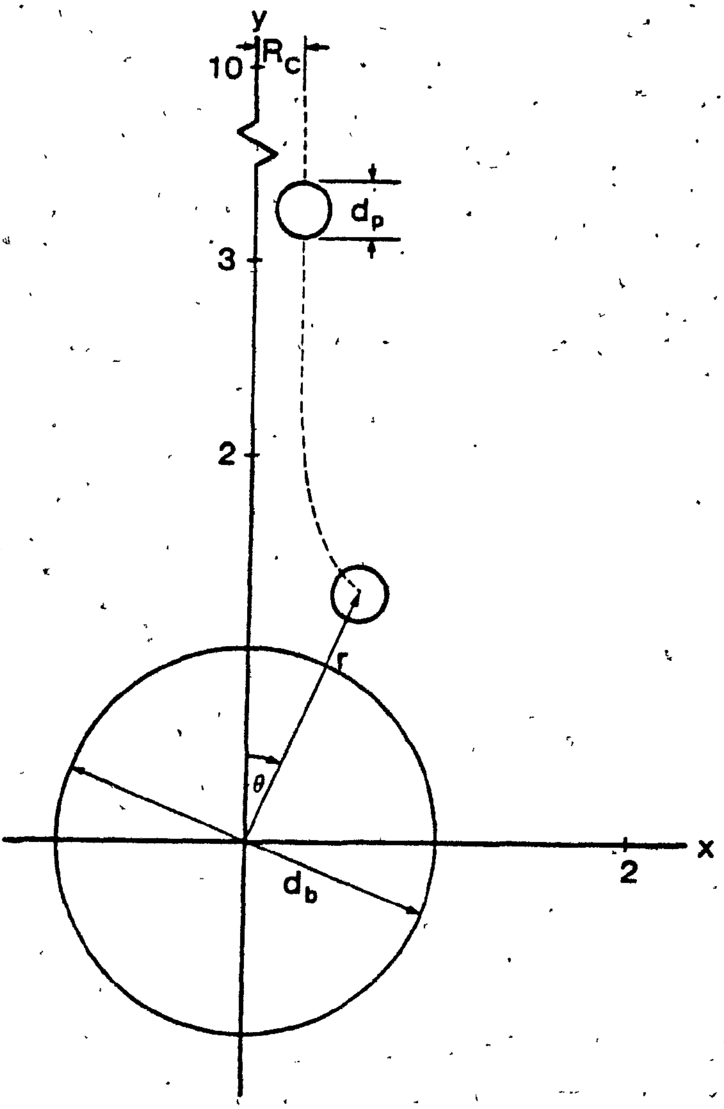

9 Illustration of a particle approaching a gas bubble. x, y and r coordinates are dimensionless; at the bubble surface $r = x^2 + y^2 = 1$.

terms of x and y coordinates and several dimensionless parameters by

$$Sk \frac{\partial v_x^*}{\partial t^*} = u_x^* - v_x^* \tag{3.2}$$

$$Sk \frac{\partial v_y^*}{\partial t^*} = (u^* + u_y^*) - v_y^* \tag{3.3}$$

where

$u_x^* = u_x/u_b$

$v_x^* = v_x/u_b$

$u_y^* = u_y/u_b$

$v_y^* = v_y/u_b$

$t^* = u_b t/d_b$

$u^* = u_p/u_b$

Sk = Stokes number

$= \frac{1}{9} \left(\frac{\rho_p}{\rho_\ell}\right) \left(\frac{d_p}{d_b}\right)^2 Re_b$

where

Re_b = bubble Reynolds number

$= u_b\, d_b\, \rho_\ell/\mu$

and, for Stokes flow

$$u_p = (\rho_p - \rho_\ell)\, d_p^2\, g/18\mu$$

In this analysis the bubble radius $r_b = 1$; so the coordinate $r = \sqrt{x^2 + y^2} = 1$ lies on the bubble surface.

The Stokes number is directly related to the ratio of inertial to drag forces. Reay and Ratcliff(41) describe Sk as the ratio of particle relaxation time $\rho_p\, d_p^2/18\mu$ to the characteristic time d_b/u_b for changes in the fluid flow. Most of the theoretical and experimental work to date has focused on relatively small particles, and bubbles with d_b = 100 to 1200 μm, so Sk << 1 (i.e., the particle adjusts almost instantaneously to changes in the fluid flow around it). This allows the inertial term of equations 3.2 and 3.3 to be ignored and, thus, assumes that gravity is the only factor that may cause the particle trajectory to deviate significantly from the fluid streamline.

Collisions are quantified by using a collision efficiency E_C that Weber(33) has defined as the rate at which particles collide with the bubble divided by the rate at which particles flow across the projected area of the bubble, that rate being $\frac{1}{4}\pi\, d_b^2\, (u_b + u_p)\, C_p$, where C_p is the particle concentration. Collision efficiency can also be thought of in terms of a capture radius R_C. All particles with center located closer to the bubble axis than R_C, at a distance far ahead of the bubble, collide with the bubble; i.e. $E_C = (\frac{R_C}{r_b})^2$.

For calculation purposes E_C is divided into an interceptional collision efficiency E_{Ci} and a gravitational collision efficiency E_{Cg}, so

$$E_C = E_{Ci} + E_{Cg} \tag{3.4}$$

Interceptional collision alone ($E_{Cg} = 0$) occurs for neutrally buoyant particles which follow the fluid streamlines exactly. Gravitational collision alone ($E_{Ci} = 0$) is hypothetical; it would occur for particles having a finite settling velocity but zero dimension. To calculate E_{Ci} and E_{Cg} the liquid velocity field around the bubble is required. For solid spheres, these velocities can be determined if either Stokes flow or potential flow is assumed (the Stokes and potential flow solutions to the Navier-Stokes and continuity equations for axisymmetric flow around a sphere are well known). It is assumed that the bubble generated in a surfactant contaminated solution behaves as a solid sphere with density zero and with little deformation from the spherical shape for $d_b \leq 0.12$ cm(33,47). Flint and Howarth(40) calculated gravitational collision efficiencies for both Stokes and potential flow. For Sk < 0.1 they arrived at the same value of E_{Cg} for either assumption,

$$E_{Cg} = u^*/(1 + u^*) \tag{3.5}$$

Reay and Ratcliff(41) arrived at a similar value for the Stokes flow solution, but they allowed for a non-zero particle diameter, giving(33)

$$E_{Cg} = \frac{u^*}{1 + u^*} \left(\frac{d_b + d_p}{d_b}\right)^2 \sin^2\theta_G \tag{3.6}$$

where θ_G is the angle on the bubble over which gravitational deposition occurs. Stokes and potential flow have fore-and-aft symmetry, consequently $\theta_G = 90^\circ$.

Weber(33) considered the real situation of flotation sized bubbles, having Re_b from 20 to 300, and noted that the liquid flow around such bubbles is not axisymmetric. For $Re_b > 1$ the streamlines are pushed toward the front of the bubble and the closest approach of a streamline occurs at an angle θ_C less than 90°. The angle of closest approach can be evaluated as a function of Re_b from the results of numerical solutions to the Navier-Stokes equations reported independently by two investigators(48,49). A plot of θ_C vs Re_b is shown in Figure 10(49,33). At angles greater than θ_C (and less than 90°) the radial component of the liquid velocity is directed away from the bubble surface, while the radial component of the particle settling velocity is directed toward the bubble surface. At some angle θ_M between θ_C and 90° the velocities will be equal. Gravitational deposition occurs up to angle θ_G, where $\theta_C \le \theta_G \le \theta_M$. Weber made the approximation that $\theta_G = \theta_C$. This has an obvious impact upon E_{Cg}, equation 3.6.

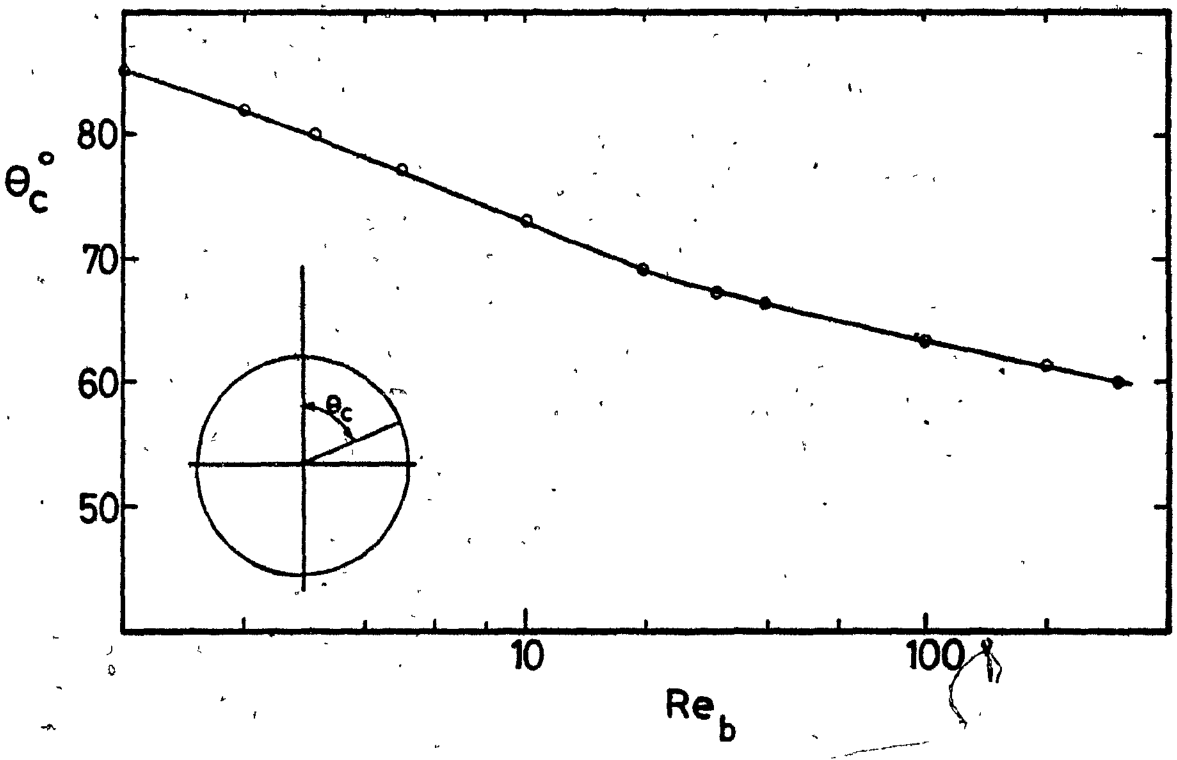

10 Angle of closest approach of fluid streamlines versus Re_b (33,49).

Weber also applied the forward shift of the grazing streamline to develop an easily applied model of interceptional collision. A model accounting for Re_b was needed, because, unlike gravitational collision, there is a large difference between the interceptional collision efficiency at Stokes flow and at potential flow. As an example, neutrally buoyant particles having $(d_p/d_b) = 0.05$ will yield $E_{Ci} = 0.00375$ assuming Stokes flow and $E_{Ci} = 0.15$ assuming potential flow(33). In collision by interception the particles follow the fluid streamlines exactly, so there will be collisions only for $\theta < \theta_C$; the grazing collision by interception occurs at θ_C. E_{Ci} is related to Re_b, and the Stokes flow interceptional collision efficiency E_{iS} by(33)

$$E_{Ci} = E_{iS} \left[1 + \frac{(3/16)\ Re_b}{1 + 0.249\ Re_b^{\ 0.56}}\right] \tag{3.7}$$

where

$$E_{iS} = \frac{1.5\ (d_p/d_b)^2}{1 + u^*} \tag{3.8}$$

Equation 3.7 is valid for $0 < Re_b \leq 300$. To complete the above example, a particle/bubble system with $(d_p/d_b) = 0.05$ and $Re_b = 100$ gives $E_{Ci} = 0.020$ by equation 3.7.

Anfruns and Kitchener(43) performed experiments with a single bubble system $(0.06 \leq d_b \leq 0.10$ cm) and very dilute suspensions of quartz particles $(12 \leq d_p \leq 41\ \mu m)$. The quartz was surface-methylated with trimethylchlorosilane and gave a contact angle of 90^o (on polished plates). They measured collection efficiency E_K and assumed that attachment efficiency was 100%, so $E_K = E_C$. Their theoretical calculation of E_C accounted for both gravitational and interceptional collision. However, they were unaware of the forward shift of the grazing streamline, and their graphically presented solution for E_{Ci} was valid only at $Re_b = 40$. Weber compared their results with his model (equations 3.4, 3.6, 3.7 and 3.8). The experimental values were close to but less than predicted. This is not unexpected, because it is unlikely that attachment efficiency would be 100%. However, the reasonable match is a good confirmation of the form of the collision model.

Unfortunately, the collision model is limited to particles with a maximum diameter of 30 - 40 μm for typical flotation sized bubbles. For particles greater than this size the particle inertia becomes significant and must be accounted for; it can not be assumed that Sk = 0. Flint and Howarth(40) calculated, from particle trajectory simulations, gravitational collision efficiency as a function of Sk and u* for both Stokes and potential flow. Reay(50) calculated E_{Cg} as a function of Sk for $d_p / d_b = 0.1$ but his calculations also included unsteady state drag terms as well as the steady state drag. (Unsteady state drag arises from the relative velocity between a particle and the fluid that it is flowing in, developed when the particle trajectory deviates from the fluid streamline.) Reay's criteria for there to be negligible effect of unsteady state drag is

$$Sk \left(\frac{\rho_\ell}{\rho_p}\right) << 0.33 \tag{3.9}$$

Neither Flint and Howarth nor Reay accounted for the forward shift of the grazing streamline. There has been no reported calculation of E_{Ci} vs Sk and Re_b.

Sutherland's calculation of collision efficiency is not realistic for small or intermediate sized particles. For example, if $d_b = 0.1$ cm, $u_b = 11.6$ cm/s, $\mu = 0.01$ poise, $\rho_p = 4.0$ g/cm^3 and $d_p = 5$ μm, then $E_C = 0.00050$ by Weber and 0.015 by Sutherland. At $d_p = 20$ μm, $E_C = 0.0080$ by Weber and 0.060 by Sutherland.

Schulze and Gottschalk(45,46) used the same method as Sutherland to estimate collision efficiencies for their experimental system, in which they photographed trajectories of particles approaching a single stationary bubble. They worked with large particles and a large bubble ($d_p = 160$ μm, $d_b = 0.30$ cm, $u^* = 0.18$ and $Sk = 0.24$) and did not account for particle inertia.

3.1.2 Contact Time

Schulze and Gottschalk also photographed, for the particle-bubble system just described, the sliding of a mineral particle over the surface of a bubble. They measured the sliding time of a particle, taken to be the time to slide from the point of contact to $\theta = 90^\circ$. They compared their data with the values predicted by Sutherland's equation(37), which assumes potential flow. The fit is reasonable; however, the Sutherland equation is in error. In the original paper, the equation for sliding time overestimates the time by a factor of two. In fact, the assumption of potential flow is not a good approximation (see also section 3.4.2).

Bogdanov, as reported by Klassen and Mokrousov(51), also studied the process of particle slippage by high speed photography. He employed a range of particle sizes, and concluded that particle contact time decreases significantly with increasing particle size, unlike Sutherland's model, which gives contact time as essentially independent of particle diameter.

A necessary assumption in calculating the sliding time is that the particle does not bounce when it hits the bubble surface. The photographic studies of Whelen and Brown(52) showed that large particles do bounce. They used coal with $d_e = 225\ \mu m$ (d_e is the volume equivalent spherical diameter). They observed not only particle bounce, but also significant deformation of the bubble surface at the point of contact. Schulze and Gottschalk(45,46) also reported particle bounce with their system ($d_p = 160\ \mu m$, $\rho_p = 2.5\ g/cm^3$) when collision occurred at angles of less than approximately 30°. The induction time for a particle-bubble system where contact occurs only during the time of impact and elastic repulsion has been estimated by Philippoff(53) and Evans(54). They considered that the liquid-gas interface acts similar to a spring, where the elasticity is caused by surface tension, and calculated the contact time from equations describing simple harmonic motion.

In summary the particle-bubble contact mechanism is slippage for small particles and impact (bounce) for large particles. The photographs of Schulze and Gottschulk show both bounce and slippage for 160 μm particles. The minimum particle size at which significant particle bounce occurs is unknown and appears to have received little attention.

3.1.3 Induction Time

During particle-bubble contact, the attachment process is determined by thinning and disruption of the liquid film separating the particle from the gas bubble. The film consists of the hydrated layers of the bubble and the particle, and develops what is termed a disjoining pressure(55). The disjoining pressure is a result of van der Waals forces, the deformation of the electrical double layers and hydration effects(56). After summarizing the results of several investigations, Finch and Smith(56) conclude that double-layer interaction dominates from ~1000 nm down to ~30 nm, and that van der Waals forces and hydration effects dominate below ~30 nm. Below 30 nm the film is unstable, rupturing readily upon shock. The time required for the complete film to thin to such a thickness that rupture can take place is termed the induction time(57). The concept of the induction time is the link between the chemistry of flotation and the physics of flotation.

A direct measurement of the induction time in a dynamic particle-bubble system is obviously a difficult, if not impossible, task. It is necessary, then, either to resort to a static system, or to infer an induction time based upon knowledge of particle contact time. Eigles and Volova(58) measured induction times in a static system. For dodecylamine treated quartz particles between 150 and 300 μm, induction time increased with increasing particle size. The size effect was dramatic; at a certain set of conditions induction time was 10 ms for 190 μm particles, compared to ~300 ms for 230 μm particles, and 3×10^5 ms for 275 micron particles. It is unlikely that these measurements are relevant to a true flotation system.

Jowett(39) has applied Sutherland's model to laboratory data in an attempt to estimate induction time as a function of particle size. From his analysis he concluded that induction time increased with increasing particle size, although it was virtually constant for $d_p < 20$ μm. However, the serious flaws in Sutherland's calculations of collision efficiency and, especially, sliding time (described in section 3.4.2) are sufficient to invalidate Jowett's assessment.

An interesting outcome of the experiments by Anfruns and Kitchener(43) is that particle shape appears to play a significant role in the attachment process. They measured collection efficiencies for methylated quartz particles as well as for methylated glass beads. The collection efficiency for the glass beads was consistently lower than that of the quartz particles, by a factor of 2 to 10. Addition of 1 molar KCl, enough to virtually eliminate electrical double-layer repulsion(43), significantly improved the rate of glass bead flotation but still not close to the rate of quartz particle capture. The difference is ascribed to the effect of angularity on the rupture of wetting films. The existence of a substantial electrostatic energy barrier on smooth surfaces, established in static measurements of equilibrium film thickness(59), is compatible with these results.

Bubble size may play a role in determining induction time. Klassen and Mokrousov(51) have reported the results of several studies showing that contact angle increases with decreasing bubble diameter. The results of experimental measurements of contact angle vs thickness of the residual hydrated layer at a mercury-air interface, and contact angle vs bubble diameter are shown in Figures 11a and 11b as reported by Klassen and Mokrousov. Figure 11a shows that with an increase in the thickness of the residual hydrated film underneath the attached bubble, the contact angle decreases. Figure 11b shows an increase in contact angle with decreasing bubble diameter. The postulated mechanisms explaining this latter phenomenon are as follows. Smaller air bubbles exhibit a higher internal pressure. The greater this pressure the thinner is the hydrated layer and the greater is the contact angle. Another consideration is that since the amount of water vapour in a bubble decreases with decreasing bubble diameter (increasing pressure) the amount of water vapour adsorbed on the mineral surface from the air bubble is reduced. Leja and Poling(60) also reported significantly increased contact angle with decreased bubble size for surfaces of lucite and galena. The relevant factor

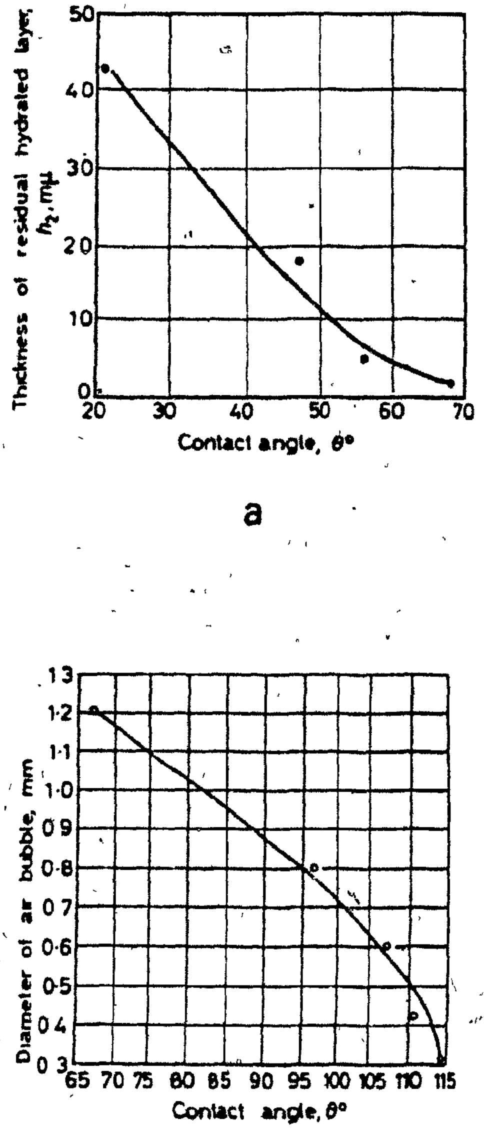

b

11 (a) Measured thickness of the residual hydrated layer versus the contact angle of wetting(51).

(b) Measured bubble size versus contact angle(51).

here is that if contact angle is reduced with decreasing bubble diameter then it is not unreasonable to assume that induction time is also reduced with decreasing bubble diameter.

3.1.4 Detachment

It has long been considered that an important cause of poor coarse-particle flotation is particle-bubble disruption by turbulence(51). Schulze(61) has comprehensively examined the detachment process with a view towards determining an upper limit to particle floatability. Jowett(39) developed an estimate of critical particle size for aggregate disruption based upon the translational velocities of the turbulent zones in mechanical flotation machines. He arrived at critical particle sizes between 100 μm (S.G. mineral = 7.5) and 200 μm (S.G. mineral = 4.2) for a contact angle of 60°. Below the critical size, detachment should be minimal. Woodburn and King(62,63) based their detachment analysis upon the tension developed in the skin of the bubble when the bubble is subjected to a sudden acceleration in the turbulent fluid. They calculated that the maximum strain induced in the bubble skin is proportional to $d_p^{1.5}$, and concluded that the probability of detachment was $(d_p/d_p \text{ max})^{1.5}$. Their experiments showed d_p max. to be between 400 and 1000 μm for many minerals(63). If d_p max. is 400 μm, then the probability of detachment is 0.13 for a 100 μm particle and 0.04 for a 50 μm particle.

It is likely that detachment probability is considerably less than the above values in a flotation column, where there is no mechanical agitation (or, alternatively, the critical size for disruption is higher).

3.1.5 Very Small Particles

In the discussion so far, two zones of liquid can be identified. One zone is the bulk-liquid that is sufficiently far from the bubble surface for the particle to be unaffected by surface related forces; hydrodynamic forces on the particle dominate. The second zone is the surface, or disjoining layer discussed in section 3.1.3. Derjaguin and Dukhin(64) have postulated the existence of a third zone positioned in between the bulk-liquid zone and the disjoining layer. They considered that upon the adsorption of an ionic surfactant at a bubble surface the flow of solution past the rising bubble and the double-layer at the gas-liquid interface would create an electrical field near the bubble surface (in addition to the field associated with the double layer). They calculated that this electric field would extend from a few to some tens of micrometers and, therefore, that it would alter the trajectory of a charged particle passing through it(65). The force exerted on a particle in this zone was termed a diffusiophoretic force.

The Derjaguin-Dukhin theory divides particles into two classes: very small particles, that are captured on a bubble because of the diffusiophoretic mechanism, and larger particles, for which the diffusiophoretic mechanism can be neglected. The impetus for their theory of fine particle flotation appears to derive from an assertion that there is a minimum particle size below which particles are incapable of colliding with the bubble surface. Reay(50) has shown that for an inertialess particle (Sk ⟶ 0) there is no such limit. The incorrect conclusion of Derjaguin and Dukhin was caused by neglecting the effect of gravity on the particle(40,50). Lyman(65), however, concures that the diffusiophoretic force exists; the question that is unanswered is to what distance away from the bubble surface it extends and, thus, to what maximum particle size it affects.

In another approach to fine particle flotation Reay(41,50) considered the collision of particles that are so small that Brownian diffusion is the dominant capture mechanism. For very small bubbles (d_b < 100 μm) he determined that diffusion dominates for d_p < 0.2 μm and that collision dominates for d_p > 3 μm with a transition range from 0.2 to 3 μm. (It is assumed that the fine particles are discrete; flocculation of fine particles will increase their rate of collision.)

A lower limit of particle size for which collision followed by film thinning is the dominant collection mechanism is unknown. However, based upon the work of Derjaguin-Dukhin, Lyman, and Reay it seems that a size between 1 and 3 μm is a practical limit, above which diffusiophoresis and Brownian diffusion need not be considered.

3.1.6 Particle Size in Flotation

Particle size plays an important role in each of the collection subprocesses. Collision efficiency is strongly dependent upon particle size. From Weber's model and Anfruns and Kitchener's experiments, $E_C \propto d_p^2$ for $d_p < 40$ µm; E_C will continue to increase with increasing d_p. Detachment probability is most significant for large particles; for minerals rendered strongly hydrophobic, detachment should be negligible for $d_p <$ ~100 µm(36,91), especially in the quiescent conditions of a flotation column. However, the role of particle size on the attachment subprocess, including contact time and induction time, is unclear.

In his 1981 review, Trahar(10) presents a qualitative view of the relationship between particle size, hydrophobicity and floatability, reproduced in Figure 12. Floatability can be thought of as a rate constant or recovery. Trahar bases his diagram on the experimental evidence that increased reagent levels are required to float large particles to the same extent as smaller particles. He concludes that a disproportionate consumption of collector by fine particles, which would lead to a less complete collector coverage of the coarser particles, does not occur, and that the behavior of coarse particles is related to the degree of hydrophobicity required to promote a high level of floatability.

There are numerous examples of size-by-size recovery that show a peak in recovery occurring at intermediate particle sizes(10,66). The peak is often observed to be between 20 and 80 µm and appears to shift toward the larger sizes as particle hydrophobicity is increased, for example by increased collector dosage(67,68). The lower recovery at small particle sizes can

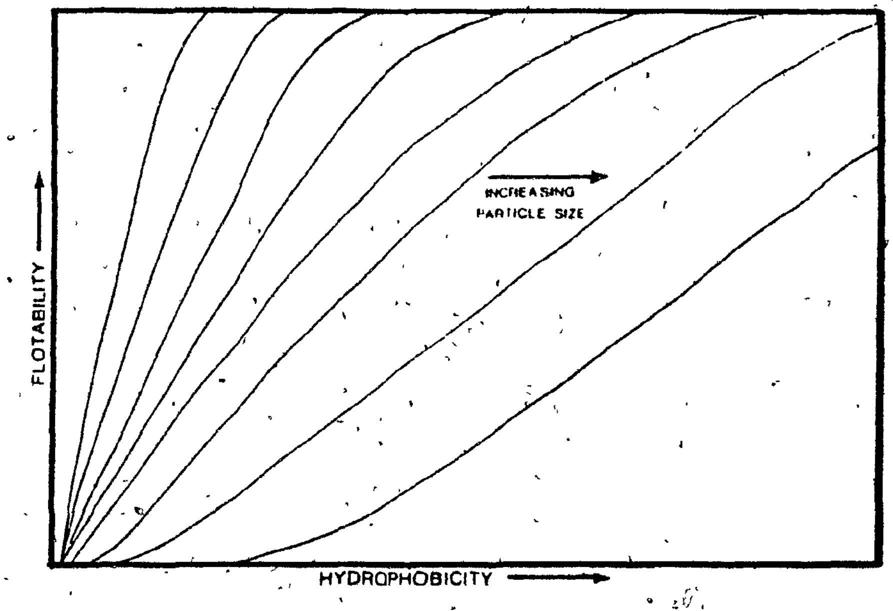

12 Conceptional relationship between floatability, hydrophobicity and particle size(10). Floatability can be thought of as recovery.

be explained by the reduced collision efficiency. The lower recovery at large, and sometimes intermediate, particle sizes is not easily explained. While there is no doubt that detachment is of importance for coarse particles, the peak and subsequent drop in recovery often occurs at sizes where detachment forces would not be significant. One way to explain this result would be to introduce a size dependent attachment process. The necessary trend would be either decreasing contact time (as per Bogdanov[51]) or increasing induction time with increasing particle size.

3.2 Proposed Flotation Model: Overview

The proposed flotation model is similar in concept to that of Sutherland. Particle collection is considered to occur by collision followed by sliding over the bubble surface. It is not intended to model the complete range of particle size; rather the focus is on fine and intermediate sized particles. Consequently, particle detachment is not considered. The initial application of the model is toward understanding the collection process occurring in a flotation column, but it is expected that the model will describe the collection process occurring in mechanical flotation machines as well.

The model construction begins with a simple system: a single spherical particle approaching a single spherical gas bubble, as illustrated in Figure 9. The gas bubble is held stationary at the center of the coordinate system by a downward flow of liquid having a velocity equal to the rise velocity of the bubble u_b. The following assumptions are made concerning the gas bubble:

a. The bubble, being generated in a surfactant contaminated liquid, behaves as a rigid sphere. Sphericity is maintained for bubbles as large as $d_b = 0.12$ cm(47). Bubbles larger than 0.12 cm are ellipsoidal, in which case d_b refers to equivalent spherical diameter d_e.

b. The terminal rise velocity of the bubble is calculated using the method of Concha and Almendra, equation 2.12. When applied to bubbles, let $u_b = U_T$ and $(\rho_p - \rho_\ell) = 1$. Comparison between the measured bubble rise velocity of Anfruns and Kitchener's(43) experiment with that predicted by equation 2.12 is shown in Figure 13. While the fit with equation 2.12 is not quite as good as for the expression employed by Anfruns and Kitchener, it is clear that equation 2.12 provides a good measure of u_b.

Weber's model for particle-bubble collision is employed. Unfortunately, the model is applicable only to relatively small particles, $d_p < 30\text{-}40\ \mu m$, which is approximately equivalent to $Sk < 0.1$. To extend the collision model into the range of intermediate sized particles (30-100 μm) collision efficiencies are determined from trajectory calculations for $Sk > 0.1$ and $20 \le Re_b \le 300$.

Attachment efficiency E_A is defined as the fraction of all colliding particles that successfully attach to the bubble. E_A is a function of induction time and contact time distribution.

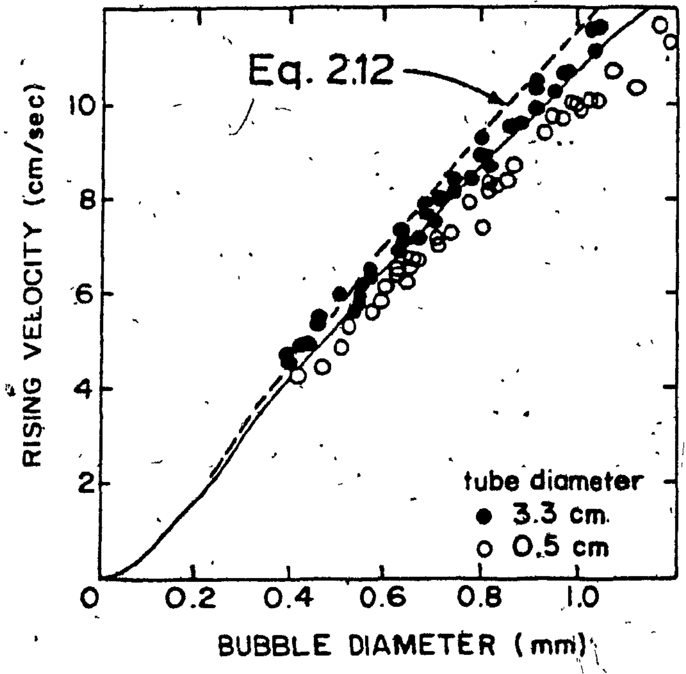

13 Rise velocity of a gas bubble measured by Anfruns and Kitchener (43) and predicted from equation 2.12.

An important aspect of the model is the use of numerical solutions to the flow of liquid around spheres for $Re_p \leq 300$. These solutions provide a relationship between tangential sliding velocity as a function of Re_b, θ and d_p. The distribution of collision angle (between the front stagnation point and the collision angle of the grazing trajectory) is determined from trajectory calculations. The particle sliding velocities, the bubble size, and the distribution of collision angle are combined to yield a distribution of sliding time. Applying a given induction time t_i to the sliding time distribution yields the fraction of colliding particles in contact with the bubble for a time greater than t_i. This fraction is equivalent to the probability of attachment E_A. Then, collection efficiency E_K is given by

$$E_K = E_C \cdot E_A \qquad (3.10)$$

To estimate the upper size limit of particle slide with no bounce, particle trajectories are calculated using the assumption of a partially elastic bubble surface. The surface elasticity is estimated by fitting a trajectory to the coal data of Whelen and Brown (52).

Finally, the single bubble model is extended to account for the effects of neighbouring bubbles in a bubble swarm.

3.3 Collision

3.3.1 Low Particle Inertia

Weber's model is valid when particle inertia can be ignored. This is equivalent to Sk < 0.1. His model has been described in section 3.1. To summarize the calculation of collision efficiency, total collision efficiency is the sum of gravitational and interceptional collision

$$E_C = E_{Cg} + E_{Ci} \qquad (3.4)$$

Assuming that the maximum angle of gravitational collision θ_G is equal to the angle where the fluid streamlines come closest to the bubble θ_C, gives$^{(33)}$

$$E_{Cg} = \frac{u^*}{1 + u^*} (1 + \frac{d_p}{d_b})^2 \sin^2\theta_C \qquad (3.11)$$

The relationship between θ_C and Re_b is shown in Figure 10. To provide a more readily usable form of θ_C vs Re_b, the results of Woo's calculations have been correlated over three linear regions to give

$$\theta_C = 78.1 - 7.37 \log Re_b \qquad 20 \leq Re_b \leq 400 \qquad (3.12a)$$

$$\theta_C = 98.0 - 12.49 \log (10\ Re_b) \qquad 1 \leq Re_b < 20 \qquad (3.12b)$$

$$\theta_C = 90.0 - 2.5 \log (100\ Re_b) \qquad 0.1 \leq Re_b < 1 \qquad (3.12c)$$

Correlation coefficients are all greater than 0.99. Interceptional collision, obtained from equations 3.7 and 3.8, is(33)

$$E_{Ci} = \frac{1.5(d_p/d_b)^2}{1 + u^*} \left[1 + \frac{(3/16)\ Re_b}{1 + 0.249\ Re_b^{0.56}}\right] \qquad (3.13)$$

Total collision efficiency for Sk < 0.1 is calculated using equations 3.4 and 3.11 to 3.13.

3.3.2 Intermediate Particle Inertia

Collision efficiencies for Sk > 0.1 are calculated in this work by determining particle trajectories using a numerical solution to equation 3.1 and finding the grazing trajectory by trial and error. The assumption is made that the particle drag coefficient is expressed by Stokes law, that is $C_D = C_{DSk}$. The error in using this simplifying assumption can be estimated by using Oseen's correction for C_D, given by(69)

$$\frac{C_D}{C_{DSk}} = 1 + \frac{3}{16}\ Re_p \qquad (3.14)$$

For example at $\rho_p = 4.0\ g/cm^3$ and $d_p = 50\ \mu m$
$C_D/C_{DSk} = 1.04$, and for $d_p = 80\ \mu m$
$C_D/C_{DSk} = 1.13$. As well, it is assumed that unsteady-state drag forces are unimportant. Reay's(50) criteria for this to be the case is given by equation 3.9.

To calculate a particle trajectory we begin at coordinates (x,y) (Figure 9) sufficiently far ahead of the bubble that the bubble has minimal effect upon the fluid steamlines.. At this location, the dimensionless particle velocities v_y^* and v_x^* are calculated, from which the coordinates of the next point are determined. This incremental procedure continues until either the particle collides with the bubble or it is swept around the bubble. Collision is considered to occur when the center of the particle arrives within one particle radius of the bubble surface. The process is repeated until a grazing collision is found, from which $E_C = x_s^2$, where x_s is the starting x coordinate for the grazing collision.

The equations for particle velocity, equations 3.2 and 3.3, include a first-order differential term when particle inertia is not neglected. To solve these equations a Runge-Kutta method is employed. Letting $v' = \frac{\partial v^*}{\partial t^*}$, and rearranging equations 3.2 and 3.3 to form $v' = f(v^*)$, gives

$$v_x' = -Sk^{-1} v_x^* + Sk^{-1} u_x^* \qquad (3.15)$$

$$v_y' = -Sk^{-1} v_y^* + Sk^{-1}(u^* + u_y^*) \qquad (3.16)$$

At a given coordinate n the Runge-Kutta approximation for v^* is(70)

$$v_n^* = v_{n-1}^* + \frac{\Delta}{6}(k_1 + 2k_2 + 2k_3 + k_4) \qquad (3.17)$$

where

$$k_1 = f\,(v_{n-1}^*) \qquad (3.18a)$$

$$k_2 = f(v^*_{n-1} + \frac{1}{2}\Delta k_1) \qquad (3.18b)$$

$$k_3 = f(v^*_{n-1} + \frac{1}{2}\Delta k_2) \qquad (3.18c)$$

$$k_4 = f(v^*_{n-1} + \Delta k_3) \qquad (3.18d)$$

and Δ is the step size in the x or y direction.

Liquid Velocities

The only further information needed to complete the numerical solution are values for u^*_x and u^*_y; the liquid velocity profile for the top half of the bubble. For Stokes flow and potential flow these velocities can be determined from an analytical solution of liquid flow around a solid sphere. For Stokes flow

$$u^*_x = 3(x^2 + y^2 - 1)xy/4A \qquad (3.19a)$$

$$u^*_y = [(x^2-y^2)/(x^2+y^2)] + [3(2y^2-x^2)(x^2+y^2) - (2y^2+x^2)]/4A \qquad (3.19b)$$

and for potential flow

$$u^*_x = 3xy/2A \qquad (3.20a)$$

$$u^*_y = (x^2-y^2)/(x^2+y^2) + (2y^2+x^2)/2A \qquad (3.20b)$$

where $A = (x^2 + y^2)^{5/2}$

The equivalent velocities in radial coordinates are, for Stokes flow

$$u_\theta^* = \sin\theta\ (1 - 0.75r^{-1} - 0.25r^{-3}) \tag{3.21a}$$

$$u_r^* = \cos\theta\ (-1 + 1.5r^{-1} - 0.5r^{-3}) \tag{3.21b}$$

and for potential flow

$$u_\theta^* = \sin\theta\ (1 + 0.5r^{-3}) \tag{3.22a}$$

$$u_r^* = \cos\theta\ (-1 + r^{-3}) \tag{3.22b}$$

where $u_\theta^* = u_\theta/u_b$ and $u_r^* = u_r/u_b$.

What is needed, however, is the velocity distribution for spheres having Reynolds numbers in the range 20-300. This is estimated in two ways. Close to the bubble surface velocities are determined using published values of surface velocity gradients, obtained from numerical analysis. Further from the surface, velocities are estimated as a value intermediate to the Stokes and potential flow values.

Consider first the region close to the bubble surface. A good illustration of velocity distributions close to the surface of a solid sphere are the experimental results of Seeley et al (71) for spheres with Re = 290, 760 and 2940, shown in Figure 14. Figure 14a shows liquid tangential velocity u_θ^* vs. distance from the surface of the sphere, r-1, at $\theta = 45^\circ$. The radial

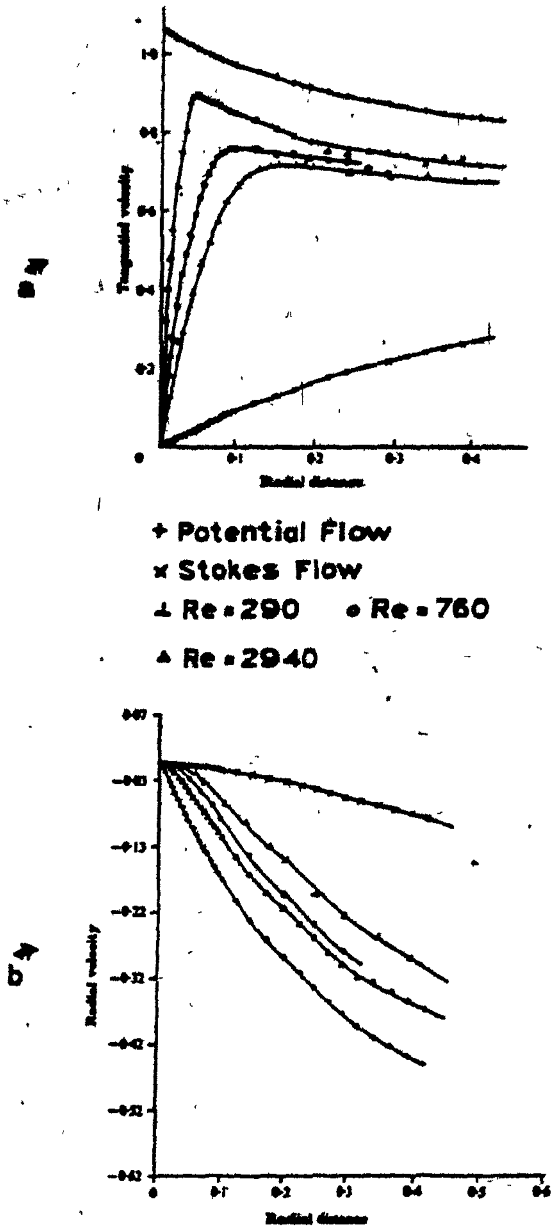

14 Liquid velocity on the surface of a solid sphere versus distance from bubble surface at $\theta = 45^{o}$ (71). Velocity and distance are dimensionless. (a) Tangential velocity, (b) Radial velocity.

velocity u_r^* at $\theta = 45^\circ$ is shown in Figure 14b. The theoretical values for potential and Stokes flow are also indicated. Our interest lies with the data for Re = 290 as this is a value close to that of flotation-sized bubbles. Note the steep tangential velocity gradient close to the surface with u_θ^* going to zero at the surface. The tangential velocity gradient at the surface is the surface vorticity ξ_s. The slope of u_θ^* vs $(r - 1)$ is approximately linear from $(r - 1) = 0$ to ≈ 0.05, and an approximate measure of that slope is ξ_s. Therefore, close to the sphere, let

$$u_\theta^* = \xi_s (r - 1) \tag{3.23}$$

An estimate of u_r^* close to the sphere is obtained as follows. For axisymmetric flow around a sphere(47)

$$u_r^* = -(r^2 \sin\theta)^{-1} (\frac{\partial\psi}{\partial\theta}) \tag{3.24}$$

where ψ is the dimensionless stream function. Near the surface of the sphere the stream function can be approximated by(33)

$$\psi = \frac{1}{2} r^2 \xi_s \sin\theta \tag{3.25}$$

Since ξ_s is known, ψ can be calculated and $\frac{\partial\psi}{\partial\theta}$ can be estimated (by $\frac{\Delta\psi}{\Delta\theta}$) at any value of r and θ. An estimate of u_r^* close to the bubble surface is

$$u_r^* = -(r^2 \sin\theta)^{-1} \frac{\Delta\psi}{\Delta\theta} \tag{3.26}$$

Figure 14a provides an estimate of ξ_s for one Re_b of interest (290) and one angle (45°). Numerical solutions to the Navier-Stokes equations for Re = 0.2 to 400 and $\theta = 0^\circ$ to 180° have been published by Woo(49) and Masliyah(48), including values of ξ_s. The ξ_s data from Woo's thesis is correlated here with θ and Re in the form

$$\xi_s = a + b\theta + c\theta^2 + d\theta^3$$

where a, b, c and d are in turn third-order polynomial regressions as a function of Re. The regression fits are divided into two groups, $20 \leq Re \leq 400$ and $0.2 \leq Re \leq 20$. The regression parameters are given in Appendix 1. By applying these numerical solution values of ξ_s to equations 3.23 and 3.25-26, estimates are obtained for u_g^* and u_r^* (and u_x^* and u_y^*) close to the bubble surface.

A less fundamental approach is used to estimate liquid velocities further from the bubble. If u_P^* denotes potential flow velocity (either tangential or radial) and u_S^* denotes Stokes flow velocity, then let the true velocity u_{Re}^* away from the bubble surface be:

$$u_{Re}^* = xu_P^* + (1 - x)u_S^* \tag{3.27}$$

where $0 \le x \le 1$. An initial value of x is taken to be the average value over the range $(r - 1) = 0.2$ to $(r - 1) = 0.4$, from Figures 14a and b. This value of x is adjusted (after particle trajectories are calculated using it) to give a calculated collision efficiency at low Sk (< 0.1) equal to that predicted by Weber's model. The boundary between the two zones, 'close' to the bubble surface and 'further' from the bubble surface, is taken to be that point $(r - 1)$ at which the velocities calculated by the two methods are equal.

Trajectories and Collision Efficiencies

In this manner, particle trajectories are calculated as a function of Sk, u* and Re_b. The final value of x in equation 3.27 (that provides the grazing trajectory at $Sk < 0.1$ which gives the same E_c as that predicted by Weber's model) does not differ greatly from the initial value (±15%). For the results that are reported here a Runge-Kutta step size $\Delta_o = 0.02$ is used; values lower than this do not improve the accuracy. The starting y coordinate y_s for all trajectories is 10; values greater than this do not improve the accuracy. A listing of the BASIC program, FLOW, developed to calculate the trajectories is given in Appendix 2.

An example of calculated trajectories is shown in Figure 15. The example is for a 40 μm particle with $\rho_p = 7.5$ g/cm^3 (e.g. galena) approaching a bubble with $Re_b = 100$. The four x_s values are 0.1, 0.15, 0.20 and 0.22; the grazing trajectory corresponding to $x_s = 0.229$ ($E_c = 0.052$) with a collision angle of 59.6°.

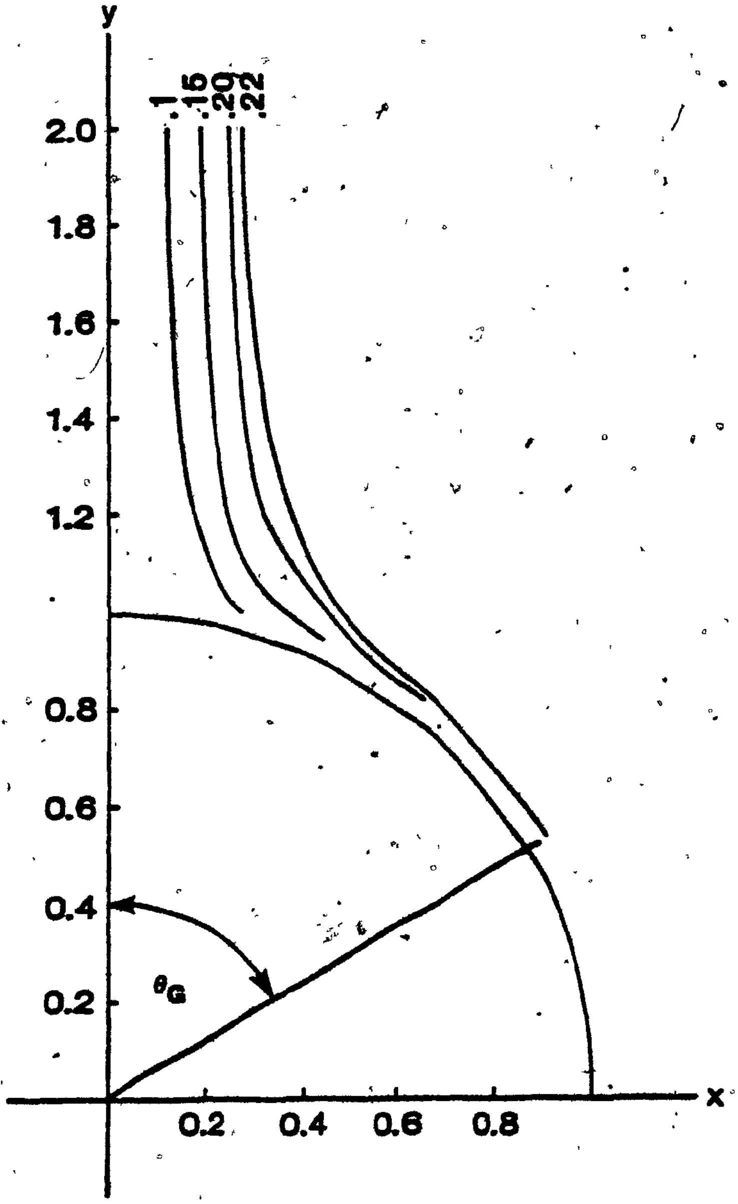

15 Particle trajectories calculated from FLOW. Re_b=100, Sk=0.133, u*=0.042 (eg. d_p=40 μm, ρ_p=7.5 g/cm^3, d_b=0.1 cm, u_b=10 cm/s and u_p=0.42 cm/s)

Calculated collision efficiencies as a function of Stokes number are shown in Figures 16 and 17 for $Sk \leq 1.0$. In Figure 16 the results at $u^* = 0.05$ and $d_p = 50$ µm are given for $Re_b = 20$, 100 and 300, Stokes flow, and potential flow. The bubble diameters are assumed to be as follows: $d_b = 0.1$ cm ($d_p/d_b = 0.05$) at $Re_b = 100$, Stokes flow and potential flow; $d_b = 0.05$ cm ($d_p/d_b = 0.10$) at $Re_b = 20$; and $d_b = 0.14$ cm ($d_p/d_b = 0.0358$) at $Re_b = 300$. (At $d_p/d_b = 0$, i.e. $E_{Ci} = 0$, the calculated collision efficiencies agree with those reported by Flint and Howarth$^{(40)}$.) Figure 17 is for $u^* = 0.10$ and shows the effect of varying the particle size from 50 to 75 µm at $Re_b = 100$. As expected, the collision efficiencies for $20 \leq Re_b \leq 300$ fall approximately midway between the Stokes flow and potential flow collision efficiencies.

An objective of this analysis is to provide a relatively simple expression relating E_C to Sk. This is attained by correlating the results in terms of E_C/E_{Co}, where E_{Co} is the collision efficiency obtained as $Sk \longrightarrow 0$ (the value at $Sk = 0.05$ is used). The multiple regression result, illustrated in Figure 18, is obtained from 40 sets of conditions representing realistic combinations of Sk, Re and u*, and is given by

$$E_C = E_{Co}(1.627\ Re_b^{0.06}\ Sk^{0.54}\ u^{*-0.16}) \qquad (3.28)$$

$$(Re_b^{0.06}\ Sk^{0.54}\ u^{*-0.16}) > 0.614$$

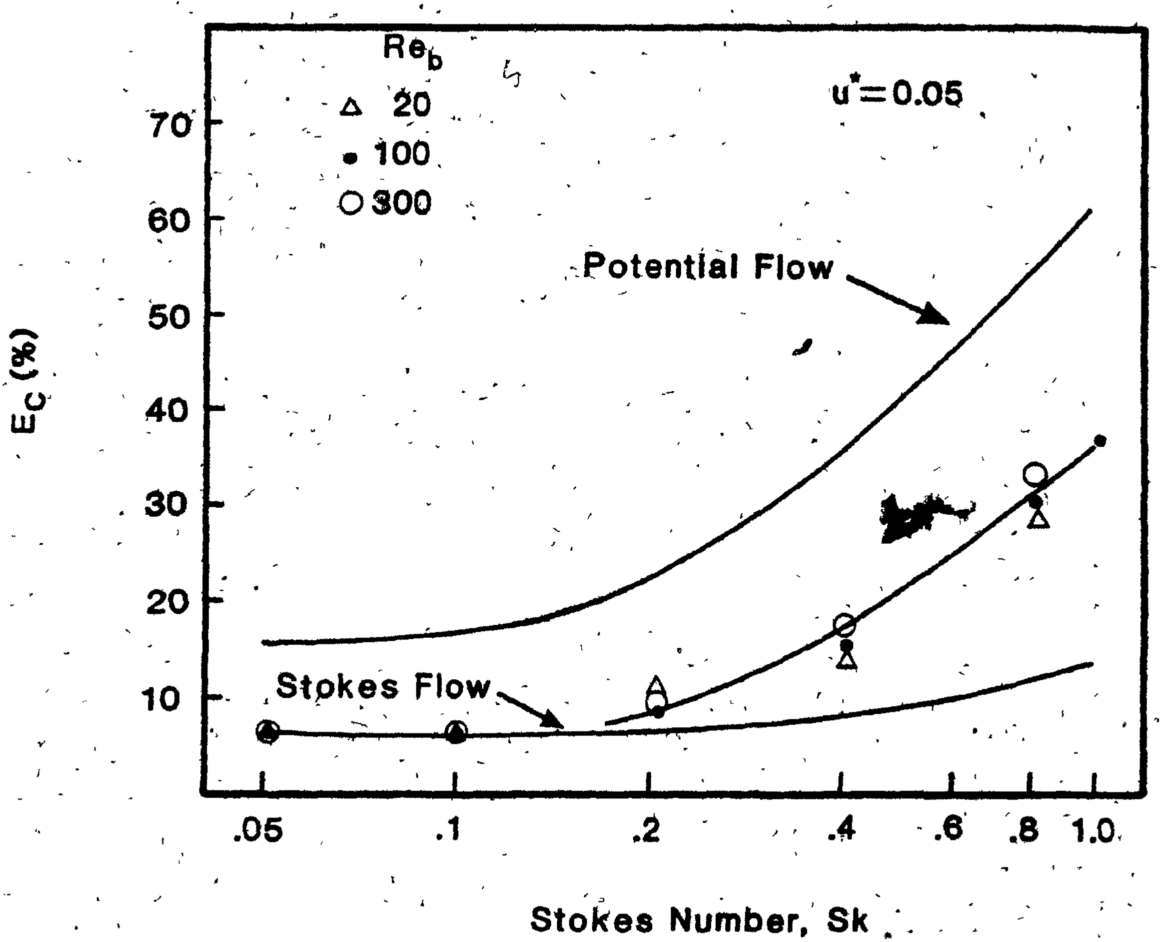

16 Trajectory calculations.

E_C versus Sk and Re_b. u*=0.05

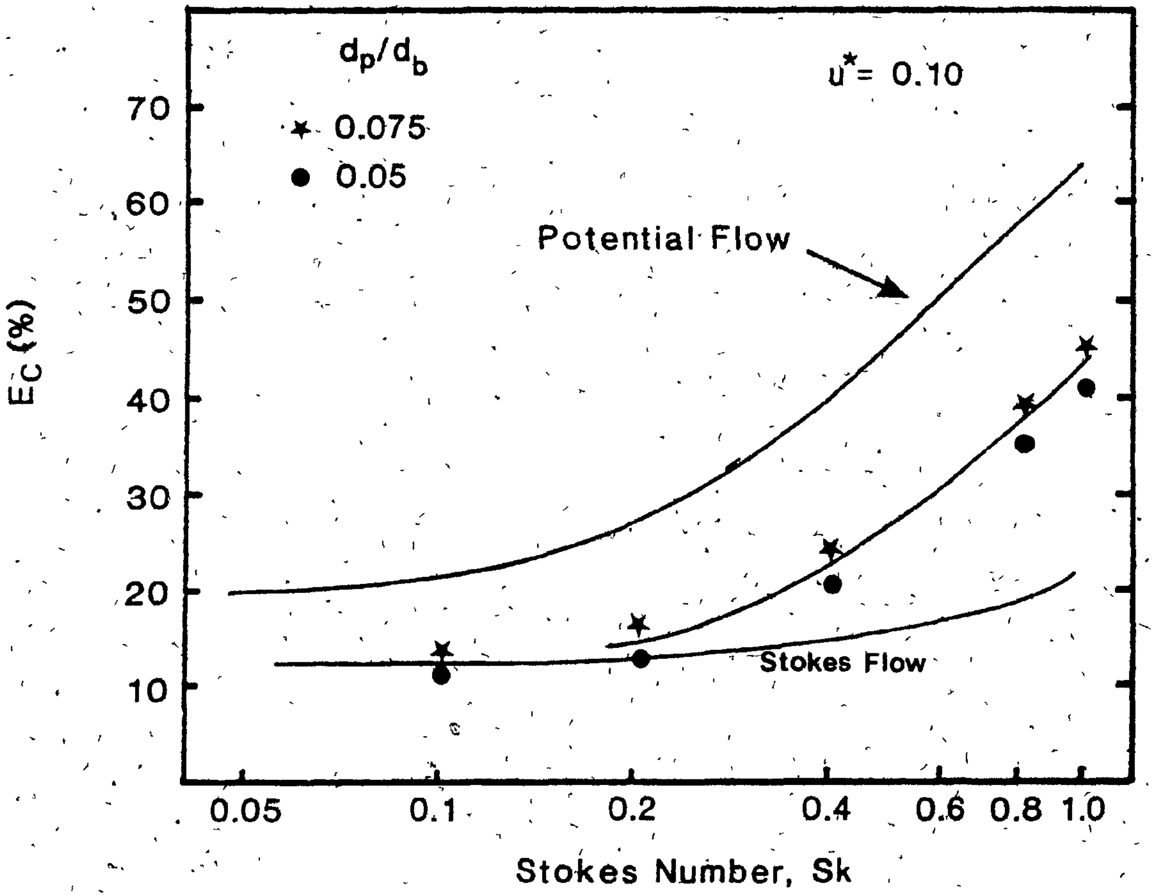

17 Trajectory calculations.

E_C versus Sk . $Re_b=100$. $u^*=0.10$.

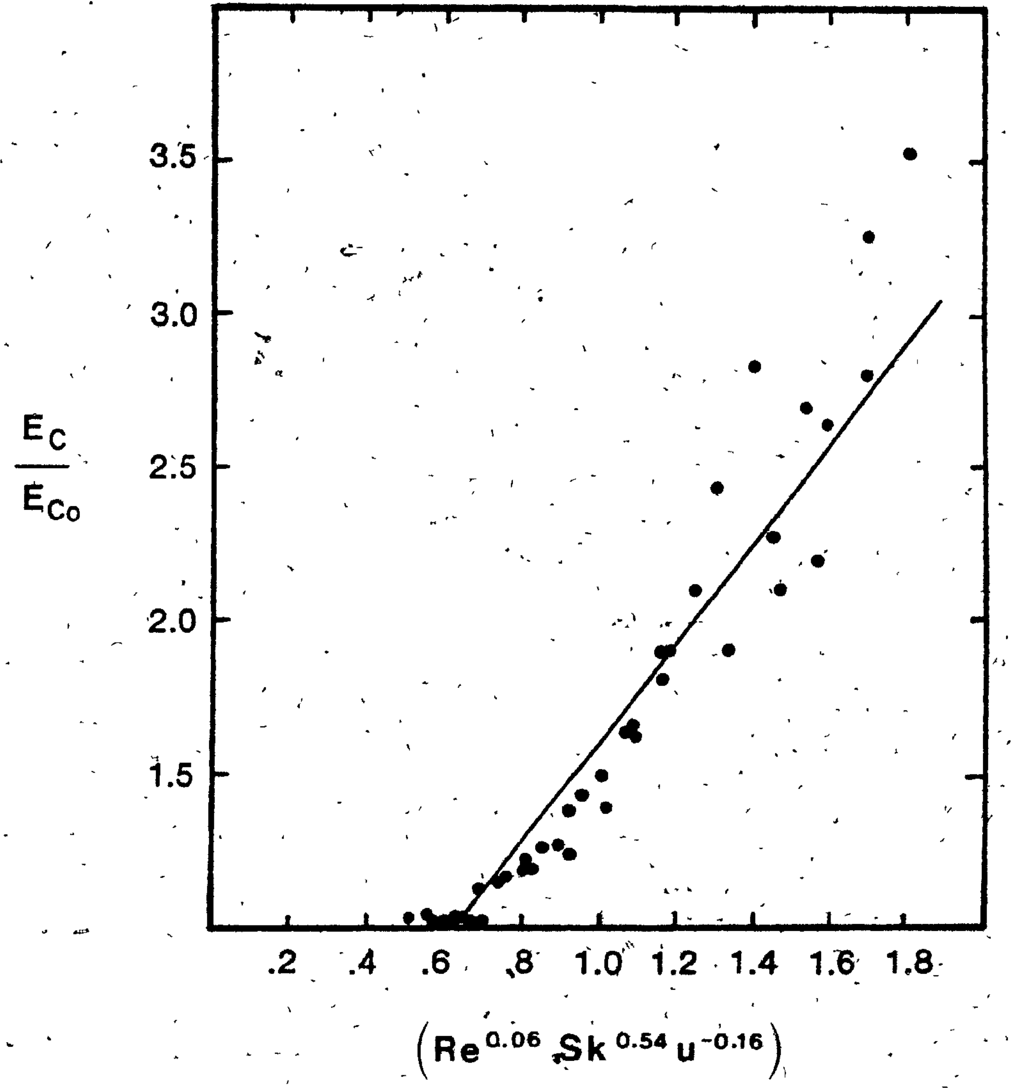

18 Correlation between E_C/E_{Co} and Re_b, Sk and u*. Regression line is $E_C/E_{Co}=1.627\ Re^{0.06} Sk^{0.54} u*^{-0.16}$.

for $20 \leq Re \leq 300$, $Sk \leq 0.8$ and $u^* \leq 0.25$. The correlation coefficient is 0.92. The data is reported in Appendix 1.

Equation 3.28 with equations 3.4, and 3.11-3.13, provides an estimate of collision efficiency for values of Sk as high as 0.8. To give some perspective, the system consisting of an 80 μm particle with $\rho_p = 5.0$ g/cm^3, and a 0.10 cm diameter bubble with $Re_b = 100$ gives $Sk = 0.36$, $Sk(\frac{\rho_\ell}{\rho_p}) = 0.07$, and $\frac{E_C}{E_{Co}} = 1.74$. Consequently, this system satisfies Reay's criteria (equation 3.9) for neglecting unsteady state drag terms.

3.4 Attachment

3.4.1 Particle Bounce

The underlying assumption of the attachment model is that particle-bubble attachment occurs through a film thinning process while the particle slides over the bubble surface. During the induction period, contact is assumed to be continuous. Yet it has been shown(52,45) that large particles bounce when they hit the bubble surface. The objective of this section is to estimate the maximum particle size for which film thinning occurs during sliding alone; that is, where significant bounce will not occur.

Consider again the trajectory model of the previous section. When collision occurs the calculations cease. Now, let the particle rebound from the surface at a radial velocity equal to a fraction z of the impact radial velocity. A portion of the particle kinetic energy will be absorbed by the bubble, so the return radial velocity will be less than the radial velocity at impact. To estimate z the trajectory data of Whelan and Brown(52) is used. Figure 19 shows their trajectories for coal, pyrite and galena particles. Consider the coal data. It can be seen that the particle colliding closest to the bubble axis bounces when it hits the bubble and reaches a height $\approx 0.05\ r_b$ before falling back to the surface. This action can be simulated using a modification to the program FLOW, letting the particle rebound at impact rather than stopping. The conditions of the coal collision tests were:

$d_p = 225\ \mu m$

$\rho_p = 1.3\ g/cm^3$

$d_b = 0.14\ cm$

$u_b = 27\ cm/s$

From equation 2.12 $u_p = 0.67\ cm/s$

$u^* = 0.025$

$Sk = 1.07$

$Re_b = 380$

$x_s = 0.2$

Using $z = 0.50$ in the trajectory program gives a rebound height of $0.088\ r_b$, and with $z = 0.40$ the rebound height is $0.06\ r_b$.

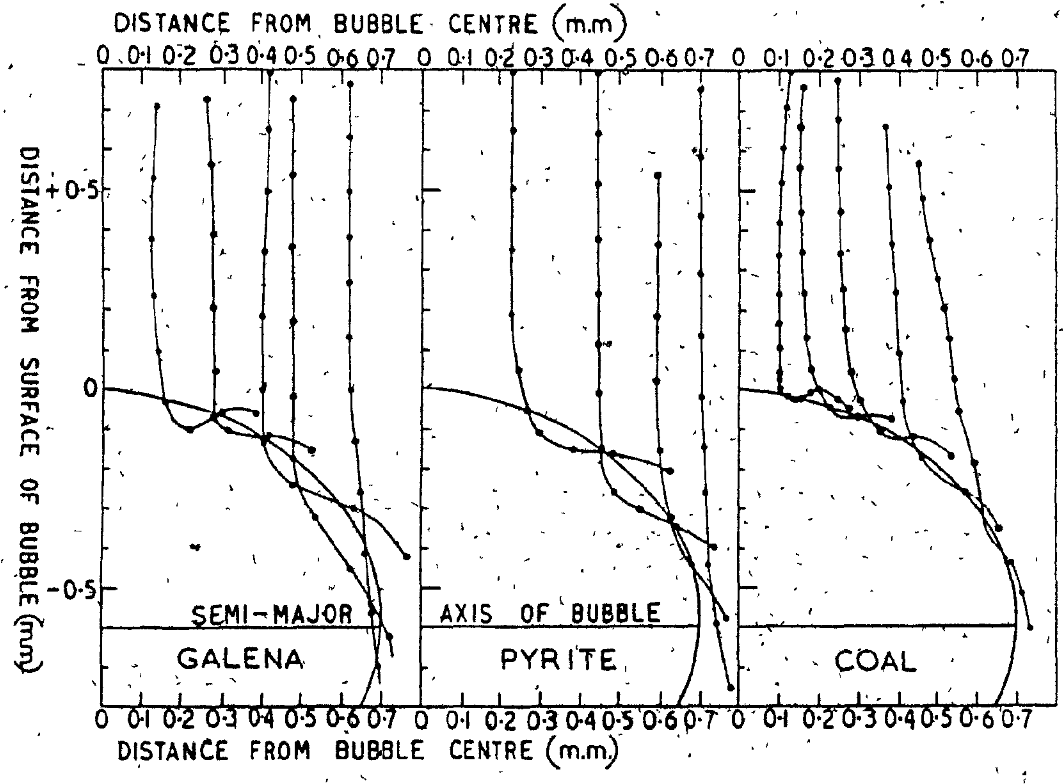

19 Particle trajectories measured by Whelan and Brown(52). For the coal data $Re_b = 380$, $Sk=1.07$ and $u^*=0.025$.

Smaller bubbles probably absorb less energy at impact, so, to calculate particle bounce for $Re_b = 100$, $z = 0.50$ is used. The results of trajectories calculated for spherical particles of density 7.5 g/cm^3 (≡ galena) and $50 \leq d_p \leq 100$ µm are summarized in Table 3. The heights of the first and second rebounds are shown. Trajectories for $d_p = 100$ µm, calculated at different x_s coordinates, show that the rebound height is not a function of the collision angle; this is also evident from the experimental coal collisions, Figure 19. Data for $d_p = 100$ µm and $\rho_p = 4.0$ g/cm^3 is also shown.

The general conclusion from these calculations is that for most minerals particle bounce will not be significant for $d_p < \sim 100$ µm (and for less dense particles ($\rho_p < \sim 3$g/cm^3) this maximum size is closer to 150 µm). Even when bounce does occur, it is often damped out quickly with no subsequent bounce, as illustrated by the 60 to 90 µm particles (Table 3).

3.4.2 Particle Sliding Velocity

It is evident from Figure 14a that there is a significant tangential velocity gradient on the upper surface of a sphere, and, therefore, on a flotation bubble. An important outcome of this velocity gradient is best illustrated with an example. Consider a bubble with $d_b = 0.12$ cm and $Re_b = 290$, and two spherical particles, 12 and 36 µm in diameter. Assume that the tangential velocity gradient is constant across the dimensions of both particles and that a particle travels at the velocity that the liquid would have at the particle center. Then, at

Table 3

Particle Bounce on Impact

Conditions: d_b = 0.10 cm ρ_p = 7.5 g/cm^3 (except at †)
u_b = 10 cm/s x_s = 10
Re_b = 100
Z = 0.5

d_p (μm)	Sk	u*	y_s	Bounce Height (μm) 1st Bounce	Bounce Height (μm) 2nd Bounce	Tangential Travel of 1st Bounce (degrees)
50	0.21	0.081	0.1	2	0	4 → 8
60	0.30	0.112	0.1	4	0	4 → 8
70	0.41	0.147	0.1	8	0	4 → 8
80	0.53	0.184	0.1	14	1	4 → 8
90	0.68	0.224	0.1	20	1.5	4 → 8
100	0.83	0.265	0.1	28	2.5	4 → 8
100	0.83	0.265	0.2	27	2.5	8 → 17
100	0.83	0.265	0.3	28	2.5	13 → 26
100	0.83	0.265	0.4	28	2.5	18 → 36
100 †	0.44	0.134	0.1	7	0	5 → 7

† ρ_p = 4.0

$\theta = 45^{\circ}$, the 12 μm particle ($(r - 1) = 0.01$) would slide at a velocity of ~0.1 u_b, while the 36 μm particle ($(r-1) = 0.03$) would slide at ~0.25 u_b. Consequently, if the two particles collided at the same angle on the bubble, the 12 μm particle would remain in contact with the bubble for a period approximately 2.5 times longer than that of the 36 μm particle.

Sutherland did not have available this detailed information on the velocity patterns around a sphere when he constructed his model. He used the best available approximation, which was potential flow. As shown in Figure 14a, the 12 and 36 μm particles would have tangential velocities equal to u_b under potential flow. Not only does the invalid assumption of potential flow yield velocities that are much too high, more importantly, it does not predict the size dependence.

Particle tangential velocity on the bubble surface can be computed from the surface vorticity. Figure 20 shows again the experimental data of Seeley et al for Re = 290 along with the surface vorticity as calculated from Woo's data (Appendix 1) for Re = 290 and $\theta = 45^{\circ}$. A calculation of the tangential velocity of a particle by using the surface vorticity would overestimate the velocity, except perhaps for the very fine particles. A more reasonable liquid velocity gradient is

$$\frac{u^*}{r - 1} = 0.7\ \xi_s \qquad (3.29a)$$

which is also shown in Figure 20. Equation 3.29a is reasonable

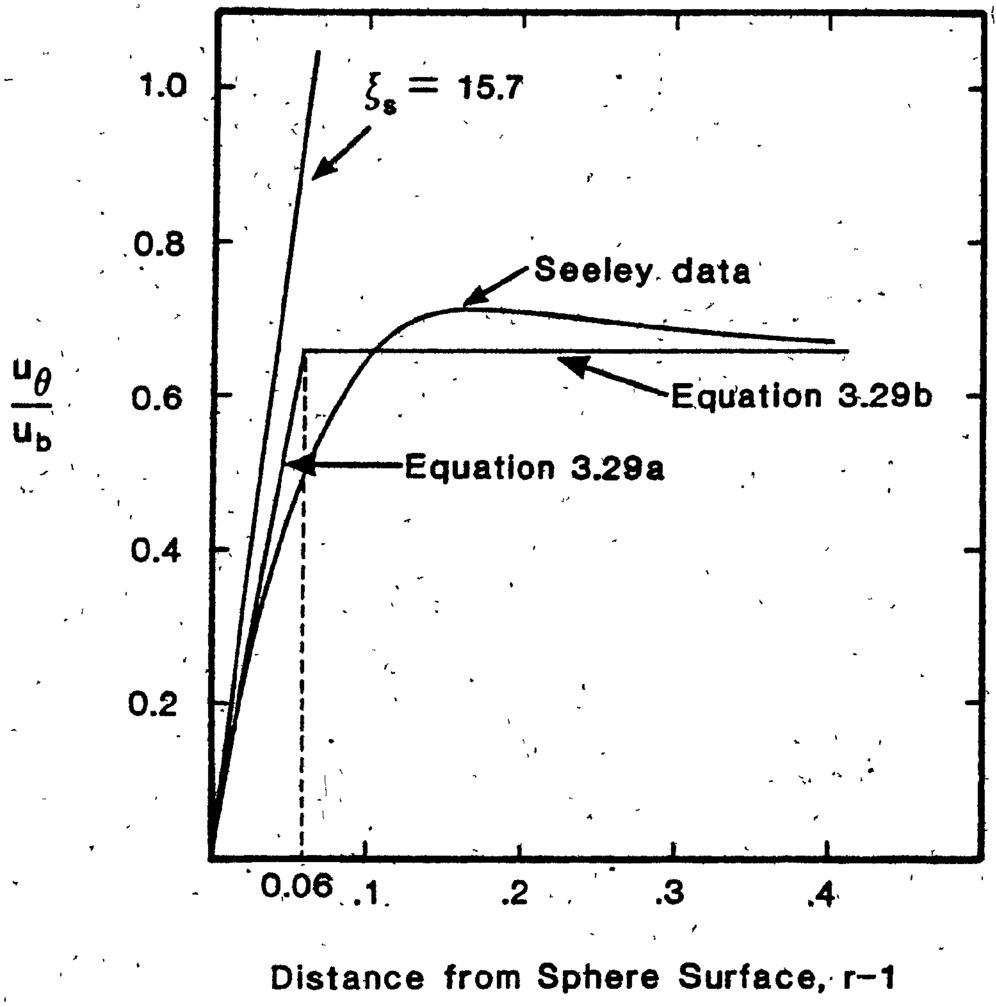

20 Tangential velocity gradient at surface of a sphere at Re=300 and $\theta=45^\circ$. From equation A1-1, $\xi_s=15.7$ at these conditions.

for $(r - 1) \leq 0.06$. For $(r - 1) > 0.06$ let u^* have the constant value given by

$$u^* = (0.06)\ 0.7\ \xi_s \qquad (3.29b)$$

The factor 0.7 fits the velocity gradient at Re = 290 and $\theta = 45^{\circ}$. The assumption is made that it is also a reasonable value at other Reynolds numbers and angles. Then, the particle tangential velocity $u_{p\theta}$ at angle θ is

$$u_{p\theta} = 0.7\ \xi_s\ u_b \left(\frac{d_p}{d_b}\right) + u_p \sin\theta \qquad (3.30)$$

for $(r - 1) = (d_p/d_b) \leq 0.03$.

A particle with $d_p > 0.03\ d_b$ will extend into the boundary layer further than the distance over which there is a velocity gradient. In this case the particle velocity is calculated by dividing the particle into two zones, one that sees a velocity gradient (described by equation 3.29a) and one that sees a constant velocity (described by equation 3.29b). Then the particle tangential velocity is

$$u_{p\theta} = u_b\ \xi_s \left[\left(\frac{d_p - 0.03 d_b}{d_p}\right) 0.06 + \left(\frac{0.03 d_b}{d_p}\right) 0.03 \right] + u_p \sin\theta \quad (3.31)$$

Rearranging gives

$$u_{p\theta} = \frac{0.03\ u_p\ \xi_s}{d_p}\ (2d_p - 0.03d_b) + u_p\ \sin\theta \qquad (3.32)$$

for $(d_p/d_b) > 0.03$.

The particle sliding time t_s can now be calculated. For a particle colliding at angle θ_n and sliding to angle θ_M (at which it begins to travel away from the bubble surface) the sliding time is given by

$$t_s = \left(\frac{\theta_M - \theta_n}{360}\right) \pi d_b / \bar{u}_{p\theta} \qquad (3.33)$$

where θ is in degrees and $\bar{u}_{p\theta}$, the average particle tangential velocity, is determined from equation 3.30 or 3.32 using average values $\bar{\xi}_s$ and $\overline{\sin\theta}$.

Equations 3.30 and 3.32 assume that there is no effect of particle inertia upon the instantaneous particle tangential velocity. This assumption is verified when the trajectory program FLOW is adapted to the situation of a sliding particle. Consider the situation of $d_p = 60\ \mu m$, $\rho_p = 7.5\ g/cm^3$ and $Re_b = 100$, for two cases - one with and one without particle inertia. The maximum difference in velocity at any point is 8% and the average $u_{p\theta}$ for travel between $\theta = 20^\circ$ and 80° is virtually identical for the two cases; 3.46 cm/s when inertia is accounted for and 3.48 cm/s when inertia is ignored.

An experimental test of the sliding time equation (3.33) is provided by the data of Schulze and Gottschalk(45,46). The conditions for their photographic tests were:

d_b = 0.306 cm

μ = 0.01 poise

d_p = 160 μm

ρ_p = 2.5 g/cm^3

$u_p + u_\ell$ = 10 cm/s

From equation 2.12 u_p = 1.58 cm/s

$\therefore$ u_b = 8.42 cm/s

The resulting distribution of sliding time as calculated by equation 3.33 is shown in Figure 21 in comparison with the experimental data. For this comparison it is assumed that a particle slides to $\theta = 90^\circ$. Also shown is the sliding time distribution if potential flow is assumed. Equation 3.33 provides a good description of the results; it is also evident that the assumption of potential flow is not reasonable. (In the original Sutherland paper, the sliding time equation (equation 13) shows a number 4 in the numerator instead of 2, the correct value. Using that equation, as Schulze and Gottschalk did, overestimates the sliding time in potential flow by a factor of two.)

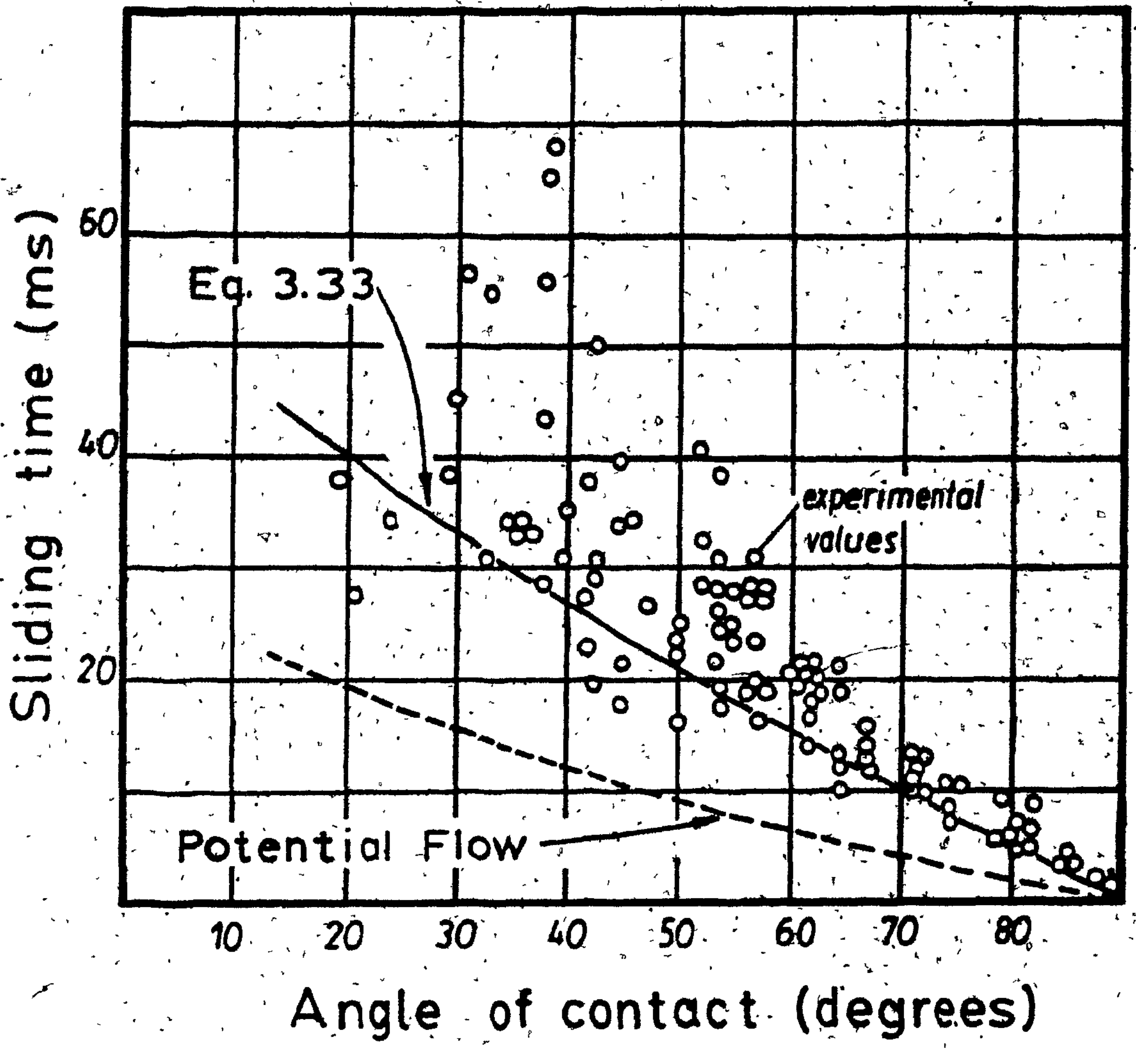

21 Particle sliding times. Measurements by Schulze and Gottschalk$^{(45,46)}$ and predictions from equation 3.33 and potential flow assumption. θ_M=90°. (Potential flow calculated using potential flow equations in the model and by the correct version of Sutherland's equation, giving the same result). See text for test conditions.

Particle Spin

In a fluid velocity gradient a sphere will develop an angular velocity, Ω. It has been shown$^{(72)}$ that in a velocity gradient G

$$\Omega = \frac{G}{2} \tag{3.34}$$

and that the period of rotation τ_r is

$$\tau_r = \frac{4\pi}{G} \tag{3.35}$$

For a spherical particle sliding along the top of a gas bubble and small enough to be completely within the surface tangential velocity gradient $(d_p/d_b < 0.03)$ the average velocity gradient is approximated by

$$\overline{G} = \frac{\Delta u_\theta}{d_p} = \frac{2u_b(0.7\,\overline{\xi}_s)}{d_b} \tag{3.36}$$

and the average period of rotation is

$$\overline{\tau}_r = \frac{2\pi d_b}{0.7\,\overline{\xi}_s u_b} \tag{3.37}$$

Combining equations 3.37 and 3.33 provides an estimate of the number of complete revolutions that a particle will make during its ti[illegible] contact on a bubble. Figure 22 shows the spin distribution for 10 and 30 μm spherical particles and $Re_b = 100$.

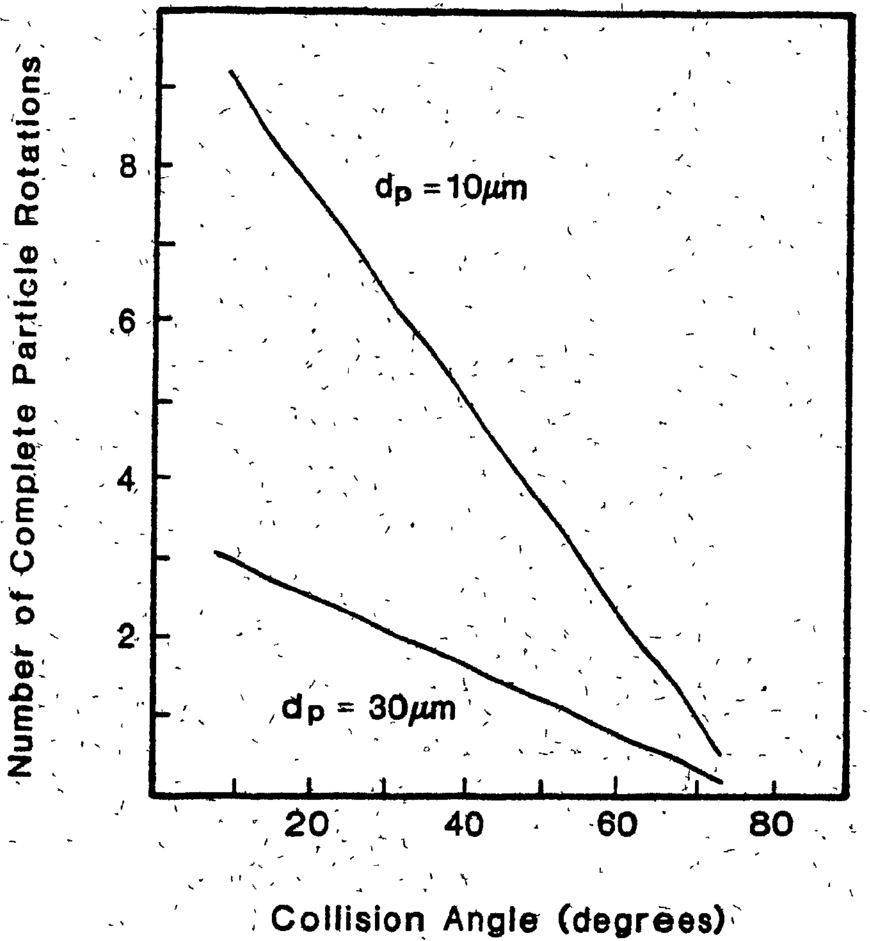

22 Particle rotation during contact with a bubble. Re_b=100, u_b=10 cm/s, ρ_p=4.0 g/cm^3.

Mineral particles are not spherical and would not necessarily exhibit the exact period of rotation described by equation 3.37. However, the above example serves to illustrate that a substantial amount of spin is imparted to a mineral particle. An important consequence is that sharp edges of the particle have a high probability of being presented to the bubble surface and piercing the wetting film.

3.4.3 Grazing Trajectory Collision Angle and Collision Angle Distribution

The distribution of collision angles as calculated by the trajectory simulation is shown in Figure 23 for five particle sizes and $Re_b = 100$. The distribution is described by n_θ the fraction of all colliding particles that collide between the front stagnation point and angle, θ_n. Consider the angle of the grazing collision θ_G. This angle is a complex function of Sk, u* and Re_b. However, it is apparent, from the data of Figure 23, as well as from the collision distribution calculations on other systems, that a reasonable approximation of θ_G is θ_C. It is assumed, therefore, that $\theta_G = \theta_C$ (in agreement with Weber's assumption).

For Stokes flow and potential flow, $n_\theta = \sin^2\theta_n$. For non-ideal flows let

$$n_\theta = \frac{\sin^2\theta_n}{\sin^2\theta_C} \qquad (3.38)$$

which is also shown in Figure 23. For most cases the fit is

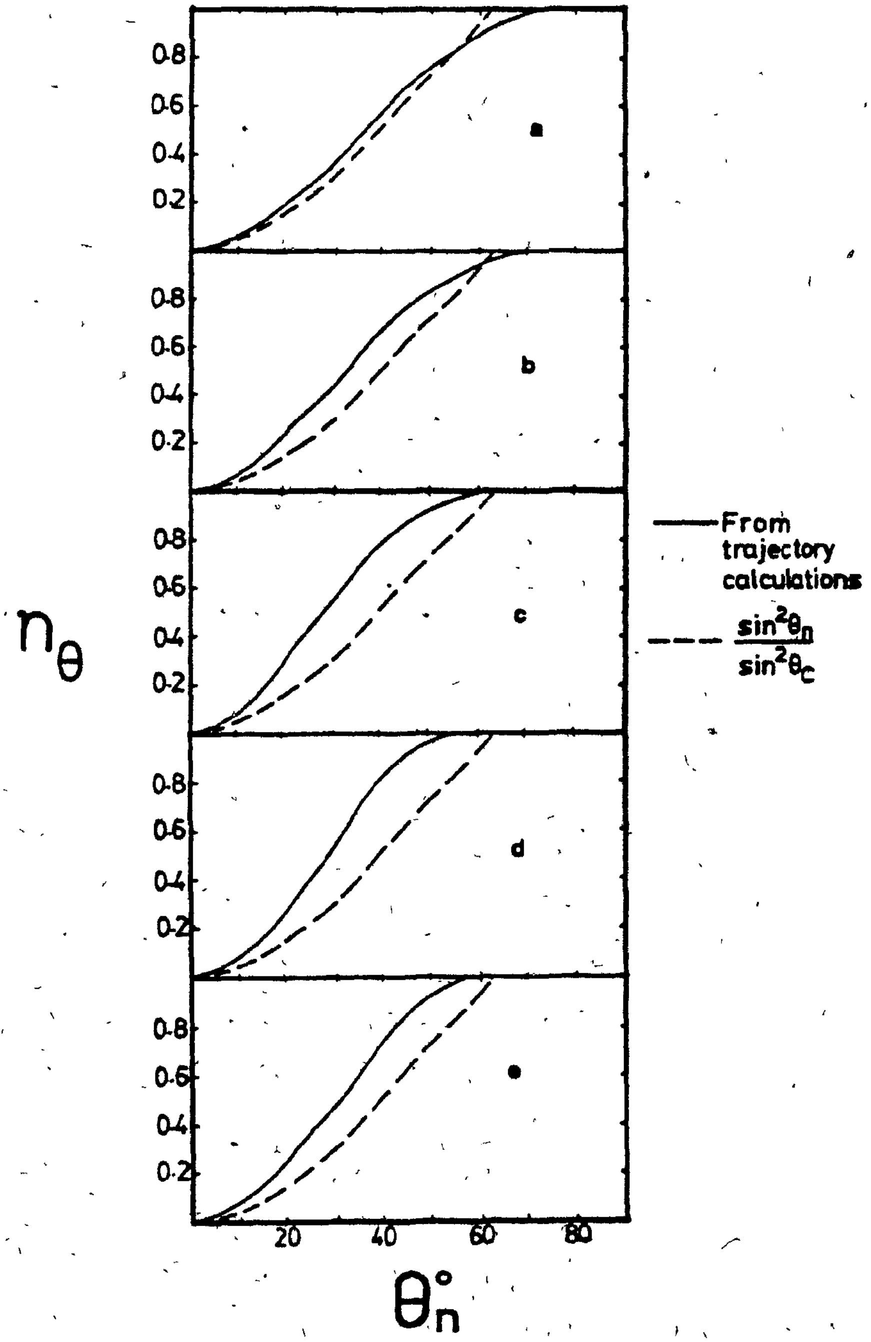

23 Distribution of collision angle. $\rho_p=7.5$ g/cm^3, $Re_b=100$. (a) $d_p=20$ µm, Sk=0.033, u*=0.013; (b) $d_p=30$ µm, Sk=0.075, u*=0.026; (c) $d_p=40$ µm, Sk=0.133, u*=0.042; (d) $d_p=50$ µm, Sk=0.208, u*=0.064; (e) $d_p=60$ µm, Sk=0.300, u*=0.084.

reasonable. When particle bounce is accounted for, the trajectory-calculated collision distributions of the larger particles are more closely represented by the distribution of equation 3.38 than is evident from Figure 23. This is because particle bounce will delay the onset of sliding by up to 10%.

3.4.4 Maximum Angle of Contact

A review of the relevant angles and the manner of estimating their values is appropriate at this point. These angles are:

θ_C - the angle of closest approach of the liquid streamlines, given by equation 3.12.

θ_n - the angle of collision for any trajectory.

θ_G - the angle of collision for a grazing trajectory; from section 3.4.3 let $\theta_G = \theta_C$.

θ_M - the maximum angle of contact for a sliding particle.

It remains now to calculate θ_M. This is done by determining the angle at which the radial component of the particle settling velocity u_{pr} (directed toward the bubble surface) is equal to the radial component of the liquid velocity u_r calculated at $(r - 1) = r_p$ (directed away from the bubble for $\theta > \theta_C$). The calculations for determining u_r^* (and thus u_r) close to the bubble surface have already been described (equations 3.25 and 3.26).

θ_M, as calculated in this manner, is reported in Table 4 for $Re_b = 100$, $d_p = 20$ μm and $\rho_p = 1.3$ to 7.0 g/cm^3. θ_M increases as the particle density increases. It can also be seen from Table 4 that θ_M is insensitive to d_p, for $d_p < 40$ μm.

Table 4

Maximum Angle of Contact θ_M

Conditions:

$d_b = 0.1$ cm
$u_b = 10.0$ cm/s
$\mu = 0.01$ poise

$Re_b = 10.0$ $\theta_C = 63.4$

A. $d_p = 20$ μm

ρ_p (g/cm^3)	θ_M (degrees)	θ_M from equation 3.40 (degrees)
1.3	67.4	69.2
2.0	70.9	70.8
3.2	75.1	73.7
4.0	76.9	75.6
5.5	79.4	79.2
7.0	81.4	82.8

B. $\rho_p = 4.0$ g/cm^3

d_p (μm)	θ_M (degrees)	θ_M from equation 3.40 (degrees)
5	76.9	75.6
20	76.9	75.6
40	76.9	75.6

A correlation between θ_M and ρ_p and θ_C is attained by plotting $(90 - \theta_M)/(90 - \theta_C)$ vs ρ_p for the data in Table 4. The regression equation is:

$$\frac{90 - \theta_M}{90 - \theta_C} = 0.90 - 0.09\ \rho_p \tag{3.39}$$

with a correlation coefficient of 0.93. Rearranging gives:

$$\theta_M = 9 + 8.1\ \rho_p + \theta_C\ (0.9 - 0.09\ \rho_p) \tag{3.40}$$

θ_M calculated from equation 3.40 is compared to the original θ_M in Table 4. Although equation 3.40 is derived at $Re_b = 100$, it includes θ_C as a parameter. It is a good estimate of θ_M for other values of Re_b as well.

3.4.5 Attachment Efficiency

A particle attaches to a bubble when it resides on the bubble surface for a time t_s equal to or greater than the induction time t_i. Equating t_s to t_i provides a measure of attachment efficiency. Let θ_n' be the angle θ_n in equation 3.33 when $t_s = t_i$. This gives

$$\overline{u}_{p\theta}\ t_i = \left(\frac{\theta_M - \theta_n'}{360}\right) \pi d_b \tag{3.41}$$

and by rearranging

$$\theta_n' = \theta_M - \frac{360\ \bar{u}_{p\theta}\ t_i}{\pi d_p} \qquad (3.42)$$

where $\bar{u}_{p\theta}$ is determined from equation 3.30 or 3.32 using average values $\bar{\xi}_s$ and $\overline{\sin\theta}$. Attachment efficiency is given by η_θ, equation 3.38, when $\theta_n = \theta_n'$, that is

$$E_A = \frac{\sin^2\theta_n'}{\sin^2\theta_C} \qquad (3.43)$$

This completes the attachment model. The computer program SLIDE (written in BASIC) uses the model to calculate a distribution of sliding times. The program flowsheet and listing is given in Appendix 2. (θ_M is calculated by comparing liquid and particle radial velocities, not by equation 3.40).

Sliding Time Examples

Some results from the attachment model are summarized in Figures 24 and 25, which are plots of E_A vs t_i. Figure 24 illustrates the effect of particle size for $d_b = 0.1$ cm, $Re_b = 100$, and Figure 25 illustrates the effect of bubble size for $d_p = 20$ and 50 μm. At a constant induction time, attachment efficiency increases with decreasing particle size. From Figure 24, if $t_i = 20$ ms, then E_A (80 μm) = 1.5%, E_A (50 μm) = 10%, E_A (20 μm) = 65%, and E_A (≤10 μm) ≅ 100%. This strong particle size effect is not unexpected, given the relationship between particle size and sliding velocity.

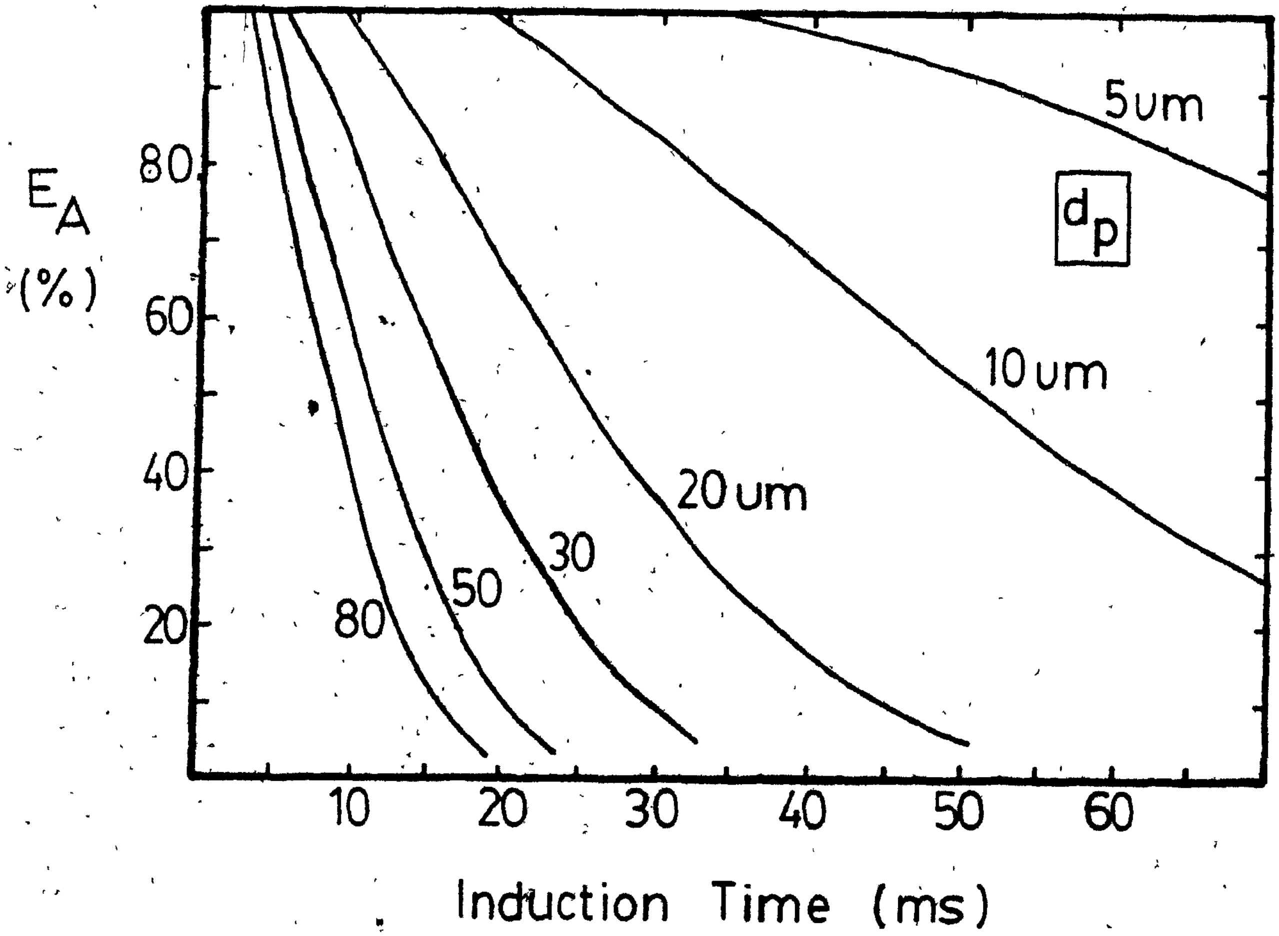

24 Attachment efficiency versus induction time and particle size, from SLIDE.

d_b=0.1 cm, u_b=10 cm/s, μ=0.01 poise, ρ_p=4.0 g/cm^3, ϕ_g=0.

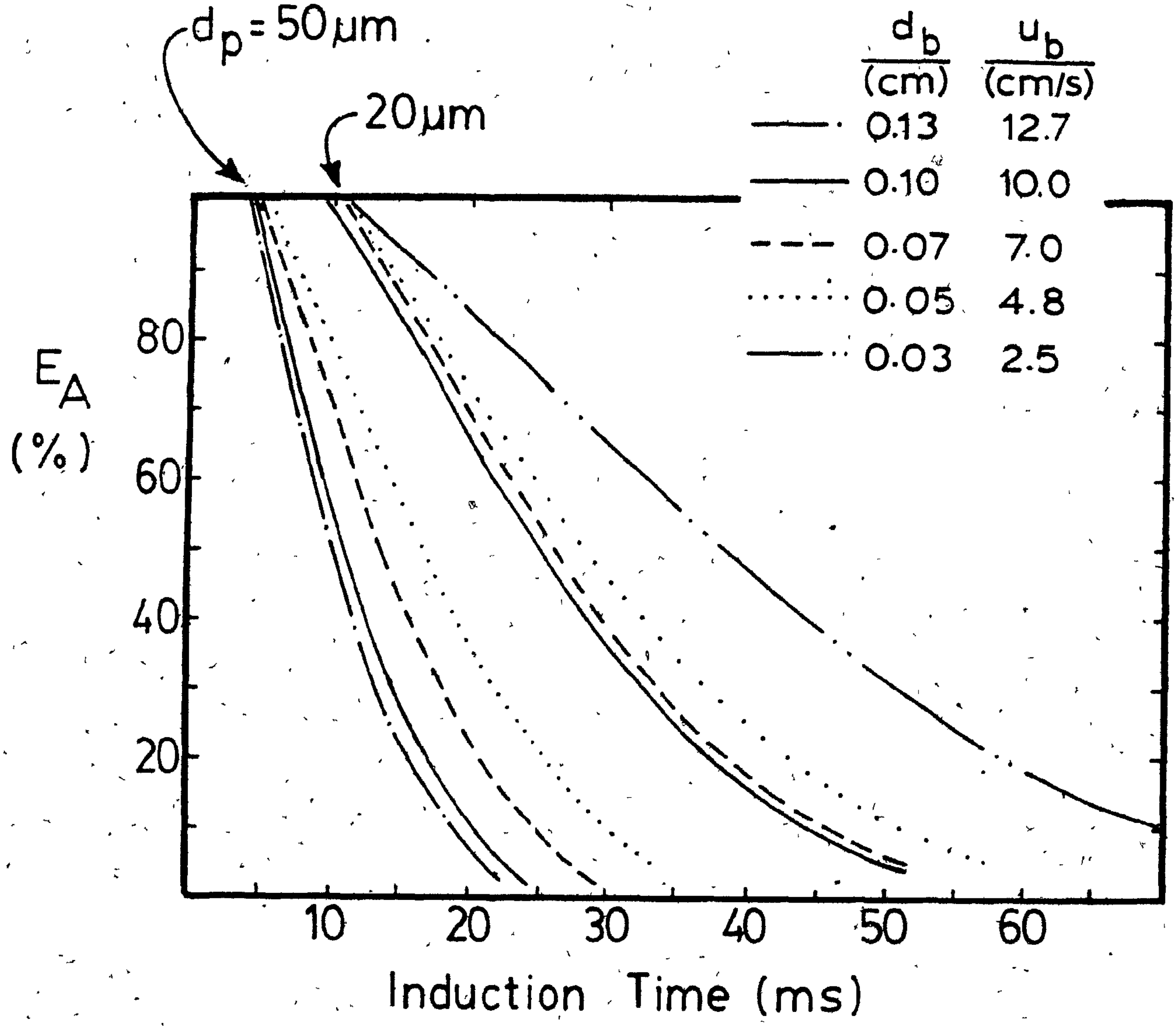

25 Attachment efficiency versus induction time and bubble size, from SLIDE. μ, ρ_p and ϕ_g as in Figure 24.

The magnitude of the bubble size effect, Figure 25, depends upon the particle size being considered. For example, at t_i = 20 ms and d_p = 20 μm E_A varies only from 66% to 73% for $0.05 \le d_b \le 0.13$ cm; while for d_p = 50 μm E_A varies from 6% to 36%. The reason for the relatively small effect of bubble size for smaller particles is that the decrease in particle sliding velocity with decreasing d_b (due to a decrease in surface vorticity) is approximately balanced by the decrease in sliding distance.

It is evident from Figure 24 that very small particles reside on the bubble surface for considerable lengths of time. An important consequence is that successful flotation separation of two types of very small particle, each having the same collision probability, requires a large difference in their induction times.

3.5 Collection

The complete collection model for a single particle-bubble system is the product of the collision and attachment models,

$$E_K = E_C \cdot E_A \tag{3.10}$$

Two computer programs (and their flowsheet) for calculating E_C, E_A and E_K are listed in Appendix 2. They are labelled COLLECT, applicable for $20 \le Re_b \le 400$, and COLLECT2, for $0.1 \le Re_b \le 20$.

Consider now the results of some sample calculations using the collection model.

Particle Size and Induction Time

Figure 26 illustrates the relationship between E_K, d_p and t_i. The figure is constructed using the assumption that induction time is constant with particle size. Since there is no evidence to date regarding the relationship between particle size and induction time relevant to the dynamic flotation situation, using a constant induction time seems a reasonable initial assumption.

There are three interesting observations from Figure 26. The first is that the peak in size-by-size recovery data that is observed in many mineral systems can be explained with the proposed collection model. The reason for the peak is the opposing effect of particle size upon collision and attachment efficiencies; as d_p increases E_C increases and E_A decreases. Note that the peak is observed without including particle-bubble detachment. The second observation is that the peak shifts to smaller particle sizes as the induction time decreases. And third, the collection efficiency for very small particles is quite insensitive to induction time, as was expected from the sliding time distribution of Figure 24.

The latter observation has important implications for selectivity of separation. Consider the separation of two particle systems, one with t_i = 15 ms and the other with t_i = 40 ms. Since rate constant is proportional to collection efficiency, the ratio of collection efficiencies of the two systems provides a good indication of their separability. For

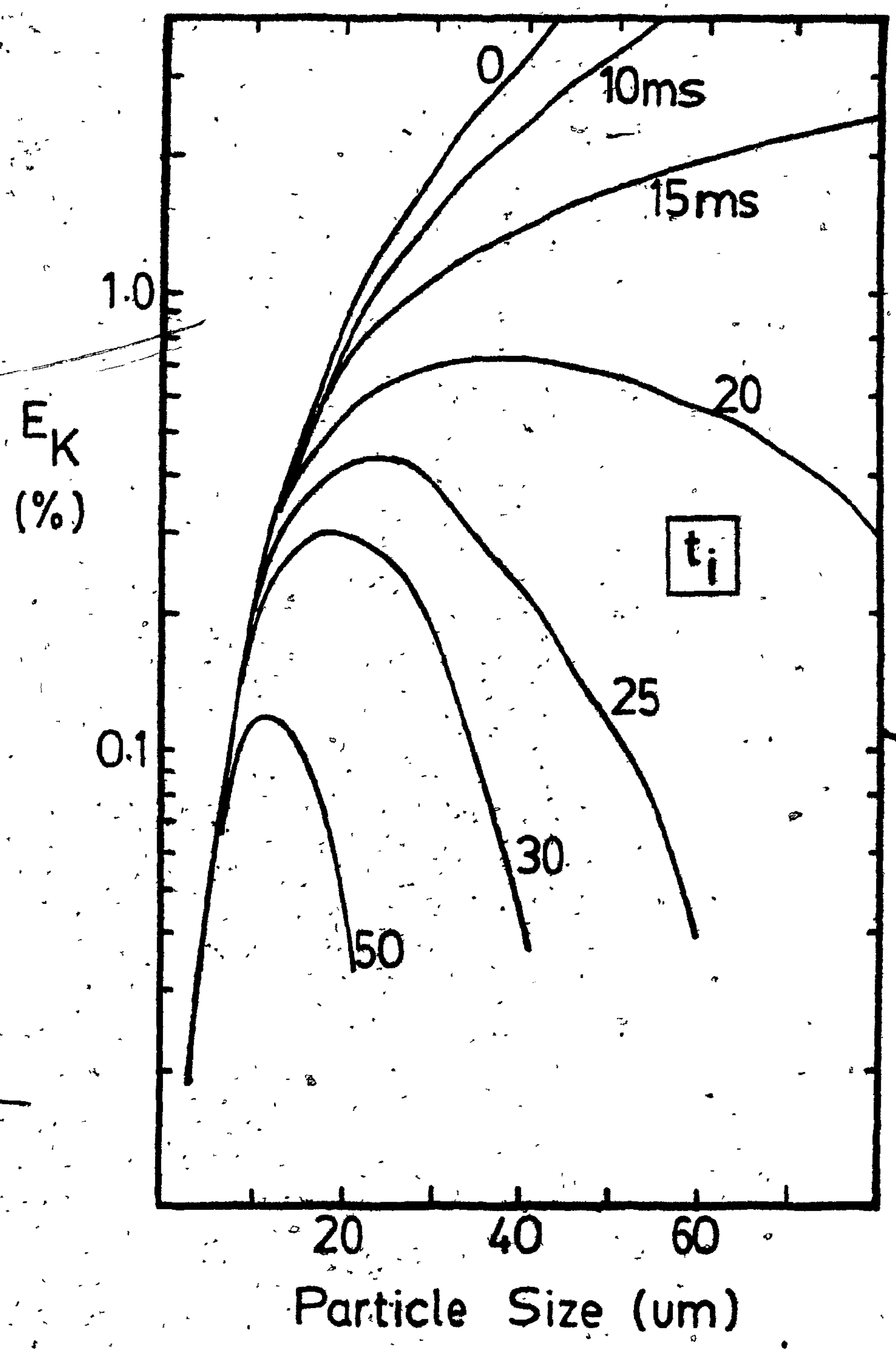

26 Collection efficiency versus particle size and induction time, from flotation model. d_b=0.1 cm, u_b=10 cm/s, μ=0.01 poise, ρ_p=4.0 g/cm^3, ϕ_g=0.

this single bubble system, E_K (t_i = 40 ms)/E_K (t_i = 15 ms) is: 0.009 at d_p = 30 μm, 0.19 at d_p = 20 μm, 0.69 at d_p = 10 μm, and 0.97 at d_p = 5 μm. The separation ranges from excellent at the coarse and intermediate sizes to virtually nonexistant for d_p < 5 μm.

Bubble Diameter

The effect of bubble diameter is shown in Figures 27 and 28. Figure 28 reports the results for each set of conditions in Figure 27 on the relative scale E_K/E_K max. It is assumed that t_i is independent of bubble diameter. The most obvious effect is that a smaller bubble increases collection efficiency for all particle sizes less than 100 μm. It is notable that this effect is also important for intermediate and large sized particles.

A smaller bubble increases collection efficiency but it does not improve separation selectivity. For d_b = 0.05 cm, E_K (t_i = 40 ms)/E_K (t_i = 15 ms) is: 0.13 at d_p = 30 μm, 0.28 at d_p = 20 μm, 0.74 at d_p = 10 μm, and 0.97 at d_p = 5 μm. These are quite similar to ratios obtained for d_b = 0.10 cm.

Particle Density

Figures 29 and 30 summarize the effect of particle density upon E_K vs d_p. The general observation is that the shape of the E_K vs d_p curve becomes progressively more peaked as the particle density increases.

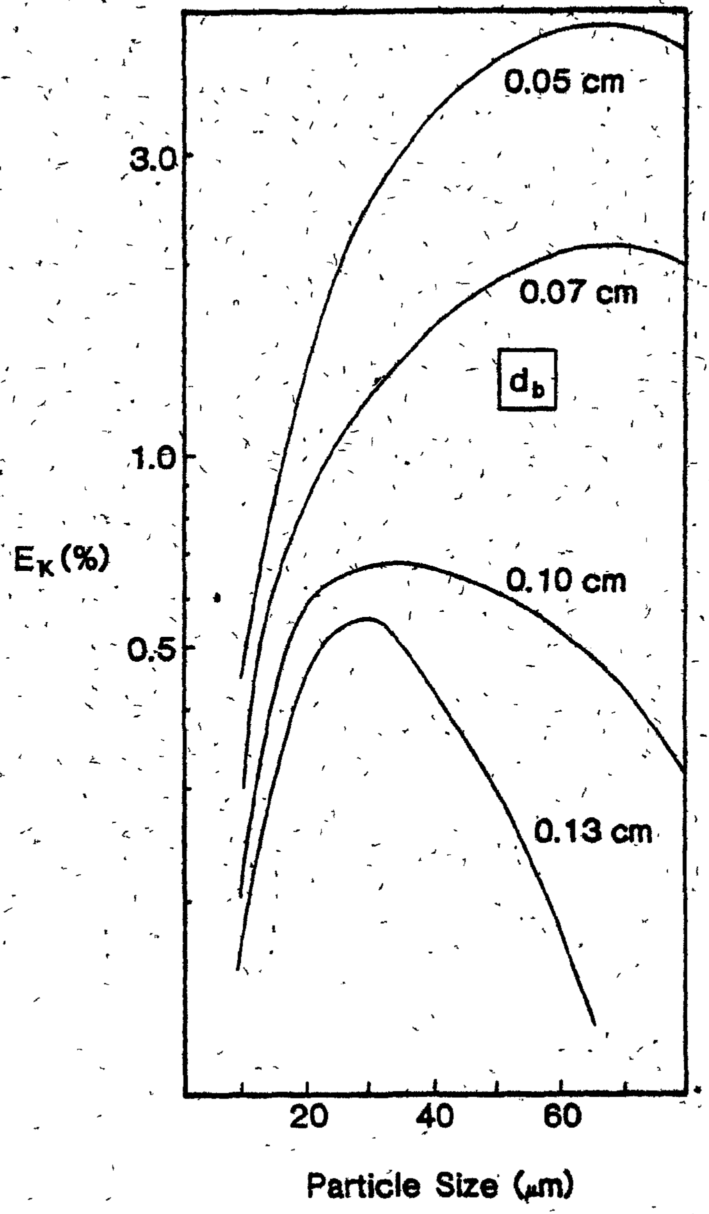

27 Bubble diameter effect on E_K, from flotation model.

t_i=20 ms, μ=0.01 poise, ρ_p=4.0 g/cm^3, ϕ_g=0, u_b as in Figure 25.

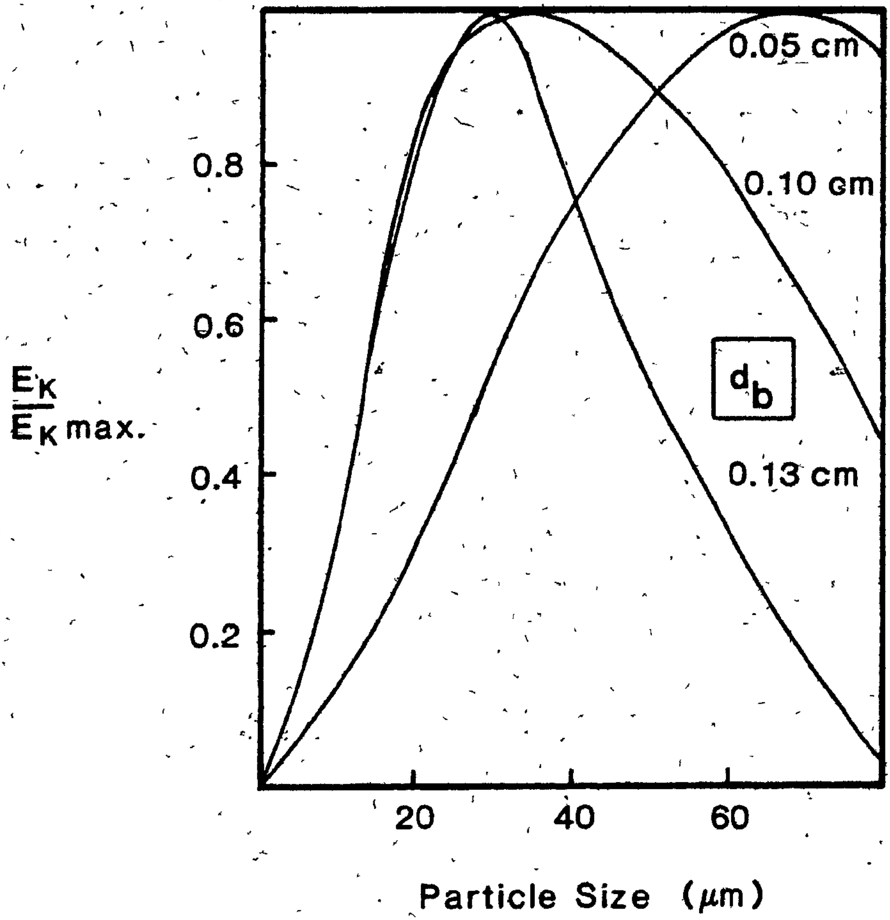

28 Bubble diameter effect on E_K; Figure 27 on a relative scale.

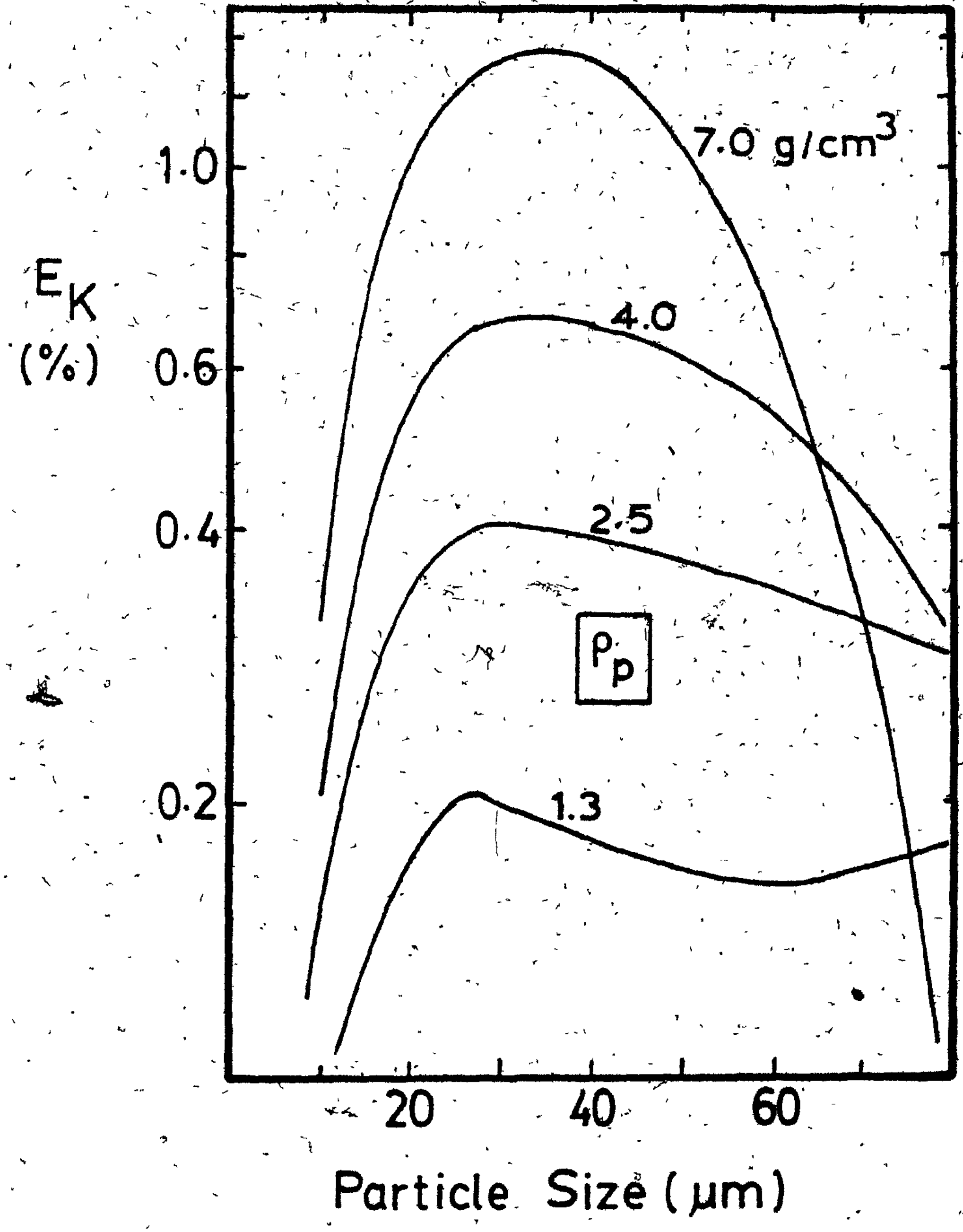

29 Particle density effect on E_K, from flotation model. t_i=20 ms, d_b=0.1 cm, u_b=10 cm/s, μ=0.01 poise, ϕ_g=0.

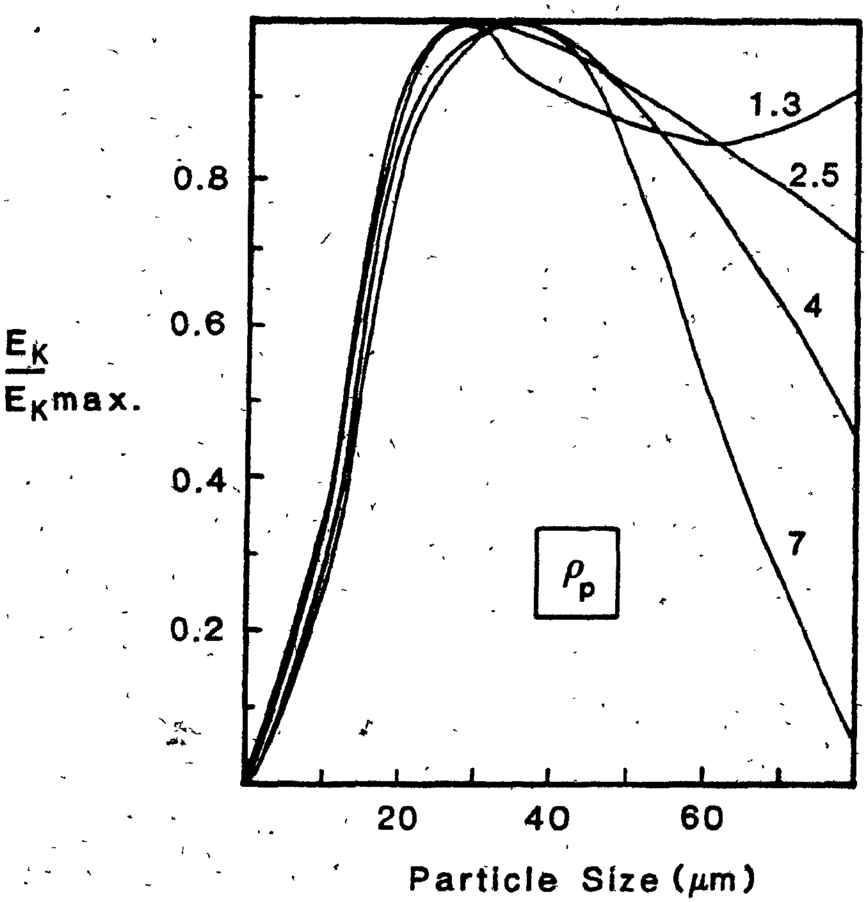

30 Particle density effect on E_K; Figure 29 on a relative scale.

Liquid Viscosity

Viscosity affects both bubble rise velocity and particle settling velocity, but more importantly it likely affects induction time. Jowett (39) has considered several mathematical relationships describing thinning time, or induction time, and they all show thinning time as proportional to fluid viscosity. (This would be the viscosity of the thin film, which might be different from the bulk fluid viscosity; however, a change in the bulk fluid viscosity should be reflected in the thin film viscosity.) Figure 31 shows the effect of liquid viscosity. It is constructed assuming t_i = 20 ms at μ = 0.01 poise, and $t_i \propto \mu$. As well it is assumed that d_b = 0.10 cm at μ = 0.01 poise, and $d_b \propto \mu^{0.25}$ (77). (This latter assumption does not affect the results nearly to the same extent as does the assumption of $t_i \propto \mu$.) It is evident that a decreased viscosity increases collection efficiency. The extent of the impact of viscosity is dependent upon particle size and induction time. The larger the particle and the higher the induction time the greater will be the effect of a change in liquid viscosity.

3.6 Collection in a Bubble Swarm

The flotation model has been developed to this point with the assumption of no interaction between neighbouring bubbles. This is not the situation in flotation. In a bubble swarm of 5% gas by volume the centre-to-centre distance between neighbouring bubbles in a cubic array is approximately

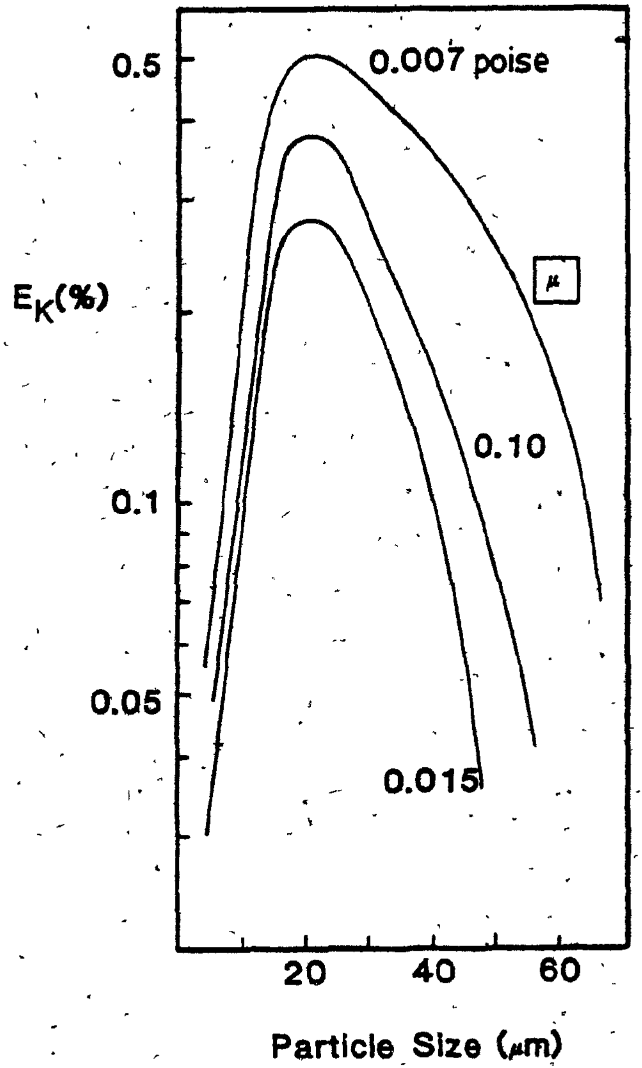

31 Viscosity effect on E_K, from flotation model. ρ_p=4.0 g/cm^3, ϕ_g=0; at μ=0.007 poise t_i=14 ms, d_b=0.091 cm, u_b=11.9 cm/s; at μ=0.010 poise t_i=20 ms, d_b=0.1 cm, u_b=11.8 cm/s; at μ=0.015 poise t_i=30 ms, d_b=0.111 cm, u_b=11.5 cm/s.

2.2 bubble diameters. It is intuitive that there would be interaction in some manner between neighbouring bubbles. LeClair and Hamielec (73,74) have calculated surface vorticity as a function of Re and the volume fraction of spheres (gas holdup in the flotation application). The calculated surface vorticity values from LeClair's thesis have been fitted by polynomial regression to the form

$$\xi_{s\phi} = \xi_s + n\,\phi_g \tag{3.44}$$

where $\xi_{s\phi}$ is the surface vorticity of a gas bubble at fractional volumetric gas holdup ϕ_g, and n is a function of Re_b and ϕ. The results of the regression fit are given in Appendix 1, with a range $0.1 \leq Re_b \leq 500$ and $0 \leq \phi_g \leq 0.259$. This correlation has been included in the collection programs COLLECT and COLLECT2.

In this manner the effect of bubble concentration upon surface vorticity and, therefore, upon attachment efficiency is accounted for. The assumption is made that collision efficiency of a bubble is not affected by a bubble swarm, except by the lowering of the bubble rise velocity in a manner similar to hindered settling of solid particles in a slurry. Thus, the effect of gas holdup upon collection efficiency can be estimated, with the following provisions: 1. E_C is affected only to the extent that u_b is reduced by a swarm, and 2. bubble diameter is constant. In this manner, Figure 32 has been obtained. Induction time is 20 ms, d_b = 0.1 cm and

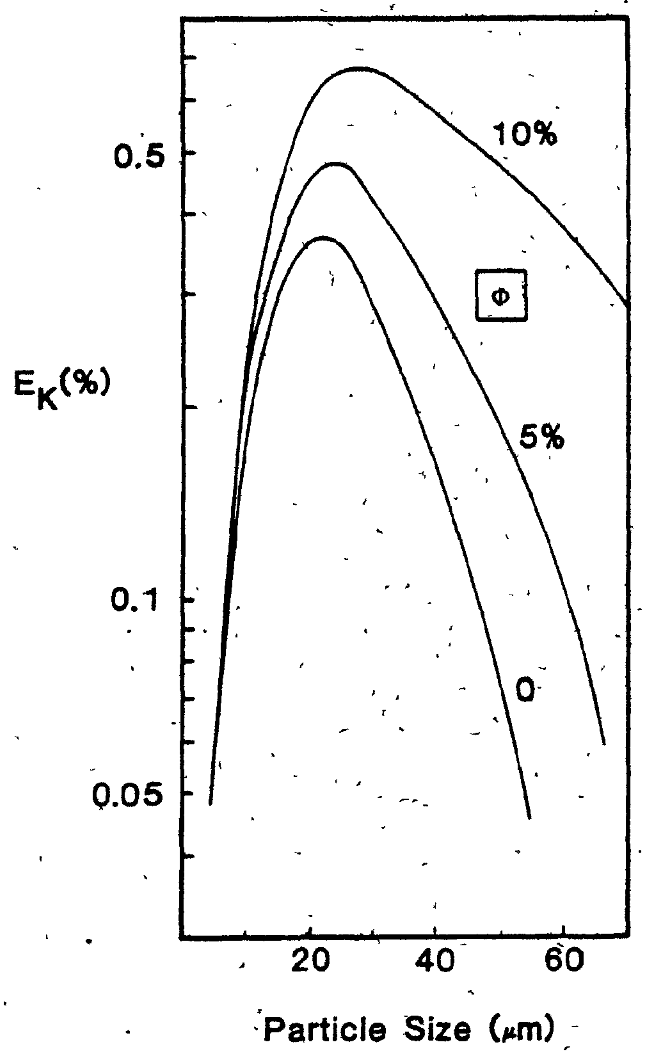

32 Gas holdup effect on E_K, from flotation model. d_b=0.1 cm, μ=0.01 poise, ρ_p=4.0 g/cm^3; at ϕ_g=0 u_b=11.8 cm/s; at ϕ_g=0.05 u_b=10.1 cm/s; at ϕ_g=0.10 u_b=8.6 cm/s.

ϕ_g = 0, 0.05 and 0.10. Bubble rise velocity in a swarm is determined from Richardson and Zaki, equation 2.13 applied to gas bubbles. It can be seen that collection efficiency increases with increasing ϕ_g, significantly so for $d_p > 30$ μm in this example. The increase is due largely to the reduced bubble rise velocity. (It is important to note that when ϕ_g is increased by increasing the gas rate it is probable that d_b will also increase.)

3.7. Collection in a Slurry

The effect of increasing solids concentration upon collection efficiency can be simulated using the model COLLECT. When the solids concentration increases, both the density of the slurry and the "slurry viscosity" increase. The correlation between viscosity and volume fraction solids ϕ_s recommended by Yen (75) for moderate concentrations of solids is that of Roscoe (76)

$$\mu_r = (1 - \phi_s)^{-2.5} \tag{3.45}$$

where μ_r is the ratio of slurry viscosity to liquid viscosity. Viscosity and density changes affect both bubble rise velocity and particle settling velocity. Table 5 summarizes the effect of solids concentration under the assumption that solid-solid interaction does not alter the trajectory that a particle would take (having accounted for velocity effects). In the example, the efficiency of collection of 25 μm particles by a 0.1 cm

Table 5

Solids Concentration Effects

Conditions: $d_b = 0.1$ cm
$\rho_p = 4.0$ g/cm^3
$\phi_g = 0$
$t_i = 20$ ms

d_p (μm)	Wt % Solids	ϕ_s	E_C (%)	E_A (%)	E_K (%)
25	0	0	1.26	28.7	0.36
	14	0.04	1.14	26.8	0.31
	31	0.10	0.98	26.8	0.26
45	0	0	4.58	2.68	0.12
	14	0.04	4.35	2.32	0.10
	31	0.10	4.00	2.62	0.11

diameter bubble decreases from 0.362% at $\phi_s \longrightarrow 0$, to 0.264% at $\phi_s = 0.10$ (31 weight % solids), while there is very little effect of solids concentration upon the collection of 45 μm particles.

3.8 Summary Remarks

A fundamental flotation model is proposed. Particle inertia effects in particle-bubble collision are accounted for, thus extending the range of the existing collision model. Recently derived solutions to the flow equations around spheres are employed to develop a detailed model of particle-bubble contact. When the collection model is tested under different conditions two broad conclusions are reached:

1. A peak in size-by-size recovery data is observed. The shape of the size-by-size curve and the location of its peak is a strong function of induction time, bubble diameter, particle density, and liquid viscosity.
2. Selectivity of separation decreases as particle size decreases which is attributable to the long contact time of smaller particles. Smaller bubbles do not improve the separability.

CHAPTER 4

APPARATUS AND EXPERIMENTAL TECHNIQUE

4.1 Plant Columns: Mixing in Collection Zone

The objective of the plant testing was the determination of typical mixing conditions in the recovery zone of industrial sized columns. Specifically, a relationship between column size and dispersion coefficient D was sought. The raw data necessary to determine D is the RTD of the mixing zone. A fitting of the experimental RTD to the theoretical RTD (equation 2.9) yields an estimate of the vessel dispersion number N_d, from which D is obtained.

Liquid and solid particle RTD measurements have been performed on two industrial columns. The test procedure and the parameter estimation method are described.

4.1.1. Experimental Technique

Tracer Selection Liquid RTD was determined using the dye fluorescein. A problem that is often encountered when using a dye in a minerals system is excessive dye adsorption by the solids. Prior to the RTD experiments, laboratory adsorption tests were performed with fluorescein in slurries of molybdenum and zinc sulfide concentrates. A reasonably small fraction (<20%) of the fluorescein was adsorbed. In contrast, tests with two other dyes, Rhodamine WT and methylene blue, showed >90% dye adsorption. As well, fluorescein was not adsorbed by air bubbles in separate tests in which water and fluorescein were sparged with air in a laboratory flotation machine. Fluorescein is light sensitive (78), so collected samples were stored in the dark.

Manganese dioxide was selected as the solids tracer because it best satisfied the following requirements of a solid tracer: 1) a low background concentration, 2) a low flotation rate (i.e., it is hydrophilic), 3) a suitable specific gravity; the MnO_2 was measured by pycnometer to be 5.19 g/cm^3, 4) ease of analysis, and 5) reasonable cost. Laboratory grade MnO_2 was dry ground and screen classified to an upper particle size of 150 μm prior to the RTD experiments.

Column Operation. The tracer experiments were performed on two flotation columns operating at Mines Noranda Limitée, Division Gaspé, Québec in a MoS_2 concentrate upgrading circuit. Operation and performance of the columns have been previously described (4,36). The two columns were 0.45 and 0.90 m square. Operating conditions for the two columns at the time of the RTD tests are listed in Table 6. Air holdup was estimated from direct measurement of voidage on the 0.45 m column when there was only water and frother in the column and no feed flow.

Test Procedure. For each of the two tests, fluorescein and manganese dioxide were mixed with water and added at the top

Table 6

Column Operating Conditions For Tracer Tests

	0.45 meter	0.9 meter
Feed flowrate (L/min)	120	380
Washwater flowrate (L/min)	35	190
Tailings flowrate (L/min)	150	530
Concentrate flowrate (L/min)	5	40
Interstitial liquid velocity, u_ℓ (cm/s)	1.3	1.1
Feed wt% solids	3	2
Volume fraction solids, ϕ_s (average)	0.006	0.004
Superficial gas velocity, v_g (cm/s)	1.4	1.8
Estimated air holdup, ϕ_g	0.055	0.070
L, feed point to air sparger (m)	9.5	10.0

of the recovery zone (just below the interface of zones 1 and 2 (Figure 4) by pouring them from the top of the column down a funnel and tube arrangement. Total injection time was approximately 30 seconds for the 0.45 meter column and 60 seconds for the 0.9 meter column. Grab samples of tailings, concentrate and feed were taken over the next 60 minutes. Tracer Analysis. Liquid from the samples was extracted using a syringe, with a filter paper assembly on the tip. A Leeds and Northrup portable spectrophotometer was used to measure fluorescein concentration at a wavelength of 476 nm.

Manganese measurements were performed only on the tailings samples from the 0.45 m column test. In preparation for manganese analysis each sample was filtered, dried and screened into five size classes: −400 mesh, +400-270 mesh, +270−200 mesh, +200-150 mesh, and +150-100 mesh. The manganese content of each size fraction was determined by atomic absorption. Sample preparation for atomic absorption was by digestion in 3/1 HCl/HNO_3.

4.1.2. Mixing Parameter Determination

The parameter estimation method is a weighted-moments method similar to that described by several workers (20,79,80) and employed by Rice and colleagues (18,19) for bubble column studies. A brief description of the method follows.

The k^{th} ordinary moment of a distribution in time, c(t), is defined as

$$\mu_k = \int_0^\infty t^k \, c(t) \, dt \qquad (4.1)$$

When t is large the weight t^k also becomes large, and increased emphasis is placed on the tail of the distribution, where the relative experimental error is greatest. A better weight is one that would approach zero for large values of t. Such a weight is(80)

$$w_k\ (t) = t^k\ e^{-st} \qquad (4.2)$$

where s is the weighting factor (also, the Laplace operator, equation 2.8). Then, the k^{th} weighted moment M_k of a distribution c(t) is

$$M_k = \int_0^\infty t^k\ e^{-st}\ c(t)\ dt \qquad (4.3)$$

The larger the weighting factor s, the less will be the emhasis given to values of the RTD at large times.

The zeroth weighted moment of c(t)

$$M_o = \int_0^\infty e^{-st}\ c(t)\ dt \qquad (4.4)$$

is also the Laplace transform of c(t), equation 2.8. For a reactor where end effects are ignored,

$$M_o = \exp\ \{\frac{1}{2N_d}\ [\ 1 - (1 + 4N_d\ \tau s)^{\frac{1}{2}}\ ]\} \qquad (4.5)$$

The recurrence relation of weighted moments(80) allows computation of subsequent moments by

$$M_{k+1} = -\frac{d}{ds} M_k \tag{4.6}$$

The model parameters, τ and N_d, are linked to the weighted moments by the use of weighted cumulants of the model. The weighted cumulants K_i are defined by

$$K_o = \ln M_o \tag{4.7}$$

and the recurrence relation,

$$K_{i+1} = -\frac{d}{ds} K_i \tag{4.8}$$

The relationships between the weighted cumulants and the RTD model parameters have been given by Rice et al (18,19) as

$$\tau = K_1 / (1-2s\, K_2/K_1)^{\frac{1}{2}} \tag{4.9}$$

$$N_d = \tau K_2 / 2K_1^{\,3} \tag{4.10}$$

where

$$K_1 = M_1 / M_o \tag{4.11}$$

and $\quad K_2 = M_2 / K_1^{\,2}$

K_1 and K_2 are obtained from the experimental RTD measurements (normalized to yield an area = 1 under the RTD curve). Then, τ and N_d are determined using equations 4.9

and 4.10. An optimum value of s is selected by minimizing the RMS error between the experimental and theoretical curves, where

$$\mathrm{RMS} = \{ \frac{1}{T} \Sigma \left[c_m (t) - c_f (t) \right]^2 t \}^{\frac{1}{2}} \qquad (4.12)$$

and c_m (t) and c_f (t) are the measured and fitted normalized concentrations at time t. For an impulse input, Anderssen and White(80) suggest that an optimum value for the weighting factor is $s_{Opt} = 2/t_M$, where t_M is the mode of the distribution. Hopkins et al(79) suggest that a suitable range for the value τs is roughly 2 - 5.5.

The derived value for τ can be compared with the measured quantity L/u_i, where $u_i = u_\ell$ for liquid and $u_i = u_\ell + u_p$ for solid particles. The diffusion coefficient D is given by $D = N_d\, L^2 / 60\tau$ meter^2/second, when L is stated in units of meters and τ in minutes.

4.2. Laboratory Column: Particle Collection

Experiments were performed using a laboratory column measuring 1.84 m high and 3.8 cm inside diameter. The column was designed with two objectives in mind. The first was the experimen~~tal~~ testing of the flotation model described in chapter 3. The second was the demonstration that a relatively short laboratory column can be utilized to measure collection kinetics as part of a column scale-up methodology. These objectives required a unique column design. This section describes the laboratory column, its mixing and operating characteristics, the experimental technique for flotation tests, and data analysis.

4.2.1. Column Design

A diagram of the laboratory column is shown in Figure 33. Feed entered the column 1.14 m above the top of the gas sparger (0.70 m below the top of the column). Unlike a conventional column, washwater was added halfway between the feed point and the column top.

Feed System. A 50 L tank with a Lightin mixer was used to prepare and retain the feed slurry. To ensure a uniform feed consist during the length of a test run, a multiholed tube was used to withdraw slurry from the tank. The tube ensured that particles were simultaneously drawn from all levels of the tank. Feed slurry was pumped into the column at a rate controlled either by a recirculation line back to the feed tank or by variable speed pumping.

Wash Water. Steady wash water rate was maintained with a head tank, fed from a 35 L tank with a rotary pump. Before entering the column the washwater rate was measured with a flowmeter. The flowmeter calibration is given in Appendix 3.

Gas System. Air was supplied from a compressed air tank and passed through a flowmeter prior to being sparged into the column. The gas flowmeter calibration, performed with a 'Precision' Wet Test Meter, is also shown in Appendix 3. Gas bubbles were generated with a porous stainless steel sparger, 7.5 cm long x 4.5 cm wide x 1.5 cm thick. In the collection zone (from feed entrance to sparger) static head varied from 0.7 m to 1.8 m of water, an average of 1.25 m.

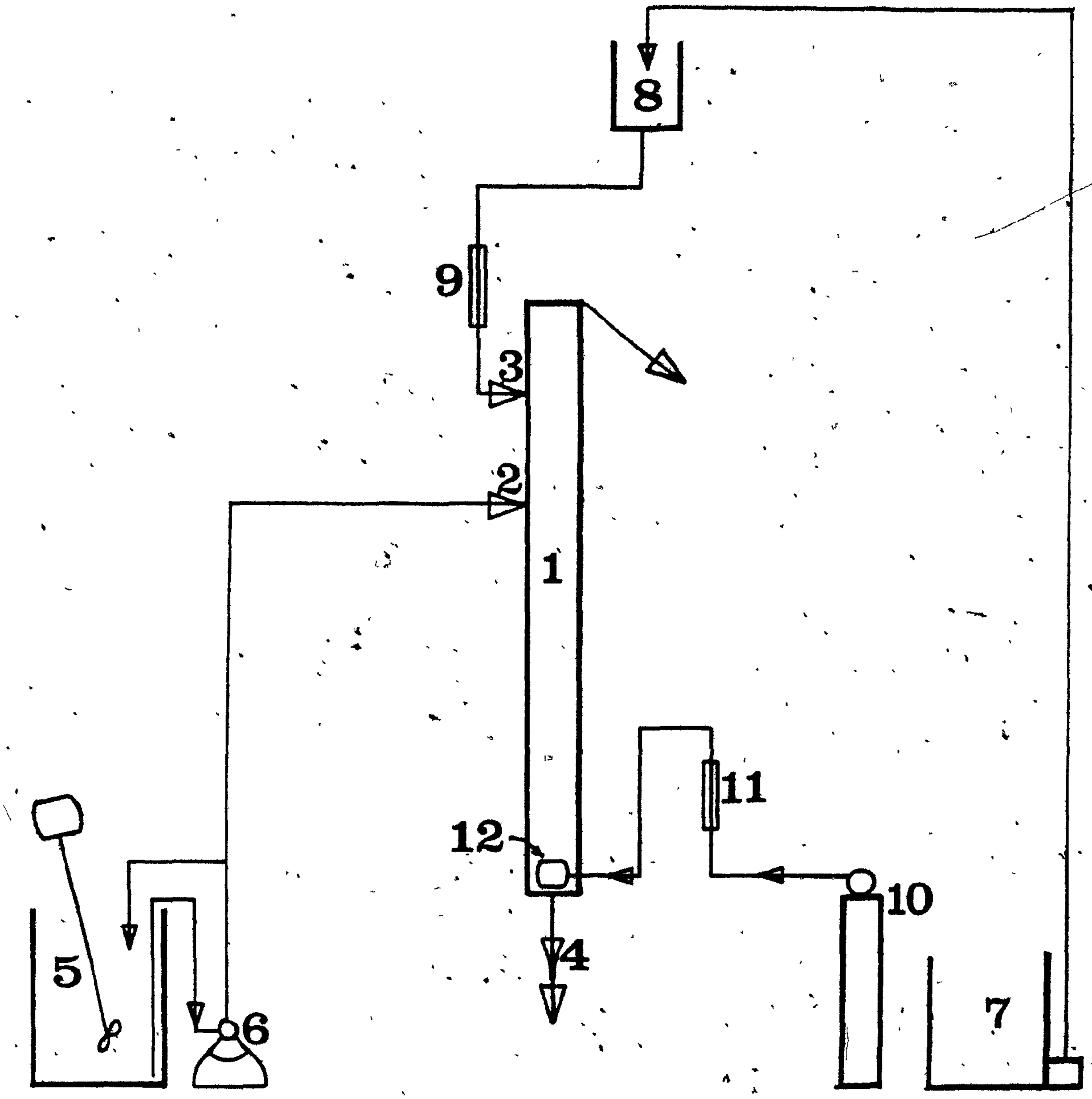

33 Laboratory flotation column and equipment. (1) Column-plexiglass; (2) Feed inlet; (3) Washwater inlet; (4) Tailings flow rate control plug; (5) Feed tank and agitator; (6) Feed pump; (7) Wash water storage tank and pump; (8) Wash water head tank; (9) Wash water flow meter; (10) Gas cylinder and pressure regulator; (11) Gas flowmeter; (12) Gas sparger-stainless steel.

This reduced the average gas flow rate in the collection zone to 90% of the flowmeter reading.

Column Operation. The large volume of water consumed during a test made the use of distilled water impractical; tap water was used. The tailings flowrate was maintained at the desired level by gravity flow through a restricting orifice located at the discharge. During a test, tailings and concentrate flowrates were manually measured and wash water flowrate was obtained from the flowmeter. Feed flowrate was obtained by difference between the sum of the two product flowrates and the wash water flowrate. Tailings flowrate was maintained at a level 2-3 times greater than the feed flowrate. The balance of flow came from the washwater, which was at a rate high enough to both makeup the feed-tailings imbalance and provide a significant liquid rise velocity in the section above the washwater entrance. Typical flowrates are summarized in the column schematic of Figure 34.

With this design and operation, the following conditions were attained:

1. Recovery of particles to the concentrate by an entrainment mechanism was virtually eliminated (see section 4.2.2.). This was a result of the very high downward liquid flowrate in the section between the washwater and feed entrances, effectively preventing the short-circuiting of solid particles to the overflow as well as stripping away particles entrained in the bubble wake.

2. Particle drop-back at the top of the column was eliminat-

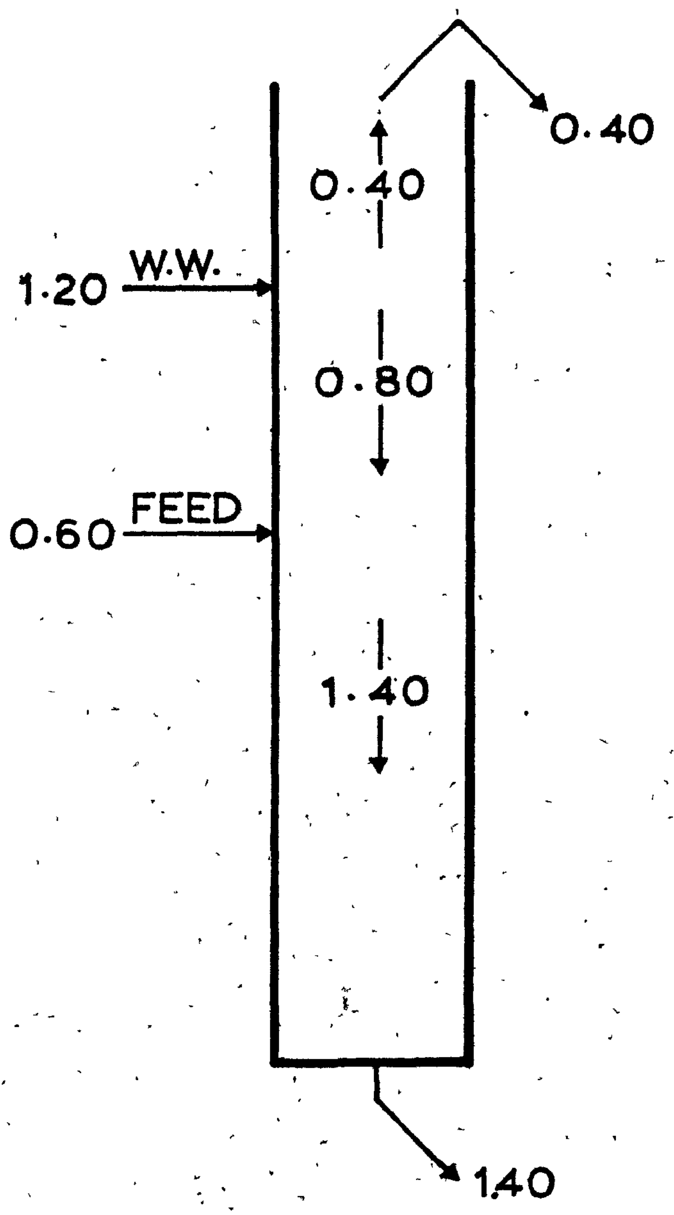

34 Schematic illustration of laboratory column showing volumetric flowrates (L/min) typical for runs 7, 8 and 9.

ed. The very thin froth that formed at the top was rapidly removed (there was a high lip length/area ratio), and the liquid rise velocity in the top section was high enough to carry over the top particles that detached from their bubble (by bursting of the bubble).

As a result, the recovery that was measured was that due to a single collection event only; there was virtually no entrainment and no froth drainage.

4.2.2. Short-circuiting

Overflow. The conditions required to ensure minimal short-circuiting of particles to the overflow were determined by measuring recovery of feed liquid to the overflow (on the assumption that short-circuiting of solids would be less than or equal to that of the water). The column was operated with no solids, air at a superficial velocity v_g = 0.26 cm/s, and a frother dosage of 5 mg/L Dowfroth 250C. The feed water contained fluorescein, the wash water did not. Samples of overflow and underflow were analysed by spectrophotometry for fluorescein content, from which a material balance was obtained. This was repeated for several rates of feed and underflow. The results are illustrated in Figure 35 as recovery to overflow vs Q_F/Q_T^2, where Q_F is the volumetric feed flowrate and Q_T is the underflow rate. Feed short-circuiting to overflow was less than 1% when $Q_F/Q_T^2 < 3.5 \times 10^{-4}$ min/cm^3.

Underflow. Shortcircuiting to the underflow is quantified by the mixing parameters τ and N_d, which has been discussed in other sections. The laboratory column dispersion coefficient

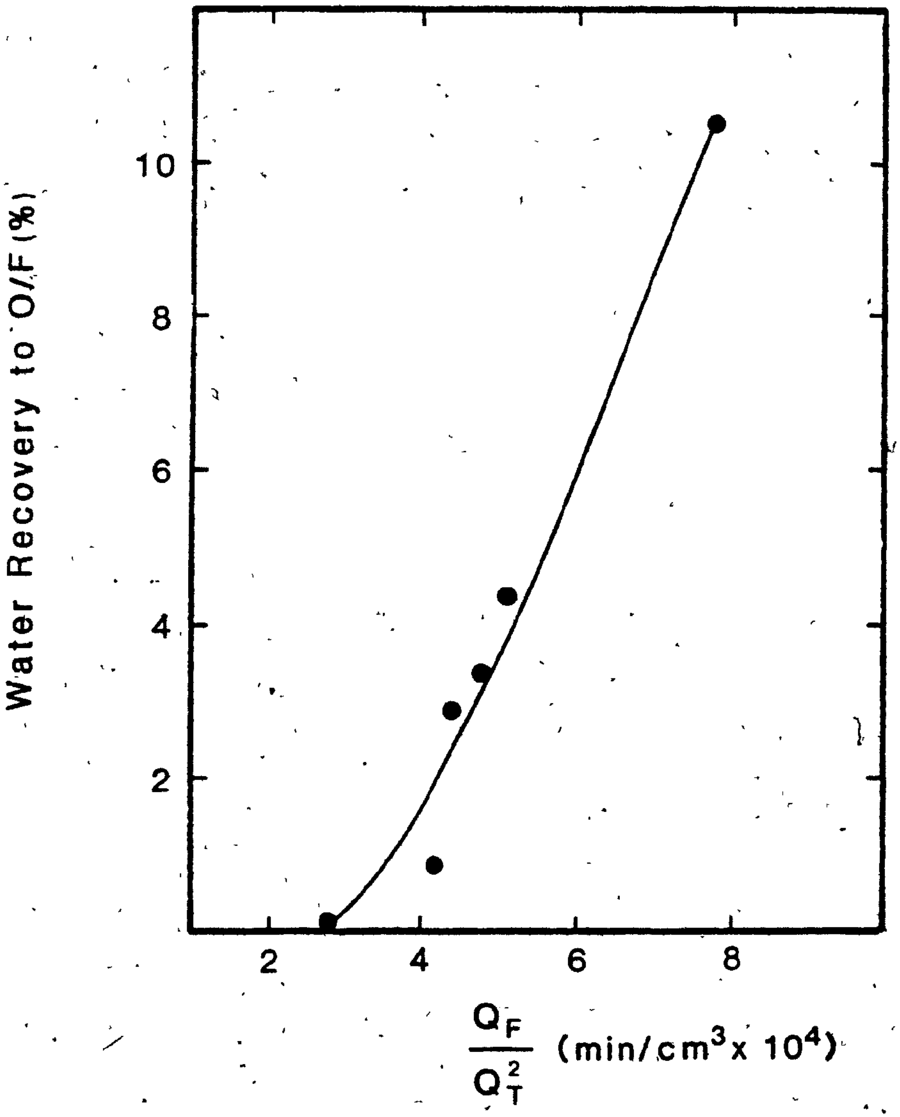

35 Shortcircuiting of feed water to overflow in laboratory column.

D was determined from the data of three RTD tests, conducted with fluorescein tracer and analyzed as described in section 4.1. The estimated parameters are summarized in Table 7. The column was operated normally in tests 1 and 3, with tracer injected at the feed point, for which L(feed point to sample point) = 1.40 m. In test 2 the column was operated with no wash water and feed addition at the top of the column, giving L = 2.00 m. By comparing N_ℓ from Table 7 with Figures 7 and 8 it is clear that the column operated at near plug flow conditions. It is interesting to note, however, that the value of D was affected by velocity u_ℓ, decreasing as u_ℓ increased. The same trend has been reported by others.(24) at high liquid velocities (> 3 cm/s). The phenomenon is attributed(81) to differing flow profiles at different velocities, a factor which would not be significant for large flotation columns operating at relatively low liquid velocities.

4.2.3. Gas Holdup, Bubble Rise Velocity and Bubble Diameter

Although several instrumental methods have been proposed, the most common approach to measuring bubble size is by photography. For dilute bubble concentrations it is simple and accurate. At high bubble concentrations, good photographic measurements are considerably more difficult. More importantly, the photographic technique is not applicable to a slurry. A bubble column provides an alternative method for estimating bubble size, applicable in water and slurries, and suitable for plant measurements as well as laboratory tests. The method consists of applying drift-flux analysis to determine the

Table 7

RTD Measurements on Laboratory Column

Test #	u_ℓ (cm/s)	τ_ℓ (s)	N_ℓ	D (cm^2/s)
1	3.0	47	0.030	12.8
2	2.3	83	0.039	17.0
3	2.3	62	0.053	17.5

v_g = 0.28 cm/s

average terminal rise velocity of bubbles in a swarm, from which the bubble diameter can be calculated.

The concept of drift-flux analysis was introduced by Wallis(82) to relate phase flow rates and gas holdup to physical properties of a two-phase system. For counter-current flow of gas bubbles and water in a bubble column the slip velocity u_s is

$$u_s = \frac{v_g}{\phi_g} + \frac{v_\ell}{1-\phi_g} \tag{4.13}$$

where v_g and v_ℓ are the superficial gas and liquid velocities, respectively (both positive quantities). Wallis postulated that u_s is a function of terminal rise velocity U_T of a single bubble and the gas holdup, in the following form:

$$u_s = U_T \ (1-\phi_g)^n \tag{4.14}$$

As noted by Bhaga(81) this form of the relationship satisfies two boundary conditions:

1. as $\phi_g \rightarrow 0$, $u_s \rightarrow U_T$, and
2. as $\phi_g \rightarrow 1$, $u_s \rightarrow 0$.

Other forms of u_s have been suggested(18,24), but they all apply the assumption that $u_s = U_T \cdot \text{fn}\ (\phi_g)$. In a 1982 review of design parameters for bubble column reactors, Shah et al(24) recommend Richardson and Zaki's(32) relation since it fits most available literature data. This relation was developed for solid spheres, which makes it particularly suitable for flotation sized bubbles. Accepting Richardson and Zaki's term, and combining equations 4.13 and 4.14 gives

$$U_T = \frac{v_g}{\phi_g (1-\phi_g)^{m-1}} + \frac{v_\ell - v_g}{(1-\phi_g)^{m-1}} \tag{4.15}$$

where m is similar to that of equation 2.13, but accounts also for column wall effects (which are significant for bubbles but not for solid particles in the present application). For flotation sized bubbles

$$m = (4.45 + 18 \frac{d_b}{d_c}) \, Re_b^{-0.1} \tag{4.16}$$

Equation 4.15 is derived under the assumption of a uniform flow profile and uniform bubble concentration across the column diameter. For large columns this is a reasonable assumption. For small columns correction factors are required, giving(81)

$$K_o \, U_T = \frac{v_g}{\phi_g (1-\phi_g)^{m-1}} + \frac{C_o (v_\ell - v_g)}{(1-\phi_g)^{m-1}} \tag{4.17}$$

When ϕ_g is uniform over the cross section, $K_o = C_o = 1$.

Terminal rise velocity U_T can be estimated from holdup measurements and the use of equation 4.17. Gas holdup measurements are made at varying levels of v_ℓ for constant v_g (since bubble diameter increases with increasing gas rate, U_T increases with v_g, so v_g must be held constant). A (drift-flux) plot of $v_g/\phi_g(1-\phi_g)^{m-1}$ vs $(v_\ell-v_g)/(1-\phi_g)^{m-1}$ results in an intercept = $K_o U_T$ and slope = $-C_o$. In countercurrent flow, it is difficult to estimate K_o, which Bhaga$^{(81)}$ has discussed in detail. Considering the relatively low gas holdup ($\phi_g < \sim 0.15$) and small bubble size common to the flotation column, the theoretical predictions of Bhaga suggest that $0.95 < K_o < 1$. For this work it is assumed that $K_o = 0.97$.

Gas holdup measurements were made with the column operating with water addition at the top and no wash water addition. With the bubble column operating at steady state the feed and underflow were rapidly and simultaneously shut off. The measurements were repeated for different gas rates, so that U_T as a function of v_g could be determined.

Bubble diameter was calculated using U_T in the equation of Concha and Almendra, equation 2.12. Knowing the relationship between U_T and v_g, gas holdup for any conditions of v_g and v_ℓ could be estimated using equation 4.17 iteratively. Then, bubble rise velocity in the swarm was given by the slip velocity, i.e. $u_b = u_s$, equation 4.13.

<u>Bubble Size Distribution</u>. The preceding analysis assumes that bubble diameter is uniform, which is seldom the case. An example of the size distribution generated by the porous steel sparger is shown in the photograph of Figure 36. The

36 Photograph of bubbles in flotation column. Scale:1 mm=0.36 mm. See text for conditions.

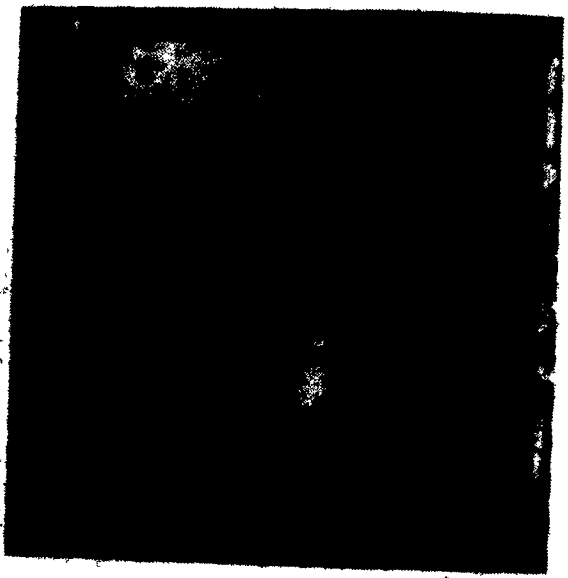

photograph was taken through the wall of the column under the following conditions:

$\mu = 0.01$ poise
$Q_\ell = 0$
$Q_g = 24\ \mathrm{cm}^3/\mathrm{min}$ ($v_g = 0.035$ cm/s)
$\phi_g = 0.0035 \rightarrow 0.0045$
frother: 10 mg/L Dowfroth 250C

At such a low gas velocity it can be assumed that $C_o = K_o = 1$. Then, calculations of bubble rise velocity give U_T between 7.9 and 10.1 cm/s, which in turn yields $d_b = 0.067$ to 0.085 cm.

The distribution of bubble size was obtained by measuring the dimensions of 200 bubbles using a Zeiss Digitizer. The counting results are summarized in Figure 37 as a number distribution, an area distribution, and a volume distribution. Each distribution is approximately linear on the probability graph paper, indicating that it can be described adequately by a mean and a standard deviation, which are noted on the diagram.

The drift-flux method for estimating bubble diameter provides a volumetric mean diameter $\bar{d}_b$. The average diameter required to calculate E_k from equation 2.4 is the area mean diameter $\bar{d}_{bA}$. From Figure 37 let $\bar{d}_{bA} = \frac{(0.78)}{(0.84)}\ \bar{d}_b = 0.93\ \bar{d}_b$.

4.2.4. Sample Preparation

Galena. 650 grams of pure lump galena from Wards Minerals was dry ground in a puck-and-ring pulverizer to -200 mesh. To remove the very fine particles the sample was subjected to repeat elutriation steps to yield 580 g of deslimed

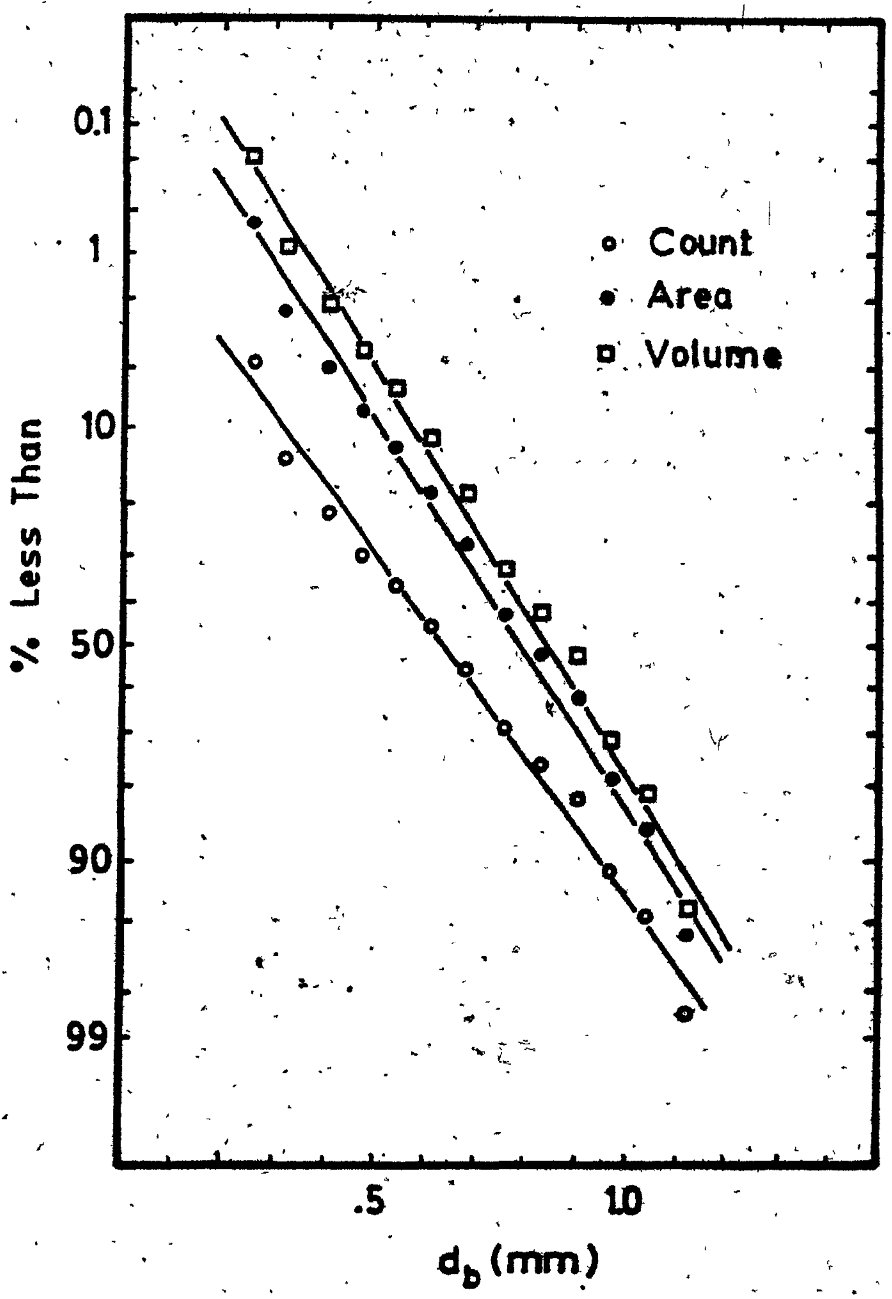

.37 Distribution of bubble diameter on probability paper (from photo in Figure 36). By count, mean d_b=0.63 mm and standard deviation=0.25 mm; by area, mean $d_b=\bar{d}_{bA}$=0.78 mm and standard deviation=0.22 mm; by volume, mean $d_b=\bar{d}_b$=0.84 mm and standard deviation=0.21 mm.

-200 mesh galena. Pycnometer measurement gave a specific gravity of 7.5 g/cm^3.

Silica. Approximately 20 kg of silica flour was subjected to repeat elutriation steps. The deslimed silica was then dry screened at 150 mesh to yield 6.1 kg of deslimed -150 mesh silica.

Sphalerite. The source of the sphalerite was a zinc concentrate from Brunswick Mining and Smelting Ltd., New Brunswick (the concentrate had not been subjected to reverse flotation for pyrite removal). The following steps were performed to obtain a relatively clean, deslimed sphalerite:

1. elutriation to remove very fine particles,
2. washing in 0.02 M NaCN for 30 minutes, to clean the surface(83),
3. batch flotation in a 5 L Agitair cell, rejecting 10% by weight as tailings. Flotation conditions were: conditioning with 0.55 mg/g sodium amyl xanthate for 5 minutes, and flotation for 1 minute.
4. pyrite removal with the Frantz Isodynamic magnetic separator at a current of 1200 mA and a side slope of 20°. 20% of the material was rejected in this manner. The magnetic susceptibility profile of the final sphalerite product is shown in Figure 38. A minor amount of pyrite locking is indicated by the levelling off of the curve at the top. However, the material appears to be reasonably clean. The final product weighed 300 g and gave a specific gravity of 4.1 g/cm^3, by pycnometer measurement. The same

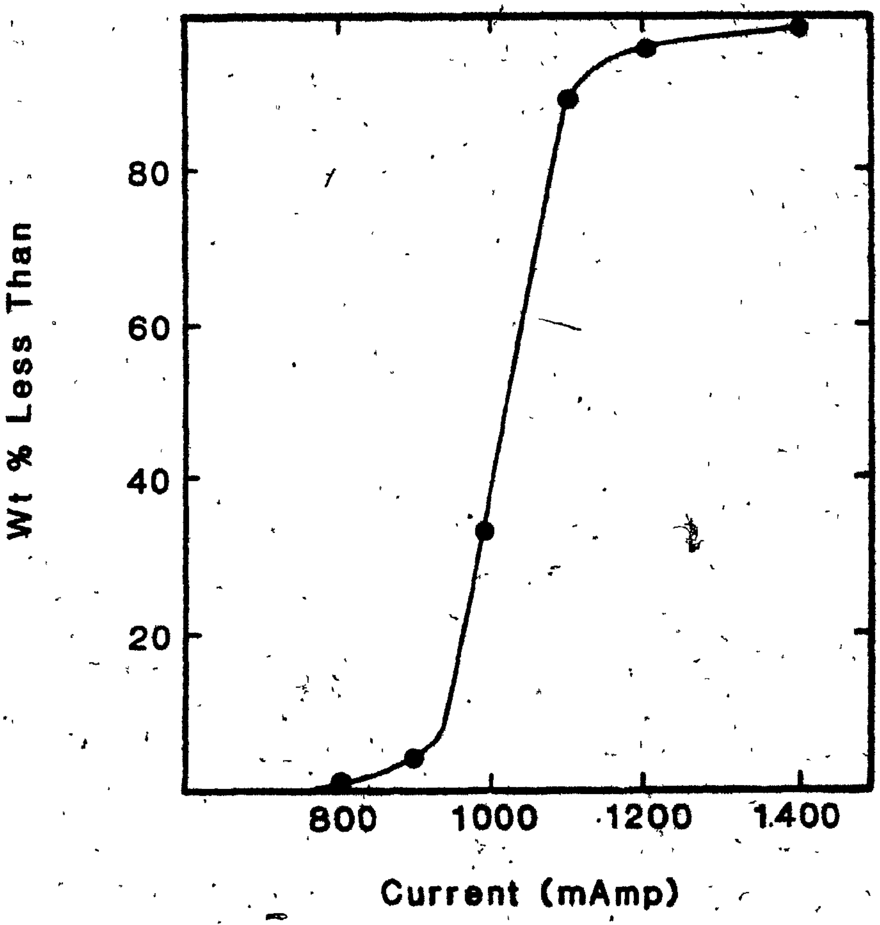

38 Magnetic susceptibility profile of cleaned sphalerite sample. Measured on Frantz isodynamic separator at side slope=20°.

sphalerite sample was used for two column runs, washed before each run in 0.02 M NaCN for 60 minutes.

Size analysis of the three samples is shown in Figure 39 (see section 4.2.6 for technique).

4.2.5. Experimental Technique

Three experimental runs, with four to seven tests per run, are reported. Runs 7 and 8 were conducted with sphalerite. Tests 9A and 9B were conducted with galena, and tests 9C to 9G with galena and silica.

On the day of each run a drift-flux analysis was performed to determine d_b and u_b as a function of v_g. For each run 6 mg/L of Dowfroth 250C was added to both feed water and wash water. Sodium ethyl xanthate was used for all three runs (sphalerite being activated first with copper sulfate). The reagent additions and the operating flowrates for the three runs are summarized in Tables 8A and B.

The experimental procedure was straight forward. Upon completion of reagent conditioning, feed and wash water flows to the column were started and underflow and air rates were set. After reaching steady state (3 to 5 minutes) concentrate and tailings samples were collected for 3 minutes. This procedure was repeated for the remaining tests.

The objectives of runs 7 and 8 and tests 9A and B were: 1. to measure the effect of particle size upon collection, and 2. to measure the effect of gas rate upon particle collection. These tests were run as described.

The objective of run 9 was to measure the effect of

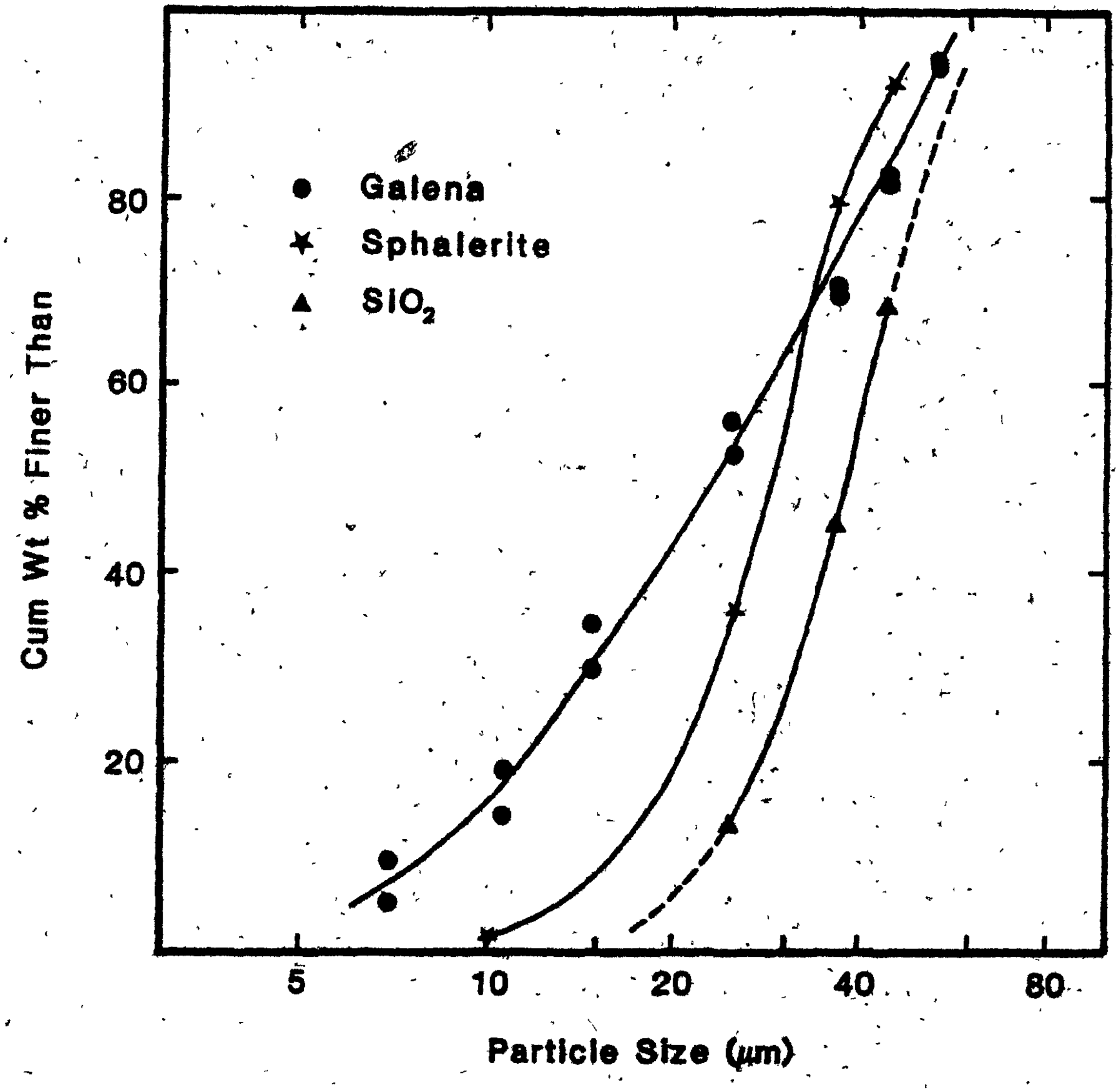

39 Particle size distribution for galena, sphalerite and silica.

Table 8A

Reagent Additions and Flowrates for Laboratory Column Runs 7 and 8

	Run 7	Run 8
Material:	300g ZnS	240g ZnS
Frother:	6 mg/L Dowfroth 250C	
Surface Cleaning:	15 min in 1L 0.02N NaCN; filter	
Activation:	15 min in 1L 0.010% $CuSO_4$; filter	
Collector:	0.0133 mg/g NaEtX	0.0420 mg/g NaEtX
	(10 min conditioning in 45L)	
pH	natural (7)	
Temperature	17°C	23°C

Test #	Q_F	Q_W	Q_T	Q_C	Q_g*	Q_F/Q_T^2	ϕ_s* Ave.
	(cm^3/min)					(x10^4)	(x100%)
7B	562	1215	1481	296	353	2.6	0.028
7C	612	1186	1246	552	225	3.9	0.034
7D	581	1186	1387	380	61	3.0	0.031
7E	598	1205	1387	416	560	3.1	0.028
8A	654	1100	1331	423	353	3.7	0.039
8C	556	1081	1150	487	225	4.2	0.040
8D	588	1091	1160	519	61	4.4	0.047
8E	604	1081	1272	413	353	3.7	0.036
8F	647	1100	1217	530	560	4.4	0.038

* Average between sparger and feed point

Table 8B

Reagent Additions and Flowrates for Laboratory Column Run 9

Galena Conditioning

Feed weight:	550g
Frother:	6 mg/L Dowfroth 250C
Collector:	0.0293 mg/g NaEtX (10 min conditioning in 45 L)
pH:	natural
Temperature:	23°C

Test #	Q_F (cm³/min)	Q_W (cm³/min)	Q_T (cm³/min)	Q_C (cm³/min)	Q_g* (cm³/min)	Q_F/Q_T^2 ($\times 10^4$)	ϕ_s* Ave. (x100%)
9A	738	1167	1509	396	225	3.3	0.047
9B	750	1167	1508	409	225	3.3	0.047
9C	773	1157	1517	413	225	3.3	0.43
9D	755	1157	1504	408	225	3.3	0.92
9E	759	1157	1506	410	224	3.3	1.76
9F	772	1148	1513	407	224	3.3	3.03
9G	757	1148	1512	393	223	3.3	3.35

* Average between sparger and feed point

solids concentration. In tests 9A and B, galena alone was floated. For subsequent tests, silica was added to the feed tank before each test, gradually increasing the slurry density. The advantage of this method for controlling solids content of the slurry is that the concentration of floatable species remains low, and thus prevents the condition of full bubble load and, hence, hindered flotation.

4.2.6. Test Product Analysis

Each test product was weighed, filtered, dried and weighed again, to provide mass flow rates of liquid and solids. Size analysis of the sphalerite products was obtained by hand sieving in methanol, using 44, 37 and 25 μm sieves. Size analysis of the galena products from tests 9A and 9B was by: a) microsieving in methanol at 74, 53, 44, 37 and 25 μm, and b) sedigraph analysis in methanol of the -25 μm fraction.

The unsized products from tests 9C to 9G, containing galena and silica, were assayed for lead content by atomic absorption. The samples were digested in two steps: in 30 mls HCl (boiled almost dry), then in 10 mls HNO_3 (boiled dry).

4.2.7. Data Analysis

A fractional collection recovery R_K of a size fraction was determined from the raw data. Of more interest is the rate constant k and collection efficiency E_K. The rate constant is usually measured by collecting concentrate over a period of time in a batch test. This is not possible in a single continuous test. However, it is feasible to estimate rate constants from a column test if a relatively pure mineral sample and a narrow size range is employed. The procedure employed here was as follows:

The recovery and mean residence time of a particular size class was measured. If plug flow was assumed then the rate constant could be estimated from the application of equation 2.5. However, since the dispersion coefficient of the laboratory column was known, it was possible to account for mixing. For a given size fraction, N_p ($= D_p u_{pi}/L$) was estimated and, together with R_K, was used to iteratively calculate $k\tau_p$ by equation 2.10. Knowing $k\tau_p$ and τ_p, gave k. (From Table 7, $D_\ell = 18$ cm^2/s at $u_\ell = 2$ cm/s (which is typical u_ℓ in the column tests) and $v_g = 0.28$ cm/s. It is shown later that $D_p = D_\ell$. For other gas rates it was assumed that

$$D_p = 18 \left[\frac{v_g}{0.28}\right]^{0.3} \text{cm}^2/\text{s}$$

(see section 2.1.1).)

Knowing k, v_g and d_b, E_K is then given by equation 2.4.

CHAPTER 5

EXPERIMENTAL RESULTS

5.1 Plant Columns: Mixing in Collection Zone

5.1.1 Liquid Dispersion

The fluorescein measurements for the 0.45 and 0.9 m columns are presented in Figure 40. Concentration of dye in the feed is also shown, indicating that a small amount of dye from the concentrate and/or tailings streams was recirculated from the subsequent flotation stages to the feed of the column being tested. As shown in Figure 40, the recycled quantity is minimal and can be safely ignored. The tailings data, normalized and fitted to the dispersion model with the procedure described in section 4.1.2, is shown in Figure 41, and the fitted parameters are listed in Table 9. In both cases the dispersion model fit is good, an indication that the Laplace solution to the open ended dispersion model is adequate to describe mixing in large flotation columns.

The flotation column dispersion coefficients are compared with previously published data on large counter-current bubble

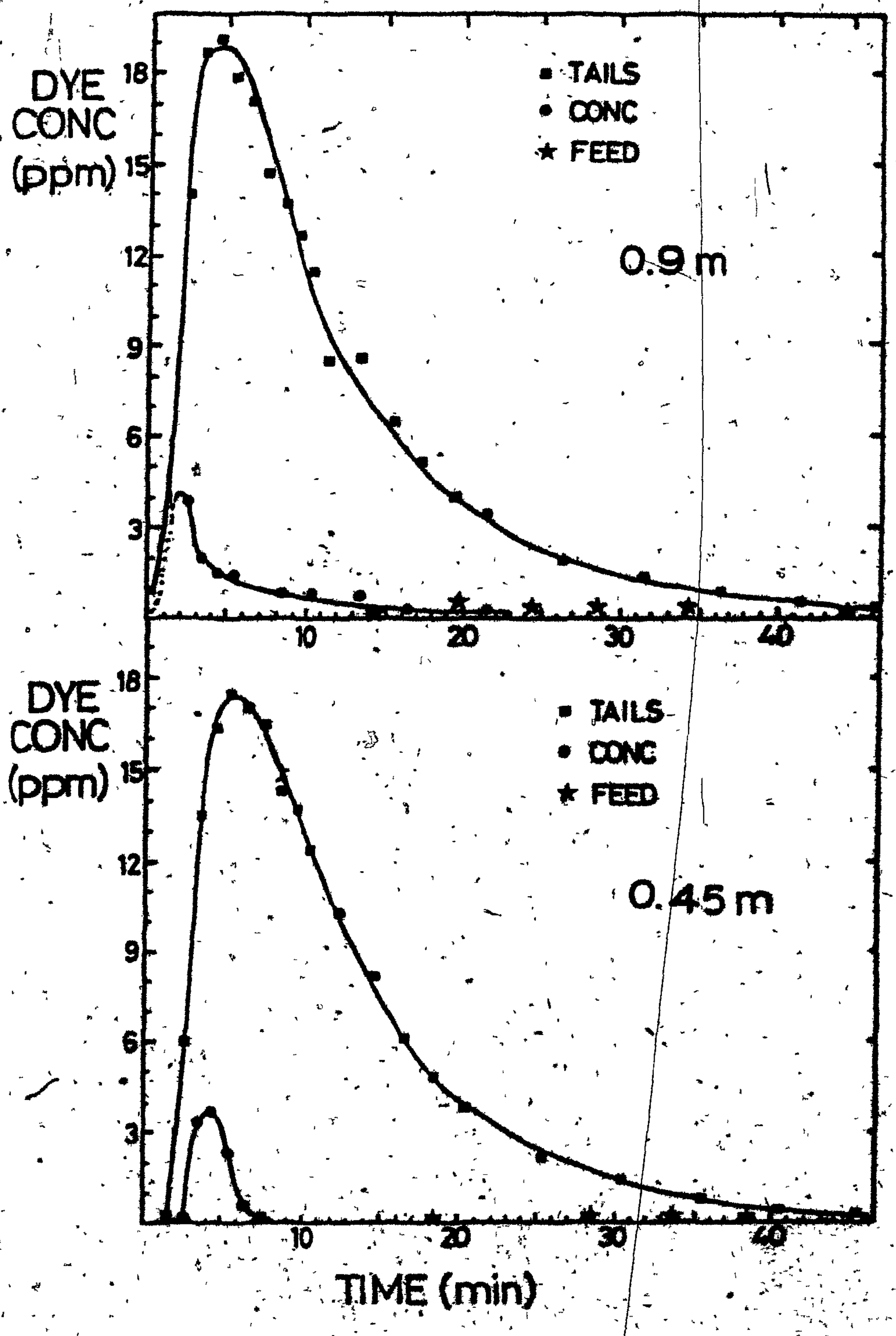

40 Dye concentration versus time for the tailings, concentrate and feed streams of the plant columns.

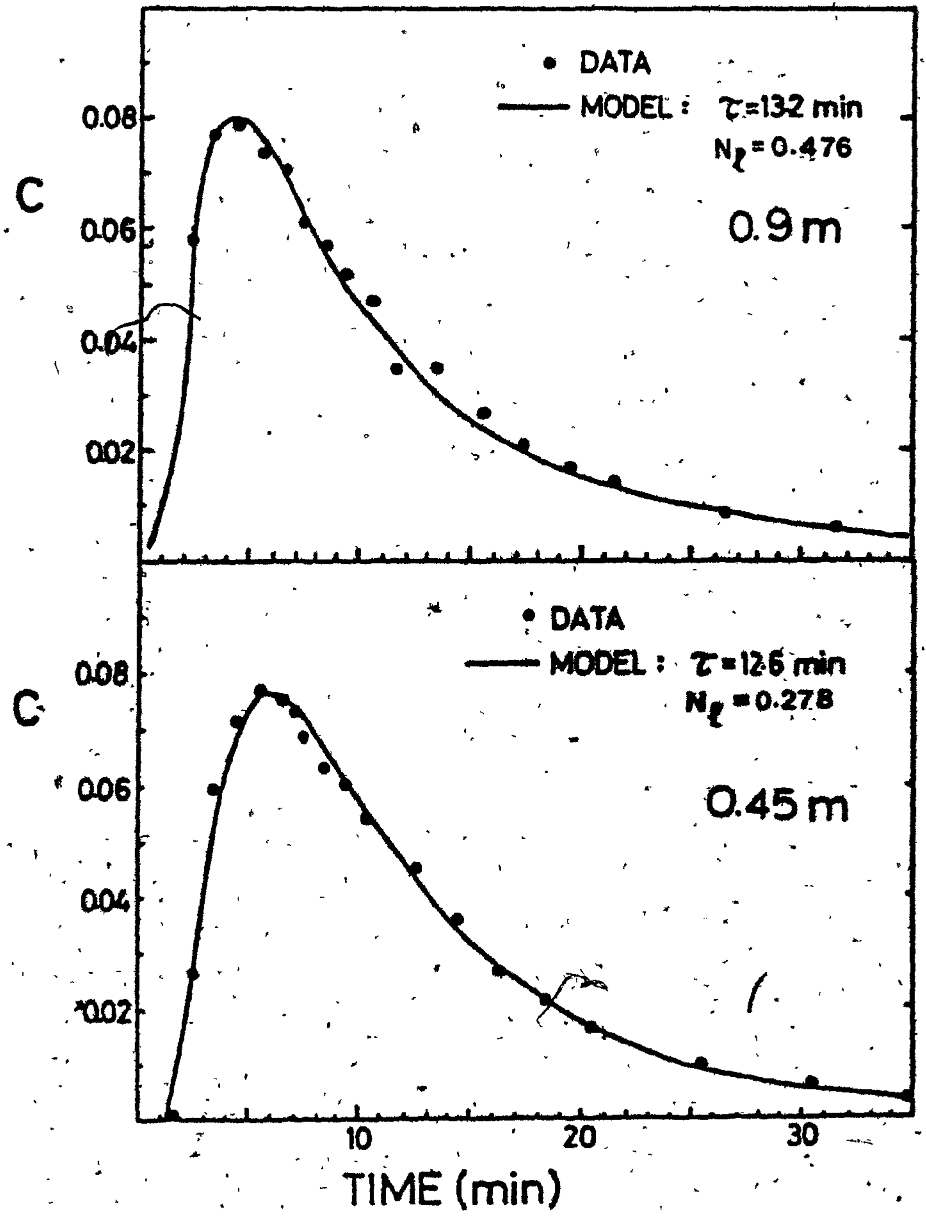

41 Liquid RTD's (normalized) for the collection zone of the plant columns.

Table 9

Liquid Dispersion Parameters

	0.45 meter	0.9 meter
N_ℓ, fitted	0.278	0.476
D_ℓ, fitted (m^2/s)	0.033	0.060
τ_ℓ, fitted (min)	12.6	13.2
τ_ℓ, estimated from L/u_ℓ (min)	12.5	14.7
s, fitted	0.16	0.11
$s_{opt.}$ †	0.17	0.23
$s\tau$ †	2.0	1.5

† See Section 4.1.2

columns in Figure 42. The radial dimension of the square sectioned column is characterized by equivalent diameter (0.52 and 1.03 m). The interval-bars for the Magnussen (25) data reflect that his measured dispersion coefficients were average values obtained over a wide range of superficial gas velocity (1 to 10 cm/s). Gas velocities in the flotation columns were 1.4 and 1.8 cm/s, so it would be expected that the dispersion coefficients of the flotation columns would fall at the lower end of the Magnussen data range. This is the case. Included in Figure 42 is the data of Rice et al (18,19) for column diameters from 0.1 to 0.3 m. Their data have been averaged over gas velocities from 1.0 to 3.3 cm/s.

If the data at low superficial gas velocities are considered, it appears that $k = 1$ for large columns, neglecting the effect of v_g. For flotation columns with $d_c > 0.2$ m and operating at gas velocities between 1 and 3 cm/s (as is typical) the dispersion coefficient is approximated by:

$$D_\ell = 0.063\, d_c \, m^2/s \qquad (5.1)$$

where d_c is the equivalent column diameter, in meters.

5.1.2 Solids Dispersion

The manganese assays for the tailings stream of the 0.45 m column are given in Table 10. The assays are corrected for background manganese content. The ratio of total background Mn to total tracer Mn measured over the duration of the test,

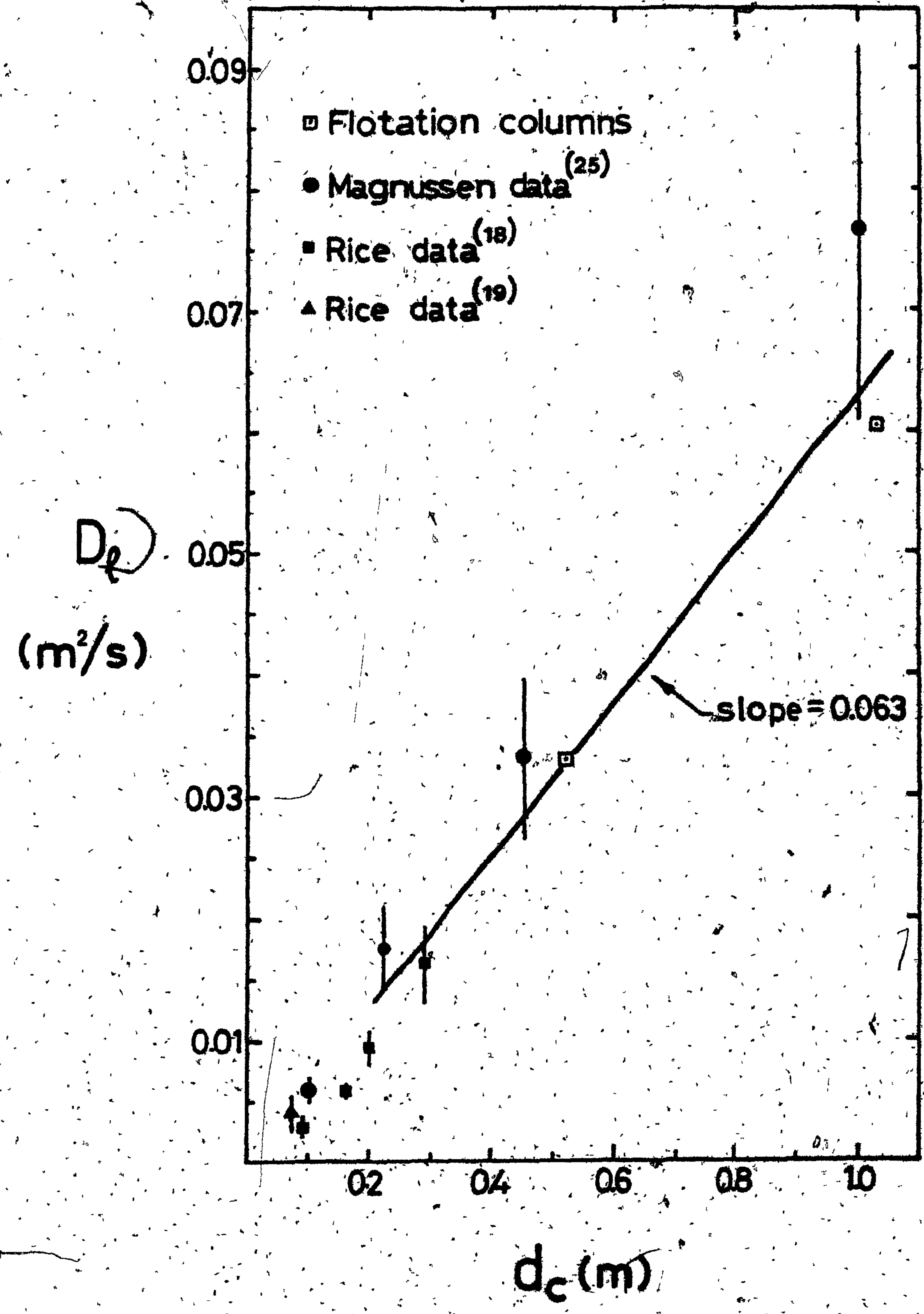

42 Column diameter effect on axial dispersion coefficient D_ℓ.

Table 10

Manganese Assays for Tailings Samples of 0.45 meter column

Mn Assays (ppm) are corrected for background

Time	Size Fraction				
(Min)	-400 mesh	+400 -270mesh	+270 -200mesh	+200 -150mesh	+150 -100mesh
Background	486	380	313	500	490
1	111	45	270	394	176
3	1617	5344	10910	18500	13020
5	1871	5569	11400	16300	10543
7	1778	5372	10080	14180	6890
10	1098	2745	5880	5610	2092
16	434	1388	2370	1890	620
20	255	559	798	400	161
(Total Background Mn) / (Total Tracer Mn)	0.56	0.15	0.06	0.08	0.12

also shown in Table 10, is between 0.06 and 0.15 for the four size fractions larger than 400 mesh. However, the ratio is 0.56 for the -400 mesh fraction; this fraction is not considered further.

The measured and fitted normalized data for MnO_2 in the 0.45 m column are given in Figure 43 and the fitted mixing parameters are summarized in Table 11. The error bars of Figure 43 represent ± two standard deviations, which accounts for analytical error (of ~2% relative standard deviation), subtraction of background Mn, and sampling error estimated by the method of Gy$^{(84)}$. It is evident that the dispersion coefficient of the particles does not vary significantly with particle size and is similar to that of the liquid; D_p average = 0.035 m^2/s, compared with D_ℓ = 0.033 m^2/s. Then, for large columns at low air rates

$$D_p = D_\ell \approx 0.063\ d_c m^2/s \qquad (5.2)$$

The predicted mean residence times of the four size classes, using equations 2.11 and 2.12, are calculated in Table 12, and the predicted and measured τ_p vs d_p are plotted in Figure 44. Agreement between measured and predicted values is good.

5.1.3 Flow Split

A material balance of the fluorescein split and hence water split between the tailings stream and the concentrate stream can be obtained with the use of the flowrates (Table 6)

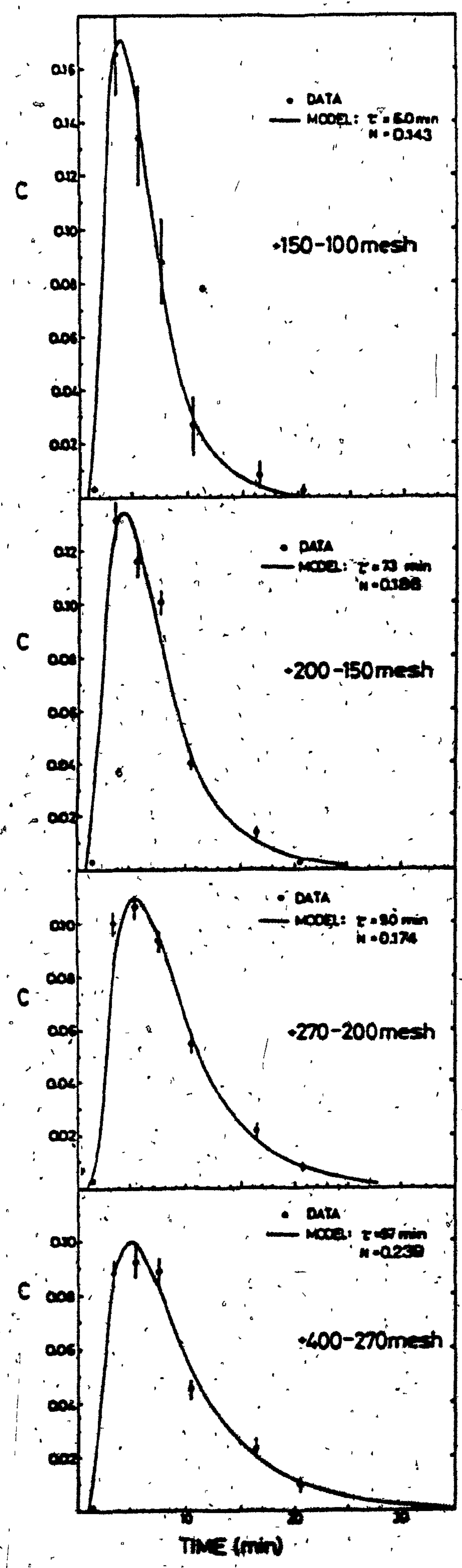

43

Solids RTD's (normalized) for the collection zone of the 0.45 m column.

Table 11

Fitted Dispersion Parameters for MnO_2 Particles in 0.45 Meter Column

Size Interval (mesh)	d_p* (μm)	τ_p (min)	N_p	D_p (m^2/s)	RMS Error ($x10^2$)
+400-270	44	9.7	0.239	0.037	0.31
+270-200	63	9.0	0.174	0.029	0.32
+200-150	88	7.3	0.186	0.038	0.43
+150-100	125	6.0	0.143	0.036	0.38
Solids Average				0.035	0.36
Water		12.6	0.278	0.033	0.13

*Geometric mean of mesh interval

d_p (μm)	s, fitted	$s_{opt.}$†	s_τ†
44	0.19	0.18	1.8
63	0.20	0.20	1.8
88	0.20	0.25	1.4
125	0.29	0.28	1.8

†See Section 4.1.2

Table 12

Prediction of τ_p for 0.45 Meter Column

Conditions:

ρ_p = 5.19 g/cm^3

μ = 0.013 poise, (9° C ± 2°)

ϕ_s = 0.006 (~ 2.5 wt% solids)

u_ℓ = 1.3 cm/s

τ_ℓ = 12.6 min

d_p (μm)	u_p† (cm/s)	$\frac{u_\ell}{(u_\ell + u_p)}$	τ_p (min) Pred.	Meas.
44	0.32	.80	10.1	9.7
63	0.62	.67	8.4	9.0
88	1.13	.53	6.7	7.3
125	2.05	.38	4.8	6.0

† from equations 2.12 & 2.13

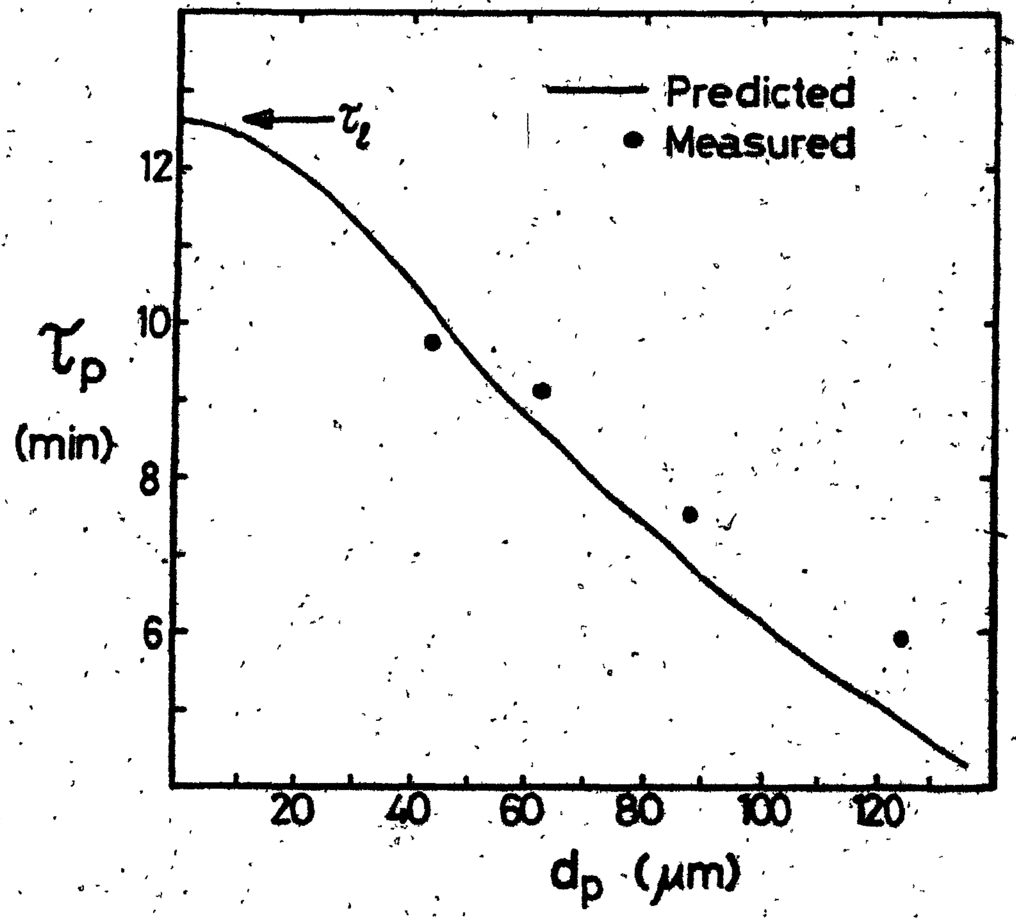

44 Particle size effect on mean residence time for 0.45 m column test. Test conditions and calculations of predicted τ_p are given in Table 12.

and RTD curves (Figure 40). In the 0.45 m column, 99.8% of the measured fluorescein reported to the tailings stream and in the 0.9 m column, 99.2% reported to the tailings. (In both cases, approximately 18% of the dye was unaccounted for and is assumed to have been adsorbed by solids.) From a flow balance it was determined that the concentrate water from the 0.45 m column was composed of 5% original feed water and 95% wash water, while concentrate water from the 0.9 m column was 8% original feed water and 92% wash water. The washwater is evidently very effective in preventing feed water, and thus entrained gangue particles, from reaching the concentrate.

5.2 Laboratory Column: Particle Collection

5.2.1 Drift-Flux Analysis

The gas holdup measurements for runs 7, 8 and 9 are presented in Figure 45 in terms of the drift-flux groupings, equation 4.17. A value m = 3.1 (equation 4.16) is suitable for the range of Re_b covered in the tests. Table 13 summarizes the results of the drift flux analysis. A correlation between the volumetric mean bubble diameter $\bar{d}_b$ and Q_g is obtained from the 8 sets of data in Table 13 when log Q_g is compared to log $\bar{d}_b$. The result is

$$\bar{d}_b = 0.0257\ Q_g^{0.25}\ \text{cm} \tag{5.3}$$

where Q_g is in cm^3/min. The correlation coefficient is 0.995. (Equation 5.3 is valid for $0.0093 \le \mu \le 0.0113$ poise and

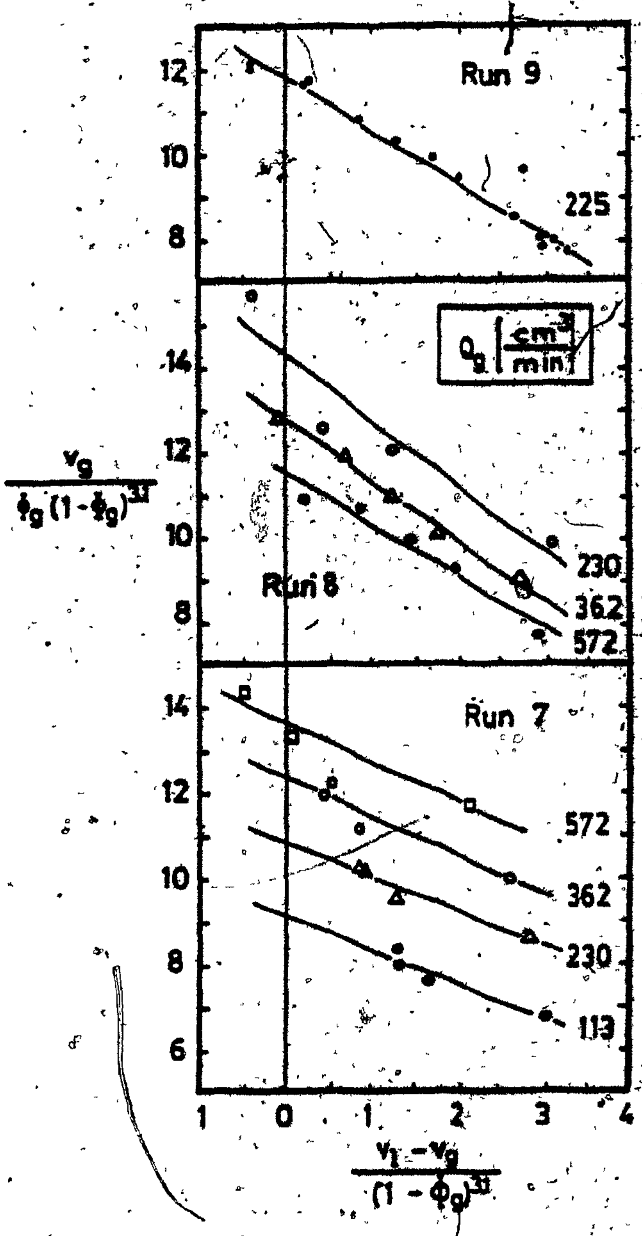

45 Drift-flux analysis for runs 7, 8 and 9. Q_g is in L/min, and v_l and v_g are in cm/s.

Table 13

Drift Flux Analysis of Runs 7, 8 and 9

$m = 3.1$

Run #	Q_g (cm^3/min)	$K_o\ U_T$ (cm/s)	C_o	U_T (cm/s)	$\bar{d}_b$† (cm)	Correlation Coefficient
7	113	9.19	0.82	9.48	0.0845	0.95
	230	10.91	0.82	11.24	0.1000	0.97
	362	12.42	0.93	12.80	0.1150	0.95
	572	13.71	0.93	14.13	0.1280	0.98
8	230	11.46	1.23	11.82	0.0995	0.97
	362	12.74	1.45	13.13	0.1120	0.99
	572	14.17	1.53	14.60	0.1260	0.94
9	225	11.86	1.24	12.23	0.1030	0.99

Run 7	$C_o = 0.44 + 0.178 \log Q_g$	0.85
Run 8	$C_o = -0.583 + 0.775 \log Q_g$	0.98

† from equation 2.12

Dowfroth 250 C at 6 mg/L.) Then, the area mean bubble diameter is given by

$$\overline{d}_{bA} \cong 0.0239\, Q_g^{0.25} \tag{5.4}$$

The drift-flux results can be used to determine the bubble conditions prevailing during each test, including ϕ_g, $\overline{d}_{bA}$, and u_s. These are shown in Table 14. For $\overline{d}_b$, bubble rise velocity u_b is given by u_s. Since the relationship between d_b and u_b is approximately linear over the region of concern here, it is reasonable to let $u_b = 0.93\, u_s$ for $\overline{d}_{bA}$.

All the operating conditions for the laboratory column runs are summarized in Tables 8 and 14.

5.2.2 Flotation Tests

Tests 9A and 9B: Galena

Size analysis of concentrates and tailings from tests 9A and B are given in Table 15, along with recovery values for each size fraction and the back-calculated feed size distribution. Table 16 presents the calculated rate constants and collection efficiencies, and E_K vs d_p is summarized in Figure 46. The peak in E_K (and the peak in recovery) occurs at approximately 30 μm.

Run 9: Galena and Silica

The results of the galena-silica tests are given in Table 17 and Figure 47. The most notable result is the

Table 14

Bubble Conditions of Runs 7, 8, and 9

Test #	$\overline{d}_b$ (1) (cm)	$\overline{d}_{bA}$ (2) (cm)	ϕ_g (3) (x100%)	u_s (4) (cm/s)
7B	0.1126	0.1047	5.95	10.92
7C	0.1002	0.0932	3.90	10.28
7D	0.0713	0.0663	1.51	7.92
7E	0.1270	0.1181	9.00	11.27
8A	0.1126	0.1047	5.92	10.73
8C	0.1002	0.0932	3.81	10.33
8D	0.0713	0.0663	1.33	8.38
8E	0.1126	0.1047	5.82	10.79
8F	0.1270	0.1181	8.80	11.20
9A → 9G	0.1030	0.0958	4.03	10.41

(1) from equation 5.2
(2) from equation 5.3
(3) from equation 4.15
(4) from equation 4.13

Table 15

Size Analysis and Recoveries
Tests 9A and B

Particle Size Fraction (μm)	d_p average (μm)	Size Dist (wt%) Conc	Tails	Feed	Wt% Rec'y
		9A			
+53-74	63	4.88	8.54	6.40	44.7
+44-53	48	11.86	11.45	11.69	59.5
+37-44	40	14.51	7.11	11.45	74.3
+25-37	30	18.92	6.66	13.85	80.1
+15-25	19	27.90	12.59	21.56	75.8
+11-15	13	12.71	15.90	14.03	53.1
+ 7-11	9	5.98	17.88	10.84	32.3
- 7	5	3.24	19.86	10.12	18.8
			Total Rec'y	=	58.6
		9B			
+53-74	63	4.65	7.98	5.94	47.9
+44-53	48	15.41	9.54	13.13	71.8
+37-44	40	14.29	6.75	11.36	77.0
+25-37	30	22.37	7.00	16.41	83.5
+15-25	19	24.89	19.59	22.83	66.7
+11-15	13	11.26	22.69	15.69	43.9
+ 7-11	9	4.97	15.12	8.91	34.1
-7	5	2.16	11.34	5.72	23.1
			Total Rec'y	=	61.2

Table 16

Rate Constants and Collection Efficiencies
Tests 9A and B

d_p (μm)	u_p+u_ℓ (1) (cm/s)	N_p (2)	$k\tau_p$ (3)	τ_p (s)	k (s^{-1})	E_K (4) (%)
			9A			
63	3.59	0.043	0.61	33	0.0182	0.36
48	3.09	0.050	0.95	39	0.0244	0.48
40	2.86	0.054	1.45	42	0.0345	0.67
30	2.62	0.059	1.76	46	0.0384	0.75
19	2.43	0.064	1.54	49	0.0312	0.61
13	2.36	0.066	0.80	51	0.0157	0.31
9	2.32	0.067	0.40	52	0.0077	0.15
5	2.30	0.068	0.21	52	0.0041	0.08
			9B			
63	3.59	0.043	0.67	33	.0200	0.39
48	3.09	0.050	1.34	39	.0345	0.67
40	2.86	0.054	1.58	42	.0376	0.73
30	2.62	0.059	1.98	46	.0432	0.84
19	2.43	0.064	1.18	49	.0239	0.47
13	2.36	0.066	0.60	51	.0118	0.23
9	2.32	0.067	0.43	52	.0083	0.16
5	2.30	0.068	0.27	52	.0052	0.10

(1) u_ℓ = 2.29 cm/s and u_p from equation 2.12

(2) $N_p = D_p/u_p^2\tau_p$; D_p = 18.5

(3) from equation 2.10

(4) from equation 2.4 using $\overline{d}_{bA}$

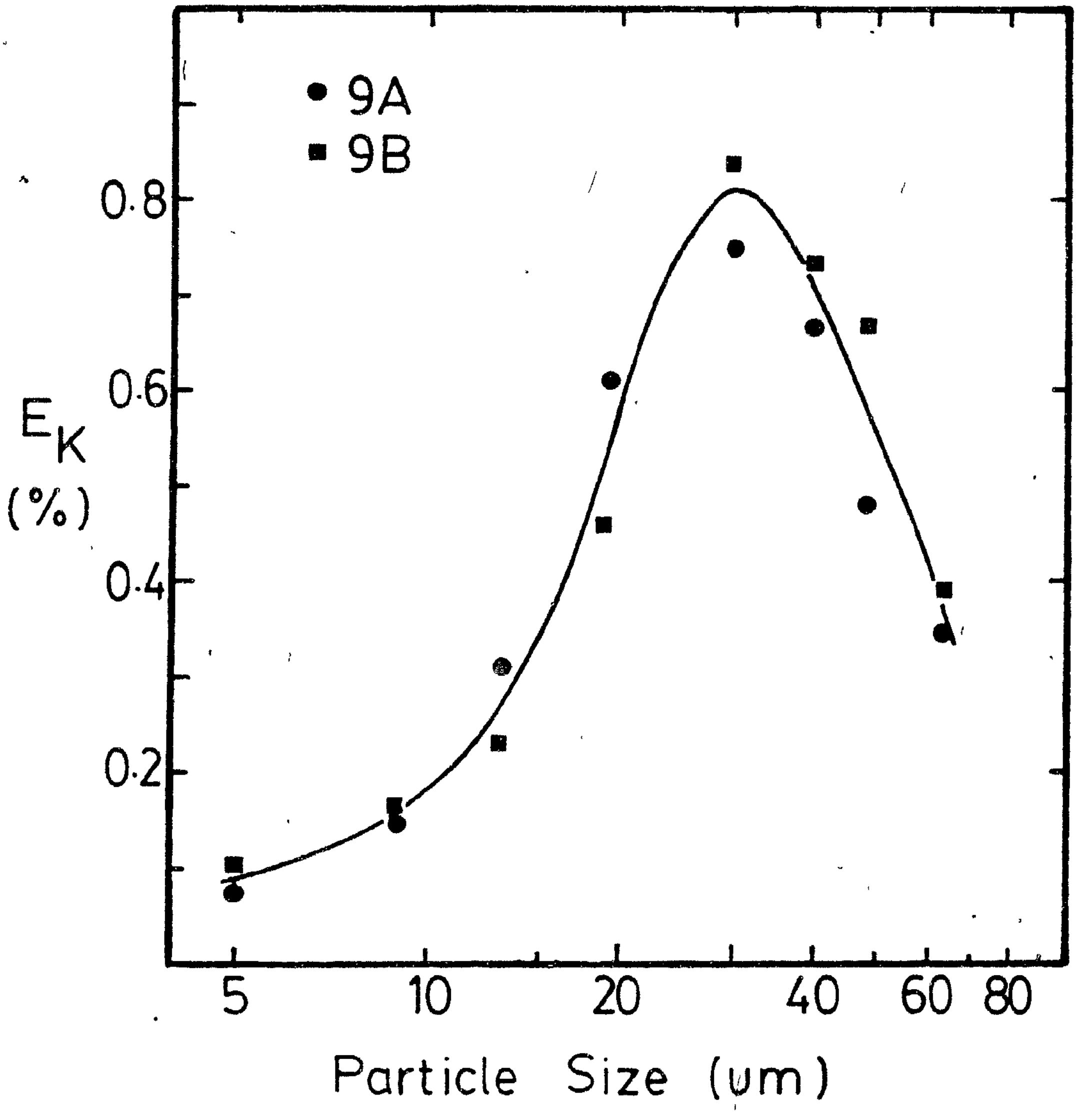

46 Column tests 9A and 9B; E_K versus d_p.

Table 17

Galena - Silica Column Tests
9A - G

Sample	%PbS	$\%SiO_2$	% Recovery			Ave. Vol % Solids
			Total Wt.	PbS	SiO_2	
C Conc	98.3	1.68	21.9	72.3	0.53	0.43
C Tails	10.6	89.4				
D Conc	94.2	5.78	13.5	76.7	0.93	0.92
D Tails	4.46	95.5				
E Conc	88.8	11.2	7.89	79.3	0.97	1.76
E Tails	1.99	98.0				
F Conc	81.7	18.3	5.24	79.1	1.0	3.03
F Tails	1.20	98.8				
G Conc	75.3	24.7	4.49	81.4	1.2	3.35
G Tails	0.81	99.2				
A Conc			58.6	58.6		0.047
B Conc			61.2	61.2		0.047

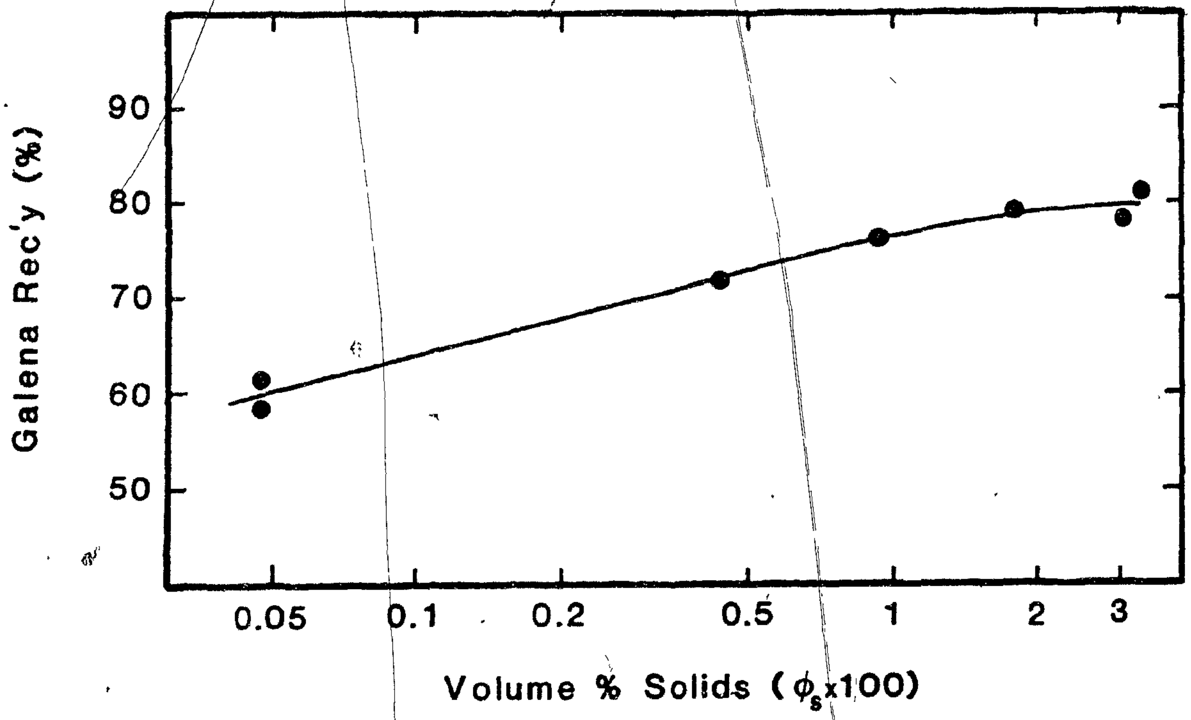

47 Column run 9; Galena recovery versus volume percent solids.

increase in galena recovery as % solids is increased; from 60% recovery at 0.047 volume % solids (0.35 weight %) to 81% recovery at 3.35 volume % solids (21.4 weight %). As well, the silica recoveries are all approximately 1%, which agrees with the measured short-circuiting of water (Figure 35). (The wide size distribution of the galena prevents measurement of rate constants from these data.)

Runs 7 and 8: Sphalerite

The results of runs 7 and 8 are summarized in Tables 18A and B and 19A and B. The weight % recoveries are given in Table 18, and the rate constants and collection efficiencies are given in Table 19. E_K vs v_g is summarized in Figure 48 and k vs v_g is summarized in Figure 49. As gas rate is increased, collection efficiency decreases, while the rate constant increases, reaching a peak for some size fractions.

Table 18A

Results: Column Run 7

Particle Size Fraction (μm)	d_p ave. (μm)	Size Dist. (wt%)			Wt% Rec'y
		Conc	Tails	Feed	
Test 7D: v_g = 0.089 cm/s					
+44	50	15.0	4.7	7.5	55.5
+37-44	40	23.0	7.6	11.9	53.9
+25-37	30	42.8	44.3	43.9	27.2
-25	20	19.2	43.5	36.7	14.6
Total					27.9
Test 7C: v_g = 0.327					
+44	50	12.9	3.3	7.9	78.2
+37-44	40	20.2	5.1	19.3	78.6
+25-37	30	49.4	35.0	41.8	56.5
-25	20	17.6	56.7	38.0	22.2
Total					47.9
Test 7B: v_g = 0.513					
+44	50	12.8	4.5	8.6	74.0
+37-44	40	17.4	5.3	11.3	76.6
+25-37	30	43.5	39.8	41.7	52.2
-25	20	26.3	50.5	38.4	34.2
Total					49.9
Test 7E: v_g = 0.814					
+44	50	11.9	3.5	8.1	80.6
+37-44	40	16.3	6.0	11.7	76.8
+25-37	30	49.9	35.4	43.3	63.1
-25	20	21.8	55.2	36.9	32.4
Total					54.8

Table 18B

Results: Column Run 8

Particle Size Fraction (μm)	d_p Ave. (μm)	Size Dist. (Wt%) Conc	Tails	Feed	Wt% Rec'y
		Test 8D: v_g = 0.089 cm/s			
+44	50	12.7	3.8	7.7	72.5
+37-44	40	14.6	7.5	10.6	60.3
+25-37	30	46.1	40.6	43.0	46.9
-25	20	26.6	48.2	38.7	30.1
Total					43.8
		Test 8C: v_g = 0.327			
+44	50	9.1	2.8	6.9	86.1
+37-44	40	13.1	4.7	10.3	84.0
+25-37	30	40.1	32.2	37.3	70.2
-25	20	37.7	60.3	45.5	54.1
Total					65.4
		Test 8E: v_g = 0.513			
+44	50	6.7	3.2	5.7	81.8
+37-44	40	12.2	5.1	9.9	83.7
+25-37	30	52.1	41.0	48.5	73.2
-25	20	29.0	50.7	36.0	55.1
Total					68.2
		Test 8A: v_g = 0.513			
+44	50	9.7	3.2	7.7	87.2
+37-44	40	12.7	5.5	10.4	83.8
+25-37	30	41.9	34.8	39.8	73.0
-25	20	35.7	56.5	42.1	58.7
Total					69.2
		Test 8F: v_g = 0.814			
+44	50	8.2	4.3	7.2	84.1
+37-44	40	13.3	4.8	11.0	88.5
+25-37	30	40.9	36.1	39.6	76.0
-25	20	37.6	54.8	42.1	65.7
Total					73.6

Table 19A

Rate Constants and Collection Efficiencies
Column Run 7

d_p (μm)	$k\tau_p$	τ_p (s)	k (s^{-1})	E_K (%)
		Test 7D: v_g = 0.089 cm/s		
50	0.84	50	0.0169	0.84
40	0.80	53	0.0151	0.75
30	0.32	55	0.0058	0.29
20	0.16	57	0.0028	0.14
		Test 7C v_g = 0.327		
50	1.68	53	0.0314	0.60
40	1.70	57	0.0300	0.57
30	0.88	59	0.0149	0.28
20	0.26	61	0.0042	0.079
		Test 7B v_g = 0.513		
50	1.46	45	0.0322	0.44
40	1.59	48	0.0334	0.45
30	0.78	49	0.0157	0.21
20	0.43	51	0.0085	0.12
		Test 7E v_g = 0.814		
50	1.83	47	0.0393	0.38
40	1.62	49	0.0330	0.32
30	1.07	51	0.0210	0.20
20	0.40	52	0.0077	0.074

Table 19B

Rate Constants and Collection Efficiencies
Column Run 8

d_p (μm)	$k\tau_p$	τ_p (s)	k (s^{-1})	E_K (%)
		Test 8D:	v_g = 0.089 cm/s	
50	1.37	56	0.0244	1.22
40	0.97	60	0.0161	0.80
30	0.66	64	0.0102	0.51
20	0.37	67	0.0054	0.27
		Test 8C:	v_g = 0.327	
50	2.23	55	0.0403	0.77
40	2.05	59	0.0345	0.65
30	1.31	63	0.0207	0.39
20	0.82	66	0.0124	0.24
		Test 8E:	v_g = 0.513	
50	1.89	50	0.0377	0.51
40	2.05	53	0.0383	0.52
30	1.44	57	0.0255	0.35
20	0.85	59	0.0145	0.20
		Test 8A:	v_g = 0.513	
50	2.33	48	0.0483	0.66
40	2.04	51	0.0397	0.54
30	1.43	54	0.0264	0.36
20	0.94	56	0.0167	0.23
		Test 8F:	v_g = 0.814	
50	2.11	51	0.0417	0.40
40	2.54	54	0.0470	0.45
30	1.60	57	0.0280	0.27
20	1.19	59	0.0200	0.19

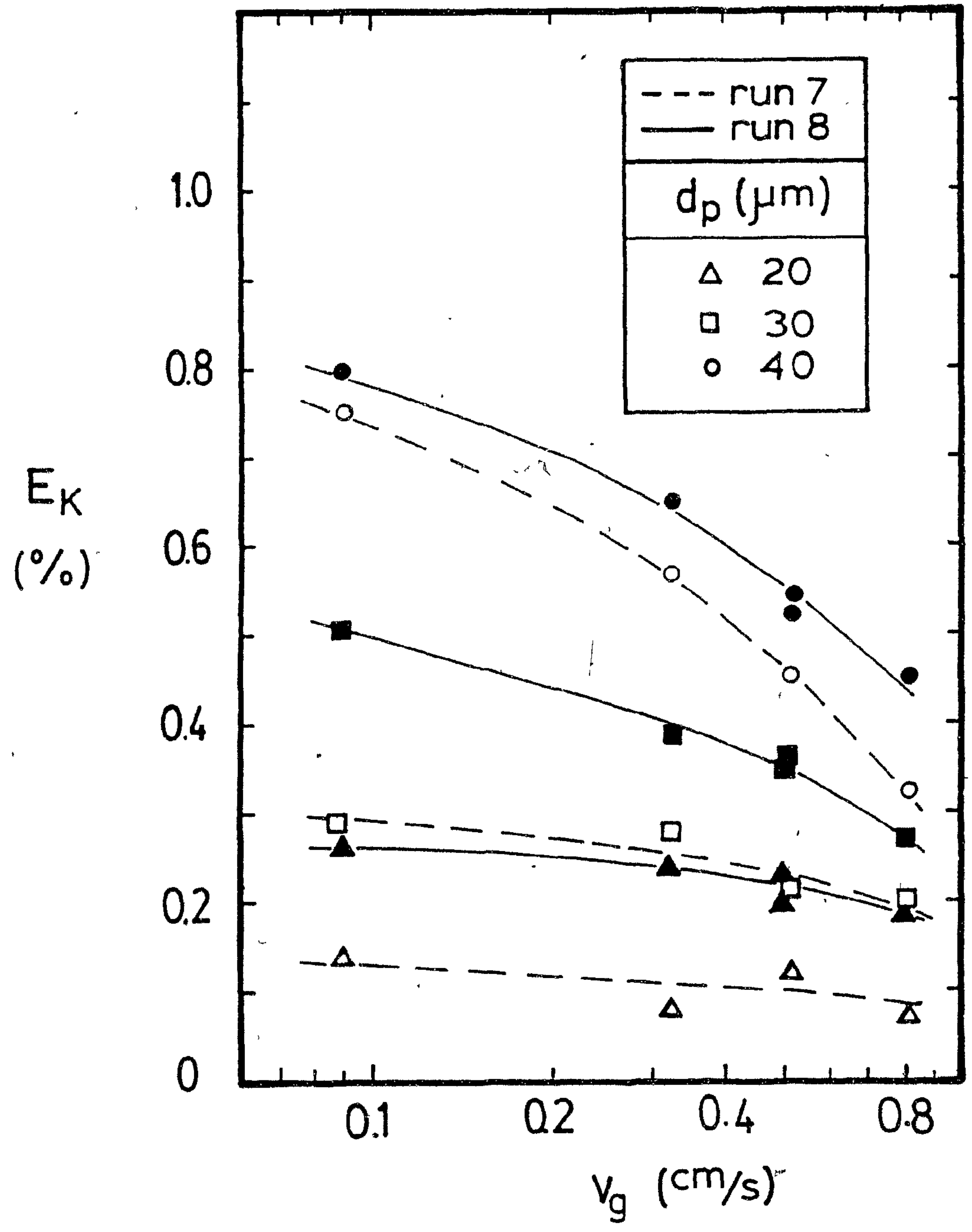

48 Column runs 7 and 8; E_K versus superficial gas velocity.

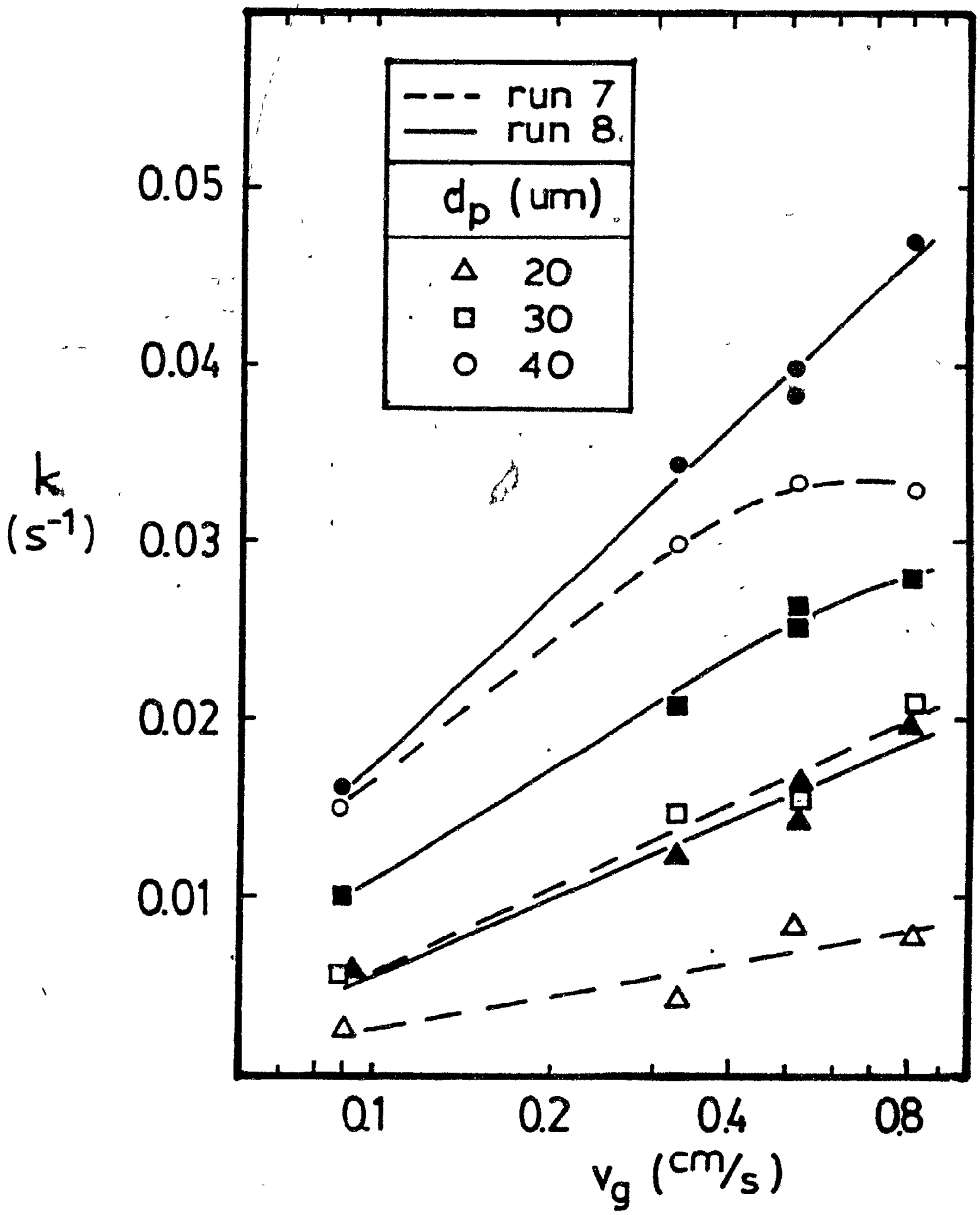

49 Column runs 7 and 8; Rate constant versus gas velocity.

CHAPTER 6

TESTING THE FLOTATION MODEL

6.1 Particle Size and Induction Time

Galena: Tests 9A and B It is shown in Chapter 3 that a peak in particle size vs collection efficiency data will be observed by the collection model when it is assumed that induction time is constant with particle size. The results of the galena flotation tests, 9A and 9B, also show a distinct peak in the d_p vs k (or E_K) data. Since all the parameters for the model have been measured, except induction time, the assumption of a constant induction time can be tested by comparing the experimental results with model predictions for different induction times. This comparison is illustrated in Figure 50 for Tests 9A and B. Three values of t_i are shown: 17, 20 and 25 ms. A good fit cannot be obtained. These model calculations were performed using the average bubble diameter, $\overline{d_{bA}}$. The model result using a distributed bubble diameter and t_i = 17 ms is also shown in Figure 50. The distribution of d_{bA} is obtained assuming $\overline{d_{bA}}$ = 0.0958 cm with a relative standard deviation of 28%, and describing the distribution by

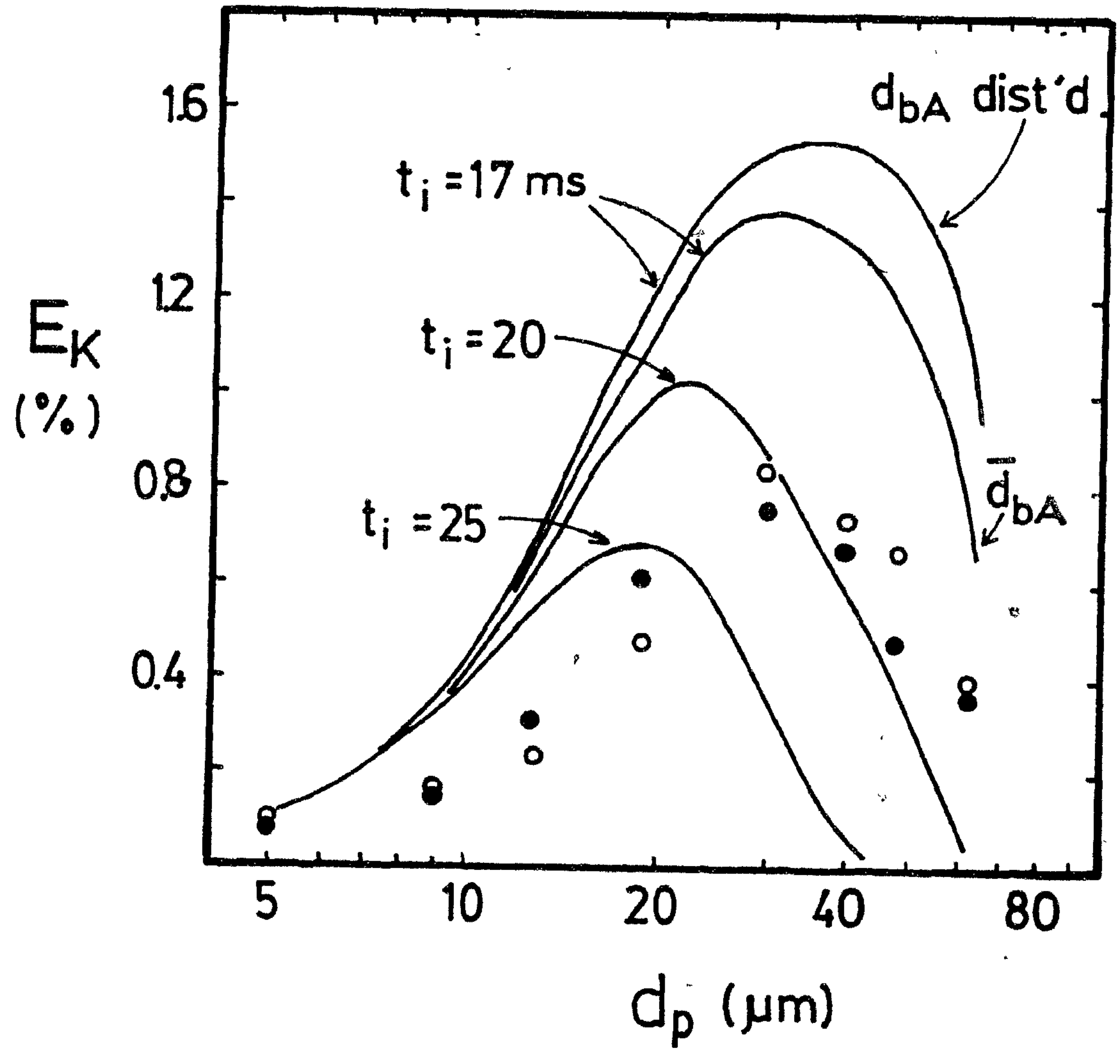

50 Flotation model fit to results of tests 9A and B, assuming $t_i \neq$ fn (d_p). For analysis with distributed bubble diameter, and t_i=17 ms, the distribution is equally split between four bubble diameters: 0.065 cm(u_b=6.6 cm/s); 0.087 cm (u_b=8.8 cm/s); 0.104 cm (u_b=10.5 cm/s); 0.127 cm (u_b=12.8 cm/s).

four values each of which represents 25% of the bubbles. The difference between using $\overline{d}_{bA}$ and using the distribution of d_{bA} is not dramatic. The remaining calculations employ $\overline{d}_{bA}$.

The induction time can be computed by comparing the measured collection efficiency to the theoretical collision efficiency. The ratio E_C (theory)/E_K (measured) is the attachment efficiency, E_A. Induction time required to attain E_A is then calculated using the program SLIDE. These computations are summarized in Table 20 for tests 9A and B, using average E_K values from Figure 46. Induction time decreases from 59 ms at 5 μm to 18.5 ms at 55 μm.

Sphalerite: Runs 7 and 8

The same method of calculating induction time can be applied to the sphalerite data of runs 7 and 8. These calculations are summarized in Tables 21A and B. Note that t_i does not vary significantly with v_g. However, the trend of decreasing t_i with increasing d_p is again observed. For run 7, average t_i is 40 ms at 20 μm and 19 ms at 50 μm, while for run 8, t_i decreases from 30 to 17 ms over the same size range.

Silica: Anfruns and Kitchener(43) Data

The results of the single bubble experiments of Anfruns and Kitchener, shown in Figure 51, provide another opportunity to fit the collection model. Using the same approach as for tests 7, 8 and 9, t_i vs d_p is computed at five bubble diameters, Table 22. It is clearly evident, again, that t_i decreases with increasing d_p. (Note that attachment efficiency is between 60 and 90%; Anfruns and Kitchener assumed E_A = 100%.)

Table 20

Induction Times for Tests 9A & B

Conditions:

$\bar{d}_{bA} = 0.0958$ cm

$u_b = 9.68$ cm/s

$\mu = 0.0093$ poise

$\rho_p = 7.5$ g/cm^3

$\phi_g = 0.04$

d_p (μm)	E_C (%) (model)	E_K (%) (Experiment)	E_A (%)$^{(1)}$	$t_i$$^{(2)}$ (ms)
5	0.104	0.09	86	59
10	0.416	0.18	43	51
15	0.931	0.34	37	36
25	2.53	0.75	30	22.6
35	5.14	0.78	15	19.8
45	9.56	0.62	6.5	19.2
55	16.7	0.47	2.8	18.5

(1) $E_A(\%) = (E_K/E_C) \times 100\%$

(2) from SLIDE

Table 21A

Induction Times for Run 7

Conditions: μ = 0.0113 poise

ρ_p = 4.1 g/cm^3

Test #	d_p (μm)	E_C(%) (model)	E_K(%) (experiment)	E_A(%)$^{(1)}$	$t_i$$^{(1)}$ (ms)
7D	$\bar{d}_{bA}$=.0663 cm	u_b=7.4cm/s	ϕ_g=1.51%,	v_g=0.089 cm/s	
	20	1.22	0.14	11.5	38.2
	30	2.74	0.29	10.6	28.5
	40	4.82	0.75	15.6	22.2
	50	7.57	0.84	11.0	21.7
7C	$\bar{d}_{bA}$=0.0932cm	u_b=9.6cm/s	ϕ_g=3.90%,	v_g=0.327 cm/s	
	20	0.86	0.079	9.1	41.6
	30	1.93	0.28	14.5	24.7
	40	3.40	0.57	16.8	19.1
	50	5.52	0.60	10.9	18.7
7B	$\bar{d}_{bA}$=.1047cm	u_b=10.2cm/s	ϕ_g=5.95%,	v_g=0.513 cm/s	
	20	0.78	0.12	15.4	37.3
	30	1.74	0.21	12.1	26.1
	40	3.06	0.45	14.7	19.2
	50	4.92	0.44	8.9	18.7
7E	$\bar{d}_{bA}$=0.1181cm	u_b=10.5cm/s	ϕ_g=9.00%,	v_g=0.814 cm/s	
	20	0.72	0.074	10.4	42.2
	30	1.60	0.20	12.5	26.8
	40	2.80	0.32	11.4	20.5
	50	4.33	0.38	8.8	18.4

(1) see Table 20

Table 21B

Induction Times for Run 8

Conditions: μ = 0.0093 poise
ρ_p = 4.1 g/cm^3

Test #	d_p (μm)	E_C(%) (model)	E_K(%) (experiment)	E_A(%)$^{(1)}$	t_i $^{(1)}$ (ms)
8D	$\bar{d}_{bA}$=0.0663cm	u_b=7.8 $\frac{cm}{s}$	ϕ_g=1.33%,	v_g=0.089 cm/s	
	20	1.37	0.27	19.7	27.7
	30	3.07	0.51	16.6	21.3
	40	5.39	0.80	14.9	18.8
	50	9.57	1.22	12.7	17.7
8C	$\bar{d}_{bA}$=0.0932cm	u_b=9.6 $\frac{cm}{s}$	ϕ_g=3.81%,	v_g=0.327 cm/s	
	20	1.00	0.24	24.0	29.0
	30	2.23	0.39	17.5	21.1
	40	3.90	0.65	16.7	17.2
	50	6.87	0.77	11.2	16.6
8E	$\bar{d}_{bA}$=0.1047cm	u_b=10.0$\frac{cm}{s}$	ϕ_g=5.82%,	v_g=0.513 cm/s	
	20	0.91	0.20	21.9	31.0
	30	2.03	0.35	17.2	21.9
	40	3.55	0.52	14.6	17.6
	50	6.10	0.51	8.4	17.3
8A	$\bar{d}_{bA}$=0.1047	u_b=10.0$\frac{cm}{s}$	ϕ_g=5.92%,	v_g=0.513 cm/s	
	20	0.91	0.23	25.2	29.4
	30	2.03	0.36	17.7	21.6
	40	3.55	0.54	15.2	17.4
	50	6.10	0.66	10.8	16.3
8F	$\bar{d}_{bA}$=0.1187	u_b=10.4$\frac{cm}{s}$	ϕ_g=8.80%,	v_g=0.814 cm/s	
	20	0.83	0.19	22.8	31.0
	30	1.85	0.27	14.6	23.1
	40	3.23	0.45	13.9	17.5
	50	5.38	0.40	7.4	17.0

(1) see Table 20

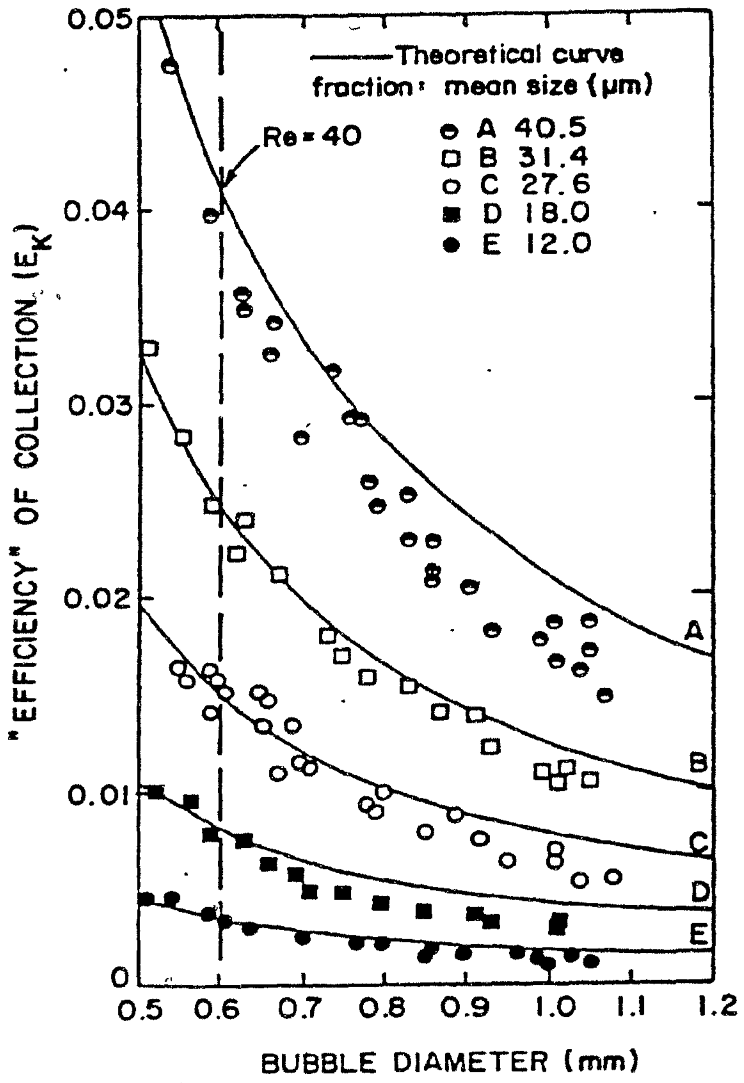

51 Experimental collection efficiencies of Anfruns and Kitchener(43) for surface-methylated silica.

Table 22

Induction Times for Data of Anfruns and Kitchener(43)

Conditions: μ=0.01 poise ρ_p=2.65 g/cm^3 u_b from Figure 13

d_b (cm)	d_p (μm)	E_C(%) (model)	E_K(%) (experiment)	E_A(%)(1)	t_i(1) (ms)
0.10	12.0	0.23	0.14	62.2	32.1
	18.0	0.51	0.30	59.1	22.3
	27.6	1.19	0.63	52.9	15.8
	31.4	1.54	1.11	72.1	10.1
	40.5	2.55	1.79	70.3	8.6
0.09	12.0	0.25	0.18	71.1	28.0
	18.0	0.57	0.36	63.2	21.3
	27.6	1.34	0.81	60.5	14.4
	31.4	1.73	1.35	78.0	9.3
	40.5	2.87	2.02	70.5	9.1
0.08	12.0	0.29	0.22	76.4	25.4
	18.0	0.65	0.42	64.6	21.0
	27.6	1.53	0.95	62.2	9.2
	31.4	1.97	1.63	82.6	8.8
	40.5	3.27	2.54	77.7	8.5
0.07	12.0	0.33	0.26	77.2	25.5
	18.0	0.75	0.56	73.6	18.1
	27.6	1.77	1.17	66.0	14.2
	31.4	2.29	1.98	86.4	8.4
	40.5	3.80	3.17	83.4	8.0
0.06	12.0	0.40	0.36	90.7	17.4
	18.0	0.90	0.81	90.4	11.6
	27.6	2.11	1.50	71.1	13.9
	31.4	2.73	2.50	91.6	7.6
	40.5	4.53	3.92	86.6	8.0

(1) see Table 20

Tables 20 to 22 are summarized in Figure 52A where induction time is plotted against particle size. Average t_i is shown for the data from Anfruns and Kitchener and runs 7 and 8, ignoring any bubble size effect. It is evident that t_i decreases significantly with increasing d_p for d_p less than approximately 30 μm, and appears to be less dependent upon d_p for larger sizes. The same data is plotted on logarithmic scales in Figure 52B. Over the size range studied, it can be assumed that $t_i \propto d_p^{\,n}$, where n is the slope in Figure 52B. Regression analysis of log t_i vs log d_p is summarized in Table 23. For the four sets of data $n = -0.75 \pm 0.25$, for $d_p \leq 55$ μm.

6.2 Bubble Size and Induction Time

The induction times computed from Anfruns and Kitchener's data are plotted vs bubble diameter in Figure 53. There is a distinct decrease in induction time with decreasing bubble diameter for $d_p = 12$ and 18 μm, while there is only a slight decrease, or none at all, for the larger particle sizes.

6.3 Gas Flow Rate

In Table 21 it is clear that the calculated induction time does not vary with superficial gas velocity (i.e. gas flow rate) for $v_g \leq 0.81$ cm/s. With reference to section 6.2 this is to be expected; bubble diameter varies from 0.066 to 0.119 cm, but $d_p \geq 20$ μm. The important implication is that the collection model correctly accounts for the effect of gas holdup.

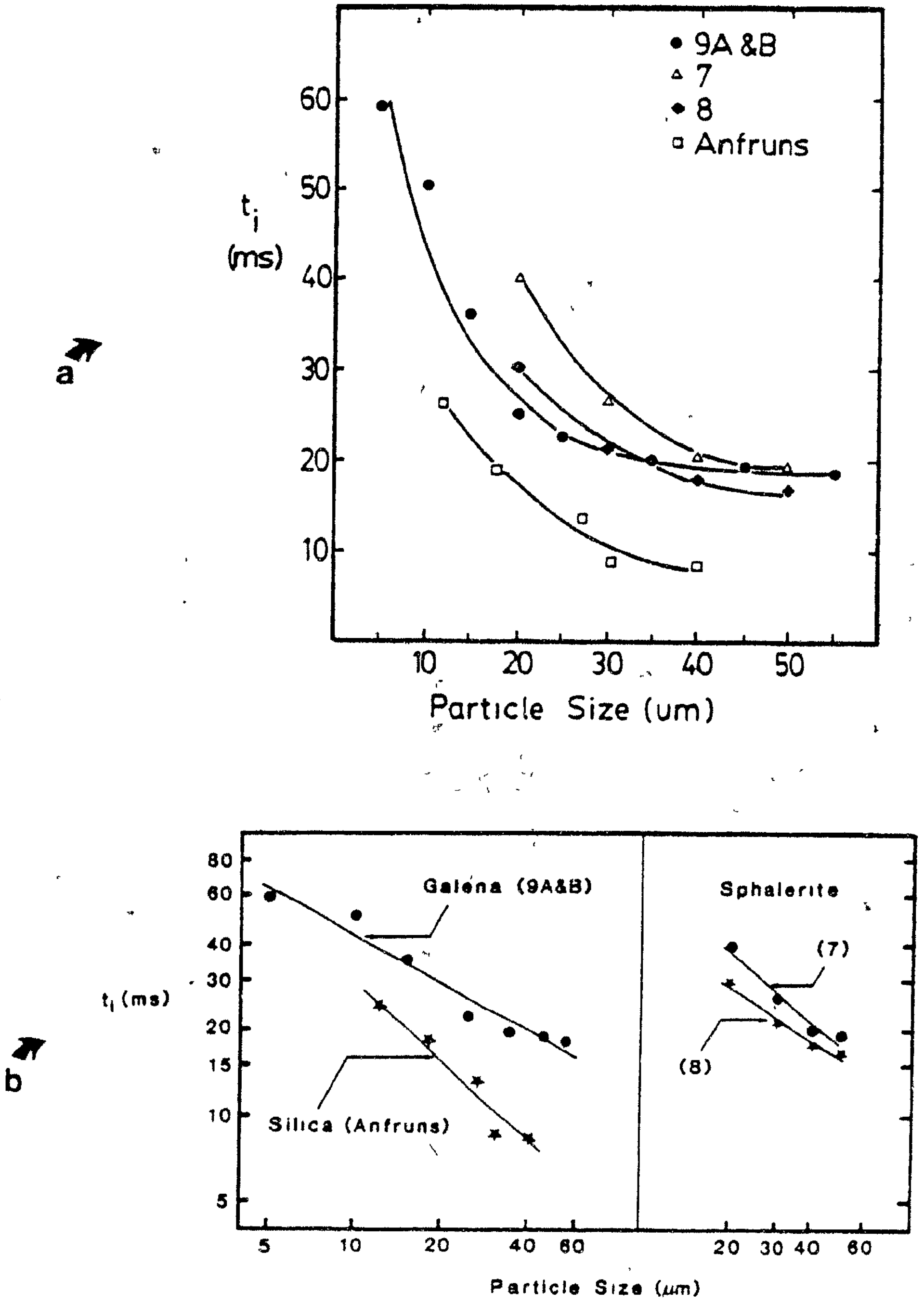

52 Particle size effect upon induction time, computed from results of runs 7, 8 and 9 and the data of Anfruns and Kitchener(43).

(a) arithmetic scales; (b) logarithmic scales.

Table 23

Correlation Between t_i and d_p

$$\log t_i = A + n \log d_p$$

$$t_i = A' d_p^{\,n}$$

t_i - ms
d_p - μm

Data	Number of Observations	Correlation Coefficient	n	A´
Tests 9A & B	7	0.97	-0.552	155
Run 7	16	0.96	-0.821	448
Run 8	20	0.97	-0.630	191
Anfruns & Kitchener	25	0.90	-0.950	277

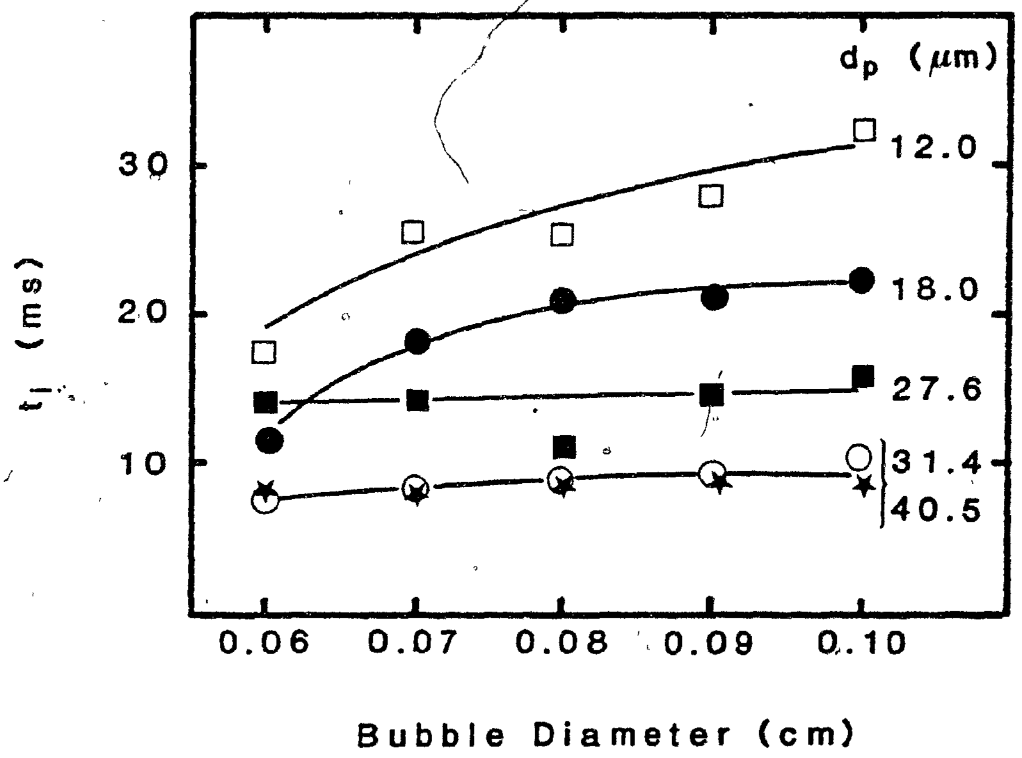

53 Bubble diameter effect upon induction time, computed from data of Anfruns and Kitchener(43).

Further verification of this statement is provided by comparison of the model prediction with the experimental data of Laplante et al$^{(85)}$. Their experiments were performed in a mechanical cell designed to remove froth rapidly. Collection rate constant as a function of gas rate was measured. Also measured as a function of Q_g was bubble diameter. From v_g and d_b, appropriate values for ϕ_g and u_b can be calculated using equations 2.12, 4.15 ($v_\ell = 0$) and 4.13. To use the collection model the only further parameter required is induction time. From the calculations of section 6.1 (Figure 52), a 25 μm particle of galena would be expected to have an induction time between 14 ms (very hydrophobic) and 30 ms (moderately hydrophobic). Table 24 summarizes the model calculations for 25 μm galena using $t_i = 20$ ms, as well as 19 μm galena with $t_i = 25$ ms and 10.5 μm galena with $t_i = 38$ ms ($n = -0.75$), for the conditions of the reported experiments. Model results and experimental results are compared in Figure 54. While the fit for the fine galena is only fair (requires a smaller value of t_i, or reflects significant recovery by entrainment in the experiments) the fit for the 19 and 25 μm galena is very good. At the very least, it can be said that the model predicts the shape of the k vs v_g curve, as well as the location of its peak.

Table 24

Model Calculations for Data of Laplante et al(84)

Conditions: $\rho_p = 7.5$ g/cm^3 $\mu = 0.01$ poise

Q_g (L/min)	v_g (cm/s)	d_b(1) (cm)	U_T(2) (cm/s)	ϕ_g(3) (x100%)	u_b(4) (cm/s)
1	0.071	0.066	7.74	0.95	7.5
2	0.143	0.071	8.37	1.8	7.9
3	0.214	0.077	9.11	2.6	8.2
5	0.357	0.090	10.6	3.8	9.4
6	0.428	0.098	11.6	4.2	10.2
7	0.500	0.106	12.4	4.6	10.9
8	0.571	0.114	13.3	4.9	11.7
9	0.642	0.121	14.0	5.3	12.1
10	0.710	0.131	15.0	5.5	12.9

(1) $\ln (r_b) = 0.0789\, Q_g$ (ref. 84)

(2) From equation 2.12

(3) From equation 4.15 ($v_\ell = o$)

(4) From equation 4.13

Q_g (L/min)	$d_p=25\mu$m $t_i=20$ms		$d_p=19\mu$m $t_i=25$ms		$d_p=10.5\mu$m $t_i=38$ms	
	E_K (%)	k (min^{-1})	E_K (%)	k (min^{-1})	E_K (%)	k (min^{-1})
1	1.32	1.28	0.83	0.81	0.36	0.35
2	1.22	2.20	0.80	1.44	0.34	0.62
3	1.22	3.06	0.82	2.04	0.34	0.86
5	1.01	3.61	0.68	2.43	0.29	1.02
6	0.89	3.51	0.60	2.36	0.26	1.00
7	0.81	3.44	0.55	2.32	0.23	0.99
8	0.70	3.16	0.48	2.16	0.21	0.94
9	0.70	3.32	0.47	2.23	0.20	0.96
10	0.63	3.08	0.43	2.07	0.18	0.89

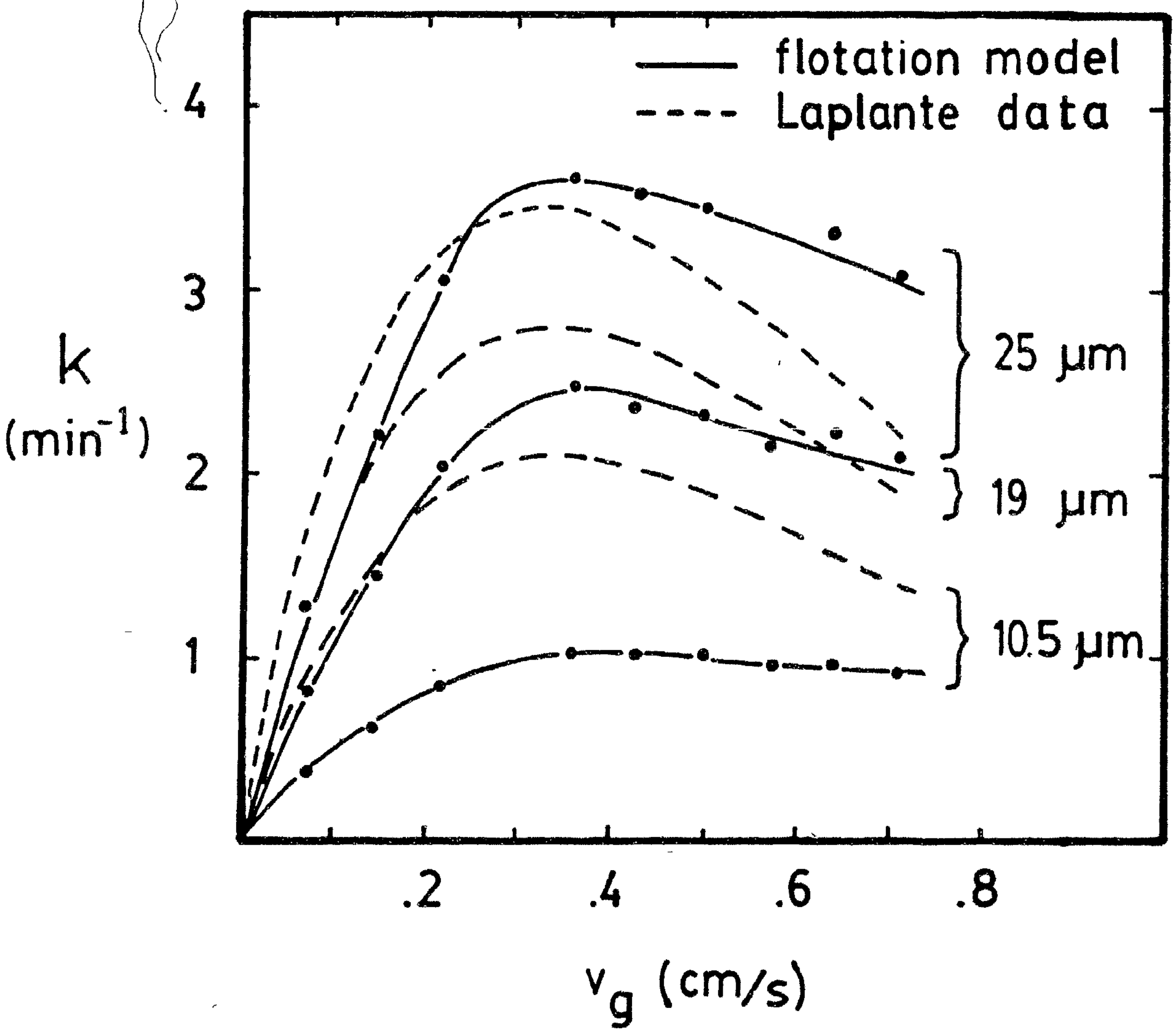

54 Gas rate effect upon rate constant, measured by Laplante et al$^{(85)}$ and fitted by the flotation model. See Table 24 for conditions and model calculations. Laplante data is given by:

25 µm, $k=2.10\ Q_g\ \exp(-0.225\ Q_g)$;
19 µm, $k=1.64\ Q_g\ \exp(-0.215\ Q_g)$;
10.5 µm, $k=1.23\ Q_g\ \exp(-0.216\ Q_g)$

where Q_g is in L/min.

CHAPTER 7

FLOTATION COLUMN SCALE-UP

A concise yet effective scale-up model for column flotation is proposed. The methodology includes:

1. laboratory measurement of collection rate constants of the component minerals,
2. calculation of collection zone recoveries for the plant column,
3. interfacing of a variable cleaning zone recovery with that of the collection zone to yield a grade-recovery relationship, and
4. ensuring that maximum bubble load is not exceeded.

Measurement of Rate Constants. It is essential that the laboratory tests for measuring the distribution of rate constants be conducted under the following conditions: (a) minimal short-circuiting of feed to the overflow, (b) no particle return from the cleaning zone, (c) operation at close to plug flow conditions, (d) sample collection with time, (e) a flotation time long enough to determine the rate constant of the slowest floating component, and (f) maximum bubble load is not approached. Conditions (a), (b), and (c) are satisfied by using a laboratory column design similar to that described in chapter 4. Condition (f) will usually be satisfied as well, since the length of bubble rise during collection is only about 1.2 m.

To attain conditions (d) and (e) the column is operated in a sequential manner. A typical test is conducted as follows: First, the test feed is conditioned with reagent(s) at the desired level. Solids are allowed to settle and water is decanted, to be used as wash water (with some make-up water if necessary). The first column test is performed at a downward slurry velocity of approximately 2 cm/s; i.e. a flotation time of about 1 minute. (The column is pre-filled with water to start the test.)

Concentrate is collected and retained for weighing and analysis. After flotation of all the feed sample a second column test is run, using the tailings from the first run as the new feed. This process is repeated several times, increasing the flotation time (by decreasing downward slurry velocity) with each stage.

In this manner recovery vs time data for each component is obtained. The distribution of rate constants is estimated from the time-recovery data using the two rate constant technique (k-fast and k-slow) described by Kelsall(86) and used by Lynch et al(87). If necessary, this procedure can be repeated at a few gas rates.

Calculating Collection Recoveries. Recovery in the collection zone is calculated using equation 2.10, which accounts for mixing in the plant column. Particle velocity and mean residence time are estimated from equations 2.12 and 2.11, and the vessel dispersion number D_p is estimated from equation 5.2. The use of equation 2.10 assumes first-order rate kinetics; pulp density effects are ignored. The total collection zone recovery R_K of a mineral component is the weighted sum of the two recoveries that are calculated using k-fast and k-slow.

Interfacing the Collection and Cleaning Zones. Final recovery of each component is calculated by assuming a value for the cleaning zone recovery R_F and applying equation 2.19,

$$R_T = \frac{R_K R_F}{1-R_K\ (1-R_F)} \qquad (2.19)$$

A typical cleaning zone recovery is not known. However, by repeating the calculations for a range of R_F a grade-recovery relationship is obtained, as described in the example of Table 2. (It is expected that R_F can be estimated in one of two ways: (a) by comparison of the scale-up model with existing columns, or (b) by comparison of the true solids holdup (as obtained by measurement of pulp density throughout the collection zone) with holdup predicted by a column material balance.)

Testing for Bubble Load. As previously discussed, overloading of gas bubbles can be a significant limitation in flotation columns. The final step in the scale-up calculations is the estimation of bubble load at the top of the recovery zone. If the calculated load exceeds the maximum load, then recovery calculations are repeated using a shorter collection zone length. Maximum bubble load is estimated by assuming a monolayer coverage of particles at fractional packing density γ. This load, expressed as Γ_M, the mass of solids per unit volume of gas, is calculated by considering the coverage on a single bubble:

$$\Gamma_M = \frac{\pi \, d_b^2 \, d_p \, \rho_p \, \gamma}{\frac{\pi}{6} \, d_b^3} \tag{7.1}$$

which reduces to

$$\Gamma_M = \frac{6 \, d_p \, \rho_p \, \gamma}{d_b} \tag{7.2}$$

The actual bubble load Γ_C is estimated by

$$\Gamma_C = \frac{Q_F \, \phi_s \, \rho_p \, (1 + T_R) \, R_K}{Q_g} \tag{7.3}$$

where Q_F is the volumetric feed flow rate, Q_g is volumetric gas flow rate, ϕ_s is the feed volume fraction solids, ρ_p

is the density of the feed solids, R_K is the fractional recovery of the collection zone and T_R is the ratio of solids mass rejected from the cleaning zone to feed mass. Γ_C cannot exceed Γ_M.

The calculation for recovery assumes that the top of the bubble is not loaded with particles, and that the reaction rate is first order. In fact, as the bubble becomes loaded with particles, the reaction rate changes gradually from first-order to zero-order. In the scale-up model, this gradual transfer is approximated by assuming that bubble loading continues as a first-order rate process until 80% of the bubble surface is covered, and then collection stops. For these calculations it is assumed that $\gamma=1$ for the 80% of the surface that is covered.

A flowchart of the scale-up computer program, COLUMN, is shown in Figure 55, and the program listing (in BASIC) is provided in Appendix 2. Table 25A illustrates an input for the program and Table 25B shows the results. The example is for a molybdenum cleaning stage with three mineral components: molybdenum, chalcopyrite and gangue. The rate constants and operating conditions are hypothetical. Note that at a froth recovery of 60% and lower, the bubbles become fully loaded and the effective collection length is reduced significantly. Important bubble loading parameters are gas rate, bubble size and particle size; the probability of complete loading increases as Q_g and d_P decrease, and as d_b increases. (The

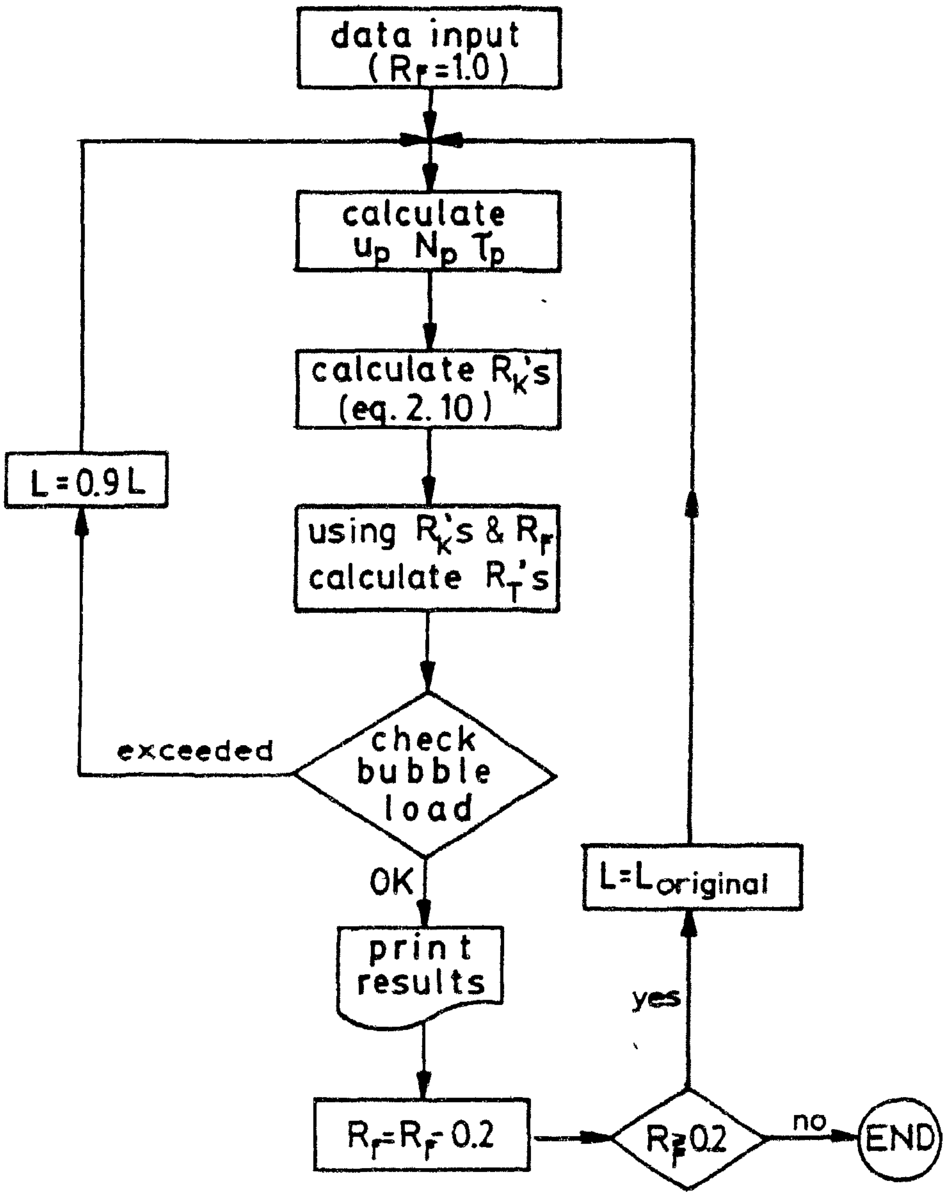

55 Flowsheet for column scale-up computer program, COLUMN. Program listing in Appendix 2.

Table 25A

Example of Input for Column Scale-up Program, COLUMN

```
                         FLOTATION COLUMN SCALE-UP


                                ***DATA INPUT***


             COLUMN DIAMETER(M) = 1
       COLLECTION ZONE LENGTH(M) = 9
                FEED RATE(L/MIN) = 750
            TAILINGS RATE(L/MIN) = 900
                 GAS RATE(L/MIN) = 800
                   GAS HOLDUP(%) = 10
             BUBBLE DIAMETER(CM) = .15
        SUPERFICIAL GAS VELOCITY = 1.7CM/S
         SLURRY VELOCITY(DOWN) = 1.91CM/S

                          FEED DESCRIPTION

          FEED WEIGHT % SOLIDS = 30
         AVE PARTICLE SIZE(UM) = 20
         # OF MINERALS IN FEED = 3
                 (TOTAL MUST = 100%)

                 MINERAL NAME : MOLY
             SPECIFIC GRAVITY = 4.7
               FEED GRADE (%) = 45
ENTER  K  AND  PROPORTION : 1.5,.8
ENTER  K  AND  PROPORTION : .1,.2

                 MINERAL NAME : CHALCOPYRITE
             SPECIFIC GRAVITY = 4.2
               FEED GRADE (%) = 30
ENTER  K  AND  PROPORTION : .5,.5
ENTER  K  AND  PROPORTION : .04,.5

                 MINERAL NAME : GANGUE
             SPECIFIC GRAVITY = 2.6
               FEED GRADE (%) = 25
ENTER  K  AND  PROPORTION : .1,.7
ENTER  K  AND  PROPORTION : 0,.3
        FEED VOLUME % SOLIDS = 9.62
            FEED MTPH SOLIDS =  17.47
```

Table 25B

Example of Output for Column Scale-up Program, COLUMN

```
                                    %RECOVERY      GRADE(%)


FOR FROTH RECOVERY  = 100%
        TOTAL                        57.89
        MOLY                         79.43          61.74
        CHALCOPYRITE                 45.41          22.54
        GANGUE                       34.0[illegible]        . 14.72
                   L = 9M
     RECYCLE RATIO =0


FOR FROTH RECOVERY = 80%
        TOTAL                        53.3
        MOLY                         75.54          63.78
        CHALCOPYRITE                 [illegible]          22.49
        GANGUE                       29.27          13.77
                   L = 9M
     RECYCLE RATIO =.13


FOR FROTH RECOVERY = 60%
        TOTAL                        44.38
        MOLY                         68.13          69.24
        CHALCOPYRITE                 30.06          23.37
        GANGUE                       18.41          10.35
                  L = 6.56M
     RECYCLE RATIO =.38


FOR FROTH RECOVERY = 40%
        TOTAL                        31.73
        MOLY                         57.4           75.74
        CHALCOPYRITE                 13.15           7.16
        GANGUE                       5               7.06
                  L = 4.3M
     RECYCLE RATIO =.42


FOR FROTH RECOVERY = 20%
        TOTAL                        17.41
        MOLY                         33.75          90.35
        CHALCOPYRITE                 8.18           14.1
        GANGUE                       3.5            5.02
                  L = 3.14M
     RECYCLE RATIO =.55
```

model uses a single value of d_b, although this actually increases by $\sim$ 20% during rise from bottom to top).

7.1. Separation Selectivity

Separation selectivity as a function of particle size can be illustrated by combining the results of the flotation model and the column scale-up model. A hypothetical separation is considered to be made between a feed consisting of 50% mineral A and 50% mineral B, completely liberated. The induction time for a 20 μm particle of A is 25 ms, for a 20 μm particle of B it is 35 ms, and for both minerals it is assumed (based on the limited data available) that $t_i \propto d_p^{-0.6}$. Table 26 lists the assumed operating conditions and the resulting collection efficiencies and rate constants for d_p between 5 and 30 μm, calculated from COLLECT.

These rate constants, when used in the scale-up model, produce recovery curves for mineral A as shown in Figure 56, given the column conditions listed in the diagram. (Bubble overloading does not occur for any of the conditions). Each curve is obtained by varying R_F from 20% to 100%, and the grade at any point is obtained by multiplying the slope (of the line connecting the point to the origin) by the feed grade, 50% A. Poorer separation at fine particle sizes is clearly indicated. For example, at a mineral A recovery of 70%, the grade of 20 μm material is 96% A, compared to 71% A for 10 μm material and 58% A for 5 μm material.

Table 26

Separation Selectivity

k and E_K Values

Conditions: v_g = 1 cm/s d_b = 0.12 cm
u_ℓ = 1.5 cm/s u_b = 12 cm/s
ρ_p = 5.0 g/cm^3
μ = 0.01 poise
ϕ_g = 10%

	d_p (μm) →	5	10	15	20	25	30
Mineral A	t_i (ms)	66	43	34	28.6	25	22.4
	E_K (%)	.030	.0742	.1032	.1175	.1175	.103
	k (min^{-1})	.225	.557	.774	.881	.881	.773
Mineral B	t_i (ms)	92	61	48	40.0	35	31.4
	E_K (%)	.0160	.0235	.0176	.00879	.00089	.00025
	k (min^{-1})	.120	.176	.132	.0659	.00665	.00188

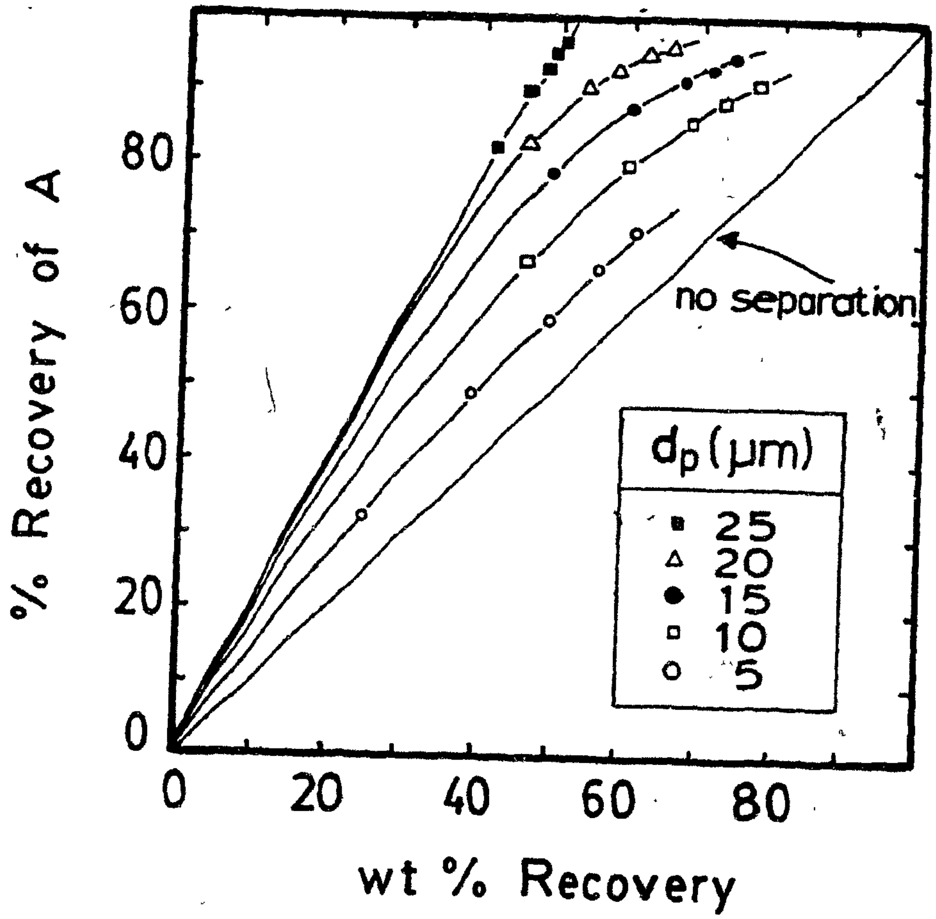

56 Example of particle size effect upon separation selectivity. Collection parameters are given in Table 26. Column conditions: d_c=0.9m, L=8m, Q_F=600 L/min, Q_T=640 L/min, Q_g=380 L/min, weight % solids = 5.0, v_g=1.0 cm/s, v_ℓ=1.86 cm/s.

CHAPTER 8

DISCUSSION

8.1. The Flotation Model

The flotation model developed here is seen as a significant advancement in the understanding of particle-bubble interaction during flotation. Its development has been made possible by solutions to the equations for fluid flow around spheres having Reynolds numbers in the range of flotation sized bubbles. The model follows the concept of Sutherland but with the benefit of knowing the velocity field around the bubble.

Collision. Trajectory calculations have been used to extend the existing collision model to a particle size range typical of most flotation systems. As an outcome of these calculations, the collision efficiency for low particle inertia $(Sk \rightarrow o)$, as calculated by Weber(33), is corrected for inertial effects by a factor that includes Stokes number.

It is recognized that certain approximations were necessary for these calculations. The trajectories were obtained by assuming that the velocity distribution away from the bubble surface could be approximated by a value intermediate to that of the Stokes flow and potential flow values. As well, the particle drag coefficient was derived from Stokes law, and it was assumed that non-steady state drag terms were insignificant. However, the error introduced by these approximations is not likely to be significant to the computed collection efficiency. This is because at larger particle sizes the collection efficiency is most strongly dependent upon the attachment efficiency, not the collision efficiency.

When the collision model was applied to the data of Anfruns and Kitchener$^{(43)}$, ratios of E_C (theory) to E_K (experimental) between 0.6 and 0.9 were attained, indicating less than 100% attachment efficiency. The mineral system employed by Anfruns and Kitchener was very hydrophobic, and it was assumed that E_A = 100% in order that E_C could be measured and compared to theory. The present work suggests E_A < 100% and the question is raised as to whether collision efficiency can be measured, since it is difficult to envisage a mineral system that exhibits an attachment efficiency of 100%.

The model assumes that collision efficiency of a bubble in a bubble swarm is calculated in a manner similar to that for a single bubble in an infinite medium; the effect of the swarm is only to slow the rise velocity of the bubble. Flint and Howarth$^{(40)}$ calculated that, aside from the lowering of the rise velocity, a bubble swarm would have the effect of straightening the fluid streamlines ahead of a bubble and, consequently, would increase the collision efficiency.

This type of calculation assumes that the concentration of particles in the fluid remains uniform. This is unlikely, as particles are concentrated in the boundary layer of bubbles; that is, bubbles would tend to disturb the uniform concentration of particles. A theoretical treatment of the effect of neighbouring bubbles is obviously complex. Experimentally, the results of runs 7 and 8, in which computed induction time remained constant over a range of gas velocity (and gas holdup), leads to the conclusion that the model assumption, of no significant effect of bubble concentration upon the collision process, is valid (at least for $v_g < 0.81$ cm/s; $\phi_g < 0.09$).

Contact. The model considers attachment to occur while the particle is sliding over the surface of the bubble, with no attachment during inertial impaction. Evidence for the validity of this assumption was provided, for fine and intermediate sized particles, by particle trajectory calculations that imposed an elastic impact at the bubble surface. These calculations indicate that significant particle bounce does not occur for particles less than about 100 μm in diameter. For intermediate sized particles, say 30-100 μm, particle bounce may occur at initial impact; however, the radial oscillation is rapidly damped and within 5 to 10° of angular travel the particle assumes a sliding-only trajectory along the bubble surface.

The key to the flotation model is recognition of the boundary layer on a bubble surface and, consequently, the existence of a significant tangential velocity gradient. As a result, small particles slide at a velocity that is lower than that of larger sized particles. The smaller a particle the longer will be its contact time. The tangential velocity of a particle on the bubble surface is conveniently represented by the surface vorticity distribution as provided by Woo(49) and others(48,73,74). Confirmation of this approach was provided by comparison of model-calculated sliding times with the sliding time measurements of Schulze and Gottschalk(45,46), Figure 21. Figure 21 also showed that the assumption of potential flow was not a good approximation. For the data of Figure 21, (r-1) is 0.053; it is clear from Figure 14A and 20 that at smaller (r-1), i.e. smaller particles, the difference between the potential flow velocity and the true velocity becomes even more significant.

8.2. Film Thinning and Induction Time

An important consequence of the velocity gradient at the surface of the bubble is that it imparts a tumbling motion to the particle, as described by equation 3.37 and summarized in Figure 22. At the same time the disjoining film between particle and bubble is undergoing a thinning process. It is of interest, then, to consider the mode of contact between a mineral particle and the bubble surface. Mineral particles are seldom rounded; usually they are very angular. Anfruns and Kitchener(43) demonstrated the importance of particle angularity, measuring the collection rate of glass spheres to be 2 to 10 times lower than that of similarly treated (angular) quartz particles. This analysis will consider a cubic shape to be a reasonable representation of the true situation. Figure 57 depicts a particle as it travels along the bubble surface. The radial component of the liquid velocity is directed toward the bubble surface, which keeps the particle in constant contact with the bubble film. The notable observation from Figure 57 is that particle-bubble contact is more closely represented by a line contact rather than a plane contact. The area of particle-bubble contact and, therefore, of film thinning, is very small. This calls into question the modelling of film thinning as applied to flotation in which it is assumed that particle-bubble contact can be simulated by: (a) the drainage of liquid from between two solid discs (Reynolds(88)), (b) liquid drainage between a sphere and a solid surface (Derjaguin and Duhkin(64)), or (c) the excess pressure inside the bubble acting on the surface of a disk or a cube (Scheludko(89), Jowett(39)). In all these cases particle size is involved in fixing the area over which forces are effective; consequently, liquid drainage time (and thus film thinning time) is considered to increase with increasing particle size. However, the situation depicted in Figure 57 suggests that the particle dimension does not play a significant role in film thinning.

In Scheludko's analysis of the thinning process he considers the time necessary for the film to thin from an initial film thickness h_i to the rupture thickness h_o. This time is believed to be a function of van der Waal's forces, electrical double-layer interaction and hydration effects(56,89).

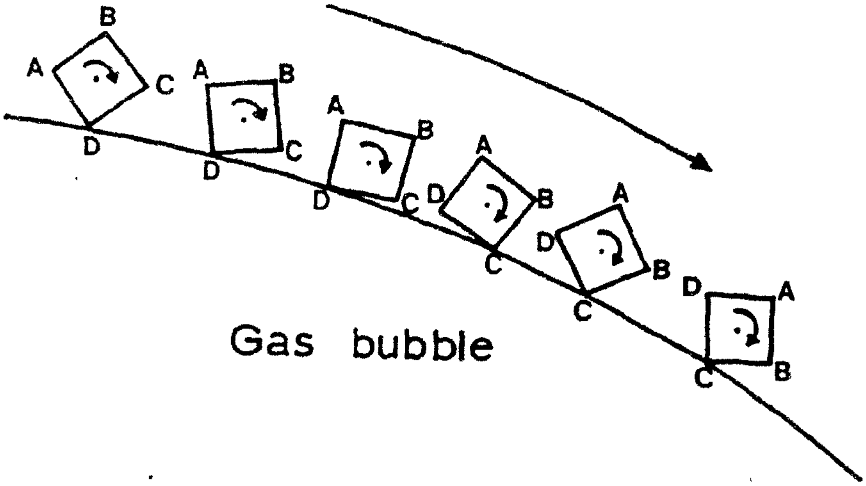

57 Motion of a cubic particle on a bubble surface.

The initial film thickness is a largely unknown parameter, as is the role of particle size in defining h_1. However, it is reasonable to consider that the greater the mass of a particle the more effective will be its initial impact in piercing the water film, i.e. in reducing h_i, and thus lowering the induction time.

To summarize these thoughts on the relationship between induction time and particle size, it is suggested that particle dimension does not significantly affect the film thinning process, but that it plays a role (in terms of particle mass) in determining the initial thickness of the thin film. The expected relationship is a decrease in induction time with increasing particle size. This trend is in agreement with the results obtained from fitting the collection model to the experimental data reported here and by Anfruns and Kitchener. This analysis was developed for an angular particle. While it was assumed that the particle is cubic, the conclusion of the analysis remains the same for any angular shape.

8.3. Flotation Parameters:

Particle Size. The role of particle size in flotation is complex. However, with the development of this flotation model the effects of particle size can start to be interpreted. The effects can be summarized as follows: when particle size increases

(a) collision efficiency increases,

(b) particle-bubble contact time decreases and,

(c) induction time decreases (at least for $d_p < 50$ μm).

The typical result is a peak in the rate constant vs size curve. Similarly a peak will occur in a size-by-size recovery plot (or a plateau if recovery is allowed to approach > 90%).

Collision rate is increased with particle size for two reasons: (a) the increased particle mass increases the tendency of the particle to deviate from the fluid streamlines toward the bubble surface, and (b) the increased particle dimension increases the probability of collision by interception. The decrease in particle-bubble contact time with increasing particle size is attributable to the velocity gradient at the bubble surface. An explanation for the reduced induction time with increased particle size has already been suggested. From the small amount of data available the relationship between particle size and induction time is proposed as $t_i \propto d_p^{-0.75 \pm 0.25}$, for moderate to strong collector additions. This has been obtained using data with a maximum particle diameter of about 50 μm; its validity at larger particle sizes is not claimed.

The location of the peak in size-by-size recovery data is dependent upon many factors, foremost of which are bubble size, particle density and induction time. Consider the latter. Figure 26 is quite dramatic in showing that the peak shifts to smaller particle sizes as induction time increases. While it is assumed in Figure 26 that $n = o$ (in $t_i \propto d_p^n$), using the experimentally derived n = -0.75 ± 0.25 will yield the same trend. There are many examples of systems that show a maximum rate constant or recovery in the range 30 to 100 μm. All these systems exhibit good or acceptable floatability. Two examples of systems that exhibit moderate to poor floatability are shown in Figure 58. In Figure 58A(90) the flotation of chalcopyrite in a nitrogen environment (grinding and flotation) is illustrated. Figure 58B(91) shows the recovery of iron sulfide in an industrial lead cleaning circuit. In both cases, flotation response is poor but finite, indicative of long induction times. In both cases, the peak in recovery occurs between 5 and 10 μm. (The data reported in Figure 58 includes recovery by physical entrainment. Elimination of this collection mechanism would yield curves that are more sharply peaked).

Further evidence of the link between induction time and location of the recovery peak is given by size-by-size recovery of sphalerite for increasing additions of copper sulfate, reported by Anthony et al(67,10). As copper sulfate dosage is increased (implying that induction time is decreased) the location of the peak recovery increases from about 15 μm to 80 μm. A similar effect for increasing collector dosage in quartz flotation is reported by Imaizumi and Inoue(68).

As a final note on particle size effects it is emphasized that the analysis presented here does not consider particle detachment, due to turbulence, to be an important factor in the fine and intermediate size range of flotation, whether in a

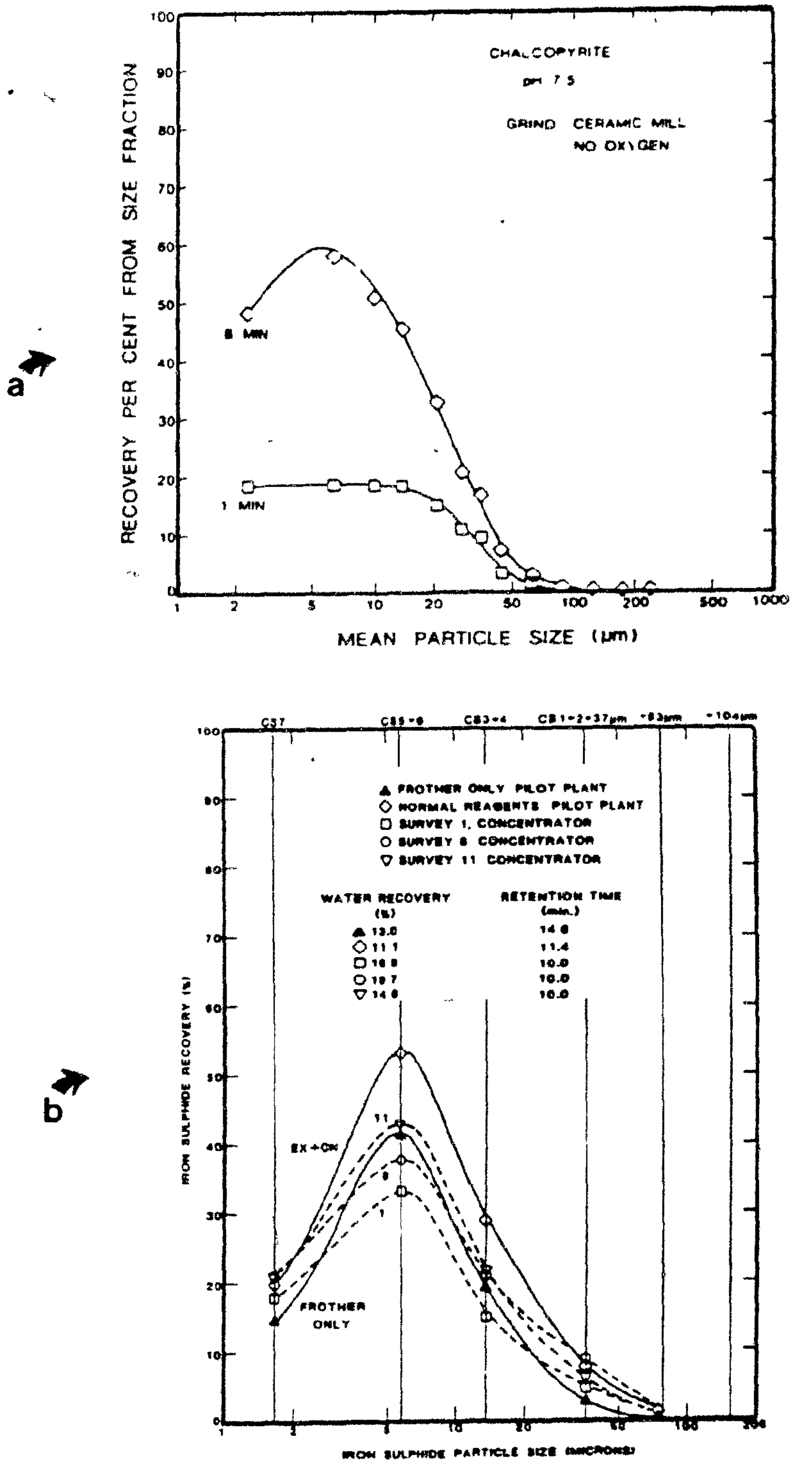

58 Size-by-size recovery data.

(a) Chalcopyrite flotation in a nitrogen environment$^{(90)}$,

(b) Iron sulfide flotation in an industrial lead cleaning circuit$^{(91)}$.

flotation column or a mechanically stirred machine.

Particle Density. Particle density strongly affects the shape of the size-by-size recovery curve as well as the maximum particle size that is floatable, as shown by the model predictions in Figure 29 (for $t_i \neq fn\ (d_p)$). Experimental confirmation of the effect described in Figure 29 is given by data for minerals at either end of the density scale. Size-by-size recovery curves for cassiterite ($\rho_p = 7.0\ g/cm^3$) are usually very steep and peak at about 20-40 μm, as reported by Trahar(10). As well, the flotation of galena ($\rho_p = 7.5\ g/cm^3$) reported here in Test 9 exhibited a sharp peak in recovery, Figure 46. At the other extreme, very flat curves and flotation at large particle sizes have been reported for phosphate ($\rho_p = 3.2$; flotation at $d_p = 20$ mesh (840 μm))(92), fluorite ($\rho_p = 3.1$; flotation at $d_p = 28$ mesh)(93), and coal ($\rho_p = 1.3$; flotation at $d_p > 20$ mesh)(94).

Chemical effects cannot be ignored as contributing to these results; however, particle density is an important factor. The density-size interaction can be explained by considering the sliding velocity of a particle on the bubble surface, given by equations 3.30 and 3.32. An increase in particle density increases the relative settling velocity of the particle. As a result the second term on the right side of equations 3.30 and 3.32 assumes greater importance, and particle-bubble contact time decreases. Thus, as density increases, E_A tends to decrease, which has the greatest impact on larger particles.

Bubble Size. A smaller diameter gas bubble increases collection efficiency in two ways: by increased collision efficiency and by increased attachment efficiency. The increase in attachment efficiency is because the fractional decrease in particle sliding velocity on a smaller bubble exceeds the fractional decrease in sliding distance. As well, there is evidence that a smaller bubble reduces the induction time of relatively small particles (< 20 μm in this work), which increases attachment efficiency beyond that predicted by the model. However, since fine particle collection is controlled primarily by collision, an increased attachment efficiency is not of great consequence.

There are three physical problems in producing very fine bubbles. The first is the difficulty in generating fine bubbles while maintaining a high gas rate. The collection rate constant is proportional to

$$\frac{v_g E_K}{d_b} .$$

Considering just v_g and d_b, a decreased d_b is only beneficial if v_g is maintained. However, if v_g cannot be maintained and decreases from its initial level then a point is reached at which there is no benefit gained by making a smaller bubble. Secondly, the high frother dosage that is necessary to make small bubbles (by conventional mechanisms, i.e. agitator, sparger) generates excessive frothing. The third problem is

specific to flotation columns. When bubble diameter is decreased, gas holdup increases. There is a maximum gas holdup that a column can maintain without flooding, the phenomenon whereby slurry is blown out the top of the column by the gas.
Viscosity. When it is assumed that induction time is proportional to viscosity, the flotation model predicts an increase in recovery with decreasing viscosity. One ramification of this is that recovery should increase for increasing water temperature. This has been reported by Klimpel(95) where the rate constant of cationic silica flotation increased from 2.5 min^{-1} at 2°C to 7.5 min^{-1} at 21°C. This increase is more than expected by viscosity effects alone and may also be due to adsorption phenomena. Nevertheless, viscosity appears to be a relevant consideration for operation in northern climates where winter temperature can range from 3°C in winter to 25°C in summer.
Gas Rate. In agreement with the experimental results of this work and the measurements of Laplante et al(85), the flotation model predicts a peak in collection rate constant as superficial gas velocity is increased. When gas rate is increased, bubble diameter increases and collection efficiency is decreased. These two factors act to decrease k while an increasing v_g acts to increase k; an optimum level of v_g exists.

It is of interest to note that the data of Laplante was obtained in a mechanical flotation machine. This is further evidence, along with the recovery - size data, that the model

is valid for flotation in conventional stirred-tank machines.
<u>Solids Concentration</u>. In Run 9 galena recovery increased with increasing solids concentration, from 60% recovery at 0.05 volume % solids to 80% recovery at 3.0 volume % solids, with the appearance of a leveling off at about 80% recovery. These tests, to the author's knowledge, have not been performed before with such close control over solids concentration, entrainment and froth removal. The implication is that collection efficiency is a function of solids concentration at low solids content (it is unclear how percent solids affects collection at intermediate and higher levels of solids concentration). When solids concentration was examined by the flotation model a trend in the reverse direction to that of the test results was predicted, Table 5. The test results are attributed, therefore, to particle-particle interaction that causes the particles to diverge more from the liquid streamlines and, consequently, to increase the collection efficiency.

These results can be interpreted in one of two ways. The first is that the rate constant varies with solids concentration. The second is that the reaction is not first-order rate dependent but rather exhibits a variable-order rate dependency. It is an illustration that the description of the flotation process in terms of a chemical reaction rate process is somewhat simplified. However, the use of the first-order rate analogy is justified because it provides a clearer mechanism for analyzing, and accounting for, the effects of the many flotation parameters.

Separation Selectivity. It has been illustrated by model calculations reported in section 3.5 and in the column simulation summarized by Figure 56, that separation selectivity decreases with decreasing particle size. This is generally considered to be the case and has been experimentally verified for example, by Trahar in separations of cassiterite from siderite(96) and galena from sphalerite(97). The flotation model provides the explanation; smaller particles reside on the bubble surface for times that are long in comparison to the induction time of either strongly floating or weakly floating particles. For example, separation of two 5 μm particles, one with t_i = 40 ms, the other with t_i = 80 ms, is obviously difficult when 70% of the colliding particles have a sliding time in excess of 80 ms (Figure 24).

Smaller bubbles do not increase selectivity. There appears to be only one method for improving the selectivity of fines separation. That is flotation at very low collector dosage, so that the consequently increased induction time of the weakly floating component results in a very low attachment efficiency for that component. The attachment efficiency of the more floatable species will also decrease, but the ratio of their attachment efficiencies will increase (and, therefore, so will the separation selectivity). Of course, the rate constant will be lowered, requiring a longer flotation time. Separate circuits and different machine types for fine, intermediate and coarse particles would be most desirable, as advocated by others (67,10,39).

8.4. Flotation Column Scale-up

The strengths of the column scale-up methodology are: 1. a unique and simple method for measuring collection rate constants in the laboratory, 2. knowledge of the mixing conditions in industrial sized columns, 3. the ability to account for overloading of gas bubbles, and 4. the ability to interface the cleaning zone recovery with that of the collection zone.

Column Mixing. Mixing parameters of large flotation columns were determined under industrial operating conditions. Results on these large columns showed that the liquid axial dispersion coefficient followed the dependance upon column diameter as suggested by Magnussen and Schumacher (25), $D_\ell \propto d_c$. The square cross-sectioned flotation columns (using equivalent diameter) gave the same dispersion coefficients as those determined by Magnussen and Schumacher for similar diameter cylindrical columns. This similarity between square and cylindrical columns also agrees with the observation of Akita and Yoshida (28). (Recently constructed flotation columns have been cylindrical (5)).

These experiments also verified the observation by other researchers that the axial dispersion coefficient of solids is equal to that of the liquid. Then, for large columns at low air rates,

$$D_p = D_\ell = 0.063\ d_c\ m^2/s \qquad (5.2)$$

For the purposes of scale-up and design of flotation columns equation 5.2 is adequate, even though it does not take into account the effect of gas velocity. Gas velocity in column flotation is relatively low so its influence on equation 5.2 should be small.

The solids RTD tests have shown that the bubble swarm has little effect on the mean residence time of a mineral particle as determined by combining the particle settling velocity with the liquid velocity. The weight fraction solids at the time of the test (3%) was lower than in normal operation (5-10%). Nevertheless, the outcome of the solids tests show that the mixing parameters for solids in a large flotation column can be predicted by equations 2.11 and 5.2; they provide good scale-up criteria.

Particle Entrainment in Columns. It is clear from the liquid tracer experiments on the plant columns that short-circuiting of feed water to the concentrate is minimal. In the laboratory experiments, Run 9, recovery of silica to the concentrate was similar to the water recovery, approximately 1%. Thus, the flotation column effectively prevents the recovery of hydrophilic particles.

Using the Scale-up Model. Column applications with fine particles and/or a high concentration of floatable solids may exhibit a condition of fully loaded bubbles. If bubble loading is a problem then gas flow rate must be increased. Plant columns are known to operate at superficial gas velocities in the range of 0.10 to 0.30 cm/s (Table 6 and reference 5) which is probably near or beyond the optimum gas rate for collection efficiency (Figures 49 and 54). Thus, increasing the gas rate to alleviate bubble overloading will likely reduce the collection rate constant.

The only further information required to complete the scale-up analysis is a value for froth recovery, R_F. Without an estimate of R_F a grade-recovery relationship is provided by the model. Comparison of the model result with plant data at existing column installations, and/or direct measurement of solids holdup will provide a measurement of R_F, preferably as a function of column diameter.

The relationship between R_F and column operating parameters is completely unknown and requires significant study. A full process model of the flotation column is not possible until the cleaning zone operation is better understood, in particular the relationship between R_F and gas rate, wash water rate and column diameter.

CHAPTER 9

CONCLUSIONS & FUTURE WORK

9.1 Conclusions

1. A comprehensive flotation model has been developed. The model considers that particle collection by a gas bubble occurs via particle-bubble collision followed by attachment during the period that the particle is sliding over the bubble surface. Collection efficiency E_K is derived as a product of collision efficiency E_C and attachment efficiency E_A. The development of expressions for both E_C and E_A has been possible by application of recent solutions to equations for fluid flow around flotation sized bubbles. A particle size range between approximately 3 and 100 μm is covered. Significantly, particle-bubble detachment is not included in the model. However, the model was validated on data from conventionally stirred flotation machines.
2. The collision efficiency of a flotation gas bubble at intermediate values of particle inertia has been

determined from particle trajectory calculations. E_C is estimated by

$$E_C = E_{Co}\ (1.627\ Sk^{0.54}\ Re_b^{0.06}\ u^{*-0.16})$$

for $Sk^{0.54}\ Re^{0.06}\ u^{*-0.16} > 0.615$, where Sk is the Stokes number for the particle-bubble system, Re_b is the bubble Reynolds number, u* is the ratio of particle terminal velocity to bubble rise velocity and E_{Co} is the collision efficiency assuming zero particle inertia as calculated by the method of Weber(33).

3. The mechanism of particle contact followed by particle sliding, without significant bounce at impact, has been shown to be valid for particles as large as about 100 μm. For particles less than this size the bounce that does occur at the initial impact is rapidly damped, and continuous particle-bubble contact is attained within 10° of tangential travel. This conclusion is developed from trajectory calculations applied to the experimental data of Whelen and Brown(52).

4. The contact time of a particle on the surface of a gas bubble decreases as particle size increases. This is a result of the significant tangential velocity gradient that exists at the bubble surface. Values of surface vorticity as a function of Re_b, angle from the front stagnation point and gas holdup, derived by other

researchers(48,49,73), have been used to describe the velocity gradient, which, in turn, has been used to develop an expression for sliding time. The sliding time relationship agrees closely with the experimentally derived sliding times of Schulze and Gottschalk(45,46). It has also been shown that potential flow (the assumption in the past) is a poor approximation for particle motion on a bubble.

5. Dynamic induction time t_i decreases with increasing particle diameter. From the relatively small quantity of data available, the relationship between t_i and d_p is shown to be

$$t_i \propto d_p^{-0.75 \pm 0.25}$$

for $d_p < 50$ μm and for moderate to strong collector addition. This has been determined by applying the flotation model to experimental data reported here for galena and sphalerite, and by Anfruns and Kitchener(43) for silica.

6. The velocity gradient at the bubble surface induces a significant spin to the mineral particle. It is shown that this tumbling motion causes mineral particles (which are angular) to contact the bubble along only the edges of the particle. The area of particle-bubble contact is roughly independent of particle size.

7. The peak in size-by-size recovery data that is often observed at intermediate particle sizes is explained by the model and by the relationship of conclusion 5. The location of the peak is a function of many parameters, most important of which is induction time; increasing the induction time (eg. decreasing collector dosage) shifts the peak to smaller particle sizes.

8. Poor separation selectivity at small particle sizes is explained by the model. It is caused by the fact that small particles reside on the bubble surface for times that are long in comparison to the induction time of either strongly floating or weakly floating particles.

9. A decrease in bubble diameter d_b increases both E_C and E_A. However, separation selectivity at small particle sizes is not improved by a smaller d_b.

10. Gas flow rate and gas holdup effects are well described by the flotation model (for gas superficial velocity $v_g < 10\%$). The gas velocity that optimizes the collection rate constant can be predicted.

11. Particle recovery increases with increasing solids concentration for volume percent solids between 0.05 and 3.0%. This can be interpreted as an effect of solids concentration upon E_K.

12. A scale-up model for flotation columns has been develop-

ed. The model uses measured values of collection rate constants and an experimental correlation of plant column mixing parameters to calculate collection zone recovery R_K. R_K is interfaced with a variable cleaning zone recovery R_F to yield a grade-recovery relationship for the plant column. The onset of bubble loading is accounted for in the scale-up model.

13. The dispersion coefficient of solid particles D_p in the collection zone of an industrial sized flotation column is the same as that of the liquid, D_ℓ, and is approximated by

$$D_p = D_\ell \simeq 0.063\ d_c\ m^2/s$$

where d_c is in meters. As well, the mean residence time of particles τ_p is related to the mean residence time of the liquid τ_ℓ by

$$\tau_p = \tau_\ell \ \frac{u_\ell}{u_\ell + u_p}$$

where u_p is the terminal particle velocity and u_ℓ is the interstitial liquid velocity. These two relationships provide good scale-up criteria for flotation columns.

14. Recovery of hydrophilic (gangue) particles in a flotation column is very low, < 1% for the two columns tested. This is attributed to the net downward flow of wash water through the packed bubble bed in the cleaning zone.

15. The success of flotation columns in multiple cleaning applications is due partially to the fact that particles rejected from the cleaning zone back to the recovery zone are subjected to a collection event with 100% of the original retention time. This is unlike conventional machines, where the retention time decreases with each subsequent collection event.

9.2 Claims for Original Research

1. The relative motion between a particle and a bubble prior to and during contact has been rigorously examined, and developed into a comprehensive model of particle collection in flotation.

2. An expression for collision efficiency that accounts for both particle inertia and bubble Reynolds number has been developed.

3. A calculation of dynamic induction times for mineral particles on gas bubbles has been made. The calculation is derived from a combination of experimental and theoretical work.

4. The effect of gas rate in particle collection has been theoretically described.

5. A scale-up model for column flotation has been de-

veloped.

6. The mixing parameters of the collection zone of industrial sized flotation columns have been measured and correlated to column diameter and downward liquid velocity.

9.3 Suggestions for Future Work

1. The relationships between induction time and particle size, and induction time and reagent conditions should be thoroughly investigated. Experimentation with a single bubble system would be preferable.
2. The problem of separation selectivity in the fine particle size range should be addressed. A starting point would be the study of starvation collector addition.
3. Measurements of collection rate constant over a wide range of solids concentration is required. A controlled method of solids addition as used here is suggested.
4. Measurements of froth recovery R_F, either directly or indirectly, should be made on plant columns. Ideally, a relationship between R_F and such parameters as column diameter, wash water rate, gas rate and particle characteristics (such as d_p) should be derived.
5. A fundamental study of water drained froths should be undertaken.

REFERENCES

1. Anon., Engng. and Mining J., 166(1), 1965, p. 76-83
2. Wheeler, D.A., Engng. and Mining J., 167(11), 1966, p. 98-193
3. Boutin, P. and Wheeler, D.A., Canadian Mining Journal, 88(3), 1967, p. 94-101
4. Coffin, V.L. and Miszczak, J., Proceedings 14th Int. Mineral Processing Congress, Toronto, Canada, Oct. 1982 paper 4-21
5. Amelunxen, R., Gibraltar Mines Ltd., British Columbia, Canada, private communication re. column flotation at Gibraltar Mines Ltd.
6. Young, P., Mining Magazine, 146, 1982, p. 35-59
7. Harris, C.C., in Flotation - A.M. Gaudin Memorial Volume', A.I.M.E., New York, 1976, p. 753-815
8. The Deister Concentrator Co., Inc., Bulletin 600
9. Anon., Engng. and Mining J., 172(7), 1971, p. 78-79
10. Traher, W.J., Int. J. of Mineral Processing, 8, 1981, p. 289-327
11. Dell, C.C. and Jenkins, B.W., Proceedings of the Seventh International Coal Preparation Congress, Sydney, Australia, A.C. Partridge (ed.), 1976, paper J3
12. Dell, C.C., Mine and Quarry, 7(3), 1978, p. 36-40
13. Dell, C.C. and Hall, G.A., Trans. Inst. Min. and Metall., 90, 1981, p. C174-C176.
14. Wheeler, D., Course notes from Professional Development Seminar - Column Flotation, McGill University, Canada, March 1983.
15. Narasimhan, R.S., Rao, S.B., and Chowdhury, C.S., Engineering and Mining Journal, 173(5), 1972, p. 153-154
16. Tyurnikova, V.I. and Naumov, M.E.,'Improving the Effectiveness of Flotation', Technicopy Limited, Glos., England, 1981, Chapter 5.2.2.

17. Jameson, G.J., Nam, S. and Moo Young, M., Minerals Sci. Engng., 9(3), July 1977, p. 103-118

18. Rice, R.G., Tupperainen, J.M.I. and Hedge, R.M., Can. J. of Chem. Engng., 59(12), 1981, p. 677-687

19. Rice, R.G., Oliver, A.D., Newman, J.P. and Wiles, R.J., Powder Technology, 10, 1974, p. 201-210

20. Ostergaard, K. and Michelsen, M.L., Can. J. of Chem. Engng., 47(4), 1969, p. 107-112

21. Wehner, J.F. and Wilhelm, R.H., Chem. Eng. Sci., 6, 1956, p. 89-93

22. Levenspiel, O., 'Chemical Reaction Engineering', Wiley, 2nd Edition, 1972, p. 286-287

23. Shah Y.T., Stiegel G.J. and Sharma M.M., AIChE Jour., 24(3), 1978, p. 369-400

24. Shah Y.T., Kelkar B.G., Godbole S.P. and Deckwer W.D., AIChE Jour., 28(3), 1982 p. 353-379

25. Magnussen P. and Schumacher V., Proc. 5th Inter. Chem. Reaction Eng. Symp., Houston, 1978, p. 337-347

26. Towell G.D. and Ackerman G.H., Proc. 2nd Inter. Chem. Reaction Engng. Symp., Amsterdam, 1972, B-3

27. Alexander B.F. and Shah Y.T., Chem. Eng. Jour., 11, 1976, p. 153-158

28. Akita K. and Yoshida F., Ind. Eng. Chem. Process Des. Develop., 12(1), 1973, p. 76-80

29. Imafuku K., Wang T.Y., Koide K. and Kubota H., Jour. of Chem. Eng. of Japan, 1(2), 1968, p. 153-158

30. Argo W.B. and Cova D.R., Ind. Eng. Chem. Process Des. Develop., 4, 1965, p. 352-359

31. Concha F. and Almendra E.R., Inter. Jour. of Mineral Proc., 5, 1979, p. 349-367

32. Richardson J.F. and Zaki W.N., Trans. Inst. Chem. Engrs., 32, 1954, p. 35-52

33. Weber, M.E., J. Separ. Proc. Tech., 2(1), 1981, p. 29-33

34. Tomlinson, H.S. and Fleming, M.G., Proc. 6th Int. Mineral Processing Congress, Cannes, 1963, Roberts, A. (ed.), Pergamon, Oxford, 1965, p. 563-579

35. King, R.P., Hatton, T.A. and Hulbert, D.G., Trans. I.M.M., 83, 1974, p. 112-115

36. Cienski, T. and Coffin, V., Proceedings of the 13th Annual Meeting of the Canadian Mineral Processors, Ottawa, Jan. 1981, p. 240-262

37. Sutherland, K.L., Jour. of Physics and Colloid Science, 52, 1948, p. 394-425

38. Arbiter, N. and Harris, C.C., in 'Froth Flotation', Fuerstenau, D. (ed.), AIME, New York, 1962, Chapter 8, p. 237

39. Jowett, A., in 'Fine Particles Processing' Proc. Int. Symp. on Fine Particles, Las Vegas, Nevada, Feb. 1980, Somasundaran P. (ed.), A.I.M.E., New York, 1980, Chapter 37

40. Flint, L.R. and Howarth, W.J., Chem. Engng. Science, 26, 1971, p. 1155-1168

41. Reay, D. and Ratcliff, G.A., Canadian J. of Chem. Engng., 51(4), 1973, p. 178-185

42. Reay, D. and Ratcliff, G.A., Canadian J. of Chem. Engng., 53(10), 1975, p. 481-486

43. Anfruns, J.F. and Kitchener, J.A., Trans. I.M.M., 1977, C9-15

44. Weber, M.E. and Paddock, D., J. of Colloid and Interface Science, 94(2), 1983, p. 328-335

45. Schulze, H.J. and Gottschalk, G., Proceedings 13th Annual Int. Mineral Processing Congress, Warsaw, June 1979, Laskowski J. (ed.), Elsevier, New York, 1981, Part A, p. 63-84

46. Schulze, H.J. and Gottschalk, G., Aufbereitungs - Technik, 5, 1981, p. 254-264 (English and German)

47. Clift, R., Grace, J.R. and Weber, M.E., 'Bubbles, Drops and Particles', Academic Press, New York, 1978, Chap. 5 and 7

48. Masliyah, J.H., Ph.D. Thesis, Univ. of British Columbia, Vancouver, 1970

49. Woo, S.W., Ph.D. Thesis, McMaster University, Hamilton, Ontario, 1971

50. Reay, D., Ph.D. Thesis, McGill University, Montreal, Quebec, 1973.

51. Klassen, V.I. and Mokrousov, V.A., 'An Introduction to the Theory of Flotation', Butterworths, London, 1963, Chapter 5

52. Whelan, P.F. and Brown, D.J., Trans. I.M.M., 65, 1956, p. 181-193

53. Philoppoff, W., Mining Engng., Trans AIME, April 1952, p. 388-390

54. Evans, L.F., Indust. Engng. Chem., 46, 1954, p. 2420-29

55. Derjaguin, B.V. and Kussakov, M., Acta Physiocochim, 10, 1939, p. 25

56. Finch, J.A. and Smith, G.W., in 'Anionic Surfactants - Physical Chemistry of Surfactant Action', Lucassen - Reynders, E.H. (ed.), Marcel Dekker, New York, 1981, Chapter 8

57. Laskowski, J., Minerals Sci. Engng., 6(4), 1974, p. 223-235

58. Eigeles, M.A. and Volova, M.L., 5th Int. Mineral Processing Congress, London, 1960, I.M.M., 1960, p. 271 - 284

59. Blake, T.D. and Kitchener, J.A., J. Chem. Soc. Faraday Trans., 68, 1972, 1435-42

60. Leja, J. and Poling, G.W., ibid. ref (58) p. 325-341

61. Schulze, H.J., Int. J. of Mineral Processing, 4(3), 1977, p. 241-260

62. Woodburn, E.T., King, R.P. and Colborn, R.P., Metallurgical Transactions, 2, 1971, p. 3163-74

63. King, R.P., in "Principles of Flotation", S. African Inst. Min. & Mettal., King,R.P.(ed.),1983,p.215-225

64. Derjaguin, B.V. and Dukhin, S.S., Trans. I.M.M., 70, 1961, p. 221-245

65. Lyman, G.J., M.E. Thesis, McGill University, Montreal, Quebec, 1974

66. Trahar, W.J. and Warren, L.J., Int. J. of Mineral Processing, 3, 1976, P. 103-131

67. Anthony, R.M., Kelsall, D.F. and Traher, W.J., Proc. Australasia Inst. Min. Metall., 254, June 1975, p. 47-58

68. Imaizumi, T. and Inoue, T., ibid. ref(34), p. 581-594

69. ibid. ref.(47), p. 42-44

70. Boyce, W.E. and DiPrima, R.C., 'Elementary Differential Equations and Boundary Value Problems', Wiley, New York, 1967, Section 8.6

71. Seeley, L.E., Hummel, R.L. and Smith, J.W., J. Fluid Mechanics, 68(3), 1975, p.591-608

72. ibid. ref.(47), p. 259-61

73. LeClair, B.P. and Hamielec, A.E., I. and E.C. Fundamentals, 7(4), 1968, p. 542-549

74. LeClair, B.P., Ph.D. thesis, McMaster University, Hamilton, Ontario, 1970

75. Yen, W.-T., Masters thesis, McGill University, Montreal, Quebec, 1968

76. Roscoe, R., Brit. J. of Appl. Phys., 3, 1952, p. 267

77. Jameson, G.J., in 'The Scientific Basis of Flotation', Ives, K.J. (ed.), NATO ASI Series, Martinus Nijhoff Publishers, Boston, 1984, p. 53-77

78. Smart, P.L. and Laidlaw, I.M.S., Water Resources Research, 13(1), 1977, p. 15-39

79. Hopkins, M.J., Sheppard, A.J. and Eisenklam, P., Chem. Engng. Sci., 24, 1969, 1131-1137

80. Anderssen, A.S. and White, E.T., Chem. Engng. Sci., 26, 1971, p. 1203-1221

81. Bhaga, D., Masters thesis, McGill University, Montreal, Quebec, 1970

82. Wallis, G.B., "One Dimensional Two-Phase Flow", McGraw-Hill, New York, 1969, chapter 9.

83. Finkelstein, N.P. and Allison, S.A., in 'Flotation-

A.M. Gandin Memorial Volume' Fuerstenau M.C. (ed.), A.I.M.E., N.Y., 1976, Vol. 1, p. 414-457

84. Gy, P.M., in Geological, Mining and Metallurgical Sampling, IMM Proceedings, London, Jan. 1972, Sept. 1972, July 1973, Jones, M.J. (ed.), I.M.M., 1974, p. 194-205

85. Laplante, A.R., Toguri, J.M. and Smith, H.W., Int. J. of Mineral Processing, 11, 1983, p. 203-219

86. Kelsall, D.F., I.M.M., 70, 1961, p. 191-204

87. Lynch, A.J., Johnson, N.W., Manlapig, E.V., and Thorne C.G., 'Mineral and Coal Flotation Circuits, Their Simulation and Control", Elsevier, N.Y., 1981, Section 5.4.

88. Reynolds, O., Philosophical Transactions, Royal Soc. of London, 177, 1886, p. 157-234

89. Scheludko, A., Advances in Colloid and Interfacial Science, 1, 1967, p. 391-464

90. Trahar, W.J., Int. J. of Mineral Processing, 11, 1983, p. 57-74

91. Johnston, N.W. and Jowett, A., Australian Inst. of Mining and Metallurgy, NorthWest Queensland Branch Mill Operators' Conference, Sept. 1982, Conference Proc. p. 271-285.

92. Smith, P.R., ibid. ref. (39), Chapter 46

93. Lay, W.C. and Bell, G.M., ibid. ref (38), p. 482-493

94. Aplan, F.F., ibid. ref. (39), Chapter 45

95. Klimpel, R.R., ibid ref. (91), p. 297-309

96. ibid. ref. (10), Figures 16 and 17

97. ibid. ref. (10), Figure 25

Appendix 1. Data Correlations

A. Surface vorticity ξ_s

The surface vorticity data of Woo(49) has been correlated to bubble Reynolds number Re_b and angle θ measured from the front stagnation point. Woo reported ξ_s for the following Reynolds numbers: 0.2, 0.5, 0.75, 1, 2, 3, 5, 10, 20, 30, 40, 100, 200, 300, and 400; and at every 12° for $Re < 40$, and every 3° for $\xi_s > 100$. The following correlations are for $0 < \theta < 84^{\circ}$.

$$\xi_s = a + b\theta + c\theta^2 + d\theta^3 \qquad \text{(A1-1)}$$

where, for $20 < Re_b < 400$

$$a = -0.01082 - 7.273\cdot10^{-4}\ Re + 1.735\cdot10^{-6}\ Re^2 - 2.046\cdot10^{-9}\ Re^3 \qquad \text{(A1-2)}$$

$$b = 0.0745 + 3.013\cdot10^{-3}\ Re - 7.402\cdot10^{-6}\ Re^2 + 8.931\cdot10^{-9}\ Re^3 \qquad \text{(A1-3)}$$

$$c = -4.276\cdot10^{-4} - 1.977\cdot10^{-5}\ Re + 5.194\cdot10^{-8}\ Re^2 - 6.520\cdot10^{-11}\ Re^3 \qquad \text{(A1-4)}$$

$$d = -1.103\cdot10^{-6} - 1.032\cdot10^{-7}\ Re + 1.397\cdot10^{-10}\ Re^2 - 1.334\cdot10^{-13}\ Re^3 \qquad \text{(A1-5)}$$

and, for $0.2 < Re_b < 20$

$$a = -1.217\cdot10^{-3} - 1.745\cdot10^{-3}\ Re + 5.143\cdot10^{-5}\ Re^2 - 1.165\cdot10^{-6}\ Re^3 \qquad \text{(A1-6)}$$

$$b = 0.02859 + 9.229\cdot10^{-3}\ \mathrm{Re} - 3.85\cdot10^{-4}\ \mathrm{Re}^2 + 9.190\cdot10^{-6}\ \mathrm{Re}^3 \qquad \text{(A1-7)}$$

$$c = -4.060\cdot10^{-5} - 5.857\cdot10^{-5}\ \mathrm{Re} + 1.620\cdot10^{-6}\ \mathrm{Re}^2 - 2.992\cdot10^{-8}\ \mathrm{Re}^3 \qquad \text{(A1-8)}$$

$$d = -9.610\cdot10^{-7} - 2.54\cdot10^{-7}\ \mathrm{Re} + 1.74\cdot10^{-8}\ \mathrm{Re}^2 -5.10\cdot10^{-10}\ \mathrm{Re}^3 \qquad \text{(A1-9)}$$

In each of the regressions, equations A1-2 to A1-9, the collelation coefficient > 0.99.

Some comparisons between Woo's values and those calculated from equation A1-1 are as follows:

Re	Angle	ξ_s by Woo	ξ by eq. A1-1	Difference (%)
0.2	12	0.344	0.354	2.8
	24	0.670	0.684	2.1
	48	1.207	1.226	1.6
	72	1.517	1.540	1.5
	84	1.571	1.586	0.9
1.0	12	0.430	0.430	0
	24	0.830	0.823	0.8
	48	1.452	1.437	1.0
	72	1.742	1.740	0.1
	84	1.754	1.743	0.6
20	12	1.401	1.436	2.5
	24	2.639	2.635	0.2
	48	4.176	4.111	1.5
	72	4.129	4.147	0.4
	84	3.596	3.544	1.5
100	12	3.207	3.362	4.7
	27	6.630	6.700	1.0
	48	9.241	9.229	0.1
	72	8.163	8.400	2.8
	84	6.240	6.248	0.1

The effect of gas holdup upon surface vorticity has been obtained from the data of LeClair(74). LeClair reported ξ_s at Re = 0.1, 1, 10, 100, and 500. The following correlation was obtained using LeClair's data at Re = 0.1, 1, 10, 100 and 500; $\theta = 12, 24, 36, 48, 60, 72$ and 84°; and $\phi_g = 0, 0.091, 0.165$ and 0.259.

Let

$$\xi_{s\phi} = \xi_s + n\,\phi_g \tag{A1-10}$$

where $$n = a' + b'\,\theta + c'\,\theta^2 + d'\,\theta^3, \tag{A1-11}$$

$\xi_{s\phi}$ is surface vorticity at gas holdup ϕ_g,

and where

$$a' = -0.0199 + 3.30\cdot10^{-3}\,\text{Re} - 4.780\cdot10^{-5}\,\text{Re}^2 + 7.939\cdot10^{-8}\,\text{Re}^3 \tag{A1-12}$$

$$b' = 0.6579 - 7.91\cdot10^{-3}\,\text{Re} + 1.269\cdot10^{-4}\,\text{Re}^2 - 2.107\cdot10^{-7}\,\text{Re}^3 \tag{A1-13}$$

$$c' = -6.165\cdot10^{-4} + 3.499\cdot10^{-5}\,\text{Re} - 7.024\cdot10^{-7}\,\text{Re}^2 + 1.160\cdot10^{-9}\,\text{Re}^3 \tag{A1-14}$$

$$d' = -2.339\cdot10^{-5} + 5.305\cdot10^{-8}\,\text{Re} - 1.177\cdot10^{-9}\,\text{Re}^2 + 2.156\cdot10^{-12}\,\text{Re}^3 \tag{A1-15}$$

For each of equations A1-12 to A1-15 the correlation coefficient > 0.99.

A comparison between LeClair's values and those obtained from equations A1-10 and A1-1 is as follows:

Re	θ (degrees)	ϕ_g	ξ_s by LeClair	ξ_s by A1-10 and A1-1	Diff. (%)
100	36	0.091	10.59	10.67	0.1
		0.165	12.64	12.75	0.1
		0.259	15.39	15.38	0
100	72	0.091	11.94	12.11	1.4
		0.165	14.82	15.12	2.0
		0.259	18.75	18.95	1.0

B. Collision Efficiency at Intermediate Values of Stokes Number

The 40 sets of data used to calculate the correlation of equation 3.28, between collision efficiency E_C, Reynolds number of the bubble Re_b, Stokes number Sk, and the ratio of particle to bubble velocities u*, are given in Table A1-1. Also shown in the table is the regression analysis. The regression performed was log E_C vs log Re_b, log Sk and log u*.

Table Al - 1

Collision Efficiency Data
E_C From Trajectory Calculations

```
     RE          SK        G         EC
  100.000       .100      .025     1.020
  100.000       .200      .025     1.413
  100.000       .100      .050     1.013
  100.000       .200      .050     1.270
  100.000       .400      .050     2.444
  100.000       .100      .100     1.037
  100.000       .200      .100     1.196
  100.000       .400      .100     1.907
  100.000       .800      .100     3.271
  100.000       .200      .150     1.170
  100.000       .400      .150     1.615
  100.000       .800      .150     2.637
  100.000       .800      .250     2.108
   20.000       .100      .025     1.032
   20.000       .200      .025     1.242
   20.000       .100      .050     1.034
   20.000       .200      .050     1.196
   20.000       .400      .050     1.908
   20.000       .100      .100     1.027
   20.000       .200      .100     1.157
   20.000       .400      .100     1.639
   20.000       .800      .100     2.686
   20.000       .200      .150     1.130
   20.000       .400      .150     1.505
   20.000       .800      .150     2.275
   20.000       .400      .250     1.387
   20.000       .800      .250     1.912
  300.000       .100      .025     1.031
  300.000       .200      .025     1.653
  300.000       .100      .050     1.012
  300.000       .200      .050     1.442
  300.000       .400      .050     2.825
  300.000       .100      .100     1.012
  300.000       .200      .100     1.272
  300.000       .400      .100     2.098
  300.000       .800      .100     3.506
  300.000       .200      .150     1.213
  300.000       .400      .150     1.811
  300.000       .800      .150     2.800
  300.000       .800      .250     2.200

                REGRESSION ANALYSIS

 DEPENDENT VAR: LEC
 RANGE: 1 TO 40                              # OBS: 40

 VARIABLE              COEFF     STD ERR     T-STAT
 --------              -----     --- ---     ------
 CONSTANT               .487        .092      5.256
 LRE                    .059        .015      3.798
 LSK                    .542        .029     18.532
 LG                    -.157        .031     -5.027
 ---------------------------------------------------

 R-SQ:               .919 CORR R-SQ:           .912
 SER:                .110 SSR:                 .442
```

Appendix 2. Computer Programs

The flowsheets, listings and sample outputs for the following computer programs are given in this appendix.

A. SLIDE - calculates sliding time distribution.

B. COLLECT and COLLECT 2 - calculate collection efficiency. COLLECT is for $20 < Re_b < 400$ and COLLECT 2 is for $0.2 < Re_b < 20$.

C. FLOW - calculates particle trajectories ($Re_b = 20$)

D. COLUMN - calculates flotation column performance for scale-up.

Programs A, B and D are in Applesoft BASIC, and program C is in IBM BASIC.

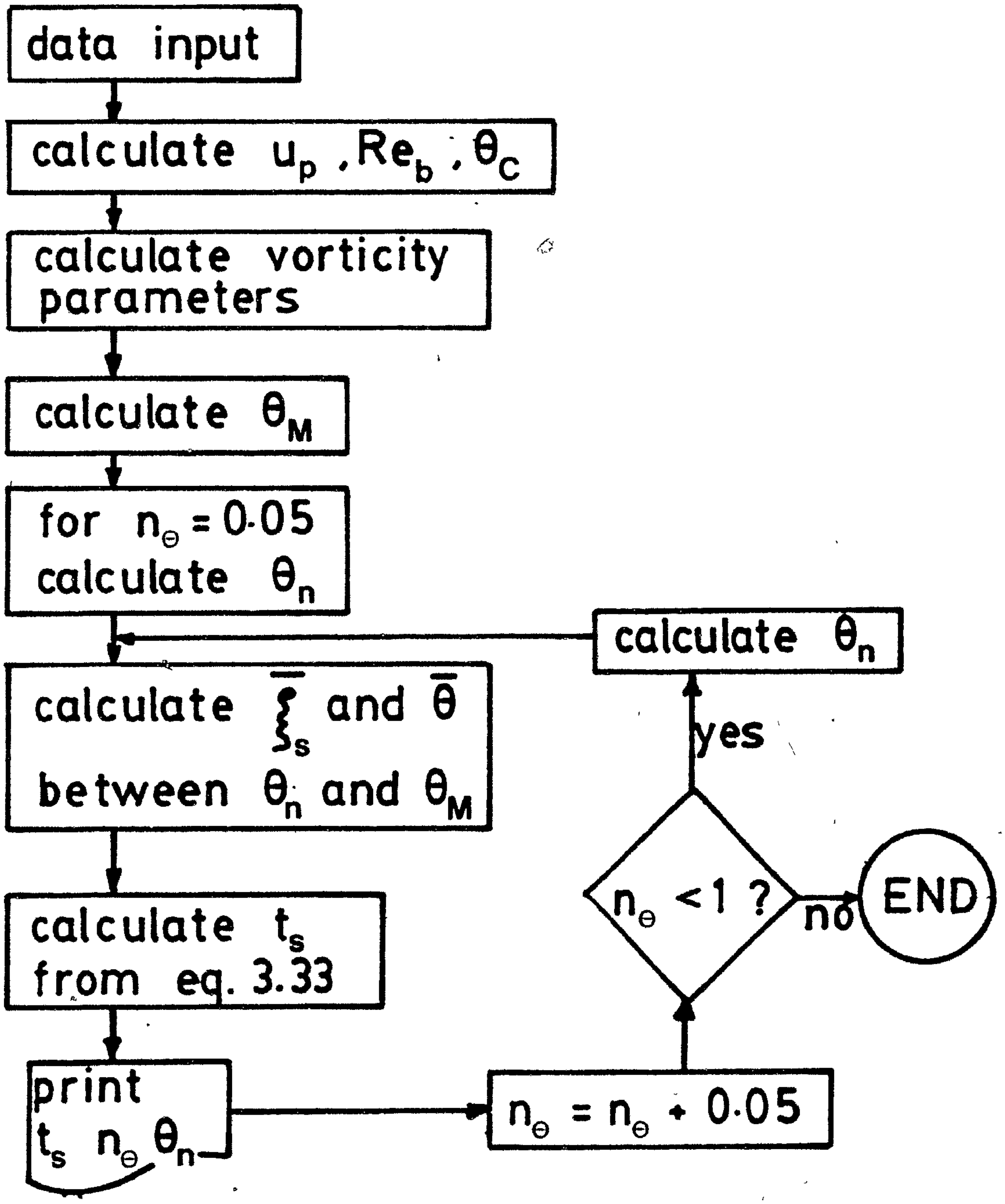

A2-1 Flowsheet for computer program SLIDE

SLIDE

```
10  REM    SLIDING TIME CALCULATION
15  REM
20  PRINT "DO YOU WANT TO PRINT? Y OR N"
25  GET A$
30  IF A$ = "N" THEN 70
35  PRINT : PRINT : PRINT
50  PRINT  CHR$ (4);"PR#1"
60  PRINT  CHR$ (9);"13L"
70  HOME
75  REM
76  REM     DATA ENTRY
77  REM
80  PRINT  SPC( 13);"SLIDING TIME DISTRIBUTION": PRINT : PRINT
90  INPUT "           DIA. BUBBLE(CM) = ";DB
100  INPUT "     VELOCITY BUBBLE(CM/S) = ";UB
110  INPUT "    DIA. PARTICLE(MICRONS) = ";DM
120  INPUT "          PARTICLE DENSITY = ";RHO
130  INPUT "          VISCOSITY(POISE) = ";VI
140  INPUT "             GAS HOLDUP(%) = ";PHI
145  INPUT "  INCREMENT(0.05 OR 0.005) = ";GG
150 DP = DM * .0001
155  REM
160  REM  CALC. UP
165  REM
170 P1 = (.0007653 * VI * VI / (RHO - 1)) ^ (1 / 3)
180 B1 = ((DP / P1) ^ 1.5 * 0.092 + 1)   0.5
190 UP = (20.52 * VI / DP) * (B1 - 1) * (B1 - 1)
235  REM
240  REM     CALCULATE RE(BUBBLE) & THETAC
245  REM
250 RZ = UB * DB / VI
255  IF RZ <  = 400 AND RZ    = 20 THEN 260
256  PRINT "**BUBBLE REYNOLDS NUMBER OUT OF RANGE**"
257  PRINT "     RANGE: 20   = RE   = 400"
258  PRINT ""
259  GOTO 1010
260 TC = 78.1 - 7.37 *  LOG (RZ) / 2.303
```

```
265  REM
270  REM     CALCULATE VORTICITY PARAMETERS
275  REM
280  REM      VORT(FOR HOLDUP=0)=A9+B9(ANGLE)+C9(ANGLE^2)+D9(ANGLE^3)

290 A9 =  - 0.01082 - 7.273E - 4 * RZ + 1.735E - 6 * RZ * RZ - 2.04
    6E - 9 * RZ * RZ * RZ
300 B9 = 0.0745 + 3.013E - 3 * RZ - 7.402E - 6 * RZ * RZ + 8.931E -
    9 * RZ * RZ * RZ
310 C9 =  - 4.276E - 4 - 1.977E - 5 * RZ + 5.194E - 8 * RZ * RZ - 6
    .52E - 11 * RZ * RZ * RZ
320 D9 =  - 1.103E - 6 - 1.032E - 7 * RZ + 1.397E - 10 * RZ * RZ -
    1.334E - 13 * RZ * RZ * RZ
330  REM     VORTICITY(HO)=VORTICITY(HO=0) + SLOPE*HO/100, WHERE
340  REM     SLOPE=A8+B8(ANGLE)+C8(ANGLE^2)+D8(ANGLE^3)
350 A8 =  - 0.0199 + 0.0033 * RZ - 4.780E - 5 * RZ * RZ + 7.939E -
    8 * RZ * RZ * RZ
360 B8 = 0.6579 - 0.00791 * RZ + 1.269E - 4 * RZ * RZ - 2.107E - 7
    * RZ * RZ * RZ
370 C8 =  - 6.165E - 4 + 3.499E - 5 * RZ - 7.024E - 7 * RZ * RZ + 1
    .16E - 9 * RZ * RZ * RZ
380 D8 =  - 2.339E - 5 + 5.305E - 8 * RZ - 1.177E - 9 * RZ * RZ + 2
    .156E - 12 * RZ * RZ * RZ
385  REM
390  REM      CALCULATE THETAM
395  REM
400 Q1 = TC
410 QA = Q1 - 0.25
420 QB = Q1 + 0.25
430 V1A = A9 + B9 * QA + C9 * QA * QA + D9 * QA * QA * QA
440 P1A = A8 + B8 * QA + C8 * QA * QA + D8 * QA * QA * QA
450 VA = V1A + P1A * PHI / 100
460 V1B = A9 + B9 * QB + C9 * QB * QB + D9 * QB * QB * QB
470 P1A = A8 + B8 * QB + C8 * QB * QB + D8 * QB * QB * QB
480 VB = V1B + P1B * PHI / 100
490 PA = 0.125 * DP * DP * UB * VA *  SIN (QA / 57.3)
500 PB = 0.125 * DP * DP * UB * VB *  SIN (QB / 57.3)
510 DT =  ABS ((PA - PB) * 57.3 / 0.5)
520 VR = DT / ( SIN (Q1 / 57.3) * (0.5 * (DP + DB)) ^ 2)
530 VP = UP *  COS (Q1 / 57.3)
540  IF VR > VP THEN 570
550 Q1 = Q1 + 0.25
560  GOTO 410
570 TM = Q1
580  DEF  FN RD(XX) =  INT (XX * 100 + 0.5) / 100
590  DEF  FN RM(XX) =  INT (XX * 10000 + 0.5) / 10000
620  PRINT " PARTICLE TERM. VEL.(CM/S) = "; FN RM(UP)
625  PRINT "     BUBBLE REYNOLDS NUMBER = "; FN RD(RZ)
630  PRINT  SPC( 20);"THETAC = "; FN RD(TC)
640  PRINT  SPC( 20);"THETAM = "; FN RD(TM)
```

```
650  PRINT : PRINT : PRINT
670  PRINT " SLIDING TIME      WEIGHT %      ANGLE    NUMBER OF"
680  PRINT "    (MS)        GREATER THAN   (DEGREES)  ROTATIONS": P
     RINT
685  REM
690  REM   **CALCULATION OF SLIDING TIME**
695  REM
700  FOR JJ = 1 TO 19
710 SS = GG * JJ
712  REM   COLLISION ANGLE IS TS
715 X1 =  SQR (SS) *  SIN (TC / 57.3)
720 TS = 57.3 *  ATN (X1 /  SQR ( - X1 * X1 + 1))
730 D2T = (TM - TS) / 20
740  REM   CALC. AVE. VORTICITY & AVE. ANGLE BETWEEN TS & TM
750 VO = 0
760 A1ANGL = 0
770  FOR LL = 1 TO 20
780 TJ = TS + (LL - 0.5) * D2T
790 V1A = A9 + B9 * TJ + C9 * TJ * TJ + D9 * TJ * TJ * TJ
800 P1A = A8 + B8 * TJ + C8 * TJ * TJ + D8 * TJ * TJ * TJ
810 VA = V1A + P1A * PHI / 100
820 A2ANGL =  SIN (TJ / 57.3)
830 A1ANGL = A1ANGL + A2ANGL
840 VO = VO + VA
850  NEXT LL
860 VO = VO / 20
870 A1ANGL = A1ANGL / 20
880  REM   CALCULATE SLIDING TIME
900  IF (DP / DB) < 0.03 THEN 930
910 T1S = 0.7 * 0.03 * VO * UB * (DB / DP) * (2 * (DP / DB) - 0.03)
     + UP *  SIN (A1ANGL)
920  GOTO 940
930 T1S = 0.7 * UB * DP * VO / DB + UP *  SIN (A1ANGL)
940 T2S = 8.73 * (TM - TS) * DB
950 T3S = T2S / T1S
960  REM   CALCULATE # OF ROTATIONS
970 P8PERIOD = 6283 * DB / (0.7 * VO * UB)
980 R1 = T3S / P8PERIOD
990  PRINT  TAB( 5): FN RD(T3S): TAB( 21): FN RD(SS * 100): TAB( 34
     ): FN RD(TS): TAB( 45): FN RD(R1)
1000  NEXT JJ
1010  PRINT  CHR$ (4);"PR#0"
1015  PRINT "TO CONTINUE: 1.SET PRINTER TO NEW PAGE. 2.PRESS C.  TO
      ESCAPE: ANY OTHER KEY"
1020  GET A$
1030  IF A$ = "C" THEN 20
1100  END
```

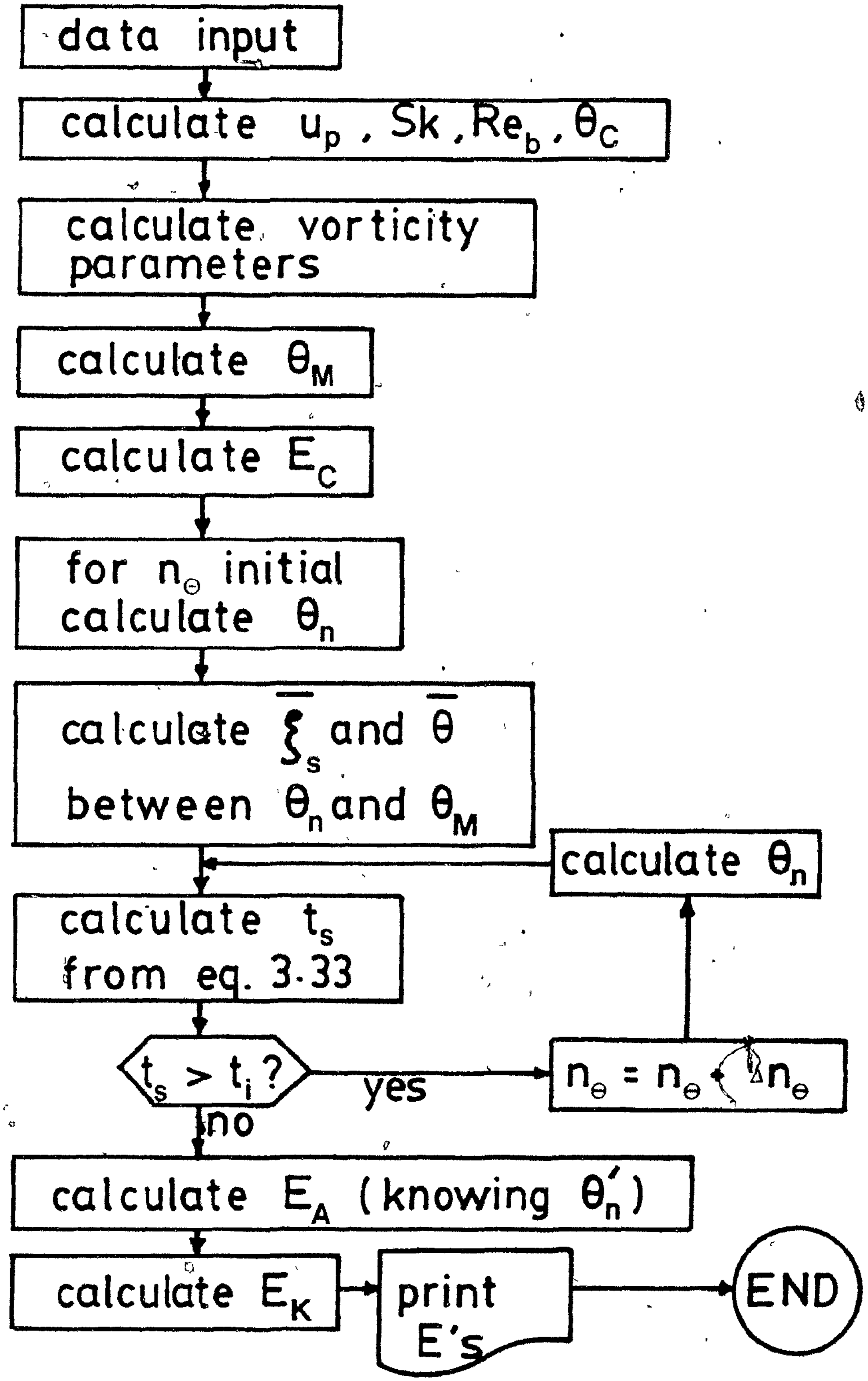

A2-2 Flowsheet for computer programs COLLECT and COLLECT 2

COLLECT

```
10  REM   ****COLLECTION EFFICIENCY****
15  REM
20  PRINT "DO YOU WANT TO PRINT? Y OR N"
25  GET A$
30  IF A$ = "N" THEN 70
35  PRINT : PRINT : PRINT
50  PRINT  CHR$ (4);"PR#1"
60  PRINT  CHR$ (9);"13L"
70  HOME
75 P2 = 0
77  REM
78  REM      DATA ENTRY
79  REM
80  PRINT  SPC( 13);"***COLLECTION EFFICIENCY***"
85  PRINT  SPC( 13);" BUBBLE RE: 20 - 400": PRINT : PRINT
90  INPUT "                DIA. BUBBLE(CM) = ";DB
100  INPUT "      VELOCITY BUBBLE(CM/S) = ";UB
120  INPUT "             PARTICLE DENSITY = ";RHO
130  INPUT "             VISCOSITY(POISE) = ";VI
140  INPUT "                GAS HOLDUP(%) = ";PHI
145  INPUT "       INDUCTION TIME(MSEC) = ";TTI
147  INPUT "STARTING PARTICLE DIA.(MICRONS) = ";DM
148  INPUT "     MAX. PARTICLE DIA.(MICRONS) = ";DX
149  INPUT "     INCREMENT PARTICLE DIAMETER = ";DQ
159  REM
160  REM    CALC. UP & STOKES #(KK)
161  REM
162  DEF  FN RD(XX) =  INT (XX * 100 + 0.5) / 100
163  DEF  FN RT(XX) =  INT (XX * 1000000 + 0.5) / 1000000
164  DEF  FN RM(XX) =  INT (XX * 10000 + 0.5) / 10000
167 DP = DM * 0.0001
168 GG = 0.05
170 P1 = (.0007653 * VI * VI / (RHO - 1)) ^ (1 / 3)
180 B1 = ((DP / P1) ^ 1.5 * 0.0921 + 1) ^ 0.5
190 UP = (20.52 * VI / DP) * (B1 - 1) * (B1 - 1)
232 KK = RHO * DP * DP * UB / (9 * VI * DB)
235  IF P2 > 0 THEN 400
240  REM      CALCULATE RE(BUBBLE) & THETAC
250 RZ = UB * DB / VI
255  IF RZ <  = 400 AND RZ >  = 20 THEN 260
256  PRINT "**BUBBLE REYNOLDS NUMBER OUT OF RANGE**"
257  PRINT "     RANGE: 20  <= RE<= 400": PRINT : PRINT
258  PRINT ""
259  GOTO 1100
260 TC = 78.1 - 7.37 *  LOG (RZ) / 2.303
```

```
265  REM
270  REM     CALCULATE VORTICITY PARAMETERS
275  REM
280  REM      VORT(FOR HOLDUP=0)=A9+B9(ANGLE)+C9(ANGLE^2)+D9(ANGLE^3)

290 A9 =  - 0.01082 - 7.273E - 4 * RZ + 1.735E - 6 * RZ * RZ - 2.04
    6E - 9 * RZ * RZ * RZ
300 B9 = 0.0745 + 3.013E - 3 * RZ - 7.402E - 6 * RZ * RZ + 8.931E -
    9 * RZ * RZ * RZ
310 C9 =  - 4.276E - 4 - 1.977E - 5 * RZ + 5.194E - 8 * RZ * RZ - 6
    .52E - 11 * RZ * RZ * RZ
320 D9 =  - 1.103E - 6 - 1.032E - 7 * RZ + 1.397E - 10 * RZ * RZ -
    1.334E - 13 * RZ * RZ * RZ
330  REM     VORTICITY(HO)=VORTICITY(HO=0) + SLOPE*HO/100, WHERE
340  REM     SLOPE=A8+B8(ANGLE)+C8(ANGLE^2)+D8(ANGLE^3)
350 A8 =  - 0.0199 + 0.0033 * RZ - 4.780E - 5 * RZ * RZ + 7.939E -
    8 * RZ * RZ * RZ
360 B8 = 0.6579 - 0.00791 * RZ + 1.269E - 4 * RZ * RZ - 2.107E - 7
    * RZ * RZ * RZ
370 C8 =  - 6.165E - 4 + 3.499E - 5 * RZ - 7.024E - 7 * RZ * RZ + 1
    .16E - 9 * RZ * RZ * RZ
380 D8 =  - 2.339E - 5 + 5.305E - 8 * RZ - 1.177E - 9 * RZ * RZ + 2
    .156E - 12 * RZ * RZ * RZ
385  REM
390  REM      CALCULATE THETAM
395  REM
400 Q1 = TC
410 QA = Q1 - 0.25
420 QB = Q1 + 0.25
430 V1A = A9 + B9 * QA + C9 * QA * QA + D9 * QA * QA * QA
440 P1A = A8 + B8 * QA + C8 * QA * QA + D8 * QA * QA * QA
450 VA = V1A + P1A * PHI / 100
460 V1B = A9 + B9 * QB + C9 * QB * QB + D9 * QB * QB * QB
470 P1A = A8 + B8 * QB + C8 * QB * QB + D8 * QB * QB * QB
480 VB = V1B + P1B * PHI / 100
490 PA = 0.125 * DP * DP * UB * VA *  SIN (QA / 57.3)
500 PB = 0.125 * DP * DP * UB * VB *  SIN (QB / 57.3)
510 DT =  ABS ((PA - PB) * 57.3 / 0.5)
520 VR = DT / ( SIN (Q1 / 57.3) * (0.5 * (DP + DB)) ^ 2)
530 VP = UP *  COS (Q1 / 57.3)
540  IF VR [illegible] VP THEN 558
550 Q1 = Q1 + 0.25
555  GOTO 410
558 TM = Q1
565  REM  571
568  REM      CALCULATE COLLISION EFFICIENCY
570  REM
571  REM  ****CALCULATE COLLISION EFFICIENCIES***
572 UU = UP / UB
573 DD = DP / DB
574 EG = (UU * (1 + DD) ^ 2) *  SIN (TC / 57.3) ^ 2 / (1 + UU)
575 ES = 1.5 * DD * DD / (1 + UU)
576 EI = ES * (1 + (0.1875 * RZ) / (1 + 0.249 * RZ ^ 0.56))
```

```
578 EC = EI + EG
579 X8 = (RZ ^ 0.06) * (KK ^ 0.54) / (UU ^ 0.16)
580  IF X8 < 0.614 THEN 610
590 EC = EC * 1.627 * X8
610  IF P2 > 0 THEN 700
620  PRINT
625  PRINT  SPC( 17);"RE BUBBLE = "; FN RD(RZ)
630  PRINT  SPC( 20);"THETAC = "; FN RD(TC): PRINT : PRINT
640  PRINT "DIA. PARTICLE   COLLISION   ATTACHMENT   COLLECTION"
642  PRINT "  (MICRONS)       EC(%)          EA(%)          EK(%)"
685  REM
690  REM       CALCULATE ATTACHMENT EFFICIENCY
695  REM
700  FOR JJ = 1 TO 19
710 SS = GG * JJ
715  REM   COLLISION ANGLE IS TS
719 X1 =  SQR (SS) *  SIN (TC / 57.3)
720 TS = 57.3 *  ATN (X1 /  SQR ( - X1 * X1 + 1))
721 T8 = TS
730 D2T = (TM - TS) / 20
740  REM  CALC. AVE. VORTICITY & AVE. ANGLE BETWEEN TS & TM
750 VO = 0
760 A1ANGL = 0
770  FOR LL = 1 TO 20
780 TJ = TS + (LL - 0.5) * D2T
790 V1A = A9 + B9 * TJ + C9 * TJ * TJ + D9 * TJ * TJ * TJ
800 P1A = A8 + B8 * TJ + C8 * TJ * TJ + D8 * TJ * TJ * TJ
810 VA = V1A + P1A * PHI / 100
820 A2ANGL =  SIN (TJ / 57.3)
830 A1ANGL = A1ANGL + A2ANGL
840 VO = VO + VA
850  NEXT LL
860 VO = VO / 20
870 A1ANGL = A1ANGL / 20
880  REM   CALC. SLIDING TIME
900  IF (DP / DB) < 0.030 THEN 930
910 T1S = 0.7 * 0.03 * VO * UB * (DB / DP) * (2 * (DP / DB) - 0.
    + UP *  SIN (A1ANGL)
920  GOTO 940
930 T1S = 0.7 * UB * DP * VO / DB + UP *  SIN (A1ANGL)
940 T2S = 8.73 * (TM - TS) * DB
950 T3S = T2S / T1S
955  REM     IS SMALLER INCREMENT(GG) REQ'D? (FOR WHEN ATT. EFF. I
     LOW)
960  IF T3S < = TTI GOTO 984
970 SK = SS
975 T46 = T3S
980  NEXT JJ
```

```
984  IF SS = 0.0025 THEN 994
985  IF SS = 0.05 THEN 992
986  IF TTI < T3S THEN 996
990 A1E = SS - GG * (TTI - T3S) / (T4S - T3S)
991  GOTO 999
992 GG = 0.0025
993  GOTO 700
994 GG = .000125
995  GOTO 700
996 A1E = SS + GG * (1 - TTI / T4S)
997  REM
998  REM   CALCULATE COLLECTION EFFICIENCY & PRINT RESULTS
999 EK = EC * A1E
1000  PRINT  TAB( 5); FN RD(DM); TAB( 18); FN RM(EC * 100); TAB( 3
      ); FN RD(A1E * 100); TAB( 44); FN RT(EK * 100)
1002  IF DM >  = DX THEN 1100
1004 DM = DM + DQ
1006 P2 = P2 + 1
1008  GOTO 167
1100  PRINT  CHR$ (4);"PR#0"
1110  PRINT "TO CONTINUE: 1.SET PRINTER TO NEW PAGE, 2.PRESS C.   T
      ESCAPE: ANY OTHER KEY"
1120  GET A$
1130  IF A$ = "C" THEN 20
1140  END
```

COLLECT2

```
10  REM    ****COLLECTION EFF. - LOW RE****
15  REM
20  PRINT "DO YOU WANT TO PRINT? Y OR N"
25  GET A$
30  IF A$ = "N" THEN 70
35  PRINT : PRINT : PRINT
50  PRINT  CHR$ (4);"PR#1"
60  PRINT  CHR$ (9);"13L"
70  HOME
75 P2 = 0
77  REM
78  REM     DATA ENTRY
79  REM
80  PRINT  SPC( 13);"***COLLECTION EFFICIENCY***"
85  PRINT  SPC( 13);" BUBBLE RE:0.1 - 20  ": PRINT : PRINT
90  INPUT "             DIA. BUBBLE(CM) = ";DB
100  INPUT "      VELOCITY BUBBLE(CM/S) = ";UB
120  INPUT "            PARTICLE DENSITY = ";RHO
130  INPUT "            VISCOSITY(POISE) = ";VI
140  INPUT "               GAS HOLDUP(%) = ";PHI
145  INPUT "        INDUCTION TIME(MSEC) = ";TTI
147  INPUT "STARTING PARTICLE DIA.(MICRONS) = ";DM
148  INPUT "     MAX. PARTICLE DIA.(MICRONS) = ";DX
149  INPUT "     INCREMENT PARTICLE DIAMETER = ";DQ
159  REM
160  REM    CALC. UP & STOKES # (KK)
161  REM
162  DEF  FN RD(XX) =  INT (XX * 100 + 0.5) / 100
163  DEF  FN RT(XX) =  INT (XX * 1000000 + 0.5) / 1000000
164  DEF  FN RM(XX) =  INT (XX * 10000 + 0.5) / 10000
167 DP = DM * 0.0001
168 GG = 0.05
170 P1 = (.0007653 * VI * VI / (RHO - 1))   (1 / 3)
180 B1 = ((DP / P1) ^ 1.5 * 0.092 + 1)   0.5
190 UP = (20.52 * VI / DP) * (B1 - 1) * (B1 - 1)
232 Kk = RHO * DP * DP * UB / (9 * VI * DB)
235  IF P2 < > 0 THEN 400
240  REM      CALCULATE RE(BUBBLE) & THETAC
250 RZ = UB * DB / VI
255  IF RZ <  = 20 AND RZ >  = 0.1 THEN 260
256  PRINT "**BUBBLE REYNOLDS NUMBER OUT OF RANGE**"
257  PRINT "     RANGE: 0.1  = RE  = 20": PRINT : PRINT
258  PRINT ""
259  GOTO 1100
260  IF RZ < 1.0 THEN 266
262 TC = 98.0 - 12.49 *  LOG (10 * RZ) / 2.303
264  GOTO 290
266 TC = 90.0 - 2.5 *  LOG (100 * RZ) / 2.303
```

```
269  REM
270  REM     CALCULATE VORTICITY PARAMETERS
275  REM
280  REM      VORT(FOR HOLDUP=0)=A9+B9(ANGLE)+C9(ANGLE^2)+D9(ANGLE^

285  REM
290 A9 =  - 0.001217 - 0.001745 * RZ + 5.143E - 5 * RZ * RZ - 1.16
    E - 6 * RZ * RZ * RZ
300 B9 = 0.0286 + 9.229E - 3 * RZ - 3.85E - 4 * RZ * RZ + 9.190E -
    6 * RZ * RZ * RZ
310 C9 =  - 4.060E - 5 - 0.586E - 4 * RZ + 1.620E - 6 * RZ * RZ -
    .992E - 8 * RZ * RZ * RZ
320 D9 =  - 9.610E - 7 - 2.540E - 7 * RZ + 1.740E - 8 * RZ * RZ -
    .100E - 10 * RZ * RZ * RZ
330  REM     VORTICITY(HO)=VORTICITY(HO=0) + SLOPE*HO/100, WHERE
340  REM     SLOPE=A8+B8(ANGLE)+C8(ANGLE^2)+D8(ANGLE^3)
350 A8 =  - 0.0199 + 0.0033 * RZ - 4.780E - 5 * RZ * RZ + 7.939E -
    8 * RZ * RZ * RZ
360 B8 = 0.6579 - 0.00791 * RZ + 1.269E - 4 * RZ * RZ - 2.107E - 7
    * RZ * RZ * RZ
370 C8 =  - 6.165E - 4 + 3.499E - 5 * RZ - 7.024E - 7 * RZ * RZ +
    .16E - 9 * RZ * RZ * RZ
380 D8 =  - 2.339E - 5 + 5.305E - 8 * RZ - 1.177E - 9 * RZ * RZ +
    .156E - 12 * RZ * RZ * RZ
385  REM
390  REM      CALCULATE THETAM
395  REM
400 Q1 = TC
410 QA = Q1 - 0.25
420 QB = Q1 + 0.25
430 V1A = A9 + B9 * QA + C9 * QA * QA + D9 * QA * QA * QA
440 P1A = A8 + B8 * QA + C8 * QA * QA + D8 * QA * QA * QA
450 VA = V1A + P1A * PHI / 100
460 V1B = A9 + B9 * QB + C9 * QB * QB + D9 * QB * QB * QB
470 P1A = A8 + B8 * QB + C8 * QB * QB + D8 * QB * QB * QB
480 VB = V1B + P1B * PHI / 100
490 PA = 0.125 * DP * DP * UB * VA *  SIN (QA / 57.3)
500 PB = 0.125 * DP * DP * UB * VB *  SIN (QB / 57.3)
510 DT =  ABS ((PA - PB) * 57.3 / 0.5)
520 VR = DT / ( SIN (Q1 / 57.3) * (0.5 * (DP + DB)) ^ 2)
530 VP = UP *  COS (Q1 / 57.3)
540  IF VR > VP THEN 558
550 Q1 = Q1 + 0.25
555  GOTO 410
558 TM = Q1
565  REM
568  REM     CALCULATE COLLISION EFFICIENCY
570  REM
572 UU = UP / UB
573 DD = DP / DB
574 EG = (UU * (1 + DD) ^ 2) *  SIN (TC / 57.3) ^ 2 / (1 + UU)
575 ES = 1.5 * DD * DD / (1 + UU)
576 EI = ES * (1 + 0.1875 * RZ) / (1 + 0.249 * RZ ^ 0.56)
```

```
577 EC = EG + EI
579 X8 = (RZ ^ 0.06) * (KK ^ 0.54) / (UU ^ 0.16)
580  IF X8 < 0.614 THEN 610
590 EC = EC * 1.627 * X8
610  IF P2 > 0 THEN 700
620  PRINT
625  PRINT  SPC( 17);"RE BUBBLE = "; FN RD(RZ)
630  PRINT  SPC( 20);"THETAC = "; FN RD(TC): PRINT : PRINT
640  PRINT "DIA. PARTICLE   COLLISION   ATTACHMENT   COLLECTION"
642  PRINT "  (MICRONS)       EC(%)          EA(%)          EK(%)"
685  REM
690  REM   CALCULATE ATTACHMENT EFFICIENCY
695  REM
700  FOR JJ = 1 TO 19
710 SS = GG * JJ
715  REM  COLLISION ANGLE IS TS
719 X1 =  SQR (SS) *  SIN (TC / 57.3)
720 TS = 57.3 *  ATN (X1 /  SQR ( - X1 * X1 + 1))
721 T8 = TS
730 D2T = (TM - TS) / 20
740  REM   CALC. AVE. VORTICITY & AVE. ANGLE BETWEEN TS & TM
750 VO = 0
760 A1ANGL = 0
770  FOR LL = 1 TO 20
780 TJ = TS + (LL - 0.5) * D2T
790 V1A = A9 + B9 * TJ + C9 * TJ * TJ + D9 * TJ * TJ * TJ
800 P1A = A8 + B8 * TJ + C8 * TJ * TJ + D8 * TJ * TJ * TJ
810 VA = V1A + P1A * PHI / 100
820 A2ANGL =  SIN (TJ / 57.3)
830 A1ANGL = A1ANGL + A2ANGL
840 VO = VO + VA
850  NEXT LL
860 VO = VO / 20
870 A1ANGL = A1ANGL / 20
880  REM  CALC. SLIDING TIME
900  IF (DP / DB) < 0.03 THEN 930
910 T1S = 0.7 * 0.03 * VO * UB * (DB / DP) * (2 * (DP / DB) - 0.03
    + UP *  SIN (A1ANGL)
920  GOTO 940
930 T1S = 0.7 * UB * DP * VO / DB + UP *  SIN (A1ANGL)
940 T2S = 8.73 * (TM - TS) * DB
950 T3S = T2S / T1S
955  REM  IS SMALLER INCREMENT(GG) REQ'D? (FOR WHEN ATT. EFF. IS L
    W)
960  IF T3S <  = TTI GOTO 984
970 SK = SS
975 T4S = T3S
980  NEXT JJ
```

```
984  IF SS = 0.0025 THEN 994
985  IF SS = 0.05 THEN 992
986  IF TTI < T3S THEN 996
990 A1E = SS - GG * (TTI - T3S) / (T4S - T3S)
991  GOTO 999
992 GG = 0.0025
993  GOTO 700
994 GG = 0.000125
995  GOTO 700
996 A1E = SS + GG * (1 - TTI / T4S)
997  REM
998  REM   CALCULATE COLLECTION EFFICIENCY AND PRINT RESULTS
999 EK = EC * A1E
1000  PRINT  TAB( 5); FN RD(DM); TAB( 18); FN RM(EC * 100); TAB( 3
       ); FN RD(A1E * 100); TAB( 44); FN RM(EK * 100)
1002  IF DM >  = DX THEN 1100
1004 DM = DM + DQ
1006 P2 = P2 + 1
1008  GOTO 167
1100  PRINT  CHR$ (4);"PR#0"
1110  PRINT "TO CONTINUE: 1.SET PRINTER TO NEW PAGE, 2.PRESS C.  T
      ESCAPE: ANY OTHER KEY"
1120  GET A$
1130  IF A$ = "C" THEN 20
1140  END
```

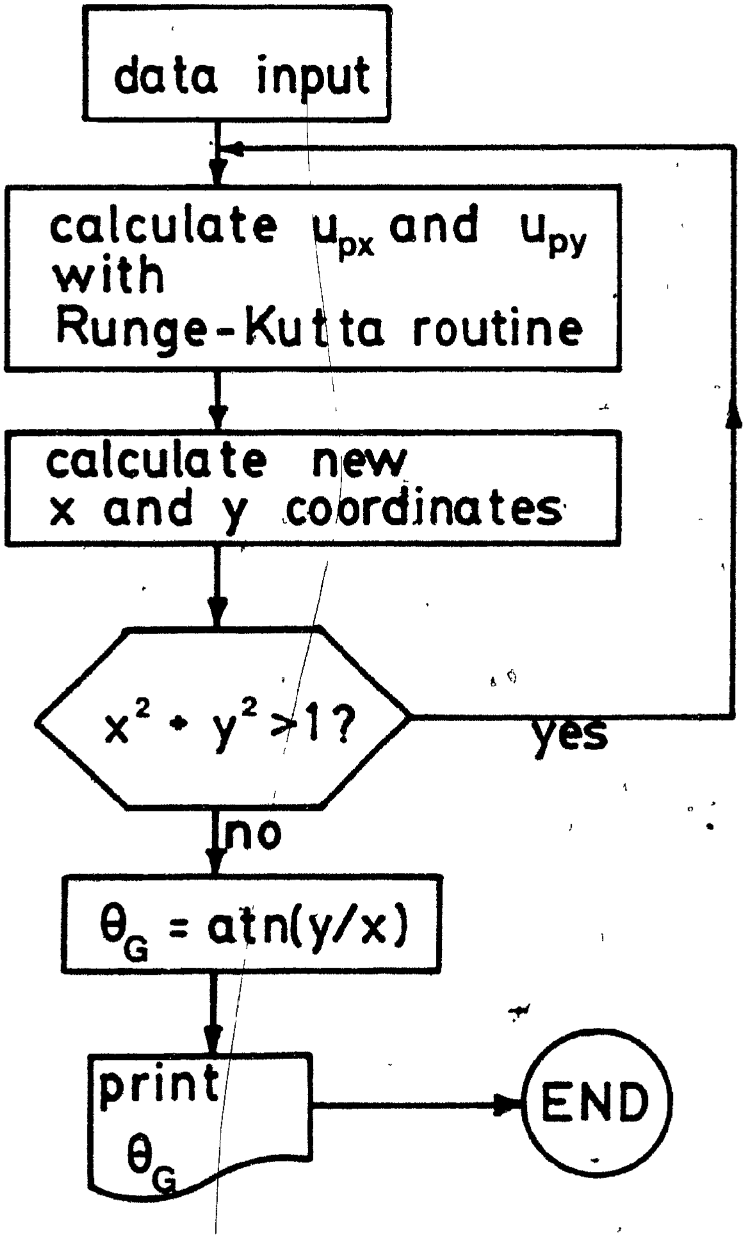

A2-3 Flowsheet for computer program FLOW

FLOW (FLOW20)

```
0010 PRINT '                    FLOW PROFILE - RE=20 '
0012 REM  ***** X AND Y ARE STARTING COORDINATES
0014 REM   ***  G IS THE RATIO OF U(PARTICLE) TO U(BUBBLE)
0016 REM   ***  K IS THE STOKES NUMBER
0018 REM    *   D IS THE RUNGE-KUTTA INCREMENT(H)
0020 PRINT 'INPUT X, Y, G,K '
0030 INPUT X5,Y5,G,K
0045 D =0.02
0050  R=(X5**2+Y5**2)**0.5
0060 T =ATN(Y5/X5)
0070 N1=0
0090 H=1
0120 GOTO 1020
0130 V =           7.556*T -2.636*T *T -0.5854*T**3
0140 F1  =(1+1/(2* R**3))*SIN(T)
0150 F2  =(1-1/(R **3))*COS(T )
0160 S1  =(1-0.75/R -0.25/( R**3))*SIN(T)
0170 S2  =(1-1.5/R +0.5/( R**3))*COS(T )
0210 U1 =(( R-0.99)**2-( R-1.01)**2)*V  /(0.04*R )
0220 U2 =0.68*F1  +0.32*S1
0230 IF U2    U1  THEN 260
0240 U0=U2
0250 GOTO 290
0260 U0=U1
0270 H=2
0290 U3=0.56*F2  +0.44*S2
0310 T =T +0.008726
0320 V  =-0.0247+ 7.556*T -2.636*T *T -.5854*T **3
0330 C1=0.5*( R-1)**2*V  *SIN(T )
0340 T =T -0.017452
0350 V =-0.0247+ 7.556*T -2.636*T *T -.5854*T **3
0360 C2=0.5*( R-1)**2*V  *SIN(T )
0370 T =T +0.008726
0380 U9=(1/( R* R*SIN(T )))*(C1-C2)/0.017452
0382 IF U3   U9 THEN 391
0384 U9 = U3
0391 IF N1   0 THEN 400
0392 V1 = U9*COS(T) + U0*SIN(T) + G
0393 W1 = U0*COS(T) - U9*SIN(T)
0394 X5 = X5 - V1*D
0395 Y5 = Y5 + W1*D
0398 GOTO 930
```

```
0400 V2 = U9*COS(T) + U0*SIN(T) +G
0410 W2 = U0*COS(T) - U9*SIN(T)
0420 K1 = (-V1 + V2)/K
0430 K2 = (-V1 - 0.5*D*K1 + V2)/K
0440 K3 = (-V1 - 0.5*D*K2 + V2)/K
0450 K4 = (-V1 - D*K3 + V2)/K
0460 V3 = V1 + (D/6)*(K1 + 2*K2 + 2*K3 + K4)
0470 L1 = (-W1 +W2)/K
0480 L2 = (-W1 - 0.5*D*L1 + W2)/K
0490 L3 = (-W1 - 0.5*D*L2 + W2)/K
0500 L4 = (-W1 -D*L3 + W2)/K
0510 W3 = W1 + (D/6)*(L1 + 2*L2 + 2*L3 + L4)
0520 X5 = X5 - V3*D
0530 Y5 = Y5 + W3*D
0540 V1 = V3
0550 W1 = W3
0930 R = (X5**2 + Y5**2)**0.5
0940 T =ATN(Y5/X5)
0980 N1=N1+1
1000 IF (T *57.3)   0 THEN 1180
1010 RETURN
1020 GOSUB 130
1030 IF R    1.1001  THEN 1180
1040 GOTO 1020
1180 PRINT "THETA=";(T *57.3)
1200 PRINT "     R=";R
1210 PRINT "LOOPS=";N1
1220 PRINT "MORE? YES-1 NO-2"
1230 INPUT Z
1240 IF Z=1 GOTO 10
1250 END
```

COLUMN

```
10   REM  FLOTATION COLUMN SCALE-UP
20   REM
30   REM     *DATA ENTRY*
35   REM
40   PRINT " PRINT?  Y OR N"
50   GET B$
60   IF B$ = "N" THEN 100
70   PRINT : PRINT
80   PRINT  CHR$ (4);"PR#1"
90   PRINT  CHR$ (9);"17L"
100  HOME
105  DEF  FN RD(XX) =  INT (XX * 100 + 0.5) / 100
110  PRINT  SPC( 13);"FLOTATION COLUMN SCALE-UP": PRINT : PRINT

120  PRINT  SPC( 20);"***DATA INPUT***": PRINT : PRINT
130  INPUT "         COLUMN DIAMETER(M) = ";DC
140  INPUT "COLLECTION ZONE LENGTH(M) = ";L1
145 L8 = L1
150  INPUT "           FEED RATE(L/MIN) = ";QF
160  INPUT "       TAILINGS RATE(L/MIN) = ";QT
170  INPUT "            GAS RATE(L/MIN) = ";QG
180  INPUT "              GAS HOLDUP(%) = ";QH
185  INPUT "        BUBBLE DIAMETER(CM) = ";DB
190  REM  SUPERFICIAL VELOCITY - V(CM/S)
200  REM  ACTUAL VELOCITIES - U(CM/S)
210 A1 = 0.25 * 3.1416 * DC * DC
220 VG = QG / (60000 * A1)
230 VF = QT / (60000 * A1)
240 UF = VF / (1 - QH / 100)
242  PRINT " SUPERFICIAL GAS VELOCITY = "; FN RD(VG * 100);"CM/S"
244  PRINT "     SLURRY VELOCITY(DOWN) = "; FN RD(UF * 100);"CM/S"
250  PRINT : PRINT  SPC( 18);"FEED DESCRIPTION": PRINT
260  INPUT "      FEED WEIGHT % SOLIDS = ";FT
270  INPUT "     AVE PARTICLE SIZE(UM) = ";DM
280 DP = DM / 10000
290  INPUT "     # OF MINERALS IN FEED = ";NM%
300  PRINT  SPC( 13);"(TOTAL MUST = 100%)"
310 N1 = 1
315  DIM K(10,10),P3(10,10),R(10,10)
317 S1G = 0
320  FOR I = N1 TO NM%
325  PRINT
330  INPUT "              MINERAL NAME : ";A$(I)
340  INPUT "          SPECIFIC GRAVITY = ";SG(I)
350  INPUT "            FEED GRADE (%) = ";P4(I)
360 P1(I) = P4(I) / 100
```

```
370  FOR J = N1 TO 2
380  INPUT "ENTER  K  AND  PROPORTION : ";K(I,J),P3(I,J)
400  NEXT J
410 S1G = S1G + SG(I) * P1(I)
420  NEXT I
421 FS = 100 / ((100 * S1G / FT) - S1G + 1)
422 T8P = 6E - 4 * QF * FS * S1G
423  PRINT "      FEED VOLUME % SOLIDS = "; FN RD(FS)
424  PRINT "          FEED MTPH SOLIDS =  "; FN RD(T8P)
425  PRINT : PRINT : PRINT  SPC( 20);"***RESULTS***": PRINT : PRINT

427  PRINT  SPC( 26);"%RECOVERY    GRADE(%)"
430  REM
440  REM   *RECOVERY CALCULATION*
450  REM
455 R5F = 1
460 D1 = 0.063 * DC
490  REM      CALC. PARTICLE VELOCITY
500 B1 = (7.653E - 8 / (S1G - 1)) ^ (1 / 3)
510 B2 = ((DP / B1) ^ 1.5 * 0.0921 + 1) ^ 0.5
520 UP = (0.206 / DP) * (B2 - 1) * (B2 - 1)
525 UP = UP * ((1 - FS / 100) ^ 4.65)
530 U1P = UP / 100 + UF
535  REM   CALCULATE MIXING PARAMETERS
540 ND = D1 / (U1P * L1)
550 T1 = L1 / (U1P * 60)
555 R2 = 0
560  FOR I = N1 TO 2
565 R1(I) = 0
570  FOR J = N1 TO NK(I)
580 A4 = (1 + 4 * K(I,J) * T1 * ND) ^ 0.5
590 A5 = 4 * A4 *  EXP (1 / (2 * ND))
600 A6 = ((1 + A4) ^ 2) *  EXP (A4 / (2 * ND))
610 A7 = ((1 - A4) ^ 2) *  EXP ( - A4 / (2 * ND))
620 R(I,J) = 1 - A5 / (A6 - A7)
630 R1(I) = R1(I) + R(I,J) * P3(I,J)
640  NEXT J
650 R2 = R2 + R1(I) * P1(I)
660  NEXT I
670  REM   TOTAL WT. RECOVERY IS R2*100%
680  REM   INDIVIDUAL MINERAL REC'Y IS RI(I)*100%
690 R3 = 0
700  FOR I = N1 TO NM%
710 RT(I) = R1(I) * R5F / (1 - R1(I) * (1 - R5F))
720 R3 = R3 + RT(I) * P1(I)
730  NEXT I
```

```
740  REM
750  REM    *CALCULATE BUBBLE LOAD*
755  REM
760  REM   RECYCLE LOAD IS R7C
765 R7C = (1 / (1 - R2 * (1 - R5F))) - 1
770 GS = QF * FS * S1G * R2 * 10 * (1 + R7C)
780 L4 = GS / (QG * 1000)
790 L5 = 0.8 * 6 * DP * S1G / DB
800  IF L5 > L4 THEN 830
810 L1 = L1 * 0.9
820  GOTO 540
824  REM
825  REM   *PRINT RESULTS*
826  REM
830  PRINT : PRINT : PRINT "  FOR FROTH RECOVERY = "; FN RD(R5F * 1
     00);"%"
840  PRINT  SPC( 10);"TOTAL"; TAB( 29); FN RD(R3 * 100)
850  FOR I = N1 TO NM%
860 C1(I) = RT(I) * P1(I) / R3
870  PRINT  SPC( 10);A$(I); TAB( 29); FN RD(RT(I) * 100); TAB( 41);
     FN RD(C1(I) * 100)
900  NEXT I
905  PRINT "                        L = "; FN RD(L1);"M"
907  PRINT "          RECYCLE RATIO ="; FN RD(R7C)
910 R5F = R5F - 0.2
920  IF R5F < 0.2 THEN 950
930 L1 = L8
940  GOTO 540
950  PRINT  CHR$ (4);"PR#0"
1000  END
```

Appendix 3. Flowmeter Calibrations

Figure A3-1. Wash water flowmeter calibration

Figure A3-2. Gas flowmeter calibration using a Precision Wet Test Meter.

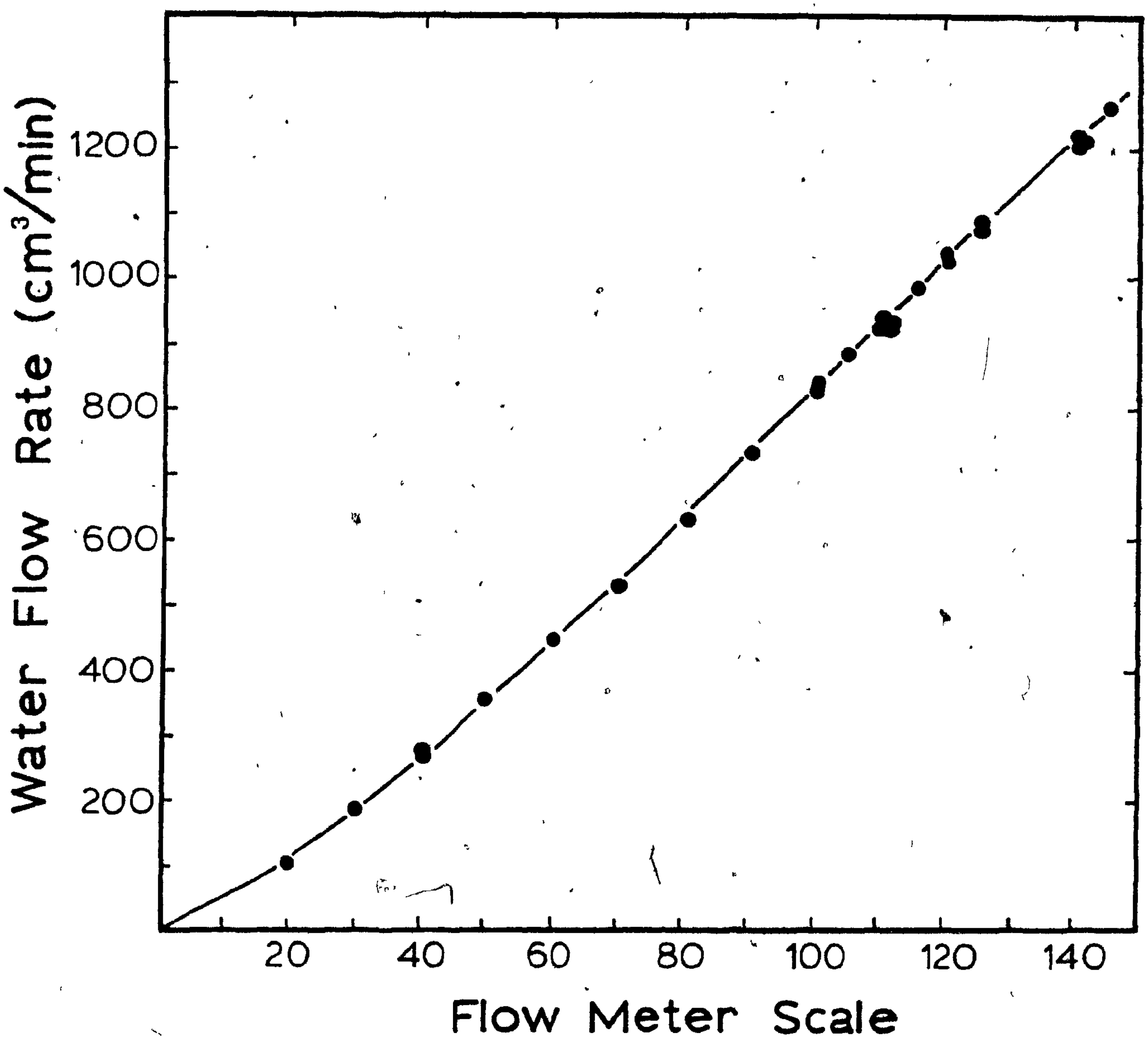

A3-1 Wash water flowmeter calibration.

Brooks R-6-15-B with steel ball.

Water temperature = 21^{o}C.

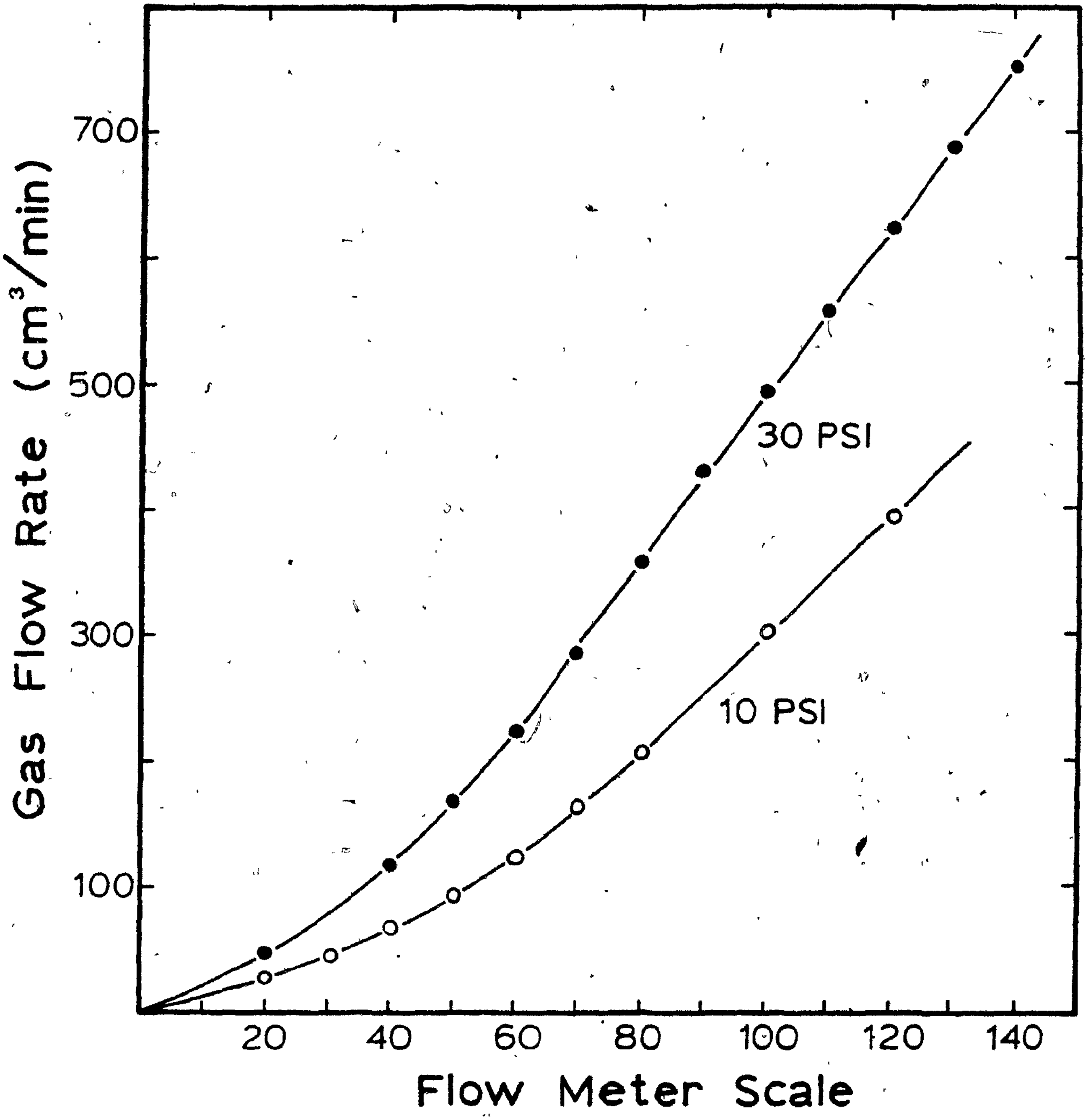

A3-2 Gas flowmeter calibration. Brooks R-2-15-D with plastic ball. Calibrated with Precision Wet Test Meter.